USGS
science for a changing world

Long-Term Continuous Acoustical Suspended-Sediment Measurements in Rivers—Theory, Application, Bias, and Error

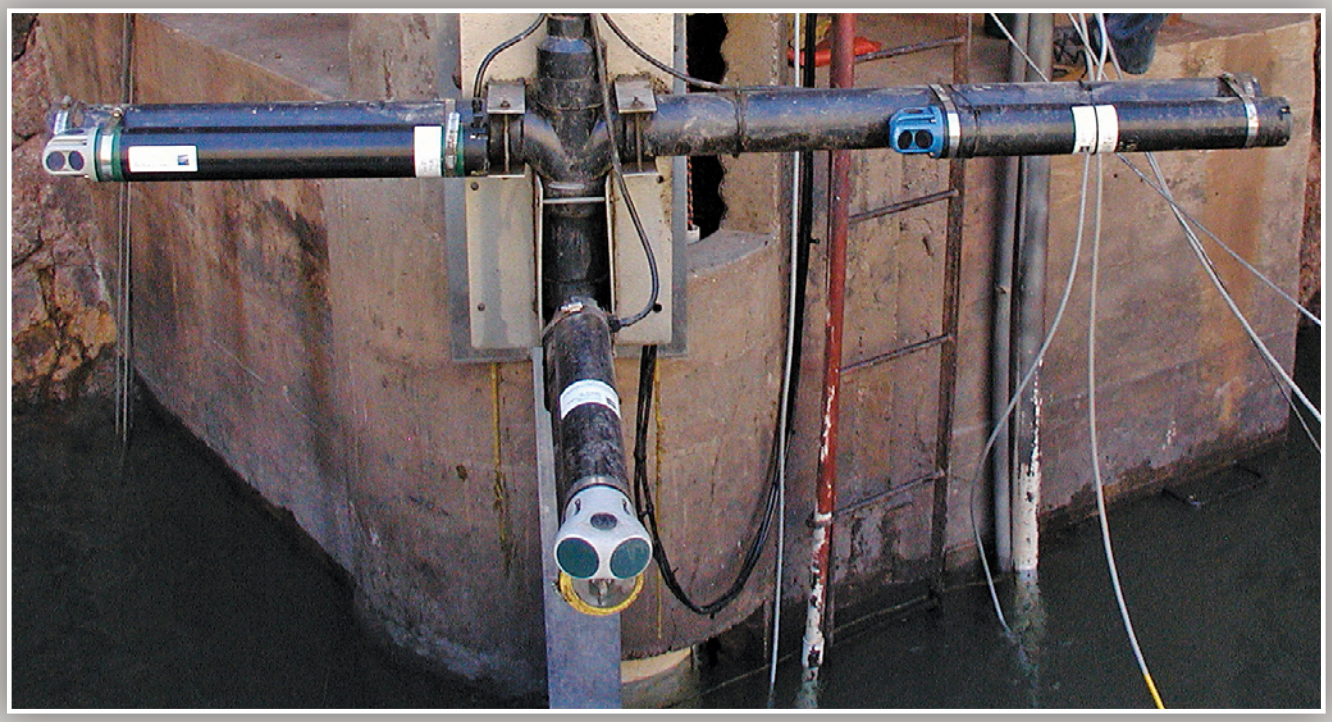

Professional Paper 1823

U.S. Department of the Interior
U.S. Geological Survey

Cover: Array of three single-frequency side-looking acoustic-Doppler profilers at the Colorado River near Grand Canyon, Arizona, gaging station (study site CR87). Array has been raised out of the water for maintenance. From left to right: 2-MHz Nortek EasyQ, 600-kHz Nortek Aquadopp, and 1-MHz Nortek EasyQ acoustic-Doppler profilers.

Long-Term Continuous Acoustical Suspended-Sediment Measurements in Rivers—Theory, Application, Bias, and Error

By David J. Topping and Scott A. Wright

Professional Paper 1823

U.S. Department of the Interior
U.S. Geological Survey

U.S. Department of the Interior
SALLY JEWELL, Secretary

U.S. Geological Survey
Suzette M. Kimball, Director

U.S. Geological Survey, Reston, Virginia: 2016

Suggested citation:
Topping, D.J., and Wright, S.A., 2016, Long-term continuous acoustical suspended-sediment measurements in rivers—Theory, application, bias, and error: U.S. Geological Survey Professional Paper 1823, 98 p., http://dx.doi.org/10.3133/pp1823.

ISSN 1044-9612 (print)
ISSN 2330-7102 (online)

ISBN 978-1-4113-4033-6

Contents

Figures

Tables

Conversion Factors

Inch/Pound to International System of Units

Multiply	By	To obtain
	Length	
inch (in.)	25.4	millimeter (mm)
foot (ft)	0.3048	meter (m)
mile (mi)	1.609	kilometer (km)
	Volume	
ounce, fluid (fl. oz)	0.02957	liter (L)
quart (qt)	0.9464	liter (L)
	Flow rate	
cubic foot per second (ft^3/s)	0.02832	cubic meter per second (m^3/s)
	Mass	
ounce, avoirdupois (oz)	28.35	gram (g)
pound, avoirdupois (lb)	0.4536	kilogram (kg)
	Pressure	
pound per square inch (lb/in^2)	6.895	kilopascal (kPa)
	Density	
pound per cubic foot (lb/ft^3)	16.02	kilogram per cubic meter (kg/m^3)
pound per cubic foot (lb/ft^3)	0.01602	gram per cubic centimeter (g/cm^3)

International System of Units to Inch/Pound

Multiply	By	To obtain
	Length	
millimeter (mm)	0.03937	inch (in.)
meter (m)	3.281	foot (ft)
kilometer (km)	0.6214	mile (mi)
	Volume	
liter (L)	33.82	ounce, fluid (fl. oz)
liter (L)	1.057	quart (qt)
	Flow rate	
cubic meter per second (m^3/s)	35.31	cubic foot per second (ft^3/s)
	Mass	
gram (g)	0.03527	ounce, avoirdupois (oz)
kilogram (kg)	2.205	pound avoirdupois (lb)
	Pressure	
kilopascal (kPa)	0.1450	pound per square inch (lb/ft^2)
	Density	
kilogram per cubic meter (kg/m^3)	0.06242	pound per cubic foot (lb/ft^3)
gram per cubic centimeter (g/cm^3)	62.4220	pound per cubic foot (lb/ft^3)

Temperature in degrees Celsius (°C) may be converted to degrees Fahrenheit (°F) as $°F=(1.8×°C)+32$.

Temperature in degrees Fahrenheit (°F) may be converted to degrees Celsius (°C) as $°C=(°F–32)/1.8$.

Abbreviations

ADP Acoustic-Doppler profiler

BBC Base backscatter calibration

EDI Equal discharge increment

EWI Equal width increment

USGS U.S. Geological Survey

Notation

$2TL$	two-way transmission loss (in units of dB)
a	acoustical measurement of generic quantity in relative error equation (in units of mg/L or mm, depending on whether the error is in concentration or grain size)
a_S	radius of the median size of the suspended sediment (in units of m)
a_T	radius of the transducer (in units of m)
A	acoustic signal strength, including noise (in units of counts)
A_N	instrument noise floor (in units of counts)
A_S	the part of the acoustic signal strength produced by the interaction of the sound emitted by the ADP with the suspended sediment in the moving water (in units of counts)
b	EDI or EWI measurement of generic quantity in relative error equation (in units of mg/L or mm, depending on whether the error is in concentration or grain size)
b_{SF}	scale factor used to convert counts to decibels (in units of dB/count)
$b(\theta,\varphi)$	transmitted beam pattern in spherical coordinates (θ,φ)
$b'(\theta,\varphi)$	received beam pattern in spherical coordinates (θ,φ)
B	relative backscatter (in units of dB)
$\bar{B}$	beam-averaged backscatter (in units of dB)
$\bar{B}_{base}$	beam-averaged base backscatter associated with $C_{XS\text{-}SAND\text{-}REF}$ (in units of dB)
$\bar{B}_{THRESH}$	threshold beam-averaged backscatter (in units of dB) above which a high-dB correction is required
B'	excess backscatter, that is, the backscatter from silt and clay (in units of dB)
B_F	fluid-corrected backscatter (in units of dB)
$B_{1\text{-}LOWf}$	effective lower-frequency $\bar{B}$ associated with the initial lower-frequency estimate of $C_{XS\text{-}SAND}$ in the two-frequency *RUTS*-based calculation of $C_{XS\text{-}SAND}$ and $D_{50\text{-}XS\text{-}SAND}$ (in units of dB)
$B_{2\text{-}LOWf}$	effective lower-frequency $\bar{B}$ associated with the initial higher-frequency estimate of $C_{XS\text{-}SAND}$ in the two-frequency *RUTS*-based calculation of $C_{XS\text{-}SAND}$ and $D_{50\text{-}XS\text{-}SAND}$ (in units of dB)

B_{HIGHf}	effective higher-frequency $\bar{B}$ associated with the initial higher-frequency estimate of $C_{XS\text{-}SAND}$ in the two-frequency *RUTS*-based calculation of $C_{XS\text{-}SAND}$ and $D_{50\text{-}XS\text{-}SAND}$ (in units of dB)
$B_{HIGH\text{-}DEFECT}$	value of *RUTS* along higher-frequency theoretical *RUTS* relation at the value of $D_{50\text{-}XS\text{-}SAND}$ calculated in the two-frequency *RUTS*-based calculation of $C_{XS\text{-}SAND}$ and $D_{50\text{-}XS\text{-}SAND}$ (in units of dB)
$B_{LOW\text{-}DEFECT}$	$B_{1\text{-}LOWf}$ minus $B_{2\text{-}LOWf}$ (in units of dB)
c	measured speed of sound in water (in units of m/s)
c_N	nominal speed of sound in water (in units of m/s)
C	concentration of suspended sediment (in units of mg/L)
C_{SAND}	suspended-sand concentration (in units of mg/L)
C_{XS}	velocity-weighted suspended-sediment concentration in the river cross section (in units of mg/L)
$C_{XS\text{-}SAND\text{-}REF}$	velocity-weighted "reference" concentration of suspended sand in the river cross section (in units of mg/L)
$C_{XS\text{-}SAND\text{-}HIGHf}$	initial $C_{XS\text{-}SAND}$ estimated using the higher-frequency ADP in the two-frequency *RUTS*-based calculation of $C_{XS\text{-}SAND}$ and $D_{50\text{-}XS\text{-}SAND}$ (in units of mg/L)
$C_{XS\text{-}SAND\text{-}LOWf}$	initial C_{SAND} estimated using the lower-frequency ADP in the two-frequency *RUTS* based calculation of $C_{XS\text{-}SAND}$ and $D_{50\text{-}XS\text{-}SAND}$ (in units of mg/L)
$C_{XS\text{-}SAND}$	velocity-weighted suspended-sand concentration in the river cross section (in units of mg/L)
$C_{SILT\text{-}CLAY}$	suspended-silt-and-clay concentration (in units of mg/L)
$C_{XS\text{-}SILT\text{-}CLAY}$	velocity-weighted suspended-silt-and-clay concentration in the river cross section (in unit of mg/L)
D	sediment grain size, that is, diameter (in units of mm)
D_{50}	median grain size of a suspended-sediment grain-size distribution (in units of mm)
$D_{50\text{-}SAND}$	suspended-sand median grain size (in units of mm)
$D_{50\text{-}XS\text{-}SAND}$	velocity-weighted suspended-sand median grain size in the river cross section (in units of mm)
$D_{50\text{-}XS\text{-}SAND\text{-}REF}$	reference D_{50} for a velocity-weighted suspended-sand grain-size distribution in the river cross section (in units of mm)
$D_{50\text{-}XS\text{-}SED}$	velocity-weighted D_{50} of the suspended-sand, silt, and clay mixture in the river cross section (in units of mm)
$D_{50\text{-}XS\text{-}SED\text{-}REF}$	reference D_{50} for a velocity-weighted suspended-sediment grain-size distribution in the river cross section (in units of mm)
DI_T	directivity index for the outgoing (transmitted) acoustic beam (in dB)
E_{68}	relative form (in units of percent) of the 68-percent-confidence level true proxy error
$E_{68\text{-}ABS}$	absolute form (in units of concentration [mg/L] or grain size [mm]) of the 68-percent confidence level true proxy error

E_{95}	relative form (in units of percent) of the 95-percent-confidence level true proxy error
$E_{95\text{-ABS}}$	absolute form (in units of concentration [mg/L] or grain size [mm]) of the 95-percent confidence level true proxy error
$E_{68\text{-FIT}}$	relative form (in units of percent) of the power-law fit to σ of the proxy relative error
$E_{68\text{-FIT-ABS}}$	absolute form (in units of concentration [mg/L] or grain size [mm]) of the power law fit to σ of the proxy relative error
$E_{95\text{-FIT-ABS}}$	absolute form (in units of concentration [mg/L] or grain size [mm]) of the power law fit to 1.96σ of the proxy relative error
$E_{(\text{EDI-EWI})68\text{-ABS}}$	absolute form (in units of concentration [mg/L] or grain size [mm]) of the 68-percent confidence-level combined field and laboratory-processing error in the concurrent EDI or EWI measurement
$E_{(\text{EDI-EWI})95\text{-ABS}}$	absolute form (in units of concentration [mg/L] or grain size [mm]) of the 95-percent-confidence-level combined field and laboratory-processing error in the concurrent EDI or EWI measurement
f	nondimensional form function that describes the backscattering strength of sediment grains in water
f_{REF}	value of f associated with the reference $D_{50\text{-XS-SAND}}$, that is, $D_{50\text{-XS-SAND-REF}}$ (nondimensional)
f_{SED}	value of f calculated for the grain-size distribution of a sand, silt, and clay mixture (nondimensional)
I_0	acoustic intensity at the reference distance 1 m from the transducer (in units of W/m^2)
I_1	acoustic intensity at some greater distance from the transducer (in units of W/m^2)
I_{INC}	incident acoustic intensity on the reverberating volume (in units of W/m^2)
I_R	reflected acoustic intensity from the scatterers in the reverberating volume at a reference distance 1 m in front of the volume (in units of W/m^2)
I_{REF}	reference acoustic intensity in water at 1 μPa one meter from the transducer (in units of W/m^2)
I_{RL}	intensity of the measured reverberation, excluding noise (in units of W/m^2)
k	wave number (in units of 1/m)
K	constant in Thevenot and others' (1992) constant-grain-size backscatter–concentration relation
K_1	constant equal to $-0.1(SL + UTS_{REF})$; this constant is also the regression determined y-intercept of the BBC relation
$K_{1\text{-HIGHf}}$	K_1 for the higher-frequency ADP in the two-frequency *RUTS*-based calculation of $C_{XS\text{-SAND}}$ and $D_{50\text{-XS-SAND}}$
$K_{1\text{-LOWf}}$	K_1 for the lower-frequency ADP in the two-frequency *RUTS*-based calculation of $C_{XS\text{-SAND}}$ and $D_{50\text{-XS-SAND}}$
K_2	regression-determined slope of the BBC relation

$K_{2\text{-HIGHf}}$	K_2 for the lower-frequency ADP in the two-frequency *RUTS*-based calculation of $C_{\text{XS-SAND}}$ and $D_{\text{50-XS-SAND}}$
$K_{2\text{-LOWf}}$	K_2 for the lower-frequency ADP in the two-frequency *RUTS*-based calculation of $C_{\text{XS-SAND}}$ and $D_{\text{50-XS-SAND}}$
K_3	constant in the high-dB correction in appendix 7
L_{BS}	acoustic backscattering length (in units of m)
m_{CELL}	measurement cell number
M	mass concentration of suspended sediment (in units of kg/m^3)
n	number of observations or measurements
N	number concentration of suspended sediment (in units of particles/m^3)
p_{NOISE}	instrument noise-floor pressure (in units of Pa)
p_{SIG}	statistical level of significance
p_{REF}	reference pressure in water (in units of Pa)
p_{rms}	reverberation-level root-mean-square pressure measured at the transducer (in units of Pa)
p_0	source-level pressure at distance r_0=1 m from the transducer (in units of Pa)
P	power of the sound (in units of W)
Q	water discharge (in units of m^3/s)
Q_{THRESH}	threshold water discharge (in units of m^3/s) in the discharge-weighting factor in appendix 7
r	axial distance (range) along the beam from the transducer (in units of m)
r_0	reference distance of 1 m from the transducer (in units of m)
r_{BLANK}	blanking distance (in m)
r_{C}	critical (Fresnel) distance between the near-field and far-field regions (in units of m)
r_{D}	larger critical distance between the near-field and far-field regions used in the Downing and others (1995) empirical near-field correction (in units of m)
RL	reverberation level (in units of dB)
RL_{OFFSET}	linear offset (in units of dB) required to shift decibels calculated using a floating scale within the ADP dynamic range to absolute decibels
$RUTS$	relative unit target strength (in units of dB)
s_{V}	backscattering cross section of a unit reverberating volume (in units of 1/m^3)
S	ratio of $C_{\text{XS-SILT-CLAY}}$ to $C_{\text{XS-SAND}}$ (nondimensional)
SL	source level (in units of dB)
t_{P}	acoustic transmit-pulse (that is, ping) duration (in units of s)
TS	target strength (in units of dB)
TS_{RI}	range-independent target strength (in units of dB)
$TS_{\text{SAND-REF}}$	range-independent target strength of $C_{\text{XS-SAND-REF}}$ (in units of dB)

TS_{SED}	range independent target strength of a sand, silt, and clay mixture in suspension (in units of dB)
UTS	unit target strength (in units of dB)
UTS_{BEAM}	beam component of the unit target strength (in units of dB)
UTS_{REF}	reference unit target strength associated with $D_{50\text{-}XS\text{-}SED\text{-}REF}$ or $D_{50\text{-}XS\text{-}SAND\text{-}REF}$ (in units of dB)
UTS_{SED}	sediment component of the unit target strength (in units of dB)
V	the reverberating volume (in units of m^3)
α	attenuation coefficient resulting from the sum of the water absorption and sediment attenuation coefficients (in units of dB/m)
α_N	attenuation coefficient resulting from the sum of the water absorption and sediment attenuation coefficients (in units of Nepers)
α_S	sediment attenuation coefficient (in units of dB/m)
α_{UNIT}	unit sediment attenuation coefficient (in units of [dB-L]/[m-mg])
α_W	coefficient of absorption for acoustic energy in water (in units of dB/m)
λ	acoustic wavelength (in units of m)
σ	sample standard deviation
σ_G	geometric sample standard deviation
ρ_S	density of suspended sediment (in units of kg/m^3)
ρ_{SAND}	density of suspended sand (set equal to quartz density, that is, 2,650 kg/m^3)
ρ_{SED}	density of a sand, silt, and clay mixture in suspension (in units of kg/m^3)
ρ_W	density of water (in units of kg/m^3)
ψ_{NF}	nondimensional near-field correction
ϕ	unit of sediment grain size, defined as $\phi = -\log_2 D$
Ψ	solid angle of a two-way acoustic beam subtended at the face of the transducer (in units of steradians)
Ω	solid angle (in units of steradians)

Long-Term Continuous Acoustical Suspended-Sediment Measurements in Rivers—Theory, Application, Bias, and Error

By David J. Topping and Scott A. Wright

Abstract

It is commonly recognized that suspended-sediment concentrations in rivers can change rapidly in time and independently of water discharge during important sediment-transporting events (for example, during floods); thus, suspended-sediment measurements at closely spaced time intervals are necessary to characterize suspended-sediment loads. Because the manual collection of sufficient numbers of suspended-sediment samples required to characterize this variability is often time and cost prohibitive, several "surrogate" techniques have been developed for in situ measurements of properties related to suspended-sediment characteristics (for example, turbidity, laser-diffraction, acoustics). Herein, we present a new physically based method for the simultaneous measurement of suspended-silt-and-clay concentration, suspended-sand concentration, and suspended-sand median grain size in rivers, using multi-frequency arrays of single-frequency side-looking acoustic-Doppler profilers. The method is strongly grounded in the extensive scientific literature on the incoherent scattering of sound by random suspensions of small particles. In particular, the method takes advantage of theory that relates acoustic frequency, acoustic attenuation, acoustic backscatter, suspended-sediment concentration, and suspended-sediment grain-size distribution. We develop the theory and methods, and demonstrate the application of the method at six study sites on the Colorado River and Rio Grande, where large numbers of suspended-sediment samples have been collected concurrently with acoustic attenuation and backscatter measurements over many years. The method produces acoustical measurements of suspended-silt-and-clay and suspended-sand concentration (in units of mg/L), and acoustical measurements of suspended-sand median grain size (in units of mm) that are generally in good to excellent agreement with concurrent physical measurements of these quantities in the river cross sections at these sites. In addition, detailed, step-by-step procedures are presented for the general river application of the method.

Quantification of errors in sediment-transport measurements made using this acoustical method is essential if the measurements are to be used effectively, for example, to evaluate uncertainty in long-term sediment loads and budgets. Several types of error analyses are presented to evaluate (1) the stability of acoustical calibrations over time, (2) the effect of neglecting backscatter from silt and clay, (3) the bias arising from changes in sand grain size, (4) the time-varying error in the method, and (5) the influence of nonrandom processes on error. Results indicate that (1) acoustical calibrations can be stable for long durations (multiple years), (2) neglecting backscatter from silt and clay can result in unacceptably high bias, (3) two frequencies are likely required to obtain sand-concentration measurements that are unbiased by changes in grain size, depending on site-specific conditions and acoustic frequency, (4) relative errors in silt-and-clay- and sand-concentration measurements decrease substantially as concentration increases, and (5) nonrandom errors may arise from slow changes in the spatial structure of suspended sediment that affect the relations between concentration in the acoustically ensonified part of the cross section and concentration in the entire river cross section. Taken together, the error analyses indicate that the two-frequency method produces unbiased measurements of suspended-silt-and-clay and sand concentration, with errors that are similar to, or larger than, those associated with conventional sampling methods.

Introduction

The instantaneous concentration of suspended sediment and the instantaneous discharge of water are not well correlated in most rivers because of discharge-concentration hysteresis in one or more size classes of the suspended load. As observed by Gray and Simoes (2008), "a lack of synchronization between peaks of water discharge and sediment concentration over a flood hydrograph is more the rule than the exception." Discharge-concentration hysteresis is common in rivers because it arises from multiple processes.

For example, it can arise from changes in the upstream sediment supply or lags between discharge and dune geometric adjustment during floods (Topping and others, 2000a, 2000b; Kleinhans and others, 2007). Both of these causal mechanisms result in hysteresis in concentration that is systematically coupled to hysteresis in grain size, but in different ways.

Depletion or enrichment of the upstream sediment supply leads to characteristic opposing styles of hysteresis in concentration and grain size during floods. Depletion of the upstream sediment supply leads to clockwise discharge–concentration hysteresis that is coupled to counter-clockwise discharge–grain-size hysteresis, herein referred to as Type 1 hysteresis (fig. 1*A–B*) (for example, Rubin and others, 1998; Dinehart, 1998; Topping and others, 1999, 2000a, b, 2007a). Conversely, enrichment of the upstream sediment supply leads to counter-clockwise discharge–concentration hysteresis coupled to clockwise discharge–grain-size hysteresis, herein referred to as Type 2 hysteresis (fig. 1*C–D*) (for example, Heidel, 1956; Dinehart, 1998; Kleinhans and others, 2007). These two opposing styles of supply-regulation hysteresis arise from the same physical process. Owing to Rouse-style mechanics (for example, McLean, 1992), finer size classes of sediment disproportionately comprise the suspended load, as compared to their proportion on the bed. Therefore, changes in the upstream supply of sediment are manifest to a greater degree in finer size classes of sediment (Topping and others, 2000b), leading to the above-described opposing styles of hysteresis.

Changes in the upstream supply of sediment are not, however, required to produce discharge–concentration hysteresis. Rivers with dunes on the bed may exhibit another type of discharge–concentration hysteresis within size classes of sediment that have essentially unlimited upstream supplies. Because it takes longer for dunes to decay than to build in wavelength and amplitude during floods, dunes in sand-bedded rivers tend to be relatively larger at an equivalent discharge of water during the recession of a flood than during the rising limb (for example, Scott and Stephens, 1966; Julien and Klaassen, 1995). This process of dune geometric adjustment results in greater bed roughness arising from greater dune form drag during the recession than during the rising limb of a flood (Julien and others, 2002; Kleinhans and others, 2007; Shimizu and others, 2009). Because of relatively greater dune form drag (and therefore lesser skin-friction boundary shear stress) during the recession of floods, less overall entrainment of sand and less upward diffusion (by Rouse mechanics) of the coarser size classes of sand occurs during the recession than during the rising limb (Kleinhans and others, 2007). This process generally leads to lower suspended-sand concentrations and finer suspended-sand median grain sizes at the same discharge during the recession than during the rising limb. Thus, the lag between discharge and dune geometric adjustment during floods produces clockwise discharge–concentration hysteresis coupled to clockwise discharge–grain-size hysteresis, herein referred to as Type 3 hysteresis (fig. 1*E–F*).

Because the systematic variation between the discharge of water and suspended-sediment concentration exhibited by discharge–concentration hysteresis is common, calculation of accurate sediment loads in rivers requires that discharge-independent measurements of suspended-sediment concentration be made at intervals shorter than the timescale over which this systematic variation occurs. Moreover, because this systematic variation commonly extends to sand-size sediment, calculation of accurate sand loads requires that these measurements include information on the grain-size distribution of the suspended sediment. This type of discharge-independent suspended-sediment measurement program using conventional sampling techniques is labor-intensive (in the field and in the laboratory), logistically difficult (floods may occur at night), and expensive.

Figure 1. **(following page)** Examples of different types of suspended-sediment hysteresis from three rivers; arrows indicate direction of hysteresis loop. ***A-B***, Type 1 hysteresis evident in suspended-sediment data collected at the Sacramento River at Sacramento, California, U.S. Geological Survey (USGS) gaging station 11447500 (USGS, 2011a). Data collected between November 16, 1964, and April 6, 1965, during a winter flood that peaked at a discharge of 2,820 m^3/s on December 25, 1964. ***A***, Clockwise discharge–concentration hysteresis in both suspended sand and suspended silt and clay. ***B***, Counter-clockwise discharge–median-grain-size hysteresis in the suspended sand. ***C-D***, Type 2 hysteresis evident in suspended-sediment data collected at the San Juan River near Bluff, Utah, USGS gaging station 09379500 (Iorns and others, 1964). Data collected between January 14 and 31, 1952, during a winter flood that peaked at a discharge of ~678 m^3/s on January 19, 1952. On the basis of regional USGS stream-gaging data, most of the water and suspended sediment in this flood likely originated in then-ungaged Chinle Creek, which enters the San Juan River ~30 km upstream from this station. ***C***, Counter-clockwise discharge–concentration hysteresis in both suspended sand and suspended silt and clay. ***D***, Clockwise discharge–median-grain-size hysteresis in the suspended sand. ***E-F,*** Type 3 hysteresis evident in suspended-sand data and Type 1 hysteresis evident in suspended-silt-and-clay data collected at the Mississippi River at St. Louis, Missouri, USGS gaging station 07010000 (Scott and Stephens, 1966; USGS, 2011b). Data were collected between February 13 and August 10, 1961, during the annual flood that peaked at a discharge of 16,700 m^3/s on May 11, 1961. ***E,*** Clockwise discharge–concentration hysteresis in both suspended sand and suspended silt and clay. ***F***, Clockwise discharge–median-grain-size hysteresis in the suspended sand. Error bars in ***A-F*** indicate the 95-percent confidence interval combined field and laboratory processing errors estimated on the basis of the methods of Topping and others (2010, 2011).

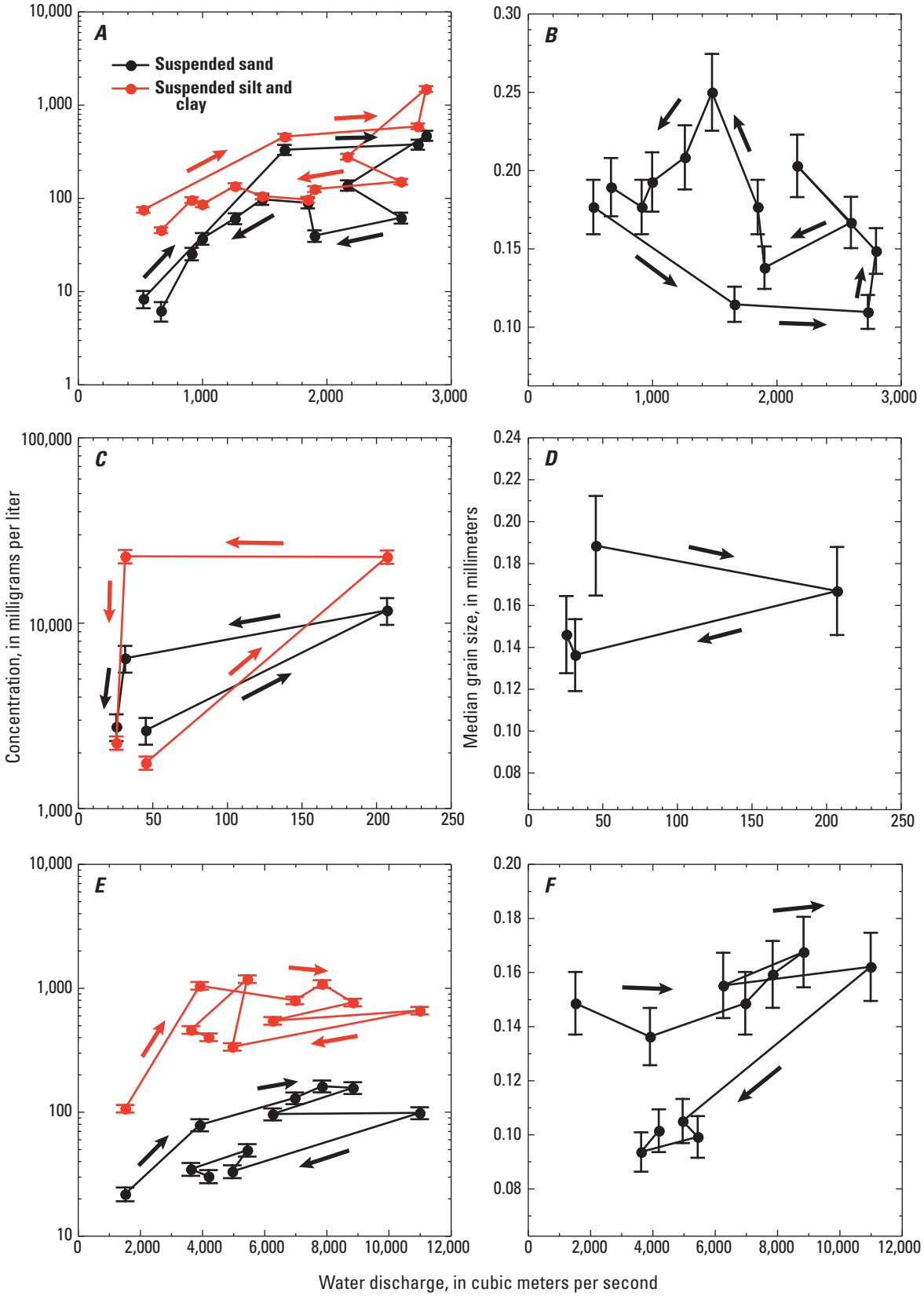
A
Suspended sand
Suspended silt and clay
B
C
D
E
F
Concentration, in milligrams per liter
Median grain size, in millimeters
Water discharge, in cubic meters per second

Figure 1.

Thus, declining budgets contributed to a decline in this type of intensive suspended-sediment monitoring by the U.S. Geological Survey (USGS) in the 1980s (Osterkamp and Parker, 1991). As daily sediment-sampling programs declined in the United States and Canada, it became more attractive to employ less expensive, statistically based monitoring programs that relied on the assumption of a strong correlation and random variability between water discharge and suspended-sediment concentration to reduce the number of required suspended-sediment measurements (Cohn, 1995). As stated in Cohn (1995), "A motivation for developing these methods is economics. Traditional methods for estimating sediment loads (Porterfield, 1972) call for near-daily sampling over many years. Such sampling programs appear to be increasingly vulnerable to government cost-cutting." Unfortunately, the systematic variation exhibited by discharge–concentration hysteresis precludes the supposed cost-effective use of time-invariant sediment rating curves in the calculation of accurate sediment loads in many cases. Use of sediment rating curves in the calculation of accurate sediment or sand loads requires that the variation in suspended-sediment or suspended-sand concentration be random (for example, Cohn and others, 1989) about the best-fit relation between discharge and concentration, an assumption that is clearly invalid in many cases. As a result of the nonrandom variability in concentration about these curves, Glysson and others (2001), in an analysis of sediment data from 10 USGS gaging stations located in different regions of the United States, showed that the absolute value of the error in the annual sediment loads predicted by these curves fit to entire periods of record could equal 526 percent, and errors in the daily sediment loads predicted by sediment rating curves could be as high as 4,000 percent.

Fortunately, the increasing availability of optical and acoustical sensors and associated advances in optical and acoustical theory have opened the possibility that these sensors may be used in conjunction with smaller numbers of conventional suspended-sediment samples to allow accurate sediment loads to be calculated (Gray and Gartner, 2009). Under conditions where suspended-sediment concentrations are not extremely high (that is, not >>1,000 mg/L), and concentration-independent changes in grain size or sediment color do not occur (for example, Conner and DeVisser, 1992; Sutherland and others, 2000; Voichick and Topping, 2014), measurements of optical-backscatterance (Schoellhamer, 2001; Schoellhamer and Wright, 2003) and turbidity (Rasmussen and others, 2009) have been shown to be highly correlated with conventional measurements of suspended-sediment concentration. Melis and others (2002, 2003) and Topping and others (2004, 2006) showed that, if maintenance were conducted at intervals frequent enough to maintain clean optics (every two days to two weeks, depending on location and season), in situ laser-diffraction and transmissometry-based measurements made using conventional-sample-calibrated LISST-100 instruments (Agrawal and Pottsmith, 1994, 2000) could be used to measure the concentration and grain-size distribution of suspended sediment at reasonable accuracy. Topping and others (2004, 2006, 2007b), Wall and others (2006), and Wright and others (2010) showed that acoustical measurements made at a single frequency could be calibrated to yield suspended-sediment concentration measurements in rivers, although these simple single-frequency methods are only accurate under extremely limited ranges of sediment grain size (as shown herein).

Purpose and Scope

In this report, we develop and test a physically based multi-frequency acoustical method for making measurements of the concentration and aspects of the grain-size distribution of suspended sediment in rivers at 15-minute intervals over long-term (that is, decadal) time scales. The biases and errors associated with this multi-frequency method and those associated with simpler single-frequency methods are evaluated. The multi-frequency acoustical method described herein is developed to provide measurements that (1) are not limited to relatively low concentrations of suspended sediment (compared to optical-backscatterance, turbidity, and LISST-100 measurements), (2) are relatively unaffected by changes in sediment grain size (compared to optical-backscatterance, turbidity, and single-frequency acoustical measurements), (3) are unaffected by changes in sediment color (compared to optical-backscatterance and turbidity measurements), and (4) do not require the intense cleaning maintenance that LISST-100 measurements require.

Instruments, Study Sites, and Field Methods

Acoustic-Doppler Profilers

This report presents the results from a 12-year study focused on the development and testing of a physically based method for the continuous measurement of suspended-sediment concentration and grain size at 15-minute intervals in rivers using multi-frequency arrays of single-frequency "side-looking" acoustic-Doppler profilers (ADPs). These arrays typically consist of 1- and 2-MHz single-frequency ADPs; at one study site, a 600-kHz ADP is also included in the array. The term "side-looking" is used to indicate an ADP with transducers that generate horizontal acoustic beams that are oriented roughly perpendicular to the main flow direction. The transducers in these ADPs are ceramic circular piston transducers and are monostatic (meaning that they are used to both transmit and receive sound). Each transducer is mounted on backing disk such that no sound is transmitted behind the plane of the transducer face. The combined ceramic transducer and backing disk is then enclosed within a transducer cup and covered by potting.

The principal type of ADP used in this study is the Nortek EasyQ (Nortek, 2002). Other ADPs used are the OTT SLD (OTT, 2014) and the Nortek Aquadopp profiler (Nortek, 2008). During the course of this study in 2006, Nortek stopped making the EasyQ and transferred manufacturing of this instrument to OTT Hydromet. OTT changed the name of this instrument to the SLD, and in 2008, changed the design of the instrument by removing one transducer, thereby eliminating one beam. These instruments were chosen for this study because they all have internal power regulation (meaning the acoustic source level remains constant regardless of daily fluctuations in battery voltage), they allow measurements to be made in a relatively large number of cells (≥50) along each acoustic beam, and they make measurements along up to four acoustic beams. The EasyQs and SLDs have transducers that generate two horizontal acoustic beams, oriented 50° apart, and one vertical beam; the Aquadopp has transducers that generate only two horizontal beams oriented 50° apart. The EasyQ came in two mounting configurations, horizontal and vertical. The horizontal configuration was the preferred configuration of this instrument because it had a fourth transducer that generated an acoustic beam that was oriented downward at a 45° angle. This fourth beam, absent in the SLD, aided in evaluating data quality, and sometimes allowed correction for sediment deposition on the transducer or organic blockage. If unobstructed by underwater bars or the opposing riverbank, the lengths of the beams along which measurements are made range from 10 to 25 m, depending on ADP frequency.

All ADPs used in this study work by the same principles:

(1) A ping, that is, a short pulse of sound, at a fixed frequency is transmitted through water along a beam. The duration of this pulse is determined by the programmed cell size and speed of sound.

(2) The intensity of sound backscattered from particles in the water following each ping is detected over specific time intervals dependent on the programmed cell size and speed of sound.

(3) The beam-parallel velocity of water in each cell along a beam is computed by measuring the Doppler shift in the frequency of this backscattered sound (Nortek, 2002, 2008, 2013). The beam-parallel velocities in each cell along the beam are then converted to velocities in each cell at the midpoint between the beams using trigonometry.

If no particles (or air bubbles) were present in the water, no sound would be backscattered (described in the next section of this report). In the case of interest, the particles responsible for backscattered sound are mostly suspended sediment, with some additional organic particles. Because air bubbles also cause attenuation and backscatter of sound (see, for example, the discussion on p. 223–229 in Urick, 1975; Medwin and Clay, 1997) and, under certain conditions, can result in greater attenuation and (or) backscatter of sound than suspended sediment, ADPs must be deployed at locations with minimal air bubbles.

EasyQs and SLDs can make acoustical measurements in two modes, a velocity-cell mode and a diagnostics mode (Nortek, 2002). This feature makes these instruments ideal for purposes of making acoustical measurements for velocity and suspended sediment, especially when the conditions at a study site require different measurement-cell configurations for these two purposes. In the velocity-cell mode, the EasyQ and SLD make acoustical measurements in 3–9 cells (depending on the model and year manufactured) along the two horizontal beams. The locations of these velocity cells can be programmed by the user to be anywhere along the lengths of the acoustic beams. In the diagnostics mode, the 1-MHz EasyQ and SLD make acoustical measurements in 64 cells, and the 2-MHz EasyQ and SLD make acoustical measurements in 50 cells. The large number of closely spaced measurement cells in the diagnostics mode is the feature that allows accurate measurements of acoustic attenuation and backscatter to be made by these ADPs, as will be documented below. Diagnostics-mode measurements are the acoustical measurements used in the methods developed in this report when the ADP is either an EasyQ or a SLD.

For all of the ADPs used in this study, the horizontal measurement cells are located at the midpoint between the two horizontal acoustic beams. Because the two horizontal beams are oriented 50° apart, the beam-parallel blanking distances and cell sizes are thus ~10 percent larger (that is, larger by a factor of 1/cos25°) than those programmed by the user. For consistency, this 10-percent increase in blanking distance and cell size applies to all beams, including the vertical beams on the EasyQ and SLD and the 45° downward beam on the EasyQ.

Each acoustical measurement made by an ADP transducer consists of a transmitted ping (that is, pulse), followed by a short period of no transducer activity (that is, blanking) to allow "settling" of the transducer before each receive cycle, followed by a series of receive windows of identical length during which the transducer is "listening" for backscattered sound (Nortek, 2008, 2013). The number of receive windows is equal to the number of programmed cells along the beam generated by the transducer. To ensure that measurement cells are located at consistent, fixed locations along an acoustic beam, ADP transmit pulse, blanking, and receive windows are defined in terms of their lengths (in m). The durations of the transmit pulse, blanking, and receive windows are then calculated on the basis of these defined lengths and the speed of sound. As water temperature, pressure, and (or) salinity change, the durations of the transmit pulse, blanking, and receive windows are modified as a function of the speed of sound so that the locations of the measurement cells remain constant along the beam (Nortek, 2013).

For the ADPs used in this study, the length of the transmit pulse and each subsequent associated receive window is identical, with both varying together as a function of ADP frequency[1]. Longer transmit pulses, and the therefore longer receive windows, are associated with lower frequencies. Blanking distance is generally constant among the ADPs used in this study. Cell size is determined by the convolution of the transmit pulse and receive window, both of which are rectangular functions. Because the length (in m) of the transmit pulse and each receive window is identical, convolution results in a triangular-weighting function (commonly referred to in the signal-processing literature as a triangular, hat, or tent function) in which the full extent of a measurement cell is equal to twice the length of the transmit pulse, but the majority of the backscattered acoustic signal is returned from particles located in only the central 50 percent of a measurement cell (fig. 5-5 in Nortek, 2013). Thus, although the full cell size is twice the transmit-pulse length, because most of the backscatter is from the middle 50 percent of the cell, the nominal cell size is essentially equal to the transmit-pulse length. In the ADPs used in this study, the nominal cell size is the cell size programmed by the user. Although the lengths of the transmit pulse and receive window are equal, the durations are not. Because, in a monostatic system, the distance sound travels from the transducer to each cell and then back to the transducer is twice the distance from the transducer to each cell, to maintain equal lengths between the transmit pulse and each receive window, the durations of the blanking and receive windows are doubled relative to the duration of the transmit pulse. An example is provided in appendix 1 to help explain how transmit-pulse, blanking, and receive-window durations together determine the locations and sizes of the measurement cells along an acoustic beam.

Convolution of the transmit pulse and receive window gives rise to the following series of general equations that describe the location and extent of a measurement cell along an acoustic beam for the case where the lengths of the transmit pulse and receive window are identical (Nortek, 2008; Nortek, 2013). First, the distance (that is, range) from the transducer to the midpoint of a measurement cell is:

$$r = r_{\mathrm{BLANK}} + ct_{\mathrm{P}} m_{\mathrm{CELL}} \tag{1}$$

where

r is distance from the transducer to the midpoint of a cell (in m),
r_{BLANK} is the blanking distance (in m),
c is the speed of sound (in m/s),
t_{P} is the transmit-pulse duration (in s), and
m_{CELL} is the cell number.

The quantity ct_{P} in equation 1 is the transmit-pulse length and is equivalent to the nominal cell size (that is, thickness) programmed into the ADP by the user. The position of the near boundary of a measurement cell, that is, the boundary of a cell nearest the transducer, is:

$$r = r_{\mathrm{BLANK}} + ct_{\mathrm{P}} \left(m_{\mathrm{CELL}} - 1 \right) \tag{2}$$

where

r is now the distance from the transducer to the near boundary of the full extent of a cell (in m);

whereas the position of the far boundary of a measurement cell, that is, the boundary of the cell farthest the transducer, is:

$$r = r_{\mathrm{BLANK}} + ct_{\mathrm{P}} \left(m_{\mathrm{CELL}} + 1 \right) \tag{3}$$

where

r is now the distance from the transducer to the far boundary of the full extent of a cell (in m).

The position of the near boundary of a nominal cell, where, by virtue of the triangular-weighting function most of the backscatter in a measurement cell originates, is:

$$r = r_{\mathrm{BLANK}} + ct_{\mathrm{P}} \left(m_{\mathrm{CELL}} - \frac{1}{2} \right) \tag{4}$$

where

r is now the distance from the transducer to the near boundary of the nominal cell (in m);

whereas the position of the far boundary of a nominal cell is:

$$r = r_{\mathrm{BLANK}} + ct_{\mathrm{P}} \left(m_{\mathrm{CELL}} + \frac{1}{2} \right) \tag{5}$$

where

r is now the distance from the transducer to the far boundary of the nominal cell (in m).

Each ADP was programmed to make time-averaged measurements for 4 minutes out of every 15-minute interval. The 4-minute measurement duration was chosen to be short enough to not consume too much battery voltage and long enough to suitably time average over turbulent fluctuations in suspended-sediment concentration (Topping and others, 2011). ADPs are thus capable of making acoustical measurements over a large horizontal slice of a river cross section for a duration sufficiently long to sample

[1]Transmit pulses and receive windows are of equal length for all Nortek Aquadopp acoustical measurements and diagnostics-mode Nortek EasyQ and OTT SLD acoustical measurements. EasyQ and SLD acoustical measurements made in the velocity-cell mode may have transmit pulses and receive windows that differ in length depending on the programmed locations and sizes of the measurement cells along the acoustic beams.

the suspended-sediment field for statistically stable estimates of the suspended-sediment concentration and grain-size distribution in this ensonified slice. Because of these features, after processing, the acoustical measurements made by the ADP arrays can yield suspended-sediment information with greater spatial and time averaging than optical or automatic-pump methods, both of which can only make point measurements. Table 1 provides a listing of the physical properties of the ADPs (and their settings) that are pertinent to the methods developed in this report.

Study Sites

At each study site, ADPs were rigidly mounted to the riverbank, although in different array configurations depending on the riverbank geometry at each site. The locations along a river at a study site chosen for installation of ADP arrays had the most spatially uniform flow so that the suspended-sediment conditions ensonified by the acoustic beams would be as uniform as possible. Ideally, ADPs are mounted adjacent to each other so that they ensonify the same part of a river cross section, and therefore "sample" the same suspended-sediment conditions. In addition to ADPs, automatic pump samplers were also deployed at these study sites, with Sequoia Scientific Laser In-Situ Scattering and Transmissometry (LISST)-100 type C (Agrawal and Pottsmith, 2000) and (or) LISST-25X type C (Sequoia Scientific, 2010) laser-diffraction instruments also deployed during the first eight years of this study (Melis and others, 2003; Topping and others, 2004, 2006). Description of the calibration and error of the point suspended-sediment measurements made with the automatic pump samplers and LISST instruments are outside the scope of this report and are the subject of a forthcoming paper.

The study sites are located on the Colorado River in Grand Canyon National Park, Arizona, and on the Rio Grande in Big Bend National Park, Texas. The locations of the study sites were chosen on the basis of a need for suspended-sediment data to aid river managers and the location of existing USGS gaging stations. Three of the six study sites were located at USGS gaging stations, two were located in reaches slightly upstream from gaging stations, and one site required installation of a new gaging station. The large range in sediment conditions across the six study sites collectively made them ideal for the purposes of this study, which sought to develop a method that is generally applicable in rivers. The locations of the study sites, as well as downloadable data, are available at http://www.gcmrc.gov/discharge_qw_sediment/ or http://cida.usgs.gov/gcmrc/discharge_qw_sediment/. Study sites on the Colorado River are at the following USGS gaging stations: "Colorado River near river mile 30, 09383050," herein referred to as the CR30 study site; "Colorado River above Little Colorado River near Desert View, AZ, 09383100," herein referred to as the CR61 study site; "Colorado River near Grand Canyon, AZ, 09402500," herein referred to as the CR87 study site; and "Colorado River above Diamond Creek near Peach Springs, AZ, 09404200," herein referred to as the CR225 study site.

Table 1. Acoustic-Doppler profiler properties and settings.

[For the Nortek EasyQ and OTT SLD, the settings described are those associated with the diagnostics mode]

ADP model	2 MHz Nortek EasyQ	2 MHz OTT SLD	1 MHz Nortek EasyQ	1 MHz OTT SLD	600 kHz Nortek Aquadopp
Number of transducers	4	3	4	3	2
Transducer diameter (m)[1]	0.0279	[2]0.025	0.0279	[2]0.045	0.045
Blanking distance (m)[3]	0.22	0.22	0.22	0.22	0.55
Nominal cell size (m)[3]	0.22	0.22	0.44	0.44	0.55
Number of cells along beam	50	50	64	64	50
Transmit-pulse length (m)[3]	0.22	0.22	0.44	0.44	0.55
Receive-window length (m)[3]	0.22	0.22	0.44	0.44	0.55
Ping rate (Hz)	12	12	4	4	4
Averaging window (s)	240	240	240	240	240
Pings per averaging window	2,880	2,880	960	960	960
Measurement interval (s)	960	960	960	960	960

[1]Diameters listed are the active diameters of the ceramic transducers that generate the horizontal beams.

[2]On OTT SLDs, the diameter of the transducer that generates the vertical (stage) beam is smaller than the diameters of the transducers that generate the horizontal beams.

[3]Distances and lengths are beam-parallel and are not the values programmed by the user.

The numbers in these abbreviations refer to the USGS river mile downstream from Lees Ferry, Arizona, the standard geographic convention used for locations along the Colorado River in Grand Canyon National Park. The study sites on the Rio Grande are at the following USGS stations: "Rio Grande above Castolon, TX, 08374535," herein referred to as the RG-CAS study site; and, "Rio Grande above Rio Grande Village, TX, 08375295," herein referred to as the RG-RGV study site. These study sites are respectively located in reaches upstream from the "Rio Grande near Castolon, TX, 08374550" and "Rio Grande at Rio Grande Village, TX, 08375300" USGS gaging stations. In addition to the standard 1- and 2-MHz ADPs, a 600-kHz ADP is also deployed at the CR87 study site. ADPs were deployed at the Colorado River study sites in 2002, and deployed at the Rio Grande study sites in 2010. Detailed descriptions and maps of the Colorado River study sites are provided in Griffiths and others (2012).

Field Methods and Required Field Conditions

Calculation of sediment loads requires integrated measurements of suspended-sediment concentration over the entire river cross section, that is, of the velocity-weighted suspended-silt-and-clay concentration, suspended-sand concentration, and suspended-sand median grain size. By convention, integrated measures of suspended-sediment concentration over an entire river cross section are made using isokinetic depth-integrating samplers that collect a physical sample of the water–suspended-sediment mixture as the samplers move through the water column (Edwards and Glysson, 1999; Topping and others, 2011). When submerged, these samplers continuously collect the water–suspended-sediment mixture at the local flow velocity, hence the term "isokinetic," until the bottle or bag inside the sampler is full (Edwards and Glysson, 1999; Topping and others, 2011; Sabol and Topping, 2013). Because the suspended sediment is being collected at the local flow velocity, the suspended-sediment concentrations measured by these samplers are "velocity-weighted." For brevity, "velocity-weighted suspended-sediment concentration in the river cross section" is hereafter referred to as C_{XS}; "velocity-weighted suspended-silt-and-clay concentration in the river cross section" is hereafter referred to as $C_{XS\text{-}SILT\text{-}CLAY}$; "velocity-weighted suspended-sand concentration in the river cross section" is hereafter referred to as $C_{XS\text{-}SAND}$; and "velocity-weighted suspended-sand median grain size in the river cross section" is hereafter referred to as $D_{50\text{-}XS\text{-}SAND}$. The "XS" in the subscripts of these terms indicates that these concentration and median-grain-size values are associated with the entire river cross section; "XS" does not appear in the subscripts for concentrations or median grain sizes that are more localized in nature, for example, in only the part of the cross section ensonified by the acoustic beams.

The method developed herein calibrates acoustical measurements made along horizontal acoustic beams that "slice" through part of a river cross section in order to calculate the suspended-sediment conditions in an entire river cross section (fig. 2). For this method to work well and produce accurate suspended-sediment measurements, the following conditions must be met:

(1) suspended-silt-and-clay concentration must be approximately uniform along the horizontal acoustic beams and, ideally, relatively uniform across the entire river cross section;

(2) the concentration of organic particles and air bubbles must be minimal, and ideally constant, along the horizontal acoustic beams;

(3) although variation in suspended-sand concentration is permissible between cells along the horizontal acoustic beams, no substantial net change in suspended-sand concentration should occur along the acoustic beams (meaning suspended-sand concentration should not generally increase or decrease along the beams in a net sense); and,

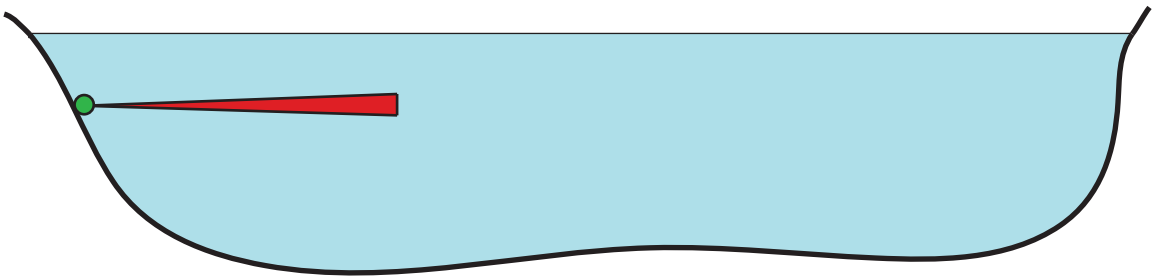

Figure 2. Cartoon sketch of a river cross section showing the location of an acoustic-Doppler profiler array (green). For the method described herein to produce the most accurate results, suspended-sediment conditions (that is, concentration and grain-size distribution) within the part of the river cross section ensonified by the horizontal acoustic beams (red) should be well-correlated with suspended-sediment conditions in the entire river cross section (blue), as described in the text.

(4) the suspended-silt-and-clay concentration, suspended-sand concentration, and suspended-sand grain-size distribution in the part of the cross section ensonified by the acoustic beams should be respectively well correlated with these parameters in the entire cross section, with no strong dependence on an external nonsediment parameter. This requirement means, for example, that suspended-sand concentration should vary over time in the ensonified part of the cross section in approximately the same way that it varies on average in the entire cross section, without this variation changing substantially as a function of water discharge.

Because the goal is to calibrate the acoustical measurements made in part of a river cross section to the suspended-sediment conditions in an entire river cross section, we skip the intermediate step of calibrating the acoustical measurements to the suspended-sediment conditions in the ensonified part of the cross section "sampled" by the acoustic beams. The ramification of this calibration approach is that it is not possible to segregate variation in the calibration, and therefore error in the calibration, that arises from only the acoustical measurements from variation (and error) in the calibration that arises from time-varying differences between suspended-sediment conditions within the ensonified part of the cross section and the entire cross section. Thus, the error we report in the ADP calibrations arises from both processes and cannot be separated.

Equal-discharge-increment (EDI) or equal-width-increment (EWI) suspended-sediment measurements (Edwards and Glysson, 1999), made using depth-integrating samplers, form the basis of the cross-section calibrations of the ADP measurements. The river cross section in which these measurements were made is herein termed the "calibration cross section." Because EDI or EWI measurements cannot typically be made over the entire range of suspended-sediment conditions at each site (most notably the conditions of highest $C_{\text{XS-SILT-CLAY}}$), cross-section-calibrated data collected by automatic pump samplers are used to aid in the development of ADP calibrations, with greater preference being given to the more accurate EDI or EWI measurements. The suspended-sediment measurements used to calibrate ADPs were made in cross sections at or near the locations of the ADP arrays. In the ideal case, ADPs were located within and therefore ensonify part of the calibration cross section, thus likely resulting in the least possible error in the ADP calibrations. As the longitudinal distance between the calibration cross section and the location of the ADP arrays increases, the error in the ADP calibrations is expected to increase. As this distance becomes extremely large (for example, >500 m), there is a chance that the suspended-sediment conditions are only poorly correlated between the calibration cross section and the part of the different cross section ensonified by the ADPs. Descriptions of the calibration measurements, the ADP-array configuration, and the distance between the calibration cross section and the ADP arrays at each study site are provided in appendix 2.

At each study site, the period of data collection was separated into two parts, an initial calibration period where suspended-sediment measurements were used to develop ADP calibrations, and a later verification period where suspended-sediment measurements were used to verify ADP calibrations. In terms of the analyses presented herein, the calibration period was used to calculate in-sample errors and the verification period was used to calculate out-of-sample errors. Depending on the range of measured sediment conditions, the duration of a calibration period at a study site may be one or more years.

Theoretical Framework

The Sonar Equation and Beam-Averaged Backscatter

The initial theoretical development that ultimately led to the use of acoustics to measure suspended-sediment concentrations and grain-size distributions occurred during the early and middle part of the 20th century, and much of this work occurred in the 1940s during World War II (Urick, 1975). Among the most important contributions of this early research were the derivation and formalization of the sonar equations (National Defense Research Committee [NDRC], 1946; Urick, 1962). In our study, the following form of the active-sonar equation from Urick (1975) for a monostatic system is used:

$$SL - 2TL + TS = RL \tag{6}$$

where

SL is the source level,
$2TL$ is the two-way transmission loss,
TS is the target strength, and
RL is the reverberation level in each cell measured by the ADP.

This equation is hereafter referred to simply as the sonar equation. By standard convention, each of the terms in the sonar equation is generally expressed as 10 times a base-10 logarithmic ratio of acoustic intensity, in units of decibels. These intensities are time-averaged quantities, expressed in units of watts per square meter (W/m^2).

Because the objective of this study was to use measurements of acoustic attenuation and backscatter to calculate suspended-sediment concentration and grain size, all terms in equation 6 were derived for the case where all scattering and all particle-related attenuation arise from only suspended sediment. Organic particles and air bubbles can dominate scattering and attenuation under certain conditions (for example, Urick, 1975; Medwin and Clay, 1997).

Backscatter from air bubbles can exceed the backscatter from suspended sediment in the Rayleigh scattering regime (fig. 8.1.2 in Medwin and Clay, 1997). In addition, when the resonant frequency of the air bubbles is near the frequency of the ADP, the backscatter from air bubbles will most likely mask the backscatter resulting from high concentrations of suspended sediment or any other particle (for example, fig. 8.10 in Urick, 1975; fig. 8.1.2 in Medwin and Clay, 1997). With respect to attenuation, bubbles in the ocean have been measured to result in acoustic attenuation exceeding 60 dB/m (p. 289 in Medwin and Clay, 1997), a value slightly higher than the highest value of the sediment attenuation coefficient measured in this study. Therefore, the methods developed on the basis of the derivations of the terms in the sonar equation in this section of the report are limited to cases where only minimal organic particles and air bubbles are present.

Knowing the exact values of all the terms in equation 6 is extremely difficult and not required to calibrate an ADP to measure suspended-sediment concentration. In many studies, only the values of $2TL$, RL, and the range-dependent part of the TS are used to develop approximate calibrations (for example, Thevenot and others, 1992; Gartner, 2004; Wall and others, 2006; Gartner and Wright, 2010; Wright and others, 2010; Wood and Teasdale, 2013). These calibrations are referred to as "approximate" because they do not take into account how changes in the suspended-sediment grain-size distribution affect TS. Depending on ADP frequency and the grain-size distributions in suspension, neglecting effects of changing grain size on TS can lead to substantial biases in ADP measurements of suspended-sediment concentration.

In our study, RL, $2TL$, and all components of the TS are used to develop calibrations that incorporate the effects of changes in both the concentration and grain-size distribution of the suspended sediment. Because SL is constant for a given ADP, we use this term only in the development of the theoretical framework; in the calibration of each ADP, we combine SL, the constant part of the RL, and the constant nonsediment parts of the TS, and replace this combined term with an empirically determined constant. On the basis of NDRC (1946) and Urick (1962, 1975), detailed definitions of the terms in equation 6 are provided in the subsections below. SL is a function of the ADP and is described first, $2TL$ is a function of the medium the sound is passing through (water plus suspended sediment), TS is a function of the properties of the suspended sediment and the acoustic beam, and RL is measured by the ADP.

Source Level

Source level is described by

$$SL = 10\log_{10}\left(\frac{I_0}{I_{REF}}\right) + DI_T \quad (7)$$

where

I_0 is the acoustic intensity at the reference distance 1 m from the transducer,

DI_T is the transmitting directivity index for the outgoing (transmitted) acoustic beam, and

I_{REF}, the reference acoustic intensity in water at 1 µPa, is:

$$I_{REF} = \frac{p_{REF}^2}{\rho_W c_N} \quad (8)$$

where

p_{REF} = 1×10^{-6} Pa is the reference pressure in water,

ρ_W = 1,000 kg/m^3 is the density of water, and

c_N = 1,500 m/s is the nominal speed of sound in water (reported to two significant digits).

For the circular piston transducers in the ADPs used in this study, the transmitting directivity index ranges from 35 to 40 dB on the basis of table 3.2 in Urick (1975) and table 1 in this report. The ADPs used in this study transmit approximately 20 W (Nortek, 2002, 2008). Because intensity is power divided by area, and the area of a sphere is equal to $4\pi r^2$, where r is distance from the acoustic source (that is, transducer) in m, this transmit power corresponds to an I_0=1.59 W/m^2. Substitution of these values into equation 7 yields a source level of ~219 to 224 dB.

Two-Way Transmission Loss

Transmission loss is described by

$$TL = 10\log_{10}\left(\frac{I_0}{I_1}\right) \quad (9)$$

where

I_0 is, again, the acoustic intensity at the reference distance 1 m from the transducer (in W/m^2), and

I_1 is the acoustic intensity at some greater distance from the transducer (in W/m^2).

Transmission losses occur because of geometric spreading of the sound with distance from the source and because of losses of sound in the medium through which the sound propagates. The geometric part of the TL varies as a function of the logarithm of the distance from the source, whereas the "medium loss" part of the TL varies linearly with distance (assuming the properties of the medium are constant along the beam). When the spreading of sound is unconstrained, the geometric part of the transmission loss is best characterized as a spherical spreading loss. Because no medium loss occurs in this first part of the TL, the power of the

sound passing through concentric spheres around the acoustic source must be equal. Therefore, because power is equal to intensity multiplied by area, and the area of a sphere is equal to $4\pi r^2$, equation 9 can be rewritten as:

$$TL = 10\log_{10}\left(\frac{\left(P/\pi r_0^2\right)}{\left(P/\pi r^2\right)}\right) = 10\log_{10}\left(\frac{r}{r_0}\right)^2 = 20\log_{10}\left(\frac{r}{r_0}\right) \quad (10)$$

where

P is the power of the sound (in W),
r is distance from the transducer (in m), and
r_0 is the reference distance of 1 m.

In the region very near the transducer, referred to as the near field, the spreading loss is not spherical owing to a complicated oscillating pressure field in this region in which the pressure amplitude increases to a maximum at a critical distance from the transducer (Lockwood and Willette, 1973). Beyond this critical distance, in the far field, the pressure decreases as a function of distance, as described by equation 10. By convention in the acoustical literature (Kino, 1987), the critical (that is, Fresnel) distance, r_C, is defined as the square of the transducer radius divided by the acoustic wavelength:

$$r_C = \frac{a_T^2}{\lambda} \quad (11)$$

where

a_T is the transducer radius (in m), and
λ the acoustic wavelength (in m).

As indicated by Medwin and Clay (1997), this definition of the critical distance is only approximate, leading some researchers (for example, Downing and others, 1995) to define a larger critical distance, r_D, where:

$$r_D = \pi r_C = \frac{\pi a_T^2}{\lambda}. \quad (12)$$

To correct for the near-field departure from spherical spreading, Downing and others (1995) derived an empirical correction that is commonly used among those making acoustical suspended-sediment measurements (for example, Wall and others, 2006; Wood and Teasdale, 2013; Latosinski and others, 2014). This correction and its effects on measurements made by ADPs in this study are provided in appendix 3. Upon inclusion of a generic near-field correction, the geometric part of the transmission loss in equation 10 becomes

$$TL = 20\log_{10}\left(\frac{r}{r_0}\right) + 10\log_{10}\left(\psi_{NF}\right) \quad (13)$$

where

ψ_{NF} is the nondimensional near-field correction.

Because (1) the ADPs used in this study do not have measurement cells located at distances less than the critical distance r_C, (2) use of the Downing and others (1995) correction generally degrades the ADP measurements of relative backscatter (appendix 3), and (3) use of no correction provides better results at our study sites (appendix 3), we use a near-field correction of ψ_{NF}=1 (that is, no correction).

Medium transmission losses arise from the absorption of the sound by water and from the attenuation of the sound from suspended sediment, organic particles, and (or) air bubbles in the water. Medium transmission losses vary linearly with distance, except for cases where the concentration of suspended sediment is exceedingly high (Hay, 1991). In this study, we assume that the relation between suspended-sediment concentration and attenuation remains approximately linear over the entire range of suspended-sediment concentrations over which ADP acoustical measurements are possible, an approximation that is supported by the results from this study.

Because, in a monostatic system, transmission losses occur between the transducer and each cell twice, that is, once when sound travels from the transducer to the cell and once when sound travels from the cell back to the transducer, the geometric and medium components of the TL are multiplied by 2, summed, and then referred to as two-way transmission losses, $2TL$ (Urick, 1962, 1975):

$$2TL = 40\log_{10}\left(\frac{r}{r_0}\right) + 20\log_{10}\left(\psi_{NF}\right) + 2\alpha_W r + 2\alpha_S r \quad (14)$$

where

$40\log_{10}\left(\frac{r}{r_0}\right)$ is the two-way spherical spreading loss term (in dB),
$20\log_{10}(\psi_{NF})$ is the two-way near-field correction term (in dB),
α_W is the coefficient of absorption for acoustic energy in water (in dB/m), and
α_S is the sediment attenuation coefficient (in dB/m).

In general, α_W depends on water temperature, salinity, and pressure. Under the relatively shallow-water and low-salinity conditions in rivers, however, α_W meaningfully depends only on water temperature (appendix 4). In our study, we use the α_W of Schulkin and Marsh (1962), which is calculated on the basis of varying water temperature while pressure and salinity are held constant at appropriate low values. α_S depends on the properties of the suspended sediment and is discussed in detail in the "Physical Basis for the Sediment Attenuation Coefficient" section below.

Target Strength

In this study, target strength, *TS*, is defined as the echo returned from a given suspension of particles in a volume of water. In this definition, *TS* is composed of two components: a part related to the properties of the suspended sediment, and a part related to the geometry of the reverberating volume in the acoustic beam. In this usage,

$$TS = 10\log_{10}\left(\frac{I_R}{I_{INC}}\right) = 10\log_{10}\left(s_v\right) + 10\log_{10}\left(V\right) \quad (15)$$

where

I_R is the reflected acoustic intensity from the scatterers in the reverberating volume at a reference distance 1 m in front of the reverberating volume (in W/m^2),

I_{INC} is the incident acoustic intensity (that is, the intensity of sound in the transmitted acoustic beam) upon the reverberating volume (in W/m^2),

s_v is the backscattering cross section of a unit reverberating volume, and

V is the reverberating volume, that is, measurement cell (in m^3).

The backscattering cross section of a unit reverberating volume has units of 1/m^3 and depends only on the properties of the scatterers in suspension. For the purposes of this study, the scatterers are assumed to be exclusively sediment grains with a concentration, grain-size distribution, and wet density. The backscattering cross section of a unit reverberating volume is derived below in the "Evaluation of Target Strength from Pressure-Based Re-Derivation of the Sonar Equation" section of this report.

The reverberating volume depends on the properties of the acoustic beam and, at an instant in time is

$$V = \frac{ct_P}{2}\Psi r^2 \quad (16)$$

where

c is the speed of sound (in m/s),

t_P is the acoustic transmit-pulse duration (in seconds), and

Ψ is the solid angle of a two-way acoustic beam subtended at the face of the transducer (in steradians), that is, the two-way beam width.

The reverberating volume is the volume of water containing the scatterers that gives rise to s_V. At an instant in time, this volume is centered distance r from the transducer and has range-gated thickness $ct_P/2$ (fig. 8.4 in Urick, 1975). The acoustical measurements made by ADPs are not at an instant in time, however, but rather are made in measurement cells of finite thickness $2ct_P$, with this larger thickness arising from the convolution of transmit pulses and receive windows of equal length. Thus, the acoustic signal strength reported by an ADP in a given measurement cell does not reflect the intensity of the backscattered sound at an instant in time, but instead is the average of the intensity of the sound backscattered over the entire duration associated with the measurement cell, with most of the backscattered intensity in the average arising from the middle 50 percent of the cell (fig. 5-5 in Nortek, 2013). The classic derivation of the reverberating volume in Urick (1975) is for the different condition where the length of the receive window is much less than the length of the transmitted acoustic pulse. Therefore, the quantity $ct_P/2$ in equation 16 should be replaced by ct_P when using measurements made by the types of ADPs used in this study. For convenience in the derivations of the relative backscatter and fluid-corrected backscatter below, replacement of the quantity $ct_P/2$ in equation 16 with ct_P, substitution of equation 16 into 15, and rearrangement yields

$$TS = 10\log_{10}\left(s_v\right) + 10\log_{10}\left(ct_P\Psi\right) + 20\log_{10}\left(r\right). \quad (17)$$

By definition, the cross-sectional area of the reverberating volume formed by the intersection of the two-way acoustic beam at distance r with a sphere centered on the face of the transducer is thus Ψr^2, where

$$\Psi = \int_0^{4\pi} b(\theta,\varphi)b'(\theta,\varphi)\,d\Omega \quad (18)$$

where

$b(\theta,\varphi)$ is the transmitted beam pattern in spherical coordinates (θ,φ),

$b'(\theta,\varphi)$ is the received beam pattern in spherical coordinates (θ,φ), and

Ω denotes a solid angle (in steradians).

As a result of the beam shaping that occurs between the transmitted and received pulses, that is, how the beam width evolves as a function of the interaction between $b(\theta,\varphi)$ and $b'(\theta,\varphi)$ (for example, fig. 8.3 in Urick, 1975), the two-way beam width is likely ~20 to 30 percent smaller than the width reported by vendors for the transmitted beam (for example, EdgeTech, 2015).

The integral in equation 18 is difficult to solve and has been evaluated using several different methods. One of the more common methods in the literature is to estimate the two-way beam width over only the part of the main lobe of the beam where the acoustic power exceeds –3 dB (that is, exceeds half) of peak power (for example, Hay, 1991; Hay and Sheng, 1992; Thorne and others, 1993). However, because suspended sediment or other particles outside this part of the main lobe still contribute small amounts to the *TS*, it is desirable to solve equation 18 over a larger part of the

two-way beam pattern. The first way this has been done is through application of the concept of the equivalent two-way beam width (Urick, 1975; Simmonds and MacLennan, 2005). As defined in Urick (1975), the equivalent two-way beam width is the two-way width of an idealized acoustic beam where the response is unity within this width and zero outside this width. Mathematically, this method results in $b(\theta,\varphi)$ and $b'(\theta,\varphi)$ both being replaced by one and equation 18 becoming:

$$\Psi = \int_0^{4\pi} b(\theta,\varphi)b'(\theta,\varphi)d\Omega = \int_0^{\Psi}(1)(1)d\Omega\,. \qquad (19)$$

A different, but mathematically equivalent, version of the integral in equation 18 was solved by Thorne and Hardcastle (1997) over the entire main lobe of the acoustic beam for transducers typical of the type used in this study; their solution to this integral is used in this study and is described in the context of equation 15 in the "Evaluation of Target Strength from Pressure-Based Re-Derivation of the Sonar Equation" section of this report below.

Reverberation Level

The reverberation level is defined as

$$RL = 10\log_{10}\left(\frac{I_{RL}}{I_{REF}}\right) = b_{SF}\left(A - A_N\right) + RL_{OFFSET}\,, \qquad (20)$$

where

I_{RL} is the intensity of the reverberation, excluding noise, measured by the ADP in a cell on a beam,

I_{REF} is the reference intensity in water at 1 µPa, as defined in equation 8,

A is the ADP-recorded strength of the returned acoustic signal, including noise, in a cell on a beam (in units of counts),

A_N is the instrument noise floor (in units of counts),

b_{SF} is a scale factor (in units of dB/count) used to convert counts to decibels using a floating scale within the dynamic range of the ADP, and

RL_{OFFSET} is a linear offset (in units of dB) required to shift decibels calculated using a floating scale within the ADP dynamic range to absolute decibels.

[2]Acoustical measurements made in this nonlinear range between the logarithm of the gain setting and A should be avoided. If measurements are made in this range, they may need adjustment as described in appendix 7.

A is a time-averaged quantity measured in each cell along each beam and is commonly referred to as the received signal strength indication, that is, RSSI (Deines, 1999; Lohrmann, 2001); the locations and dimensions of each cell are determined by c and t_p, as described in the previous section. Upon reception at the transducer, the returned acoustic signal is amplified by the electronics in the ADP (Nortek, 2008; Nortek, 2013). Measured in units of counts, the RSSI is an inverse measure of the amount of amplification (that is, gain) that must be applied to a given returned acoustic signal, where the logarithm of the gain setting is inversely proportional to the number of counts (Nortek, 2008). Weaker acoustic returns require greater gain, and are therefore recorded as a lower number of counts. For the ADPs used in this study, the dynamic range in the quantity $b_{SF}A$ is ~90 dB (Nortek, 2002, 2008). The relation between the logarithm of the gain setting and A is linear and has an accuracy of 1 to 2 dB over a 70-dB range (Lohrmann, 2001). Outside this range, that is, at values of the quantity $b_{SF}A$ much greater than ~90 dB, the relation between the logarithm of the gain setting and A is nonlinear (Lohrmann, 2001)[2]. A is recorded in the ADP datalogger to the nearest integer. Therefore, the precision of the RL is limited by the value of b_{SF}. For the ADPs used in this study, 1 count is equal to 0.40 to 0.45 dB within the linear range between the logarithm of the gain setting and A (Nortek, 2008). For these ADPs, the precision in measured A is therefore 0.45 dB within this linear range (Nortek, 2002, 2008).

A is the sum of two components, both measured in counts, such that

$$A = A_N + A_S \qquad (21)$$

where

A_S is the part of the RSSI produced by the interaction of the sound emitted by the ADP with the suspended sediment in the moving water.

The instrument noise floor, A_N, typically ranges from 25 to 30 counts among the ADPs used in this study, and is a combination of noise produced by the ADP electronics and environmental noise. A_N is directly measured by the ADP every 15 minutes (that is, the same interval as measurements of A) by recording the intensity of the backscattered sound in receive windows that are associated with a zero-transmit pulse. Manufacturers do not typically calibrate ADPs so that a given value of A corresponds to a fixed value of decibels. Thus, although the relation between counts and decibels is precise to within 0.45 dB and is accurate to within 1–2 dB in a relative sense within the linear range between the logarithm of the gain setting and A, the relation between counts and decibels is somewhat unconstrained in an absolute sense. In other words, a change in A of +1 count equates to a change in the RL of +0.40 to +0.45 dB, but this change could be, for

example, from 50 dB to 50.40–50.45 dB, or from 60 dB to 60.40–60.45 dB. This "floating-scale" bias is accounted for by the RL_{OFFSET} term in equation 20. In addition to removing the floating-scale bias in RL, the value of RL_{OFFSET} also compensates for any bias in SL. On the basis of full solution of the sonar equation using the version of equation 6 re-derived in the "Evaluation of Target Strength from Pressure-Based Re-Derivation of the Sonar Equation" section of this report below, the value of RL_{OFFSET} was found to typically be in the 75- to 85-dB range among the ADPs used in this study, although in several cases it was much larger. RL_{OFFSET} is required only to close the sonar equation and is not needed or used to develop ADP suspended-sediment calibrations, because the calibrations are instrument specific such that the value of RL_{OFFSET} is embedded in the calibrations.

Because the particles associated with A_S are moving with the water, a Doppler shift is produced, and the frequency associated with A_S is slightly different than the transmitted acoustic frequency. For ADP deployments in rivers, this frequency shift is small and has negligible effect on the accuracy of the methods described in this report. For example, under typical values of c in rivers, when the velocity of water through the acoustic beams is ~3 m/s, the frequency associated with A_S could differ from the transmitted acoustic frequency by as much as 0.2 percent, depending on the angle between the acoustic beams and the velocity vector.

The value of b_{SF} varies substantially between different ADPs (Deines, 1999) and may vary substantially between different beams on the same ADP (Wall and others, 2006). For example, Deines (1999) reported a range of 0.35 to 0.55 in b_{SF} among different model acoustic-Doppler current profilers, and Wall and others (2006) reported a range of 0.41 to 0.46 among different beams on the same acoustic-Doppler profiler. This small variation in b_{SF} is not important, however, because knowing the exact value of b_{SF} is not required to develop accurate ADP calibrations using the methods described in this report, so long as b_{SF} is kept constant for a given ADP. Therefore, in this study, b_{SF} is set equal to 0.43 on the basis of Lohrmann (2001).

Relative Backscatter

The two quantities calculated on the basis of ADP measurements that are used in the methods described in this report to measure suspended-sediment concentration and grain size are the sediment attenuation coefficient, α_S, and the beam-averaged backscatter, $\overline{B}$. To calculate these quantities from the raw measurements of A in each cell on each ADP beam, it is useful to first develop a relation between the relative backscatter, B, and r. Relative backscatter, B, represents the backscatter recorded by the ADP adjusted for losses that occur along the beams; it is the sum of the reverberation level, RL, instrument noise floor (converted to dB using b_{SF}), and the two-way transmission loss, $2TL$, minus the range-dependent part of the TS (that is, the $20\log_{10}r$ term) in equation 17, and the reverberation level offset, RL_{OFFSET}. Following the convention of Thevenot and others (1992), the relative backscatter in each cell on each beam is, thus,

$$B = \left(RL + b_{SF}A_N - RL_{OFFSET}\right) + 2TL - 20\log_{10}\left(r\right). \quad (22)$$

Note that, in this form, the first three terms on the right side are simply equal to $b_{SF}A$ by equation 20. Equation 22 is written in this form because RL_{OFFSET} is an unknown positive constant and A_N is not recorded in the datalogger of every model ADP, whereas A is. Substitution of equations 14 and 20 into equation 22 then yields

$$B = b_{SF}A + 20\log_{10}\left(\psi_{NF}r\right) + 2\alpha_W r + 2\alpha_S r - 40\log_{10}\left(r_0\right). \quad (23)$$

Because r_0=1 m, the $40\log_{10}(r_0)$ term on the right side of equation 23 is zero, and is therefore dropped from equations 24 and 25 below. As everything needed to calculate the first three terms on the right side of equation 23 is stored in the ADP datalogger, for simplification it is convenient to define another term, the fluid-corrected backscatter (Wright and others, 2010), as

$$B_F = b_{SF}A + 20\log\left(\psi_{NF}r\right) + 2\alpha_W r, \quad (24)$$

which allows equation 23 to be written in the following simplified form:

$$B = B_F + 2\alpha_S r, \quad (25)$$

where

B is the relative backscatter (in dB),
B_F is the fluid-corrected backscatter (in dB),
α_S is the sediment attenuation coefficient (in dB/m), and
r is the distance from the transducer to the midpoint of each measurement cell (in m).

When two horizontal beams are used on an ADP, B_F in each cell is calculated on the basis of A averaged among equivalent cells on each beam. This "beam averaging" among equivalent cells allows greater accuracy in the calculation of α_S (described below) because the ensonified volume used to calculate α_S is doubled in comparison to that associated with only one beam.

Calculation of the Sediment Attenuation Coefficient and Beam-Averaged Backscatter

For the condition where the concentration, density, and grain-size distribution of suspended sediment are all approximately constant along the horizontal acoustic beams, there is no net change in B along the beams. Under this assumed condition, all variation in B should average out along the beams (or at least over most of the beams), and B can therefore be treated as constant along the beams for any single ADP measurement. When B is held constant along the beams, the sediment attenuation coefficient α_S can then be calculated using a least-squares linear regression between B_F and r (after Topping and others, 2006, 2007b) while iteratively solving for the effective noise floor. The effective noise floor is related to curvature in the measurements of A along the acoustic beams as the noise floor is approached, and is greater than the instrument noise floor, A_N. Determining the effective noise floor is an iterative process described completely in appendix 7. In this regression, α_S is equal to –1/2 times the slope of the relation between r and B_F. Once α_S is known, B is then calculated in each cell where A exceeds the effective noise floor (using equation 23) and then averaged among the equivalent cells in each beam used. Once this first beam-averaging step is completed, the values of B in each cell are then averaged among all cells along the beams where A exceeds the effective noise floor. This final averaged quantity is termed the beam-averaged backscatter, $\overline{B}$, used extensively below. Figure 3 illustrates the steps required to compute the fluid-corrected backscatter, sediment attenuation coefficient, relative backscatter, and beam-averaged backscatter for several measurements from the CR87 study site.

Physical Basis for the Sediment Attenuation Coefficient

Acoustic attenuation caused by the presence of suspended sediment arises from two distinctly different physical processes that vary in importance largely as a function of ADP frequency, sediment grain size, and sediment density (Flammer, 1962; Flammer and others, 1969). These include losses arising from viscous drag between the water and sediment grains (Urick, 1948), and losses arising from the scattering of sound by sediment grains in directions other than “back” toward the detector (Lamb, 1945; Urick, 1948; Morse, 1948; Sheng and Hay, 1988; Hay, 1991; Schaafsma and Hay, 1997; Thorne and Buckingham, 2004; Thorne and Meral, 2008). For typical ADP frequencies, viscous losses dominate when the suspended sediment is relatively fine, whereas scattering losses dominate when the suspended sediment is relatively coarse. The transition between these two loss regions depends largely on acoustic frequency, the characteristics of the suspended-sediment grain-size distribution, and sediment density (Urick, 1948; Flammer, 1962; Flammer and others, 1969; Moore and others, 2013). Flammer (1962) and Flammer and others (1969) divided the scattering-loss region into three parts: a scattering-loss region where losses were produced primarily by redirection of sound away from the direction of the detector, a diffraction-loss region where larger sediment grains “shadowed” other grains in addition to redirecting the sound away from the detector, and a transition-loss region between the scattering and diffraction loss regions. Most recent investigators have treated Flammer’s (1962) scattering, transition, and diffraction-loss regions as one scattering-loss region (Sheng and Hay, 1988; Hay, 1991, Thorne and others, 1993; Schaafsma and Hay, 1997; Thorne and Buckingham, 2004; Thorne and Meral, 2008; Moore and others, 2013). In this study, we follow this more-recent convention and distinguish only between viscous- and scattering-loss regions.

In this study, we calculate the sediment attenuation coefficient (α_S) for each ADP measurement using the least-squares linear regression between B_F and r, described in the previous section of the report, and then compare this empirical measurement of α_S with theoretically predicted values of α_S at multiple acoustic frequencies to estimate the grain-size distribution of the suspended sediment that gives rise to the acoustic attenuation. Our study uses the conventions of Urick (1948), Flammer (1962), Hay (1983), and Moore and others (2013) to calculate this theoretical value of α_S that includes the effects of both viscous and scattering losses. In addition, we use the approach of Thorne and Meral (2008) and Moore and others (2013) to account for the effect on α_S of multiple grain sizes of sediment. Finally, we follow Moore and others (2013) and correct for the fact that probability density functions describing grain-size distributions measured in the laboratory are not equivalent to those derived in the acoustical literature.

Acoustical theory typically treats sediment grain-size distributions as “number size distributions,” where particles are treated identically regardless of their size. Sediment grain-size distributions are, however, always measured in the laboratory in terms of either the mass or volume of sediment in each size class. Thus, a sediment grain-size distribution measured in a laboratory must be converted to a “number size distribution” before either the form function or scattering cross section (Thorne and Meral, 2008) associated with this grain-size distribution can be calculated. This mathematical operation is conducted by simply dividing the measured amount (mass or volume) of sediment in each size class by the volume of a sediment grain in that size class. So long as the sediment density is constant across the grain-size distribution, dividing by volume has the equivalent effect of dividing by mass in making this correction, regardless of whether the grain-size distribution was analyzed by volume or mass in the laboratory.

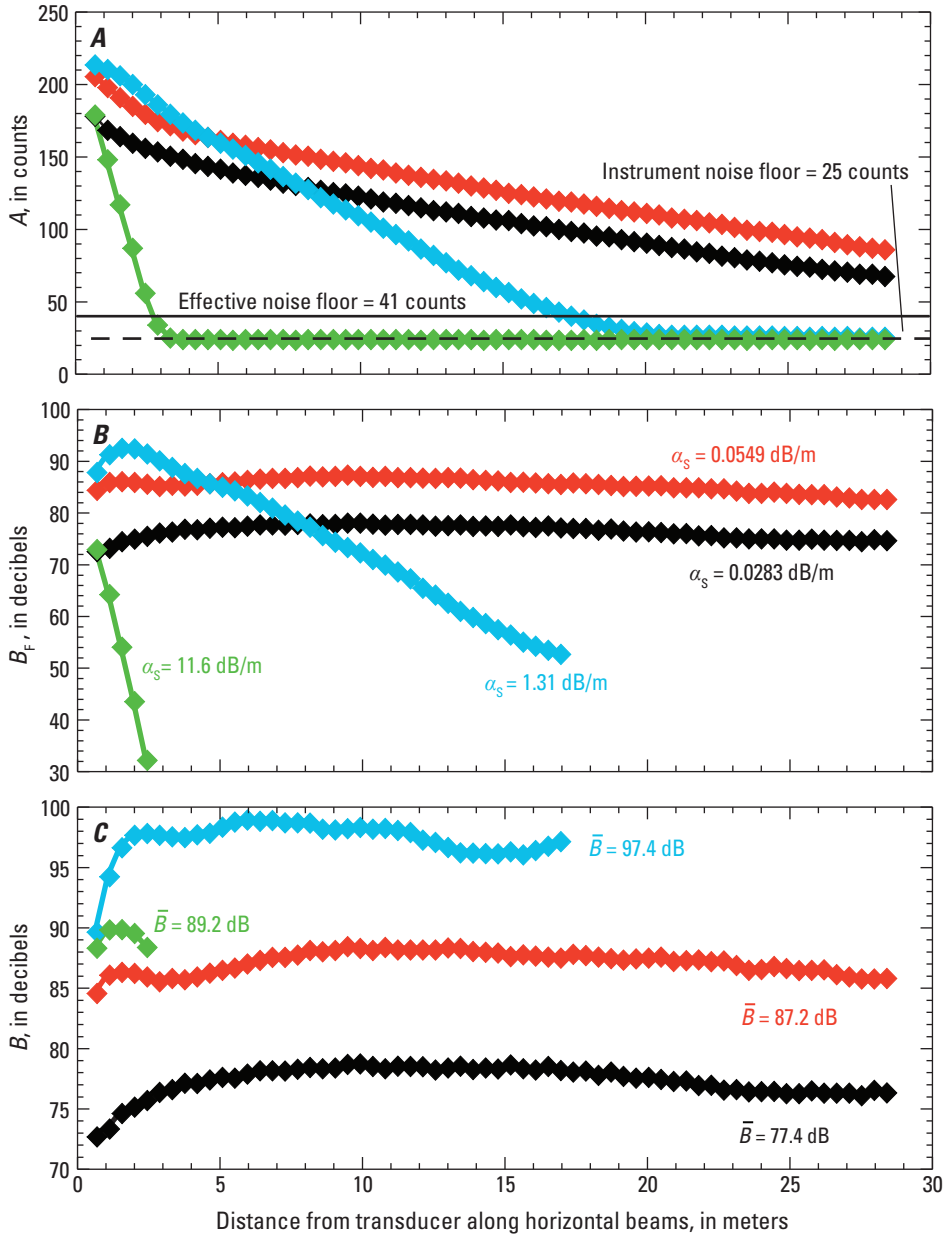

Measurement number	$C_{XS\text{-}SILT\text{-}CLAY}$	$C_{XS\text{-}SAND}$	$D_{50\text{-}XS\text{-}SAND}$
1	37.9 ±2.7	23.2 ±3.1	0.116 ±0.011
2	76.4 ±5.4	335 ±41	0.116 ±0.011
3	1,940 ±140	4,330 ±530	0.115 ±0.011
4	17,500 ±1,000	281 ±29	0.090 ±0.009

Figure 3. Examples of the steps in the conversion from the raw acoustical measurements (in counts) to beam-averaged backscatter (in dB) for four very different suspended-sediment conditions at the CR87 study site. Acoustical measurements are from the 1-MHz acoustic-Doppler profiler (ADP). Measurement 1 was made at 17:34 on March 2, 2007; measurement 2 at 17:47 on January 29, 2008; measurement 3 at 15:17 on March 6, 2008; and measurement 4 at 6:35 on August 25, 2012. Indicated values of $C_{XS\text{-}SILT\text{-}CLAY}$ (in mg/L), $C_{XS\text{-}SAND}$ (in mg/L), and $D_{50\text{-}XS\text{-}SAND}$ (in mm) with 95-percent-confidence-level errors are from concurrent equal-discharge increment measurements. ***A***, Acoustic signal strength, *A*, averaged between the corresponding cells (1–64) in the two horizontal acoustic beams plotted as a function of *r*. Shown are the instrument noise floor of 25 counts (dashed horizontal line) and the effective noise floor of 41 counts (solid horizontal line), calculated on the basis of an iteratively determined best noise-floor offset of 16 counts. ***B***, Fluid-corrected backscatter, B_F, plotted as a function of *r*. Shown for each measurement are the values of α_S determined by least-squares linear regressions fit to the values of B_F. ***C***, Relative backscatter, *B*, plotted as a function of *r*. Shown for each measurement are the values of the beam-averaged backscatter, $\bar{B}$.

Following Urick (1948), α_S is the product of the unit sediment attenuation coefficient, α_{UNIT}, and the concentration of suspended sediment, C:

$$\alpha_S = \alpha_{UNIT} C \,. \tag{26}$$

In our study, α_{UNIT} is defined as α_S at a suspended-sediment concentration of 1 mg/L, where α_S is expressed in units of dB/m and C expressed in units of mg/L. α_{UNIT} is the combined ensemble-averaged viscous- and scattering-loss attenuation coefficient and is derived in this study using equations 4–10 in Moore and others (2013), and making the appropriate conversions, such that α_{UNIT} is expressed in units of decibel-liter per meter-milligram or [dB-L]/[m-mg]. Importantly, the following four conditions are assumed for equation 26 to apply: the suspended-sediment grains are randomly distributed within the ensonified volume of water, the scattering is incoherent, the effects of multiple scattering are unimportant, and the effects of extremely high concentrations on attenuation are also unimportant.

Changes in the sorting of the suspended-sediment grain-size distribution have a major effect on α_{UNIT}. As illustrated by Moore and others (2013) and suggested by Flammer (1962), a grain-size distribution of sediment with median grain size D_{50} has different attenuation characteristics than does sediment of uniform size; the grain-size distribution tends to have lower peaks and higher troughs in the D_{50}–α_{UNIT} relation (fig. 4*A*). As the sorting of the suspended-sediment grain-size distribution decreases (meaning the geometric sample standard deviation, σ_G, of the distribution increases), the magnitudes of the viscous-loss maximum and scattering-loss maximum in α_{UNIT} both decrease while the magnitude of the minimum in α_{UNIT} between the viscous- and scattering-loss regions increases. As the magnitudes of the two maxima decrease, the positions of these maxima shift to the right in figure 4*A*, meaning that the D_{50} associated with the viscous- and scattering-loss maxima in α_{UNIT} both increase slightly. In contrast, as the magnitude of the minimum increases, the position of the minimum between the viscous- and scattering-loss regions shifts to the left and the D_{50} associated with this minimum in α_{UNIT} decreases. Ultimately, as the sorting becomes extremely poor and σ_G increases to ~4ϕ, the minimum in α_{UNIT} between the viscous- and scattering-loss regions disappears. In this report, all grain-size distributions are approximated as log-normal distributions, and sorting of sediment is measured using ϕ units, defined as: $\phi = -\log_2 D$, where D is the diameter of the sediment grain in mm (Krumbein, 1936).

Changes in the density of suspended sediment (ρ_S) also result in large changes in the magnitudes of the maxima in α_{UNIT} and a slight shift in the position of the minimum in α_{UNIT} between the viscous- and scattering-loss regions (fig. 4*B*). In cases where the suspended sediment is dominated by clay, and depending on whether the clay in suspension is composed dominantly of smectite-, kaolin-, illite-, or chlorite-group minerals, the density of the suspended sediment can vary from ~1,800 kg/m³ to ~3,300 kg/m³ (DeWit and Arens, 1950; Deer and others, 1966; Gartner and Carder, 1979). The wet density of montmorillonite determines the lower limit of this range and the (wet or dry) density of chlorite determines the upper limit of this range. Not only does the density vary between different clays, but the density of kaolin- illite-, and smectite-group clays generally decreases when wet as water gets absorbed into and adsorbed onto the clay structure (DeWit and Arens, 1950; Deer and others, 1966; Gartner and Carder, 1979). Among the clays that decrease in density when wet, smectite-group clays have the largest decrease in density and kaolin-group clays have the least decrease in density. Voichick and Topping (2014) showed empirically that, absent any major change in silt and clay grain-size distribution, changes in the amount of smectite comprising the suspended clay results in large changes in α_S. Their analysis showed that, in cases where the suspended clay was composed of less smectite than normal, α_S was approximately twice that under more typically smectite-rich silt-and-clay conditions. To illustrate why this observed difference occurred, an example of a theoretical D_{50}–α_{UNIT} relation for three sediment densities is shown in figure 4*B*. The three densities used in this example are: (1) the standard 2,650 kg/m³ quartz density that best approximates the typical densities of sand and silt, (2) the 3,300 kg/m³ density that is the upper limit of chlorite density, and (3) the density of 1,800 kg/m³ (DeWit and Arens, 1950; Gartner and Carder, 1979) that best approximates the fully saturated wet density of montmorillonite, a dominant smectite-group clay mineral found in the suspended sediment of the tributaries of the Colorado River in the study area (Beverage and Culbertson, 1964). For simplicity, the values of α_{UNIT} in this example were calculated for constant sediment density across the entire grain-size distribution.

The example in figure 4*B* shows that changes in sediment density result in major changes in the magnitudes of the viscous-loss (left peak) and scattering-loss maxima (right peak). In addition, changes in sediment density also result in slight changes in the D_{50} associated with these maxima (especially in the case of the viscous-loss maximum). As sediment density increases from 2,650 to 3,300 kg/m³, the magnitude of the viscous-loss maximum in α_{UNIT} is predicted to increase by ~31 percent and the magnitude of the scattering-loss maximum in α_{UNIT} is predicted to decrease by ~17 percent. Conversely, as sediment density decreases from 2,650 to 1,800 kg/m³, the magnitude of the viscous-loss maximum in α_{UNIT} is predicted to decrease by roughly a factor of two and the magnitude of the scattering loss maximum in α_{UNIT} is predicted to increase by roughly a factor of 1.5. Although this increase in the scattering-loss maximum may seem unrealistic, because the density of sand-size sediment typically remains constant at ~2,650 kg/m³ in rivers, flocs of low-density clay can approach

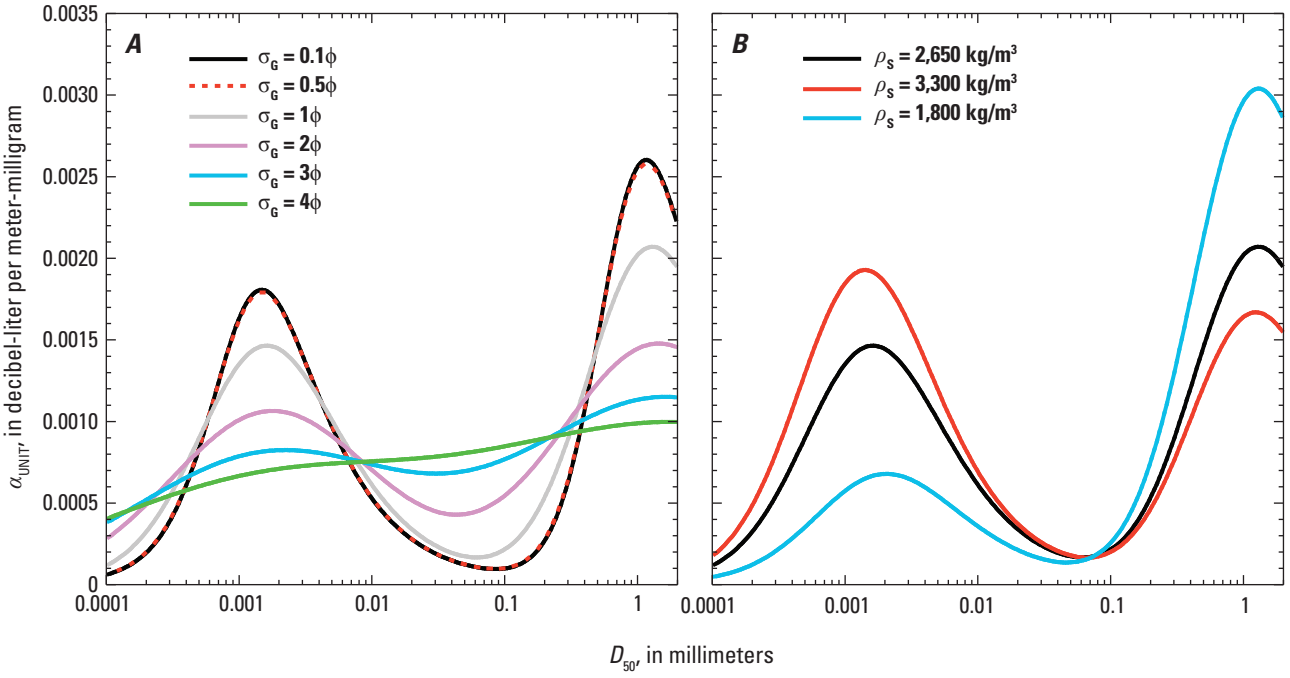

Figure 4. Effects of changes in (***A***) sediment sorting and (***B***) sediment wet density (ρ_S) on α_{UNIT}, at an acoustic frequency of 1 MHz. ***A***, Predicted values of α_{UNIT} at the 1-MHz frequency for the median grain size (D_{50}) of log-normal suspended-sediment grain-size distributions with geometric standard deviations (σ_G) of 0.1ϕ, 0.5ϕ, 1ϕ, 2ϕ, 3ϕ, and 4ϕ. The wet density of the suspended sediment is held constant at 2,650 kg/m³ (quartz density) in this example. ***B***, Predicted values of α_{UNIT} at the 1-MHz frequency for the D_{50} of a log-normal suspended-sediment grain-size distribution with σ_G=1ϕ and sediment densities of 2,650 kg/m³ (quartz density), 3,300 kg/m³ (chlorite density), and 1,800 kg/m³ (fully-saturated montmorillonite wet density). Although α_{UNIT} is predicted to decrease as wet density decreases for silt-and-clay-sized sediment, α_{UNIT} for sand-size flocs of fully saturated montmorillonite is predicted to exceed the values of α_{UNIT} for quartz-density sand.

1 mm in diameter under the right conditions, especially in estuaries and marine environments (Dyer and Manning, 1999; Hill and others, 2001; Curran and others, 2007), and the formation of flocs can substantially alter the acoustic backscattering and attenuation characteristics of suspended clay (MacDonald and others, 2013; Rouhnia and others, 2014; Thorne and others, 2014).

In addition to the controls of sediment sorting and density, acoustic frequency also exerts a strong control on α_{UNIT} (fig. 5*A*). For a given sorting, as acoustic frequency increases, the magnitude of α_{UNIT} increases and the positions of the maxima and minimum in the D_{50}–α_{UNIT} relation shift to the left. Because of this leftward shift, the D_{50} associated with the transition from viscous (left peak) to scattering (right peak) losses decreases as ADP frequency increases. For example, for grain-size distributions with σ_G=1ϕ, the 600-kHz transition from viscous to scattering losses dominating α_{UNIT} occurs at a D_{50} of ~0.1 mm, whereas the 3-MHz transition from viscous to scattering losses dominating α_{UNIT} occurs at a D_{50} of ~0.025 mm (fig. 5*A*).

From the example in figure 5*A*, it is evident that there exists an optimal range of acoustic frequency, suspended-sand D_{50}, and suspended-silt-and-clay D_{50} where the sand contributes very little to α_{UNIT} and the sediment attenuation coefficient can be approximated as

$$\alpha_S \approx \alpha_{UNIT} C_{SILT\text{-}CLAY} . \quad (27)$$

In many rivers, the D_{50} of the suspended sand ranges from 0.0625 to ~0.25 mm (very fine to fine sand) and the D_{50} of the suspended silt and clay ranges from ~0.0005 to ~0.01 mm (fine clay to fine silt). For the sorting of the grain-size distributions portrayed in figure 5*A*, these D_{50} result in a fair degree of separation between the value of α_{UNIT} associated with the sand and the value of α_{UNIT} associated with the silt and clay, especially at the 600-kHz and 1-MHz acoustic frequencies. For these D_{50} and ADP frequencies, $C_{XS\text{-}SILT\text{-}CLAY}$ can be reasonably accurately predicted by α_S so long as the following three conditions are met: (1) the suspended-silt-and-clay concentration ($C_{SILT\text{-}CLAY}$) is approximately uniform within the ensonified volume along the acoustic beams, (2) the spatial distribution of suspended silt and clay in the river cross section is approximately uniform such that $C_{SILT\text{-}CLAY}$ in the ensonified volume is approximately equal to $C_{XS\text{-}SILT\text{-}CLAY}$, and (3) the suspended-sand concentration (C_{SAND}) does not greatly exceed the suspended-silt-and-clay concentration ($C_{SILT\text{-}CLAY}$) along the

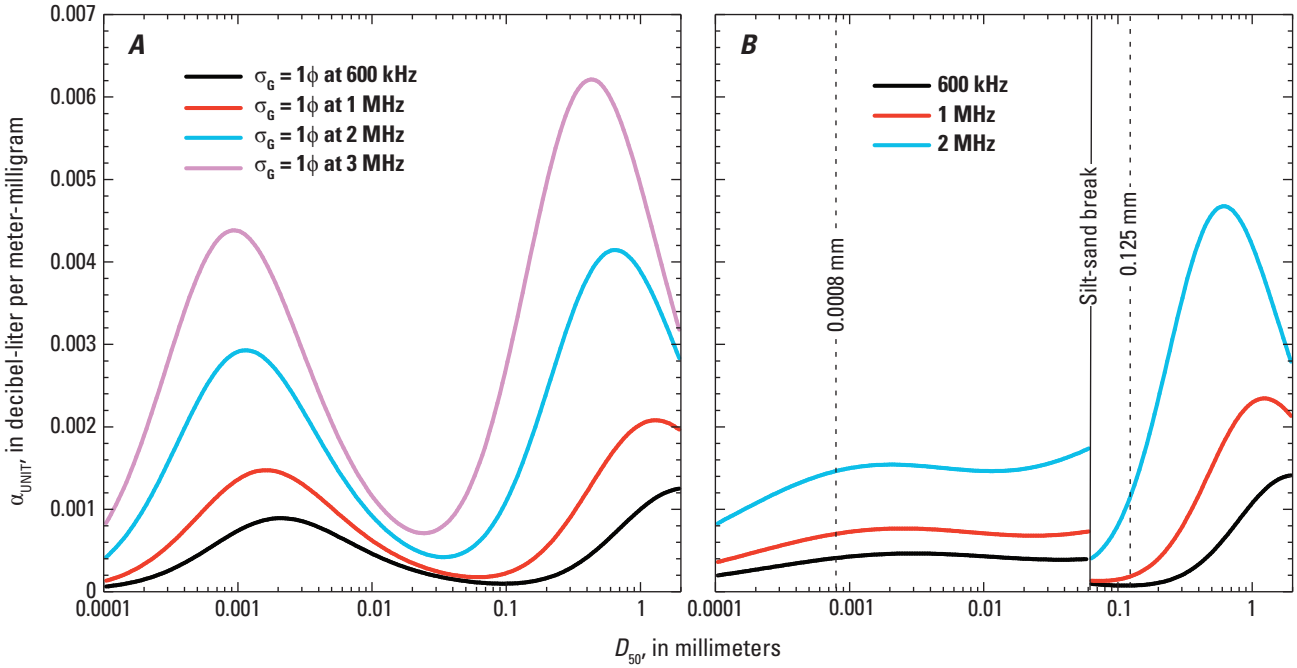

Figure 5. Effects of acoustic frequency and grain-size-dependent differences in sorting on α_{UNIT}. ***A***, Predicted values of α_{UNIT} at acoustic frequencies of 600 kHz, 1 MHz, 2 MHz, and 3 MHz for the D_{50} of log-normal suspended-sediment grain size distributions with σ_G=1ϕ. ***B***, Predicted values of α_{UNIT} at acoustic frequencies of 600 kHz, 1 MHz, and 2 MHz for the likely typical case where the suspended silt and clay is much more poorly sorted than the suspended sand and has slightly lower density than the suspended sand. σ_G=3ϕ and ρ_S=2,500 kg/m^3 for all silt-and-clay-sized sediment and σ_G=0.63ϕ and ρ_S=2,650 kg/m^3 for all sand-size sediment in this plot. The unrealistic downward step changes in the values of α_{UNIT} at the silt-sand break are artifacts mostly of the abrupt decrease in σ_G at the silt-sand break. In reality, the decrease in σ_G across this break is likely more gradual, resulting in more gradual decreases in the values of α_{UNIT} across the silt-sand break. Indicated are the typical D_{50} values measured for the suspended sand (0.125 mm) and calculated for the suspended silt and clay (0.0008 mm) at the CR87 study site. Among 1,770 equal discharge increment (EDI) measurements made at this site between 1999 and 2013, the mean D_{50} of the suspended sand was 0.125 mm (to the nearest ¼-ϕ increment) and the mean σ_G of the suspended sand was 0.63ϕ.

acoustic beams. This result allowed Topping and others (2006, 2007b) and Wright and others (2010) to develop their first-cut single-frequency approximate method of using acoustic attenuation to measure $C_{XS\text{-}SILT\text{-}CLAY}$ and acoustic backscatter to measure $C_{XS\text{-}SAND}$, as reviewed by Hanes (2012, 2013).

Sorting differences between the grain-size distributions of the suspended sand and the suspended silt and clay will typically increase the separation between the value of α_{UNIT} associated with the sand and the value of α_{UNIT} associated with the silt and clay, making the key assumption in the method of Topping and others (2006, 2007b) and Wright and others (2010) expressed by equation 27 all the more valid, especially at the 600-kHz frequency. In the Colorado River and Rio Grande basins, the sorting of the suspended sand is much better than the sorting of the suspended silt and clay, a condition that is likely in most rivers. For example, in each of the 22 rivers selected by Wright and others (2010) to be representative for rivers in all regions of the United States, σ_G for the suspended silt and clay was much larger than σ_G for the suspended sand (on the ϕ scale). At the Colorado River and Rio Grande study sites, σ_G of the suspended sand measured among many EDI and (or) EWI measurements was ~0.63 to 0.65ϕ, whereas σ_G of the suspended silt and clay was estimated to range from ~2.5 to 3.0ϕ. An example of how these sorting differences increase the separation between the sand α_{UNIT} and the silt and clay α_{UNIT} at the CR87 study site is provided in figure 5*B*.

Figure 5*B* illustrates that the separation between the sand α_{UNIT} and the silt and clay α_{UNIT} is much greater at lower acoustic frequencies. At 2 MHz, the silt and clay α_{UNIT} is 1.4 times the value of the sand α_{UNIT}; at 1 MHz, the silt and clay α_{UNIT} is 4.5 times the value of the sand α_{UNIT}; and at 600 kHz, the silt and clay α_{UNIT} is 7.3 times the value of the sand α_{UNIT}. Thus, because of the greater validity of the approximation in equation 15 at lower frequencies, we generally use the values of α_S measured at the lowest-frequency present at a study site to calculate $C_{XS\text{-}SILT\text{-}CLAY}$.

Estimation of the Grain-Size Distribution and Wet Density of the Silt and Clay: Attenuation Constraint

Two constraints are used to estimate the grain-size distribution and the wet density of the suspended silt and clay. The first of these constraints is to use multiple acoustic frequencies to solve for the values of the D_{50}, σ_G, and ρ_S for the silt and clay grain-size distribution that best agree with the values of α_{UNIT} empirically determined using ADP-calculated values of α_S and measured values of $C_{XS\text{-}SILT\text{-}CLAY}$ (fig. 6). This first constraint is a slightly modified version of the method devised by Moore and others (2013). Whereas Moore and others (2013) held the density of the silt and clay constant at quartz density, we allow it to vary between the reasonable bounds set by the density of chlorite (3,300 kg/m^3) and the wet density of montmorillonite (1,800 kg/m^3). The second constraint is to use multiple acoustic frequencies to solve for the values of the D_{50}, σ_G, and ρ_S for the silt and clay that, in combination with the known values of the D_{50}, σ_G, and ρ_{SAND} for the suspended sand (appendix 5), best predict the observed values of the excess backscatter, B', associated with higher relative concentrations of suspended silt and clay (described below in the section called "Estimation of the Grain-Size Distribution and Wet Density of the Silt and Clay: Backscatter Constraint"). Both of these constraints must be met to achieve a reasonably accurate estimation of the silt and clay grain-size distribution and density.

For example, on the basis of using three acoustic frequencies to satisfy both of these constraints at the CR87 study site, the estimated typical median grain size of the silt and clay is 0.0008 mm, the estimated typical σ_G of the silt and clay is 3ϕ, and the estimated typical wet density of the silt and clay is 2,500 kg/m^3. These estimations of the D_{50} and σ_G for the suspended silt and clay are consistent with the measurements of the suspended silt-and-clay grain-size distribution reported in the USGS National Water Information System database for this study site and for the tributary river (that is, the Little Colorado River) that supplies most of the silt and clay transported in suspension at this study site, and are consistent with 210,228 measurements of the suspended-silt-and-clay grain-size distribution made at this study site using a LISST-100 at 15-minute intervals between 2002 and 2010. These measurements indicate that most of the silt and clay in suspension at this study site is composed of clay-size particles. In addition, the estimated wet density of 2,500 kg/m^3 that is slightly lower than the density of quartz is consistent with lower-density clays comprising part of the suspended silt and clay at this study site. The effects of this silt and clay grain-size distribution and density on backscatter at the 600-kHz, 1-MHz and 2-MHz frequencies at the CR87 study site are depicted in figure 14 below in the section of this report called "Estimation of the Grain-Size Distribution and Wet Density of the Silt and Clay: Backscatter Constraint."

Figure 6. (**following page**) Comparison of empirical and theoretical relations between α_S calculated by the acoustic-Doppler profiler (ADP) and physically measured $C_{XS\text{-}SILT\text{-}CLAY}$ at the CR87 study site at the (***A***) 600-kHz, (***B***) 1-MHz, and (***C***) 2-MHz acoustic frequencies. Empirical relations are least-squares linear regressions forced through the origin; theoretical relations are derived for a log-normal grain-size distribution of silt and clay with D_{50}= 0.0008 mm, σ_G=3ϕ, and ρ_S=2,500 kg/m^3. Differences in the goodness-of-fit, R^2, values between the empirical and theoretical relations are insignificant when defined over such a large range in α_S and $C_{XS\text{-}SILT\text{-}CLAY}$. The high R^2 values indicate that, on the basis of Moore and others (2013), the density and grain-size distribution of the suspended silt and clay at this study site is fairly constant. α_S error bars are 95-percent-confidence-level error bars that include a 2 percent estimated error in the ADP-calculated values of α_S and the 95-percent-confidence-level error in the mean value of the α_S time-averaged over the 1-hour interval centered on the temporal midpoint of the time of each EDI or calibrated-pump measurement. Silt-and-clay-concentration error bars are 95-percent-confidence-level error bars that include both field and laboratory-processing errors. As expected, the approximation that $\alpha_S \approx \alpha_{UNIT} C_{XS\text{-}SILT\text{-}CLAY}$ is better at the 600-kHz and 1-MHz frequencies than it is at the 2-MHz frequency, as indicated by the greater increase in the variance in $C_{XS\text{-}SILT\text{-}CLAY}$ in ***C*** that is absent in ***A*** and ***B*** during high-sand-concentration conditions. An expanded view of the lower-left part of ***C*** is provided in ***D*** to better show the effect of higher suspended-sand concentrations on the relation between α_S and $C_{XS\text{-}SILT\text{-}CLAY}$ at the 2-MHz frequency. The 992 measurements made between September 29, 2006, and November 25, 2012, are plotted in ***A***, of which 135 are equal-discharge-increment (EDI) measurements and 857 are calibrated-pump measurements; 752 measurements made between August 25, 2005, and March 12, 2008, are plotted in ***B***, of which 96 are EDI measurements and 656 are calibrated-pump measurements; 564 measurements made between February 10, 2006, and March 12, 2008, are plotted in ***C***, of which 76 are EDI measurements and 488 are calibrated-pump measurements.

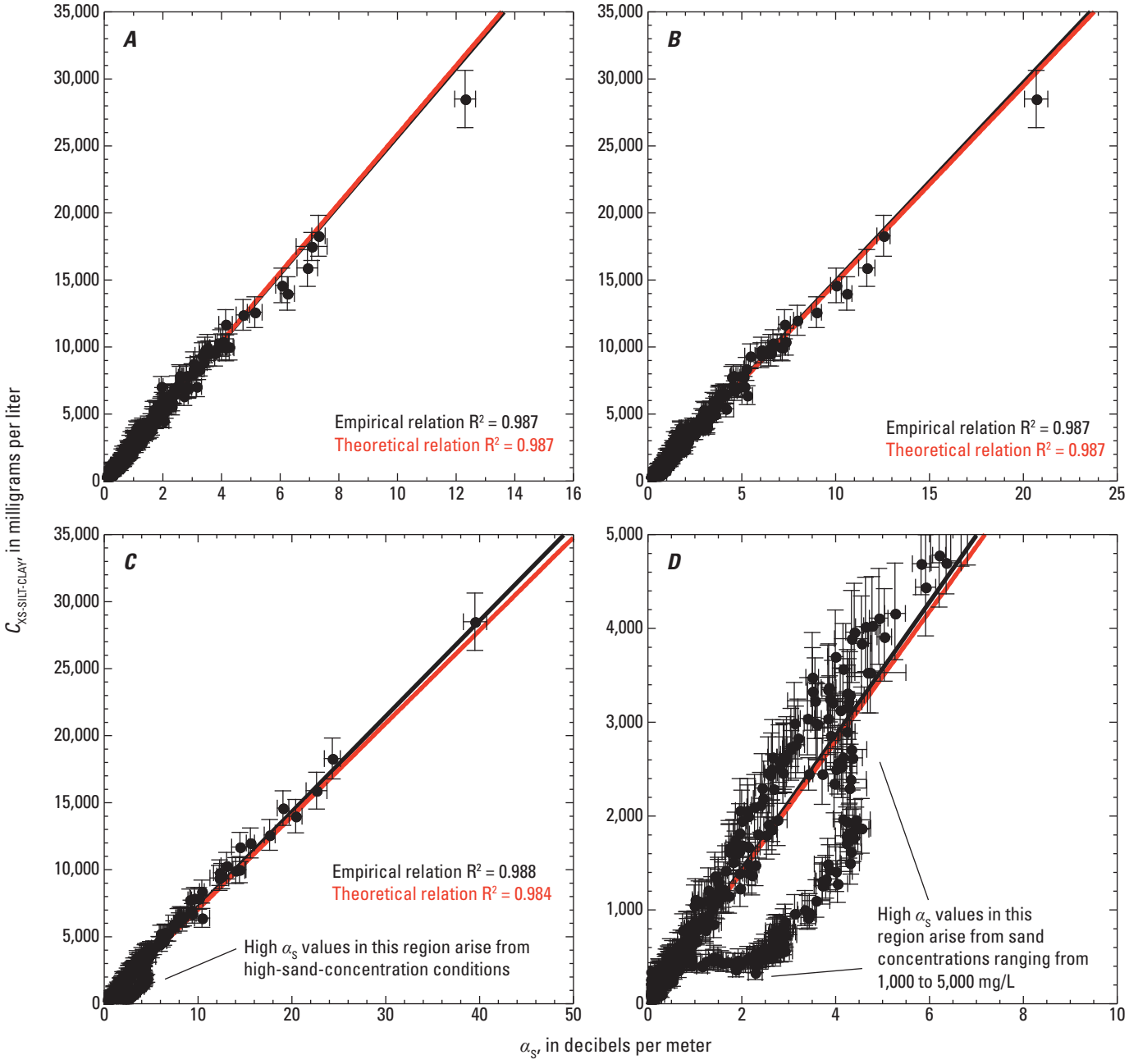
A
Empirical relation R² = 0.987
Theoretical relation R² = 0.987
B
Empirical relation R² = 0.987
Theoretical relation R² = 0.987
C
Empirical relation R² = 0.988
Theoretical relation R² = 0.984
High αs values in this region arise from high-sand-concentration conditions
D
High αs values in this region arise from sand concentrations ranging from 1,000 to 5,000 mg/L
CXS-SILT-CLAY, in milligrams per liter
αs, in decibels per meter

Figure 6.

Evaluation of Target Strength from Pressure-Based Re-Derivation of the Sonar Equation

Target strength, *TS*, is determined by the amount and nature of the particles in suspension and by the dimensions of the ensonified volume (NDRC, 1946; Urick, 1975; Reichel and Nachtnebel, 1994). Much research has been completed on the acoustic scattering effects of individual and, later, concentrations of particles in suspension (Rayleigh, 1896; NDRC, 1946; Anderson, 1950; Hickling, 1962; Urick, 1975; Sheng and Hay, 1988; Hay, 1991; Hay and Sheng, 1992; Thorne and Campbell, 1992; He and Hay, 1993; Thorne and others, 1993, 1995, 1997; Thorne and Hanes, 2002; Thorne and Buckingham, 2004; Thorne and Meral, 2008; Moore and Hay, 2009). Although the initial work in this field was conducted on regularly shaped particles (for example, spheres, cubes), sufficient work using natural sand grains (in both single and mixtures of grain sizes) has allowed a sufficiently robust theory on how sound is backscattered by suspensions of sediment in water. To allow a greater understanding of the physics underlying the sonar equation (equation 6), we re-derive equation 6 on the basis of the equation relating the acoustic pressure backscattered from sediment in suspension to the incident acoustic pressure. As a result of this re-derivation, the heretofore-undefined part of the *TS* in equation 15, associated with only the amount and nature of the sediment in suspension, that is, s_V (the backscattering cross section of a unit reverberating volume), can be defined.

The starting point for this re-derivation is the following version of the equation relating the root-mean-square acoustic pressure backscattered from a volume of water containing sediment in suspension to the acoustic pressure produced by a transducer; this equation is formulated on the basis of all of the literature cited in the previous paragraph. It is assumed that the suspended-sediment grains are randomly distributed within the ensonified volume of water, the scattering is incoherent, the effects of multiple scattering are unimportant, and the effects of extremely high concentrations on attenuation are also unimportant. In this equation,

$$p_{\mathrm{rms}} = \frac{p_0 r_0 L_{\mathrm{BS}}}{\psi_{\mathrm{NF}}} \sqrt{N \left\{ \int_{r-t_{\mathrm{P}}c/4}^{r+t_{\mathrm{P}}c/4} \int_0^{4\pi} \frac{\mathrm{e}^{-4\alpha_{\mathrm{N}} r}}{r^2} b(\theta,\varphi) b'(\theta,\varphi) d\Omega dr \right\}} + p_{\mathrm{NOISE}}\,, \tag{28}$$

where

p_{rms} is the reverberation-level root-mean-square backscattered pressure measured at the transducer (in Pascals),

p_0 is the source-level incident pressure (in Pascals) at distance r_0=1 m from the transducer,

p_{NOISE} is the instrument noise-floor pressure (in Pascals),

L_{BS} is the acoustic backscattering length (in m) defined below,

ψ_{NF} is the nondimensional near-field correction that accounts for nonspherical spreading very near the transducer,

N is the number concentration (in particles/m^3) of suspended sediment,

r is the range (that is, distance) along the beam from the transducer (in m),

t_{P} is the acoustic pulse (ping) duration (in seconds),

c is the measured speed of sound (in m/s),

α_{N} is the attenuation coefficient (in nepers/m) resulting from the sum of the water absorption and sediment attenuation coefficients,

$b(\theta,\phi)$ is the transmitted beam pattern in spherical coordinates (θ,ϕ),

$b'(\theta,\phi)$ is the received beam pattern in spherical coordinates (θ,ϕ), and

$\boldsymbol{\Omega}$ denotes a solid angle (in steradians).

Some of the variables in equation 28 have already been defined in previous sections of this report and are defined again here simply for convenience. Also, although different in form, the double integral in equation 28 is mathematically equivalent to the triple integral in equation 5 in Thorne and Hanes (2002), given the condition that the region behind the plane of the transducer face contributes zero to the solid angle of the two-way acoustic beam subtended at the face of

the transducer. This condition is commonly referred to as the "infinite planar baffle" approximation and originated with Rayleigh (1896). Finally, the integration limits of r-$t_p c/4$ and r+$t_p c/4$ arise from the previously described $t_p c/2$ range-gated thickness of the reverberating volume at an instant in time.

As described in Medwin and Clay (1997), the acoustic backscattering length, L_{BS}, originated with the work of Anderson (1950), and is defined as

$$L_{BS} = \frac{a_S}{2} f \,, \tag{29}$$

where

a_S is the radius of the median grain size of the suspended sediment (in m),
f is the nondimensional form function that describes the backscattering strength of the grain-size distribution of suspended sediment as a function of ka_S, and
$k=2\pi/\lambda$ is the wave number (in 1/m), and
λ the acoustic wavelength (in m).

As defined by Anderson (1950), the $a_S/2$ scaling in equation 29 is the geometric scattering length, that is, the length scale that best describes the scattering of sound by a sphere with radius a_S in the ka_S>1 geometric scattering regime. Anderson (1950) did not use the letter f, nor did he use the term "form function" to describe the f in equation 29, but rather referred to this parameter as the "reflectivity factor." Hickling (1962) later used $|f_\infty|$ for this nondimensional function that he termed the "reflection function," which described echo form, and only later did it become convention to refer to this function as the form function (Medwin and Clay, 1997). In essence, Anderson's (1950) reflectivity factor (later the form function) is the nondimensional parameter that allows equations like equation 28 to be solved continuously over both the Rayleigh (ka_S<1) and geometric scattering regimes.

The form function for grain-size distributions of natural, nonspherical suspended sediment is very different than that for a single size class of spheres. Because it was derived for grain-size distributions of suspended-sediment with naturally shaped grains, the form function, f, used in our study is that derived using equation 3 in Thorne and Meral (2008). The input to this equation is a number size distribution; in our study, laboratory-measured grain-size distributions are approximated as log-normal distributions and then converted to equivalent number size distributions using the approach described above in the Physical Basis for the Sediment Attenuation Coefficient section. The Thorne and Meral (2008) form function takes into account both the effect of the nonspherical shape of natural sediment grains and the effect of multiple grain sizes. Relative to form functions evaluated for single-size spheres, these two effects combine to result in a substantial increase in f in the Rayleigh scattering regime (ka_S<1), and a smaller decrease in the geometric scattering regime (Thorne and Buckingham, 2004; Thorne and Meral, 2008).

The Thorne and Meral (2008) form functions used in this study are derived for either unimodal or bimodal grain-size distributions of suspended sediment, depending on the situation. When the form function is derived for sand-size sediment only, the grain-size distribution of the suspended sand is assumed to be unimodal. This assumption is justified because the vast majority of the laboratory grain-size analyses of the suspended-sand samples used in this study are approximately unimodal. It is important to note, however, that this unimodal approximation may limit the ability of the method developed herein to accurately predict the concentration and median grain size of the suspended sand in cases where the suspended sand in a river is highly bimodal. When the form function is derived for grain-size distributions of suspended sediment consisting of a sand mode and a silt and clay mode, the form function derived is that for a bimodal distribution composed of a unimodal grain-size distribution of suspended sand combined with a unimodal grain-size distribution of suspended silt and clay.

Over the next several paragraphs, the steps involved in re-deriving the sonar equation (equation 6) from equation 28 are shown in detail. Herein we use the solution of Thorne and Hardcastle (1997) for the range-dependent integral modified for the larger reverberating volume (that is, measurement cell) associated with the types of ADPs used in this study,[3]

$$\int_{r-t_p c/2}^{r+t_p c/2} \frac{e^{-4\alpha_N r}}{r^2} dr = \frac{t_p c}{r^2} e^{-4\alpha_N r} \,. \tag{30}$$

Substitution of this solution, along with equations 18 and 29, into equation 28, and squaring (because $I = p^2/\rho_W c$ and pressure must be ultimately converted to intensity) yields:

$$p_{rms}^2 = \frac{p_0^2 r_0^2}{\psi_{NF}^2} f^2 \frac{a_S^2}{4} N \left\{ \frac{t_p c}{r^2} \Psi e^{-4\alpha_N r} \right\} + p_{NOISE}^2 \,. \tag{31}$$

Using the equation for the volume of a sphere, the number concentration in equation 31 can be converted into a mass concentration by

$$N = \frac{3M}{4\pi a_S^3 \rho_S} \,, \tag{32}$$

where

M is the mass concentration (in kg/m^3) of suspended sediment, and
ρ_S is the density of the suspended sediment (in kg/m^3).

[3]Please note that the original form of this range-dependent integral in Thorne and Hardcastle (1997) and within equation 28 is for acoustical measurements made in the smaller reverberating volumes associated with an instant in time, and is: $\int_{r-t_p c/4}^{r+t_p c/4} \frac{e^{-4\alpha_N r}}{r^2} dr = \frac{t_p c}{2r^2} e^{-4\alpha_N r}$

Employing equations 3 through 7 in Thorne and Hardcastle (1997) for the integral in equation 18 yields, as found by Mouraenko (2004),

$$\Psi = 2\pi\left(\frac{0.96}{ka_{\mathrm{T}}}\right)^2 . \tag{33}$$

Equation 33 calculates two-way beam widths that agree within 2 percent of those estimated for the equivalent two-way beam in table 8.1 in Urick (1975) on the basis of Reverberation Group, University of California Division of War Research (1943). The two-way beam widths calculated by this equation are, however, ~63 percent of the vendor-estimated one-way -3 dB beam widths for the ADPs used in this study and 54 to 72 percent of the one-way -3 dB beam widths measured in the laboratory by Hay (1991). These results are in general agreement with the statement by EdgeTech (2015) that beam shaping results in two-way beam widths that are ~72 percent of the one-way beam widths. Making further substitutions of equations 32 and 33 into equation 31, with slight rearrangement, yields the following equation:

$$p_{\mathrm{rms}}^2 - p_{\mathrm{NOISE}}^2 = \frac{p_0^2 r_0^2}{\psi_{\mathrm{NF}}^2} f^2 \frac{3M}{16\pi a_{\mathrm{S}}\rho_{\mathrm{S}}}\left\{\frac{t_{\mathrm{P}}c}{r^2}2\pi\left(\frac{0.96}{ka_{\mathrm{T}}}\right)^2 \mathrm{e}^{-4\alpha_{\mathrm{N}}r}\right\}. \tag{34}$$

The next steps in the re-derivation of the sonar equation involve conversion of equation 34 to the logarithmic form of equation 6, where each term is expressed as 10 times a base-10 logarithmic ratio of acoustic intensity. The first step in this process is to multiply equation 34 by unity in the form of the quantity $(r/r_0)^2/(r/r_0)^2$. This operation allows for the re-derived terms in equation 6 match the definitions of those terms provided above. Following this operation, equation 34 becomes

$$p_{\mathrm{rms}}^2 - p_{\mathrm{NOISE}}^2 = \frac{p_0^2 r_0^2}{\psi_{\mathrm{NF}}^2} f^2 \frac{3M}{16\pi a_{\mathrm{S}}\rho_{\mathrm{S}}}\left\{\frac{t_{\mathrm{P}}c}{r^2}2\pi\left(\frac{0.96}{ka_{\mathrm{T}}}\right)^2 \mathrm{e}^{-4\alpha_{\mathrm{N}}r}\right\}\left(\frac{(r/r_0)^2}{(r/r_0)^2}\right). \tag{35}$$

Following some rearrangement, equation 35 can then be rewritten in the following 10 times base-10 logarithmic, decibel form:

$$\begin{aligned} &10\log_{10}\left(p_{\mathrm{rms}}^2 - p_{\mathrm{NOISE}}^2\right) = 10\log_{10}\left(p_0^2\right) - 20\log_{10}\left(\psi_{\mathrm{NF}}\right) - 40\log_{10}\left(r\right) + 20\log_{10}\left(r\right) \\ &+10\log_{10}\left(f^2\frac{3M}{16\pi a_{\mathrm{S}}\rho_{\mathrm{S}}}\right) + 10\log_{10}\left(2t_{\mathrm{P}}c\pi\left(\frac{0.96}{ka_{\mathrm{T}}}\right)^2\right) - 40\alpha_{\mathrm{N}}r\log_{10}\left(\mathrm{e}\right) \\ &+40\log_{10}\left(r_0\right) - 20\log_{10}\left(r_0\right). \end{aligned} \tag{36}$$

Even though more simplification is possible at this stage, the r and r_0 terms are kept in four separate logarithms in equation 36 so that they can be properly assigned to the 2*TL* and *TS* terms in the re-derived sonar equation. Because 1 neper=$20\log_{10}(\mathrm{e})$=8.686 dB, following conversion of α_{N} to α in units of dB/m, separation of α into α_{W} and α_{S}, and more rearrangement, equation 36 becomes:

$$\begin{aligned} &10\log_{10}\left(p_{\mathrm{rms}}^2 - p_{\mathrm{NOISE}}^2\right) = 10\log_{10}\left(p_0^2\right) - 20\log_{10}\left(\psi_{\mathrm{NF}}\right) - 40\log_{10}\left(\frac{r}{r_0}\right) \\ &+10\log_{10}\left(f^2\frac{3M}{16\pi a_{\mathrm{S}}\rho_{\mathrm{S}}}\right) + 10\log_{10}\left(2t_{\mathrm{P}}c\pi\left(\frac{0.96}{ka_{\mathrm{T}}}\right)^2\right) - 2\alpha_{\mathrm{W}}r - 2\alpha_{\mathrm{S}}r \\ &+20\log_{10}\left(\frac{r}{r_0}\right). \end{aligned} \tag{37}$$

Conversion of $p_{rms}^2 - p_{\mathrm{NOISE}}^2$ to I_{RL}, the intensity of the reverberation measured by the ADP in each cell, and conversion of p_0^2 to I_{SL}, the intensity of the transmitted acoustic signal 1 m from the transducer, requires that both of these terms be divided by $\rho_{\mathrm{W}}c$. Furthermore, because $RL = 10\log_{10}\left(I_{\mathrm{RL}}/I_{\mathrm{REF}}\right)$, $SL = 10\log_{10}\left(I_{\mathrm{SL}}/I_{\mathrm{REF}}\right)$, and I_{REF} (defined in equation 8) is the same quantity in both *RL* and *SL*, it is possible to simply replace $10\log_{10}\left(p_{\mathrm{rms}}^2 - p_{\mathrm{NOISE}}^2\right)$ in equation 37 with *RL* and replace $10\log_{10}\left(p_0^2\right)$ in equation 37 with *SL*, such that equation 37 becomes

$$RL = SL - \left\{40\log_{10}\left(\frac{r}{r_0}\right) + 20\log_{10}\left(\psi_{\mathrm{NF}}\right) + 2\alpha_{\mathrm{W}}r + 2\alpha_{\mathrm{S}}r\right\} + 10\log_{10}\left(f^2\frac{3M}{16\pi a_{\mathrm{S}}\rho_{\mathrm{S}}}\right) \tag{38}$$
$$+\left\{10\log_{10}\left(2t_{\mathrm{P}}c\pi\left(\frac{0.96}{ka_{\mathrm{T}}}\right)^2\right) + 20\log_{10}\left(\frac{r}{r_0}\right)\right\}.$$

Substitution of equation 14 into equation 38 and minor rearrangement finally allows for

$$RL = SL - 2TL + 10\log_{10}\left(f^2\frac{3M}{16\pi a_{\mathrm{S}}\rho_{\mathrm{S}}r_0^2}\right) + \left\{10\log_{10}\left(2t_{\mathrm{P}}c\pi\left(\frac{0.96}{ka_{\mathrm{T}}}\right)^2\right) + 20\log_{10}\left(r\right)\right\}. \tag{39}$$

Comparison of equation 39 with equation 6 reveals that the target strength (when sediment comprises the only particle in suspension and zero air bubbles are present),

$$TS = 10\log_{10}\left(f^2\frac{3M}{16\pi a_{\mathrm{S}}\rho_{\mathrm{S}}r_0^2}\right) + \left\{10\log_{10}\left(2t_{\mathrm{P}}c\pi\left(\frac{0.96}{ka_{\mathrm{T}}}\right)^2\right) + 20\log_{10}\left(r\right)\right\}, \tag{40}$$

and can be solved only when $M>0$. On the basis of the early work by NDRC (1946) and Urick (1975), *TS* is a negative number of order 10 to 100 for sand- and finer-sized particles, and calculation of *TS* using equation 39 for the 600-kHZ, 1-MHz, and 2-MHz ADPs used in this study is consistent with this prediction. Because $TS = 10\log_{10}\left(s_{\mathrm{v}}\right) + 10\log_{10}\left(V\right)$, by equation 15, the backscattering cross section of a unit reverberating volume is

$$s_{\mathrm{V}} = \left(f^2\frac{3M}{16\pi a_{\mathrm{S}}\rho_{\mathrm{S}}r_0^2}\right), \tag{41}$$

in units of $1/m^3$, as required on the basis of equation 15. The reverberating volume is

$$V = 2t_{\mathrm{P}}c\pi\left(\frac{0.96}{ka_{\mathrm{T}}}\right)^2 r^2, \tag{42}$$

in units of m^3, as required also on the basis of equation 15. Because, by convention, sediment grains are generally measured in terms of their diameter in mm and not their radius in m, and, in this study, the central tendency used to best describe a log-normal grain-size distribution is the median grain size, the following relation is used, where *M* is now the mass concentration of all sediment in the grain-size distribution with median grain size D_{50} (in mm):

$$s_{\mathrm{V}} = \left(f^2\frac{3000M}{8\pi D_{50}\rho_{\mathrm{S}}r_0^2}\right). \tag{43}$$

To be consistent with the use of D_{50} to characterize the central tendency of the grain-size distribution in suspension, f in equation 43 is the form function associated with a log-normal suspended-sediment grain-size distribution with median grain-size D_{50} and geometric standard deviation σ_G, derived on the basis of Thorne and Meral (2008), as described previously.

The fact that f and D_{50} are associated with a grain-size distribution and not just a single grain size has major implications with respect to the derivation and physical interpretation of *TS*. The *TS* derived in equation 40 is therefore that for the entire grain-size distribution of sediment in suspension. In cases where the amount of silt and clay greatly exceeds the amount of sand in suspension, the *TS* will approach that for the suspended-silt-and-clay grain-size distribution and will be much different from the *TS* for the suspended-sand grain-size distribution.

The typical sortings of the suspended-sand grain-size distributions at the study sites are used to derive the Thorne and Meral (2008) form functions used in this study for the sand-size sediment. On the basis of the EDI and EWI measurements, the value of σ_G that best characterizes the suspended-sand grain-size distributions in the Colorado River at the CR30, CR61, CR87, and CR225 study sites is 0.63ϕ, and the value of σ_G that best characterizes the suspended-sand grain-size distributions in the Rio Grande at the RG-CAS and RG-RGV study sites is only slightly larger at 0.65ϕ. Because grain-size analyses published in the USGS NWIS database and in Voichick and Topping (2014) indicate that the suspended silt and clay is much more poorly sorted than the suspended sand, versions of the Thorne and Meral (2008) form function used in this study for silt-and-clay-sized sediment are derived for broader grain-size distributions with values of σ_G ranging from ~2ϕ to ~3ϕ. As shown below, the effect of this broader grain-size distribution is to increase the target strength of the suspended silt and clay relative to what it would be if the grain-size distribution of the silt and clay were as narrow as that of the suspended sand.

To finish the derivation of *TS* such that it is compatible with the backscatter–sediment-concentration relations derived from the sonar equation for constant grain size by Thevenot and others (1992) and Gartner (2004), we convert M from SI units into the more conventional sediment-concentration units of mg/L and replace M with C. All other parameters are retained in SI units. This conversion and the previously described conversion from a_S to D_{50} results in equation 40 becoming

$$TS = 10\log_{10}\left(f^2 \frac{3C}{8\pi D_{50}\rho_S r_0^2} \right) + \left\{ 10\log_{10}\left(2t_P c\pi \left(\frac{0.96}{ka_T} \right)^2 \right) + 20\log_{10}(r) \right\}. \quad (44)$$

Unit Target Strength

Because the range-dependent part of the *TS* is included in the relative backscatter, B, and therefore is not used to determine the relative effects of changes in concentration or grain size on the *TS*, it is useful to define another term, the range-independent target strength,

$$TS_{RI} = 10\log_{10}\left(f^2 \frac{3C}{8\pi D_{50}\rho_S r_0^2} \right) + 10\log_{10}\left(2t_P c\pi \left(\frac{0.96}{ka_T} \right)^2 \right) \quad (45)$$

and then separate this new quantity into two components to separate the effects of changes in suspended-sediment concentration on TS_{RI} from all other controls on TS_{RI}:

$$TS_{RI} = 10\log_{10}(C) + UTS\,, \quad (46)$$

where *UTS*, the unit target strength, is

$$UTS = 10\log_{10}\left(f^2 \frac{3}{8\pi D_{50}\rho_S r_0^2} \right) + 10\log_{10}\left(2t_P c\pi \left(\frac{0.96}{ka_T} \right)^2 \right). \quad (47)$$

Thus, $UTS = TS_{RI}$ when C=1 mg/L. Based on equations 45 and 46 (and under constant t_P, c, k, and a_T), if the grain-size distribution and density of the suspended sediment remain constant, a tenfold change in C will result in a 10-dB change in the target strength. Similarly, if the grain-size distribution and concentration of the suspended sediment remain constant, a factor of 2 change in ρ_S will result in a 3-dB change in the target strength. Changes in the grain-size distribution affect both f and D_{50} in equation 45, resulting in a more complicated influence on target strength than do either changes in C or ρ_S.

Finally, for maximum clarity in the examples plotted below, it is useful to further subdivide the *UTS* into two components: UTS_{SED}, associated with the control on the *UTS* of the suspended-sediment properties (grain-size distribution and density); and UTS_{BEAM}, associated with the control on the *UTS* provided by the range-independent aspects of the geometry of the acoustic beam.

$$UTS = UTS_{SED} + UTS_{BEAM}, \tag{48}$$

where

$$UTS_{SED} = 10\log_{10}\left(f^2 \frac{3}{8\pi D_{50}\rho_S r_0^2}\right), \tag{49}$$

and

$$UTS_{BEAM} = 10\log_{10}\left(2t_P c\pi\left(\frac{0.96}{ka_T}\right)^2\right). \tag{50}$$

Evaluation of the relative importance of UTS_{SED} and UTS_{BEAM} in calculations of the *UTS* is provided in figure 7 for the different model ADPs used in this study.

The more complicated influence on *TS* of changes in the grain-size distribution under constant C is best illustrated by UTS_{SED}. Based on the behavior of UTS_{SED} (fig. 7*B*), backscatter measurements made with higher-frequency ADPs are generally less sensitive to changes in suspended-sand D_{50} (that is, $D_{50\text{-SAND}}$) than are backscatter measurements made with lower-frequency ADPs, at least over the 600-kHz to 2-MHz range in frequency of the ADPs tested in this study. As shown in figure 7*B*, UTS_{SED} increases rapidly as a function of increasing D_{50} over most of the Rayleigh scattering regime, and only begins to plateau around ka_S ~0.5. The main implication of this result is that, when ka_S<0.5, use of single-frequency acoustics to measure C_{SAND} will be highly biased as a result of concentration-independent variation in $D_{50\text{-SAND}}$, as illustrated by the following examples. $D_{50\text{-XS-SAND}}$ measured in this study typically ranged from about 0.09 mm to 0.25 mm. Over this range in $D_{50\text{-SAND}}$, UTS_{SED} associated with 2-MHz ADPs increases by ~5.2 dB, with most of this increase occurring between 0.09 and 0.125 mm. Given that a 10-dB increase in *TS* is associated with a factor of 10 increase in sediment concentration at constant D_{50}, neglecting the influence of changing grain size on backscatter over the 0.09- to 0.25-mm range in $D_{50\text{-SAND}}$ will lead to factor of 4 biases in C_{SAND} calculated on the basis of backscatter at only the 2-MHz frequency. As frequency decreases, the increase in UTS_{SED} becomes much larger over the 0.09- to 0.25-mm range in $D_{50\text{-SAND}}$, leading to much larger biases in C_{SAND} calculated on the basis of backscatter. Over this range in $D_{50\text{-SAND}}$, the UTS_{SED} associated with 1-MHz ADPs increased by ~9.2 dB and the UTS_{SED} associated with 600-kHz ADPs increased by ~11.5 dB. These increases in dB lead to factor of ~8 and factor of ~14 respective potential biases in backscatter-calculated C_{SAND} if grain-size effects on backscatter are neglected.

In addition to the above-described influence of changes in D_{50} on UTS_{SED} at different frequencies, changes in the sorting of a grain-size distribution in suspension also have profound effects on UTS_{SED}. As a grain-size distribution of suspended sediment broadens, the difference in UTS_{SED} between silt-and-clay-sized and sand-size sediment lessens as a result of the effect of decreased sorting on the form function (fig. 8). In cases where σ_G of a grain-size distribution is less than ~1.5ϕ, the UTS_{SED} associated with silt grain-size distributions will be much less than the UTS_{SED} associated with sand grain-size distributions. In these cases, backscatter will be dominantly from sand-size sediment. Conversely, in cases where σ_G of a grain-size distribution exceeds ~1.5ϕ, the UTS_{SED} associated with silt grain-size distributions becomes a larger fraction of the *UTS* associated with sand grain-size distributions, and measurable backscatter will be from silt-size sediment in addition to the backscatter from sand-size sediment. Ultimately, in cases where σ_G of a grain-size distribution exceeds ~3ϕ, the UTS_{SED} associated with grain-size distributions of silt and clay will be nearly equal to the UTS_{SED} associated with grain-size distributions of sand. Under these conditions, backscatter from the suspended silt and clay is nearly as much as that from the suspended sand. Because the sorting of suspended silt and clay (σ_G=2 to 3ϕ) is much broader than the sorting of suspended sand (σ_G=0.63 to 0.65ϕ) at the study sites, again a condition likely in most rivers as described in the previous section, the effect of silt and clay on backscatter must be accounted for under conditions when the concentration of the suspended silt and clay greatly exceeds that of the sand.

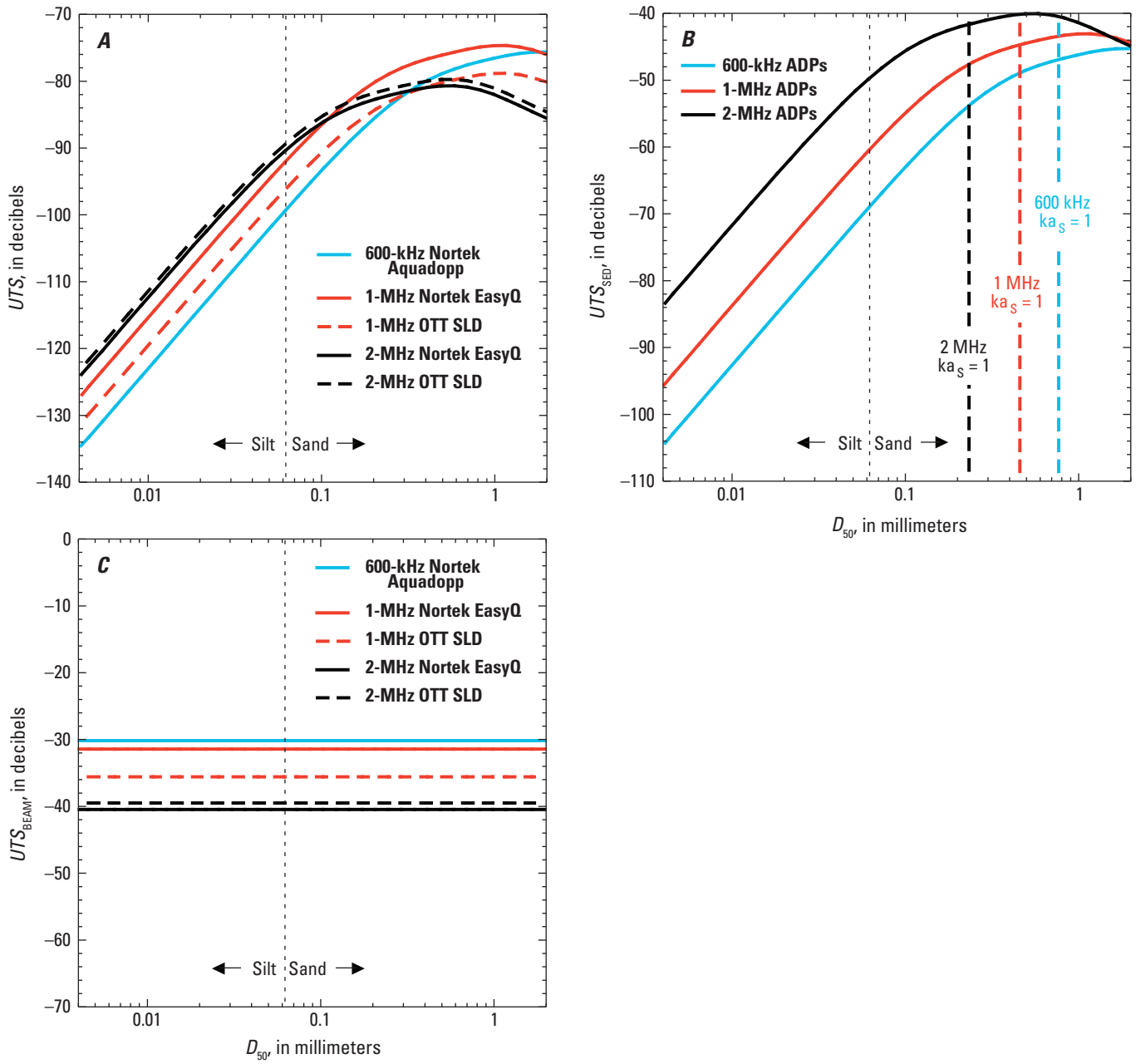

Figure 7. ***A***, Unit target strength, *UTS*, for the various model and frequency acoustic-Doppler profilers (ADPs) used in this study plotted as a function of D_{50} of a grain-size distribution of suspended sediment with σ_G=0.63ϕ. The break between silt and sand is indicated. ***B***, Sediment component of the unit target strength, UTS_{SED}, plotted as a function of the D_{50} of a grain-size distribution of suspended sediment with σ_G=0.63ϕ. The break between silt and sand is indicated, as are the values of D_{50} at the three acoustic frequencies where ka_S=1, the boundary between Rayleigh and geometric scattering. ***C***, Beam component of the unit target strength, UTS_{BEAM}, plotted as a function of the D_{50} of a grain-size distribution of suspended sediment with σ_G=0.63ϕ. At a given frequency, UTS_{BEAM} depends only on transducer radius, transmit-pulse length, and receive-window length, and therefore does not depend on D_{50}.

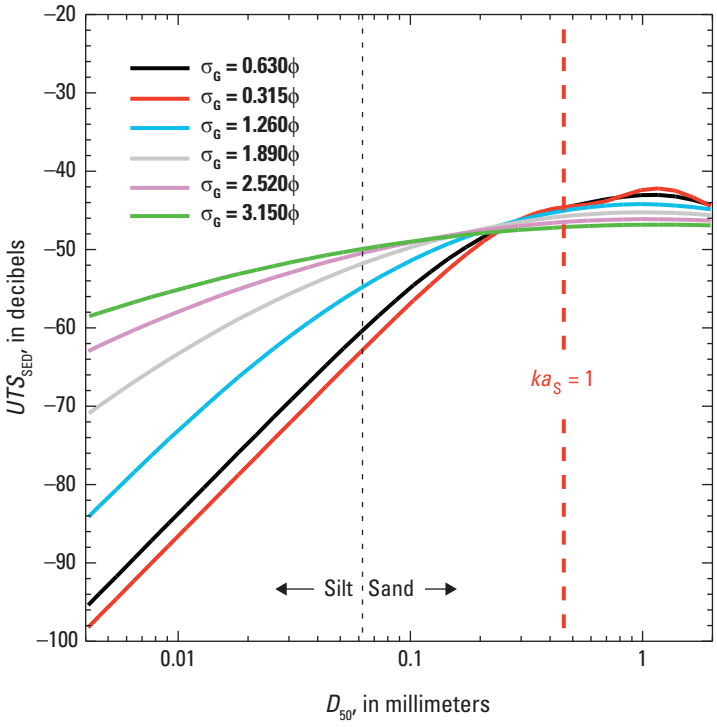

Figure 8. Effects of changes in sediment sorting of the sediment portion of the unit target strength, UTS_{SED}, at 1 MHz. Shown are calculated values of UTS_{SED} for D_{50}s of suspended sediment with σ_G=0.63ϕ, 0.315ϕ, 1.26ϕ, 1.89ϕ, 2.52ϕ, and 3.15ϕ. These values of σ_G were chosen for this example because they are all multiples of 0.63ϕ, that is, the measured typical σ_G for the suspended sand at the CR30, CR61, CR87, and CR225 study sites. As the sorting of the suspended sediment gets poor and the σ_G approaches 3ϕ, the difference between the UTS_{SED} of silt- and sand-size sediment is greatly reduced, and suspended silt can be associated with almost as much backscatter as suspended sand.

Relative Unit Target Strength

The behavior of UTS_{SED} as a function of frequency and D_{50} is the physical process that allows accurate, that is, relatively unbiased, backscatter-based measurements of $C_{XS\text{-}SAND}$ and $D_{50\text{-}XS\text{-}SAND}$ to be possible when multiple acoustic frequencies are used. To more easily use the UTS_{SED} to this end, we define a new term, the relative unit target strength (*RUTS*), that is, the *UTS* relative to the *UTS* associated with a reference D_{50} in the river cross section, denoted as $D_{50\text{-}XS\text{-}SED\text{-}REF}$ or $D_{50\text{-}XS\text{-}SAND\text{-}REF}$. $D_{50\text{-}XS\text{-}SED\text{-}REF}$ is the median grain size at a given location that best characterizes the D_{50} of the velocity-weighted suspended-sediment grain-size distribution in the river cross section over the widest possible range in concentration. Likewise, for sand-size sediment only, $D_{50\text{-}XS\text{-}SAND\text{-}REF}$ is the median grain size at a given location that best characterizes $D_{50\text{-}XS\text{-}SAND}$ over the widest possible range in concentration. In the calibration procedure described below, $D_{50\text{-}XS\text{-}SAND\text{-}REF}$ is used to determine the base-backscatter-calibration relation for a given frequency ADP that is used with the backscatter measured at other frequencies to solve for both $C_{XS\text{-}SAND}$ and $D_{50\text{-}XS\text{-}SAND}$ in the multi-frequency calibration approach. Many measurements of the suspended-sand grain-size distribution over a wide range in concentration are required to determine $D_{50\text{-}XS\text{-}SAND\text{-}REF}$, as a great deal of variation in D_{50} is possible. For convenience, the *UTS* associated with either $D_{50\text{-}SAND\text{-}REF}$ or $D_{50\text{-}XS\text{-}SAND\text{-}REF}$ is abbreviated as UTS_{REF}. *RUTS* is calculated by simply subtracting UTS_{REF} from the *UTS* for all values of D_{50}:

$$RUTS = UTS - UTS_{REF}, \quad (51)$$

and is depicted in figure 9. Comparison of the theoretical *RUTS* with measurements can then be conducted to evaluate whether the derivation of *TS* in this section of the report is realistic.

Of all our study sites, the site with the largest concentration-independent range in $D_{50\text{-}XS\text{-}SAND}$ is the CR30 study site. Thus, data from CR30 were used to test the ability of the theory developed herein to predict the observed values of *RUTS*. Comparisons between measured and theoretically determined values of *RUTS* at CR30 are good (fig. 10). As justified in the next section of this report, to avoid cases where *RUTS* could be substantially affected by relatively large $C_{XS\text{-}SILT\text{-}CLAY}$, only those cases where the EWI-measured $C_{XS\text{-}SILT\text{-}CLAY}$ was less than twice the EWI-measured $C_{XS\text{-}SAND}$ are included in figure 10. As a possible result of the theoretical *RUTS* having a steeper slope over the 0.09 to 0.25-mm range in $D_{50\text{-}XS\text{-}SAND}$ at the 1-MHz frequency than at the 2-MHz frequency, the agreement between the measured and theoretical values of the *RUTS* is better at the 1-MHz frequency than at the 2-MHz frequency. For the same reason, the measured RUTS at the 2-MHz frequency is much less affected by changes in $D_{50\text{-}XS\text{-}SAND}$ than is the measured *RUTS* at the 1-MHz frequency over the 0.09 to 0.25-mm range in $D_{50\text{-}XS\text{-}SAND}$.

The above derivation of *UTS* and *RUTS* allows the commonly used Thevenot and others' (1992) simplification

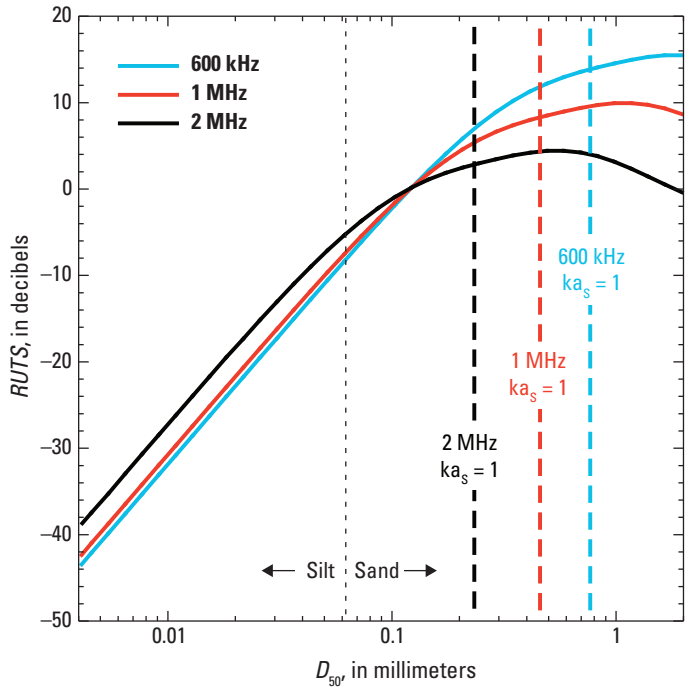

Figure 9. Relative unit target strength associated with the D_{50} of a suspended-sediment grain-size distribution with σ_G=0.63ϕ at acoustic frequencies of 600 kHz, 1 MHz, and 2 MHz. The reference median grain size, $D_{50\text{-XS-SED-REF}}$, used to derive these values of the *RUTS* is 0.125 mm. The break between silt and sand is indicated, as are the values of D_{50} at the three acoustic frequencies where ka_S=1, the boundary between Rayleigh and geometric scattering.

of the sonar equation to be re-derived in a convenient form for cases of varying grain size; a form that we employ in this study to use backscatter measured at multiple frequencies to solve for both $C_{\text{XS-SAND}}$ and $D_{\text{50-XS-SAND}}$. In their uniform-grain-size simplification of the active sonar equation, Thevenot and others (1992) showed that, when grain size is constant:

$$C = 10^{-0.1K+0.1B} \tag{52}$$

where

B is relative backscatter (replaced in our study by $\overline{B}$, beam-averaged backscatter), and

K is a constant.

Following equations 6, 14, 20, and 22, and because $\overline{B}$ is B averaged among beams and cells,

$$\overline{B} = TS_{\text{RI}} + SL + b_{\text{SF}}A_{\text{N}} - RL_{\text{OFFSET}}\,. \tag{53}$$

Following equation 46,

$$\overline{B} = 10\log_{10}(C) + UTS + SL + b_{\text{SF}}A_{\text{N}} - RL_{\text{OFFSET}}\,. \tag{54}$$

Rearranging equation 54 to be in the form of Thevenot and others (1992) indicates that, when grain size is allowed to vary, K is not truly constant, but rather is the sum of constant (SL–RL_{OFFSET}), nearly constant $b_{\text{SF}}A_{\text{N}}$, and varying UTS. The rearranged version of equation 54 after these substitutions is

$$C = 10^{-0.1(SL+b_{\text{SF}}A_{\text{N}}-RL_{\text{OFFSET}})-0.1UTS+0.1\overline{B}}\,. \tag{55}$$

For the special case where C is the concentration of suspended sediment with D_{50}=$D_{\text{50-XS-SED-REF}}$,

$$C = 10^{-0.1(SL+b_{\text{SF}}A_{\text{N}}-RL_{\text{OFFSET}})-0.1UTS_{\text{REF}}+0.1\overline{B}}\,. \tag{56}$$

Substituting equation 51 into 55 allows the general case where D_{50} varies to be written as

$$C = 10^{-0.1(SL+b_{\text{SF}}A_{\text{N}}-RL_{\text{OFFSET}})-0.1UTS_{\text{REF}}-0.1RUTS+0.1\overline{B}}\,. \tag{57}$$

Because UTS_{REF} is constant at a given study site, it is convenient to define another new constant,

$$K_1 = -0.1\left(SL + b_{\text{SF}}A_{\text{N}} - RL_{\text{OFFSET}} + UTS_{\text{REF}}\right), \tag{58}$$

which finally allows for

$$C = 10^{K_1+0.1\left(\overline{B}-RUTS\right)}\,. \tag{59}$$

If only one frequency ADP is present, it is therefore theoretically impossible to solve for both C and *RUTS* for a given measured $\overline{B}$. However, if two or more frequencies are present, it is possible to use equation 59 to iteratively solve for C and *RUTS*.

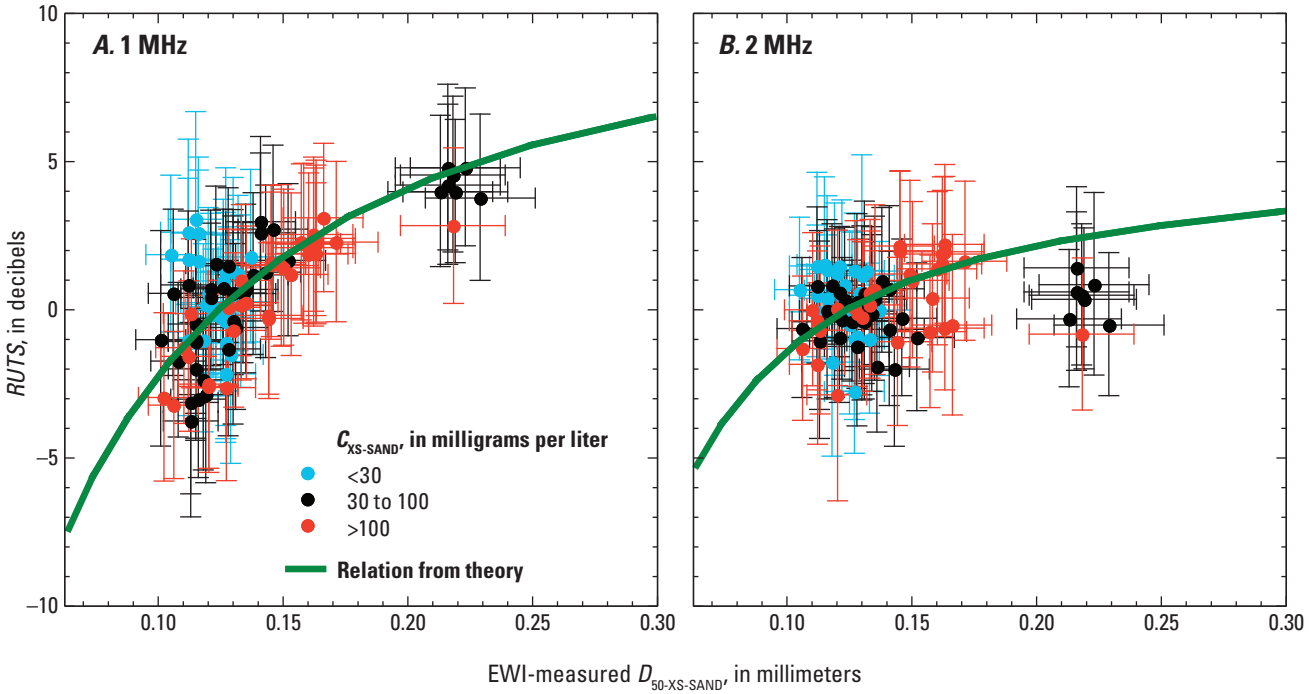

Figure 10. Comparisons of measured and theoretical values of the *RUTS* at the CR30 study site, at (***A***) 1-MHz and (***B***) 2-MHz acoustic frequencies. The measurements of *RUTS* at each frequency were determined by (1) fitting a linear regression relating the independent variable $\log_{10}(C_{XS\text{-}SAND})$ and the dependent variable $\overline{B}$ for all sand-size sediment within ¼ϕ of $D_{50\text{-}XS\text{-}SAND\text{-}REF}$ (that is, sand with D_{50} ranging from 0.105 to 0.149 mm at this study site), and (2) detrending the data by subtracting the values of $\overline{B}$ calculated using this relation from the measured values of $\overline{B}$ associated with each equal width increment (EWI) measurement of $C_{XS\text{-}SAND}$ and $D_{50\text{-}XS\text{-}SAND}$. Measured values of the relative unit target strength (*RUTS*) are segregated into three different concentration ranges in these plots to allow evaluation of dependence on concentration; as indicated in these plots, there is no discernable dependence of the measured *RUTS* on concentration. $D_{50\text{-}XS\text{-}SAND}$ error bars are 95-percent-confidence-level error bars that include both field and laboratory-processing errors in the EWI measurements of $D_{50\text{-}XS\text{-}SAND}$; *RUTS* error bars are 95-percent-confidence-level error bars that include (1) both field and laboratory-processing errors in the EWI measurements of $C_{XS\text{-}SAND}$, (2) a 2 percent estimated error in the acoustic-Doppler-profiler-calculated values of $\overline{B}$, and (3) the 95-percent-confidence-level error in the mean value of $\overline{B}$, time-averaged over the 1-hour interval centered on the temporal midpoint of the time of each EWI measurement. Ninety-three measurements made between February 22, 2007, and February 18, 2013, are plotted in ***A***; 89 measurements made between August 24, 2007, and February 18, 2013, are plotted in ***B***; the discrepancy in dates between ***A*** and ***B*** is because a 2-MHz ADP was not deployed at this study site until August 2007.

Development of Base-Backscatter-Calibration Relations

To allow accurate acoustical measurements of $C_{XS\text{-}SAND}$ to be made when even large values of $C_{XS\text{-}SILT\text{-}CLAY}$ are present (and a considerable amount of $\overline{B}$ arises from the amount of silt and clay in suspension and not from the amount of sand in suspension), we developed a data-processing method to allow separation of the part of $\overline{B}$ arising from sand-size sediment from the part of $\overline{B}$ arising from silt-and-clay-sized sediment. This method utilizes the differing theoretical behaviors of *UTS* and α_S under different combinations of suspended silt and clay and suspended sand. An early empirical version of this method was described in Topping and others (2007b).

The basis for the *UTS* part of this method is the development of a base-backscatter-calibration (BBC) relation between $\overline{B}$ and $\log_{10}(C_{XS\text{-}SAND})$ for conditions where the suspended sediment is dominated by sand-size sediment with D_{50} within ¼ϕ of $D_{50\text{-}XS\text{-}SAND\text{-}REF}$ and assumed constant sorting (fig. 11). Relations are then developed using both theory and empirical analysis to account and correct for the excess backscatter relative to this relation for conditions where the amount of silt and clay greatly exceeds the amount of sand in suspension. Ideally, the BBC relation is developed using only the more-accurate EDI or EWI measurements (Edwards and Glysson, 1999; Topping and others, 2011) and not using the less-accurate cross-section-calibrated pump measurements (Edwards and Glysson, 1999), although this is not always

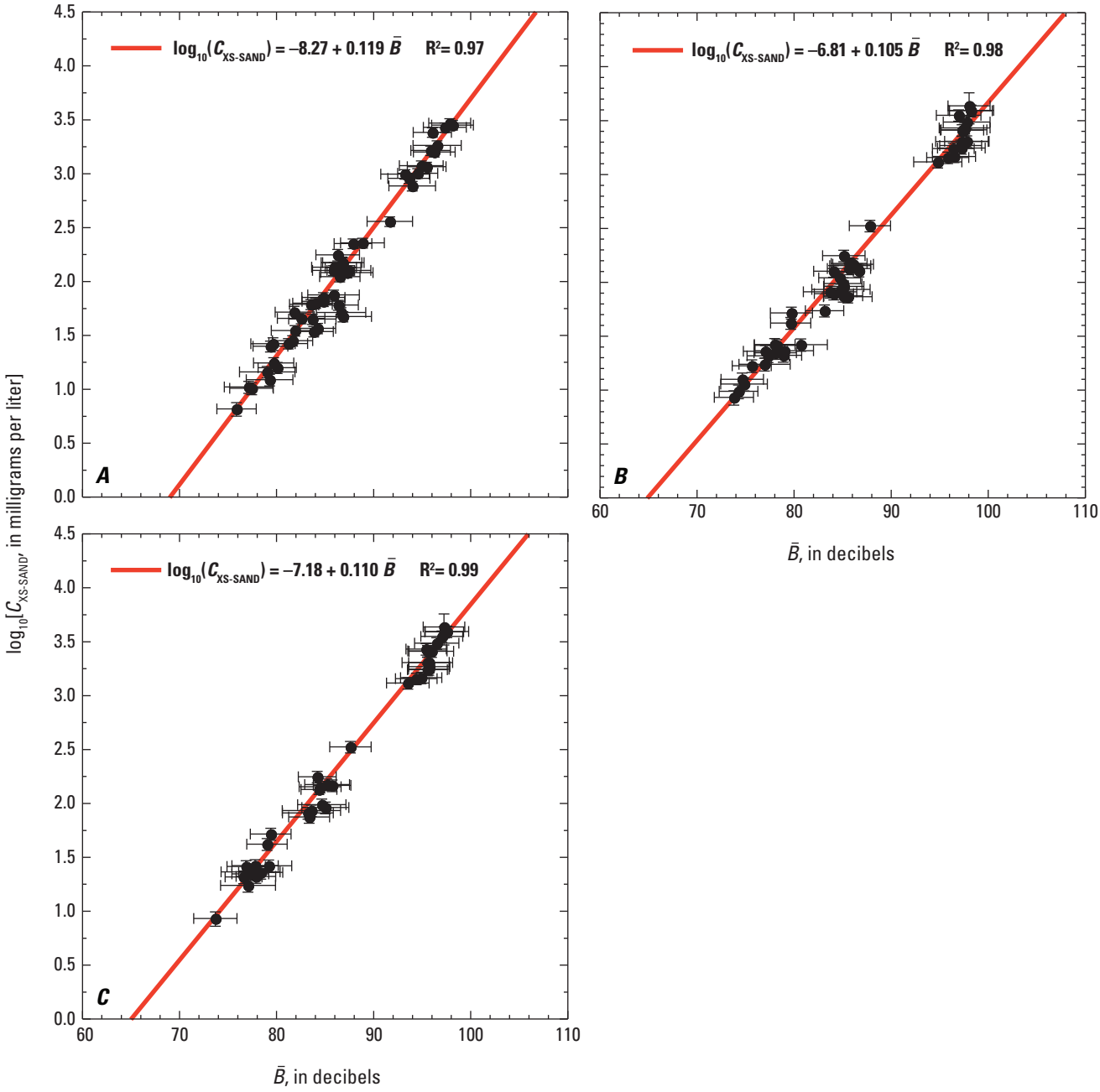

Figure 11. Base-backscatter-calibration (BBC) relations, depicted as red lines and equations, at the CR87 study site for acoustic-Doppler profilers (ADPs) operating at (***A***) 600-kHz, (***B***) 1-MHz, and (***C***) 2-MHz frequencies. To ensure that these relations are developed for cases where backscatter results mainly from suspended sand with a consistent grain-size distribution that is typical for this study site, only those measurements where the equal-discharge-increment (EDI) measured $C_{XS\text{-}SILT\text{-}CLAY}$ is less than twice the EDI-measured $C_{XS\text{-}SAND}$, and the EDI-measured $D_{50\text{-}XS\text{-}SAND}$ is within 1/4ϕ of $D_{50\text{-}XS\text{-}SAND\text{-}REF}$=0.125 mm are included in the least-squares linear regressions used to develop these relations. $\bar{B}$ error bars are 95-percent-confidence-level error bars that include a 2-percent estimated error in the ADP-calculated values of $\bar{B}$ and the 95-percent-confidence-level error in the mean value of $\bar{B}$ time-averaged over the 1-hour interval centered on the temporal midpoint of the time of each EDI measurement; $C_{XS\text{-}SAND}$ error bars are 95-percent-confidence-level error bars that include both field and laboratory-processing errors in the EDI measurements of $C_{XS\text{-}SAND}$. Fifty EDI measurements made between June 20, 2007, and November 23, 2012, with either a US D-96 or US D-96-A1 sampler are plotted in ***A***; 50 EDI measurements made between August 25, 2005, and March 9, 2008, with either a US D-96 or US D-96-A1 sampler are plotted in ***B***; 39 EDI measurements made between February 10, 2006, and March 9, 2008, with either a US D-96 or US D-96-A1 sampler are plotted in ***C***.

possible. Because many EDI or EWI measurements are available under low silt-and-clay concentration conditions, BBC relations at the Colorado River study sites are developed for each ADP using only EDI or EWI measurements. In other rivers, such as the Rio Grande at the RG-CAS and RG-RGV study sites, low silt-and-clay-concentration conditions are rare and it is often difficult to make EDI or EWI measurements when the amount of silt and clay in suspension does not greatly exceed the amount of sand in suspension, and both EDI or EWI and calibrated-pump measurements must be included in these BBC relations, which sometimes leads to less-accurate calibrations than if only EDI or EWI measurements could be used.

For accurate BBC relations to be developed, two conditions must be met. First, either C_{SAND} along the beam must be constant or any systematic variation in C_{SAND} along the beam must average out. This first condition requires that slowly varying spatial patterns in the cross-stream distribution of C_{SAND}, observed by Topping and others (2011) to be stable for many hours, must average out along the length of the beam. As shown below, this first condition is likely rarely met in a strict sense. Second, the average C_{SAND} along the beam must systematically relate to the value of $C_{XS\text{-}SAND}$ in the calibration cross section. Ideally, but not always, this second condition is met without any dependence of this relation on water discharge.

Because of how the flow and suspended-sediment-concentration fields interact with the local channel geometry at the locations of ADP deployments, there are typically differences between the average C_{SAND} or $D_{50\text{-}SAND}$ along the ADP beams and the values of $C_{XS\text{-}SAND}$ or $D_{50\text{-}XS\text{-}SAND}$ in the calibration cross section. These differences (ideally small) lead to differences between the theoretically predicted and empirically determined slopes and y-intercepts of the BBC relations. Because the grain-size distribution of the suspended sand is constant for the data used to develop a BBC relation, if the spatial distribution of suspended sand in the river cross section were uniform, equation 56 suggests that the slope of the BBC relation should be 0.1. By extension, equation 56 then also suggests for a 1- or 2-MHz ADP with SL=194 dB, b_{SF}=0.43 dB/count, A_N=25 counts, RL_{OFFSET}=0 dB, and UTS_{REF}~–85 dB (for $D_{50\text{-}XS\text{-}SAND\text{-}REF}$=0.125 mm and σ_G=0.63ϕ) that the y-intercept, K_1, of the BBC relation should be about –12. In practice, although close to these theoretically determined values, regression-determined slopes of the BBC relations typically range from about 0.07 to about 0.15, and regression-determined values of K_1 typically range from about –9 to –4. These less-negative empirical values of K_1 arise largely because the value of the RL_{OFFSET} is an unknown positive constant (see equation 22). Using the above values of SL, b_{SF}, A_N, and UTS_{REF}, a range in K_1 from –9 to –4 would therefore lead to a range in RL_{OFFSET} from +30 to +80 dB for the case where the slope of the BBC relation is equal to 0.1. The large variation in the regression-determined values of K_1 arises both from the variation in the regression-determined slopes of the BBC relations and because RL_{OFFSET} varies between ADPs.

Non-0.1 slopes of BBC relations at particular study sites result from a variety of physical processes. The most important of these processes is likely concentration-dependent changes in the relation between the average C_{SAND} along the acoustic beams and $C_{XS\text{-}SAND}$. By this process, BBC-relation slopes <0.1 are explained by there being proportionally more suspended sand "sampled" by the acoustic beams than is present on average in the entire cross section, as $C_{XS\text{-}SAND}$ decreases. In other words, the ratio of ADP-sampled C_{SAND} to $C_{XS\text{-}SAND}$ decreases as $C_{XS\text{-}SAND}$ increases. By this same logic, BBC-relation slopes >0.1 are explained by increases in the ADP-sampled C_{SAND} to $C_{XS\text{-}SAND}$ ratio as $C_{XS\text{-}SAND}$ increases. Slopes of BBC relations will therefore only equal 0.1 when the proportionality relating C_{SAND} along the acoustic beams to $C_{XS\text{-}SAND}$ is constant. For cases where the BBC-relation slopes are not equal to 0.1, sand-concentration dependent changes in the ADP-sampled C_{SAND} to $C_{XS\text{-}SAND}$ ratio also exert influence on the y-intercept (in addition to the influence on the y-intercept of RL_{OFFSET}, SL, UTS_{REF}, and k_{SF}). Because regression-determined values of the slope and y-intercept incorporate the effects of local channel geometry and account for the differences in RL_{OFFSET}, SL, and b_{SF} between different ADPs—and therefore compensate for mistakenly using incorrect values of RL_{OFFSET}, SL and b_{SF}—empirical-regression-determined values of the slope and y-intercept result in more accurate BBC relations than theoretically determined values.

To allow use of empirically determined BBC-relation slopes and y-intercepts, equation 59 is rewritten in the following final BBC-relation form:

$$\log_{10}\left(C_{XS\text{-}SAND\text{-}REF}\right) = K_1 + K_2\bar{B}_{BASE}\,, \qquad (60)$$

where

$C_{XS\text{-}SAND\text{-}REF}$ is the reference $C_{XS\text{-}SAND}$ with $D_{50\text{-}XS\text{-}SAND}$=$D_{50\text{-}XS\text{-}SAND\text{-}REF}$,

$\bar{B}_{BASE}$ is the beam-averaged base backscatter associated with $C_{XS\text{-}SAND\text{-}REF}$,

K_2 is the regression-determined slope of the BBC relation, and

K_1 becomes the regression-determined y-intercept of the BBC relation.

$RUTS$ does not appear in equation 60; it is set equal to zero because only those measurements of $C_{XS\text{-}SAND}$ where $D_{50\text{-}XS\text{-}SAND}$ is within 1/4ϕ of $D_{50\text{-}XS\text{-}SAND\text{-}REF}$ are included in the least-squares linear regression used to develop the BBC relation.

At a given study site, the slope of the BBC relation tends to be approximately constant for a given frequency ADP; that is, changing an instrument for maintenance purposes

may change the y-intercept but does not greatly affect the slope of the BBC relation. This observation is consistent with theory. Changing an instrument can cause large changes in the RL_{OFFSET}, small changes in the SL (and to a much lesser degree, can also cause changes in b_{SF}), but does not change the UTS_{REF} so long as the transducer diameter, transmit-pulse length, and receive-window length are constant. RL_{OFFSET} is known to vary between identical-model ADPs (Nortek, written commun., September 30, 2015). When ADPs have been replaced at a given study site, regression-determined y-intercepts may change by as much as 30 percent. Because this magnitude of difference cannot be explained by likely variation in b_{SF} or SL, substantial differences in RL_{OFFSET} between identical-model ADPs made by the same manufacturer are the most likely explanation for large changes in the y-intercepts of BBC relations when ADPs are replaced. Although knowing the RL_{OFFSET} is not required to use the ADP-calibration method described herein, it may be possible to determine the value of RL_{OFFSET} for a known value of SL using the method of Stanton and Chu (2008).

Calculation of the Backscatter from Silt and Clay

Owing to the behavior of the UTS_{SED} illustrated in figures 7 and 8, it is impossible to develop accurate relations between $\overline{B}$ and suspended-sediment concentration in rivers where (1) the grain-size distribution of the suspended silt and clay is broader than the grain-size distribution of the suspended sand and (or) (2) a large range in the concentration of suspended silt and clay is possible for any given concentration of suspended sand. As shown in figures 7 and 8, over the range in grain size from the 0.004-mm boundary between clay and silt to the 0.5-mm boundary between medium and coarse sand (a range encompassing grain sizes that are common in suspension), UTS can vary by as much as 57 dB for 600-kHz ADPs, 52 dB for 1-MHz ADPs, and 44 dB for 2-MHz ADPs when the suspended sediment is reasonably well sorted with $\sigma_G = 0.63\phi$. Thus, when a wide range in $C_{XS\text{-}SILT\text{-}CLAY}$ is possible for any given $C_{XS\text{-}SAND}$, the variation in suspended-sediment concentration at any given value of $\overline{B}$ can be large, although not typically as large as the 44- to 57-dB range in UTS suggests. In practice, the variation in suspended-sediment concentration at any given value of $\overline{B}$ is much less than the factor of 10,000 to 100,000 variation implied by this range in UTS because (1) the difference in UTS across the 0.004- to 0.5-mm grain-size range is reduced as the grain-size distribution of the suspended sediment broadens, and (2) the UTS is dominated by the median grain size of the sand, silt, and clay mixtures in suspension and does not reflect the entire range of all grain sizes in suspension. For example, at the CR87 study site, the observed variation in suspended-sediment concentration at any given value of $\overline{B}$ is about a factor of 100 at 1- and 2-MHz frequencies (fig. 12). In this example, the D_{50} of the suspended sediment ranges from about 0.009 to 0.2 mm, with σ_G decreasing from ~3ϕ to 0.63ϕ as the D_{50} increases over the 0.009- to 0.2-mm range. This coupled change in D_{50} and sorting corresponds to a ~28-dB range in UTS for 600-kHz ADPs, a ~23-dB range in UTS for 1-MHz ADPs, and a ~19-dB range in UTS for 2-MHz ADPs. These ranges in UTS correspond to predicted factors of 600, 200, and 80 variations in suspended-sediment concentration, respectively, on 600-kHz, 1-MHz, and 2-MHz ADPs at any given value of $\overline{B}$. Thus, neglecting the contribution of silt and clay to backscatter will result in errors in $C_{XS\text{-}SAND}$ calculated on the basis of $\overline{B}$ that can equal a factor of 100, a magnitude of error that is unacceptably high.

The additional beam-averaged backscatter resulting from the presence of suspended silt and clay at a given value of $C_{XS\text{-}SAND}$ is referred to as the excess backscatter, B'. Excess backscatter is calculated as

$$B' = \overline{B} - \overline{B}_{BASE} . \tag{61}$$

Following equation 54, equation 61 can be rewritten as

$$B' = \left(TS_{SED} + SL\right) - \left(TS_{SAND\text{-}REF} + SL\right), \tag{62}$$

and simplified to

$$B' = TS_{SED} - TS_{SAND\text{-}REF} \tag{63}$$

where

TS_{SED} is the range-independent target strength of a sand, silt, and clay mixture in suspension, and

$TS_{SAND\text{-}REF}$ is the range-independent target strength of $C_{XS\text{-}SAND\text{-}REF}$.

By definition, when all the suspended sediment is composed of sand with $D_{50\text{-}XS\text{-}SAND}$=$D_{50\text{-}XS\text{-}SAND\text{-}REF}$, then B'=0.

B' is well predicted on the basis of the target-strength theory described above. As the amount of silt and clay varies in the presence of a constant concentration of suspended sand, B' is affected by both changes in the grain-size distribution and density of the sand, silt, and clay mixture. As the amount of silt and clay in suspension increases in the presence of suspended sand with a constant concentration and grain-size distribution, the D_{50} of the suspended sediment decreases. Moreover, as the grain-size distribution of the suspended sediment evolves through the addition of silt and clay, the form function also changes, in response to both the decrease in D_{50} and the decrease in sorting. Finally, if the density of the clay is substantially different than the density of the silt and sand, and the silt and clay fraction of the suspended sediment is dominated by clay, addition of silt and clay will result in

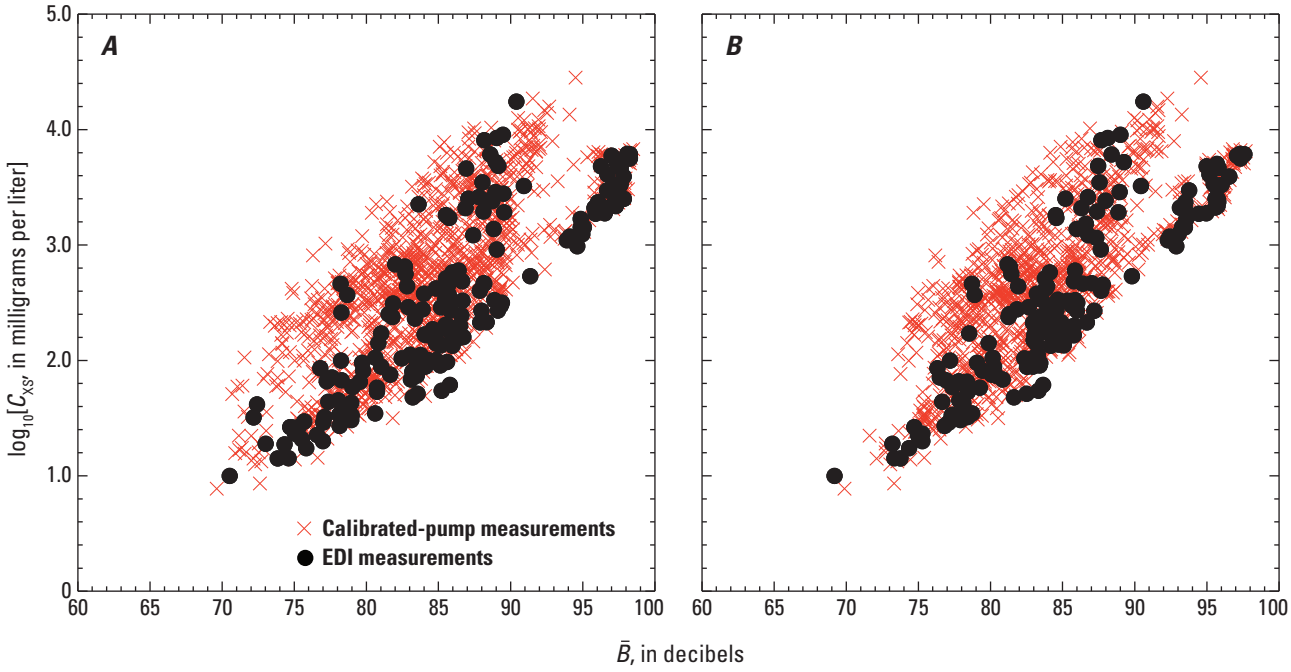

Figure 12. A factor of 100 variation in the velocity-weighted suspended-sediment concentration in the river cross section (C_{XS}) is possible at the CR87 study site for any given value of $\bar{B}$ at (***A***) 1-MHz and (***B***) 2-MHz acoustic frequencies. This large variation arises from large changes in the relative amounts of sand and relative amounts of silt and clay comprising the suspended sediment. To prevent clutter given the large number of measurements, error bars are not plotted. One hundred seventy-five EDI measurements and 1,191 calibrated-pump measurements made between August 25, 2005, and November 25, 2012, are plotted in ***A***; 163 EDI measurements and 1,022 calibrated-pump measurements made between February 10, 2006, and November 25, 2012, are plotted in ***B***.

either an increase or decrease in the density of the sand, silt, and clay mixture[4], as described previously in the derivation of α_{UNIT}. The combined effect from the increase in suspended sediment concentration, decrease in D_{50}, modification of the form function, and possible change in sediment density is first a gradual increase and then a more rapid increase in the target strength of the suspended sediment. As the concentration of silt and clay increases and greatly exceeds the concentration of sand, the increase in the concentration of the suspended sediment dominates the behavior of TS, albeit with a D_{50}, form function, and density of the sand, silt, and clay mixture that all evolve to ultimately equal the D_{50}, form function, and density of the silt and clay.

To derive the theoretically based value of B' at constant sand concentration and D_{50}, it is useful to first rewrite equation 46 as

$$TS_{SED} = 10\log_{10}(C) + UTS_{SED} = 10\log_{10}(C) + 10\log_{10}\left(f^2 \frac{3}{8\pi D_{50}\rho_S r_0^2}\right). \qquad (64)$$

[4]Because the density of chlorite-group clays exceeds the density of quartz, the wet density of kaolin-group clays are slightly less than the density of quartz, and the wet densities of illite- and especially smectite-group clays can be much less than the density of quartz (DeWit and Arens, 1950; Deer and others, 1966; Gartner and Carder, 1979), the density of a sand, silt, and clay mixture in suspension can be substantially different than the density of only suspended sand and silt, depending on the type of clay present.

For cases where the slope of the BBC relation equals the theoretical slope of 0.1, equation 63 can then be written as

$$B' = 10\log_{10}\left[\frac{f_{SED}^{\ 2}}{D_{50\text{-XS-SED}}\rho_{SED}}\right] + 10\log_{10}\left(C_{XS\text{-SAND-REF}} + C_{XS\text{-SILT-CLAY}}\right) - 10\log_{10}\left[\frac{f_{REF}^{\ 2}}{D_{50\text{-XS-SAND-REF}}\rho_{SAND}}\right] - 10\log_{10}\left(C_{XS\text{-SAND-REF}}\right) \quad (65)$$

and, after rearrangement and substitution of quartz density (2,650 kg/m^3) for the density of sand (ρ_{SAND}) and replacement of the 0.1 theoretical BBC-relation slope with K_2, finally written as

$$B' = \left(\frac{1}{K_2}\right)\log_{10}\left[\left(\frac{f_{SED}}{f_{REF}}\right)^2\left(\frac{D_{50\text{-XS-SAND-REF}}}{D_{50\text{-XS-SED}}}\right)\left(\frac{2650}{\rho_{SED}}\right)\left(1+\frac{C_{XS\text{-SILT-CLAY}}}{C_{XS\text{-SAND-REF}}}\right)\right], \quad (66)$$

where

$D_{50\text{-XS-SED}}$ is the velocity-weighted D_{50} of the bimodal suspended-sand, silt, and clay mixture in the river cross section,

f_{SED} is the value of the Thorne and Meral (2008) form function calculated for the bimodal grain-size distribution of the sand, silt, and clay mixture,

ρ_{SED} is the density of the sand, silt, and clay mixture calculated on the basis of quartz density for the sand-size sediment and a specified density for the silt-and-clay-sized sediment (ranging from 1,800 to 3,300 kg/m^3), and

f_{REF} is the value of the Thorne and Meral (2008) form function associated with the reference $D_{50\text{-XS-SAND}}$ (that is, $D_{50\text{-XS-SAND-REF}}$) for the unimodal grain-size distribution of the suspended sand in the river cross section.

B' is most sensitive to changes in the D_{50} and sorting of the suspended silt and clay, and less sensitive to both changes in the grain-size distribution of the suspended sand and changes in the density of the suspended silt and clay (fig. 13). Factor of two changes in the σ_G of the silt and clay are similar to factor of 10 changes in the D_{50} of the silt and clay in their effect on B'. As either the D_{50} of the suspended silt and clay coarsens or the σ_G of the silt and clay increases, B' for a given value of S (defined as the ratio of $C_{XS\text{-SILT-CLAY}}$ to $C_{XS\text{-SAND}}$) increases substantially. Under higher values of S and constant suspended-sand grain-size-distribution conditions, factor of 10 increases in the D_{50} of the silt and clay can result in increases in B' exceeding 20 dB, and, depending on the D_{50} of the silt and clay, factor of 2 increases in the σ_G of the silt and clay can result in increases in B' exceeding 30 dB (fig. 13*A*).

In contrast to this high sensitivity of B' to changes in the silt and clay grain-size distribution, decreases in the D_{50} of the suspended sand result in relatively small (<5 dB) increases in B', and reasonable increases in the σ_G of the suspended sand result in negligible decreases in B' under constant suspended-silt-and-clay grain-size-distribution conditions (fig. 13*B*). Furthermore, changes in the density of the silt and clay in the absence of substantial flocculation results in only minor changes in B'. A fifty percent change in the density of the sand, silt, and clay mixture (a large change) will only lead to biases in B' of ~2 dB. For example, because the density of the sand, silt, and clay mixture could be as low as ~1,800 kg/m^3 if the suspended sediment were dominated by montmorillonite, neglecting the effect of changing sediment density (for example, setting ρ_{SED}=2,650 kg/m^3) results in negative biases in the calculated value of B' of up to only about –2 dB (fig. 13*C*). This relatively weak influence of sediment density on B' stands in contrast to the strong influence of sediment density on attenuation described above and illustrated in figure 4*B*. Because the grain-size distribution of the silt and clay is not precisely knowable without in situ physical measurements, the small potential bias in B' arising from use of incorrect sediment densities may be acceptable in some cases.

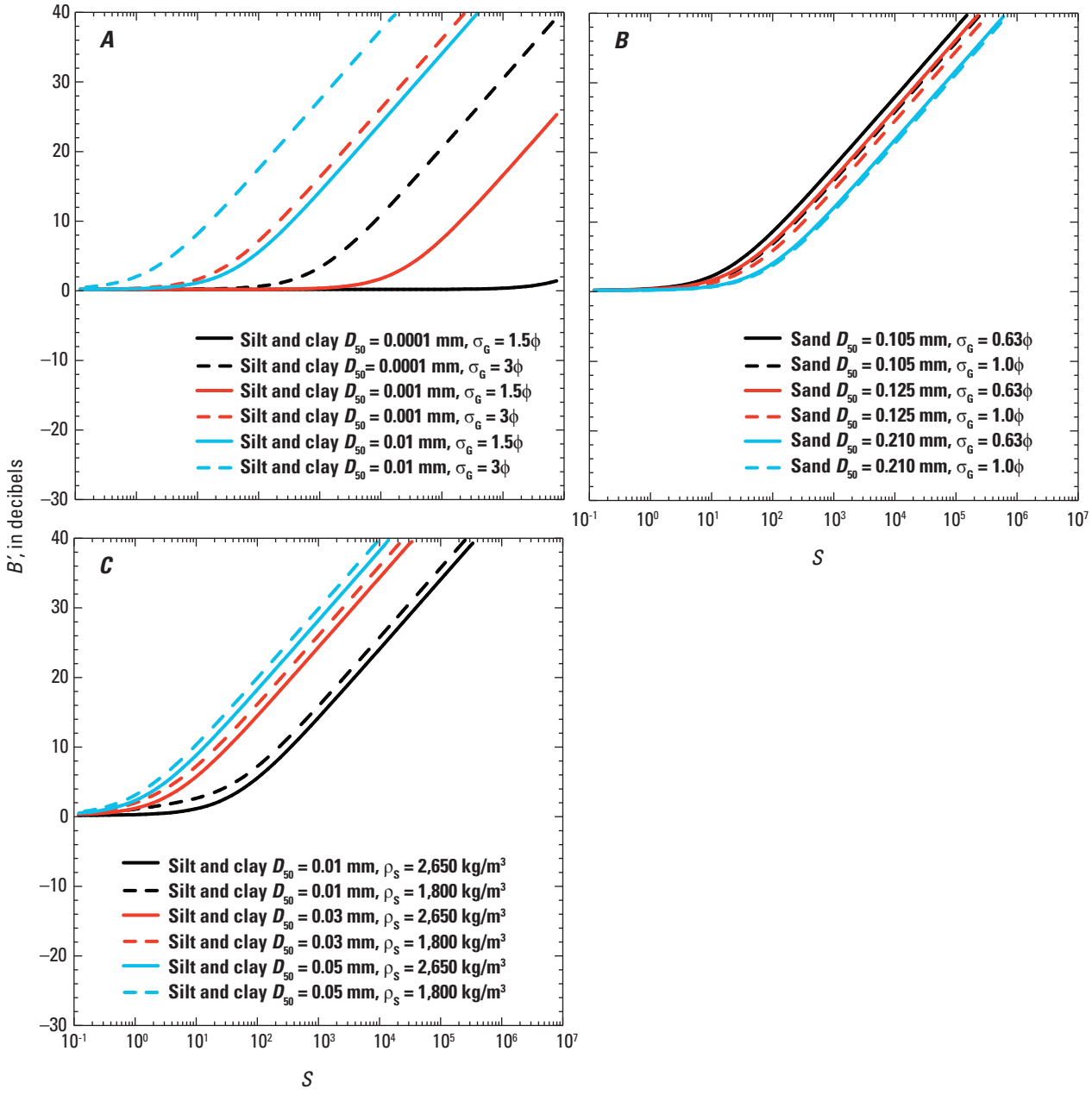

Figure 13. Theoretical behavior of B' under different silt and clay grain-size distributions, sand grain-size distributions, and silt and clay wet densities at the 1-MHz acoustic frequency. ***A***, B' plotted as a function of the ratio of suspended-silt-and-clay concentration to suspended-sand concentration, S, for a constant sand grain-size distribution and for silt and clay grain-size distributions with D_{50} values of 0.0001 mm, 0.001 mm, and 0.01 mm, and σ_G values of 1.5ϕ and 3ϕ. The suspended-sand grain-size distribution used in this example is held constant with D_{50}= 0.125 mm and σ_G= 0.63ϕ. ***B***, B' plotted as a function of S for a constant silt and clay grain-size distribution and sand grain-size distributions with D_{50} values of 0.105 mm, 0.125 mm, and 0.210 mm, and σ_G values of 0.63 ϕ and 1ϕ. The suspended-silt-and-clay grain-size distribution used in this example is held constant with D_{50}= 0.001 mm and σ_G= 3ϕ. The sediment density used in the examples in ***A*** and ***B*** is 2,650 kg/m³. ***C***, B' plotted as a function of S for a constant sand grain-size distribution and silt and clay grain-size distributions with D_{50} values of 0.01 mm, 0.03 mm, and 0.05 mm, and σ_G=1.5ϕ, and silt and clay wet densities (ρ_S) of 2,650 kg/m³ and 1,800 kg/m³. These seemingly large D_{50} values for silt and clay were chosen because, as the wet density of clay decreases, it tends to form larger flocs (see discussion in "Physical Basis for the Sediment Attenuation Coefficient" section of the text).

Changes in the density and grain-distribution of clay cannot necessarily be separated. As the wet density of clay decreases, it tends to form larger flocs (for example, Dyer and Manning, 1999; Hill and others, 2001; Curran and others, 2007). Evidence of some flocculation is evident in historical USGS suspended-sediment samples that were analyzed for silt-and-clay grain-size distribution in both native river water and after addition of a deflocculating agent. Although unlikely to be common in rivers, as flocs get extremely large (that is, with $D \geq 1$ mm), densities of flocs decrease to approach the 1,000 kg/m^3 density of water (Curran and others, 2007). Comparison of the results plotted in figures 13*A*-*C* indicates, however, that neglecting the influence of decreases in silt and clay density from flocculation on B' would result in a much smaller bias in B' than would neglecting the increase in silt and clay D_{50} that would be associated with an increase in flocculation. To simplify equation 66, ρ_{SED} can therefore be set equal to 2,650 kg/m^3 in many situations, allowing any bias from making the constant-sediment-density assumption to be compensated by relatively small biases in the estimated silt and clay grain-size distribution.

Estimation of the Grain-Size Distribution and Wet Density of the Silt and Clay: Backscatter Constraint

As stated above in the section called "Estimation of the Grain-Size Distribution and Wet Density of the Silt and Clay: Attenuation Constraint," the second constraint used to estimate the properties of the silt and clay in suspension is to use multiple acoustic frequencies to solve for the values of the D_{50}, σ_G, and ρ_S for the silt and clay that, in combination with the known values of the D_{50}, σ_G, and ρ_{SAND} for the suspended sand, best predict the observed values of the excess backscatter, B', associated with higher relative concentrations of suspended silt and clay. In addition to providing information on the silt and clay grain-size distribution, requirement of this second (backscatter) constraint, in combination with the requirement of the first (attenuation) constraint depicted in figure 6, allows a fairly robust theoretical method for calculating the backscatter arising from higher relative concentrations of suspended silt and clay. Once the excess backscatter from silt and clay is calculated using the properties of the silt and clay that satisfy both the attenuation (fig. 6) and backscatter (fig. 14) constraints, it can then be separated from the backscatter arising from sand-size sediment.

As shown in figure 14, the theoretical behavior of B' illustrated in figure 13 agrees well with the empirical behavior of B' observed at study sites on the Colorado River and Rio Grande. In addition, it is evident from the comparison between theoretical and empirical B' in figure 14 that when $S >> 2$, the backscatter from silt-and-clay-sized sediment cannot be ignored if unbiased acoustical measurements of $C_{XS\text{-}SAND}$ are to be made. This observation forms the basis of our preference to use only those measurements of $C_{XS\text{-}SAND}$ associated with $S \leq 2$ in the development of BBC relations. Details of the grain-size distributions used to develop the theoretical B' relations depicted in figure 14 are provided in appendix 5. Finally, calculation of $\overline{B}$ using BBC relations and the above theoretical values of B' agree well with the measured values of $\overline{B}$ for different ranges in S at both the CR87 and RG-RGV study sites (fig. 15).

Figure 14. (**following page**) Comparison of empirical and theoretical values of B' on the Colorado River and Rio Grande. ***A***, B' plotted as a function of S, the ratio of $C_{SILT\text{-}CLAY}$ to C_{SAND}, for the 600-kHz acoustic-Doppler profiler (ADP) at the CR87 study site. The base-backscatter-calibration (BBC) relation used to calculate values of B' for the equal-discharge increment (EDI) and calibrated pump measurements is the relation plotted in figure 11*A* that has a slope of 0.119. The mean value of S among the measurements used to develop the BBC relation is 0.5. ***B***, B' plotted as a function of S for the 1-MHz ADP at the CR87 study site. The BBC relation used to calculate values of B' for the EDI and calibrated pump measurements is the relation plotted in figure 11*B* that has a slope of 0.105. The mean value of S among the measurements used to develop the BBC relation is 0.6. ***C***, B' plotted as a function of S for the 2-MHz ADP at the CR87 study site. The BBC relation used to calculate values of B' for the EDI and calibrated pump measurements is the relation plotted in figure 11*C* that has a slope of 0.110. The mean value of S among the measurements used to develop the BBC relation is 0.6. In ***A***–***C***, the theoretical relations for B' are derived using a sand grain-size distribution with $D_{50\text{-}XS\text{-}SAND\text{-}REF}$=0.125 mm, σ_G=0.63ϕ, and quartz density and a silt and clay grain-size distribution with D_{50}=0.0008 mm and σ_G=3ϕ and a density of 2,500 kg/m^3. These are the same properties of the silt and clay used to derive the theoretical relations for α_S for these ADPs in figure 6. ***D***, B' plotted as a function of S for the 2-MHz ADP at the RG-RGV study site. The BBC relation used to calculate values of B' for the equal-width increment (EWI) and calibrated pump measurements has a slope of 0.078 and is plotted in figure 15*B*. The theoretical relation for B' is derived using a sand grain-size distribution with $D_{50\text{-}XS\text{-}SAND\text{-}REF}$=0.105 mm, σ_G=0.65ϕ , and quartz density, and a silt and clay grain-size distribution with D_{50}=0.002 mm, σ_G=2.7ϕ, and a density of 3,200 kg/cm^3. Because low S values in the Rio Grande are rarer than in the Colorado River, the mean value of S among the measurements used to develop the BBC relation in this example is 6, a factor of 10 higher than in the example plotted in ***A***–***C***; this higher mean value of S leads to the slightly negative values of B' discernable in this plot at values of S less than 6. Eighty-eight EDI measurements and 572 calibrated pump measurements made between March 22, 2007, and November 23, 2012, are plotted in ***A***; 96 EDI measurements and 659 calibrated pump measurements made between August 25, 2005, and March 12, 2008, are plotted in ***B***; 76 EDI measurements and 484 calibrated pump measurements made between February 10, 2006, and March 12, 2008, are plotted in ***C***; 21 EWI measurements and 349 calibrated pump measurements made between July 20, 2012, and October 5, 2014, are plotted in ***D***.

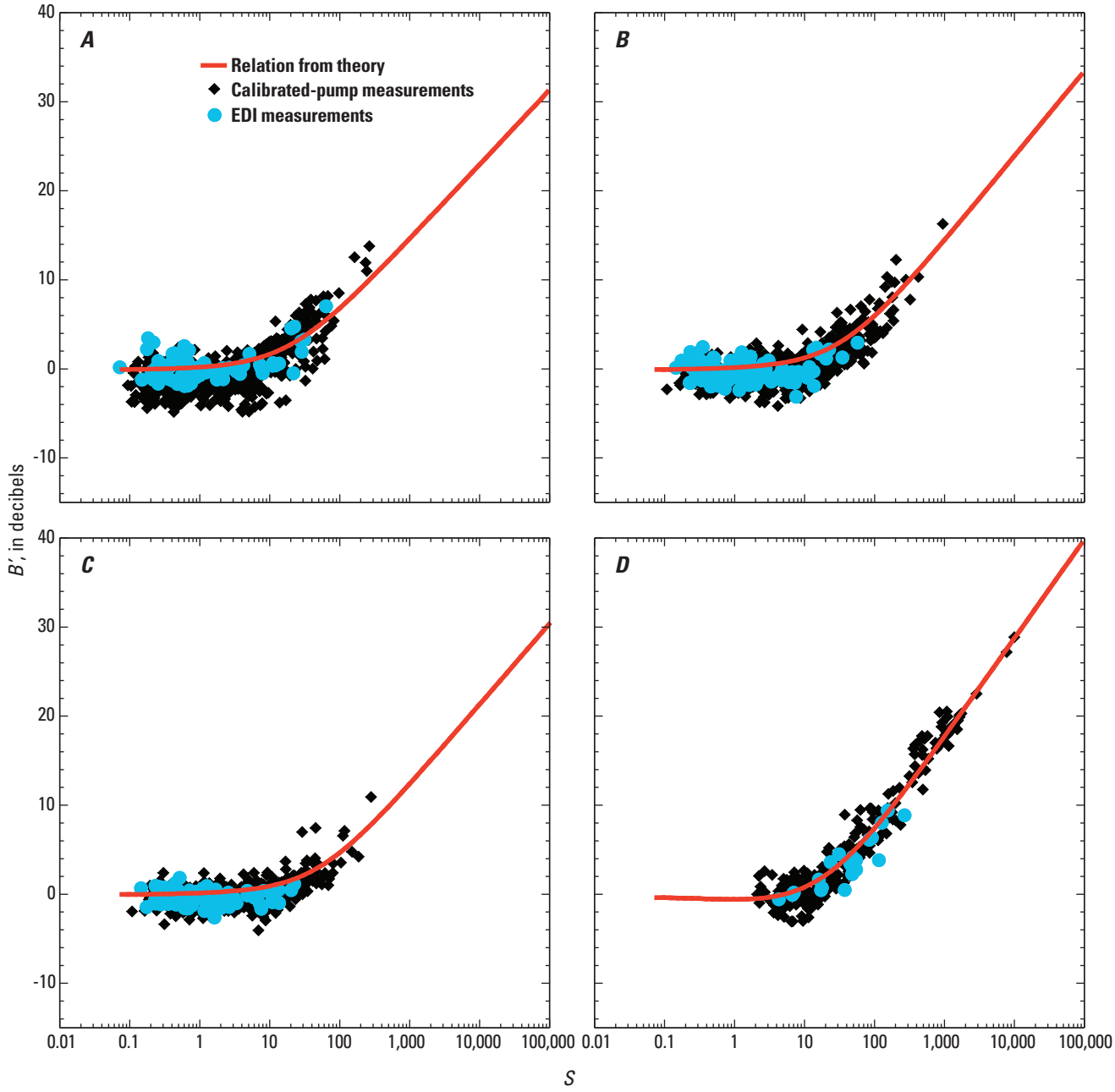
A
B
C
D
Relation from theory
Calibrated-pump measurements
EDI measurements
B′, in decibels
S
40
30
20
10
0
-10
0.01
0.1
1
10
100
1,000
10,000
100,000

Figure 14.

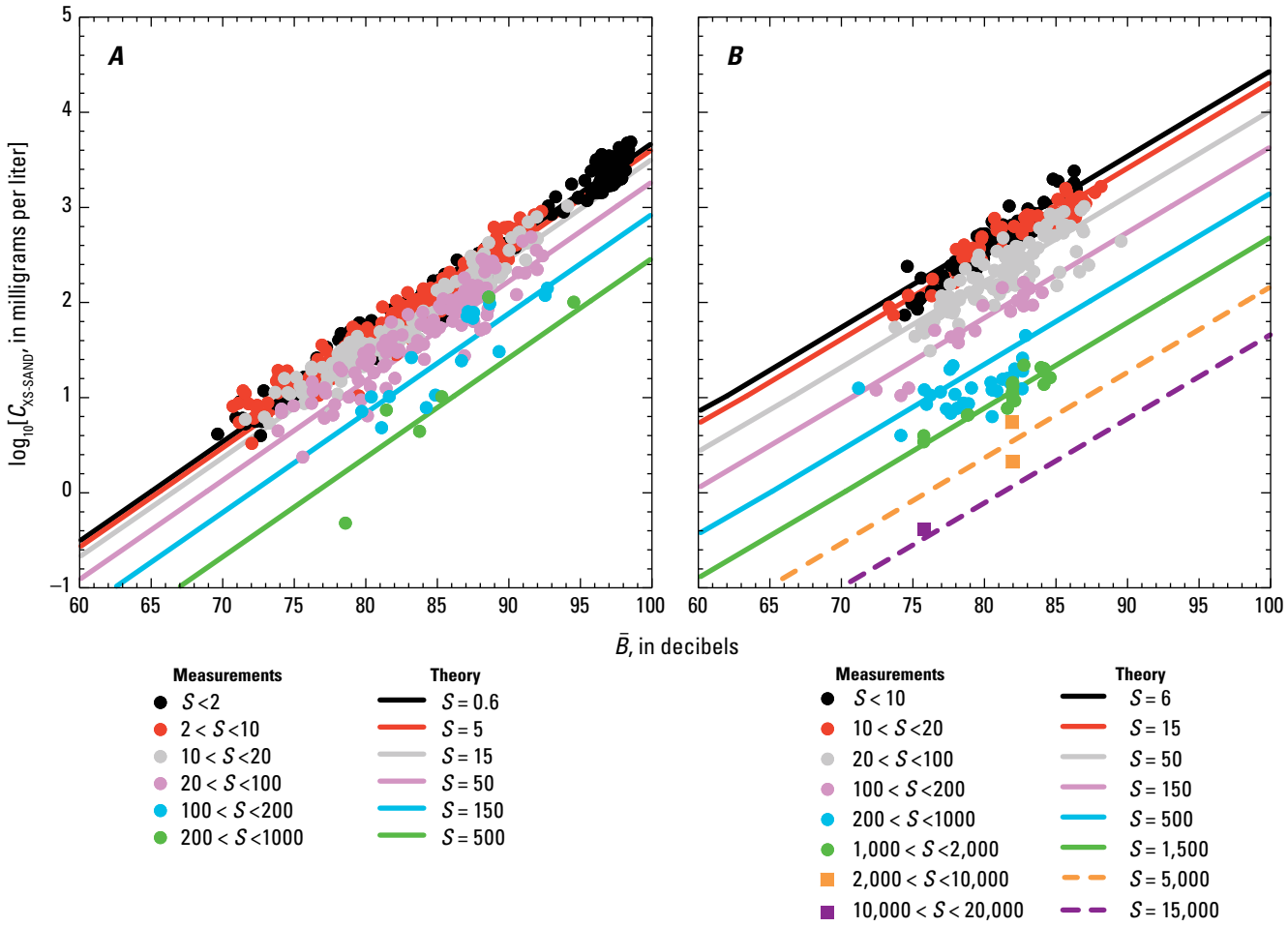

Figure 15. Comparison of empirical and theoretical relations between $\bar{B}$ and the logarithm of $C_{XS\text{-}SAND}$ in the Colorado River and Rio Grande for different ranges of S. ***A***, $Log_{10}(C_{XS\text{-}SAND})$ plotted as a function of $\bar{B}$ for 6 different ranges of S for the 1-MHz acoustic-Doppler profiler (ADP) at the CR87 study site. Measurements plotted are the same as in figure 14*B*; equal-discharge increment (EDI) and calibrated-pump measurements are not segregated in this plot to prevent clutter. Base-backscatter-calibration (BBC) relation is fit to EDI measurements with $S \leq 2$ shown as solid black line (BBC relation same as that in figure 11*B* with mean S among measurements used to develop this relation being 0.6); theoretical relations between $\bar{B}$ and $\log_{10}(C_{XS\text{-}SAND})$ at higher values of S calculated using the theoretical B' relation in figure 14*B*. ***B***, $Log_{10}(C_{XS\text{-}SAND})$ plotted as a function of $\bar{B}$ for 8 different ranges of S for the 2-MHz ADP at the RG-RGV study site. Measurements plotted are the same as in figure 14*D*; equal-width increment (EWI) and calibrated-pump measurements are not segregated in this plot to prevent clutter. BBC relation fit to EWI and calibrated pump measurements with $S \leq 10$ shown as solid black line (mean S among measurements used to develop this relation is 6); theoretical relations between $\bar{B}$ and $\log_{10}(C_{XS\text{-}SAND})$ at higher values of S calculated using the theoretical B' relation in figure 14*D*.

Suspended-Sediment-Grain-Size-Distribution Effects on Relations between $\bar{B}$, α_s, $\log_{10}(S)$, and $\log_{10}(C_{XS\text{-}SAND})$

The theoretical behaviors of backscatter and attenuation under different suspended-sediment grain-size distributions control the shapes of the relations between $\bar{B}$, α_s, $\log_{10}(S)$ and $\log_{10}(C_{XS\text{-}SAND})$. As a result of these behaviors, backscatter resulting from extremely high concentrations of suspended silt and clay can effectively mask the backscatter from sand. Examples of relations between $\bar{B}$ and $\log_{10}(C_{XS\text{-}SAND})$ at different values of α_s and relations between α_s and $\log_{10}(S)$ at different values of $\bar{B}$ are depicted in figure 16. Although the acoustic frequency used in these examples is 1 MHz, the general behaviors of the relations in these examples are unaffected by acoustic frequency. These relations were developed using BBC relations with a slope of 0.1 (the case where the proportionality relating C_{SAND} along the acoustic beams to $C_{XS\text{-}SAND}$ is constant), and the typical "washload" case where $C_{SILT\text{-}CLAY} \approx C_{XS\text{-}SILT\text{-}CLAY}$. The theoretical relation between $\log_{10}(S)$ and B' was then calculated on the basis of a rearranged version of equation 66. $\bar{B}$ values associated with different combinations of $C_{XS\text{-}SAND}$ and $C_{XS\text{-}SILT\text{-}CLAY}$ were then calculated, with α_s determined for each concentration combination.

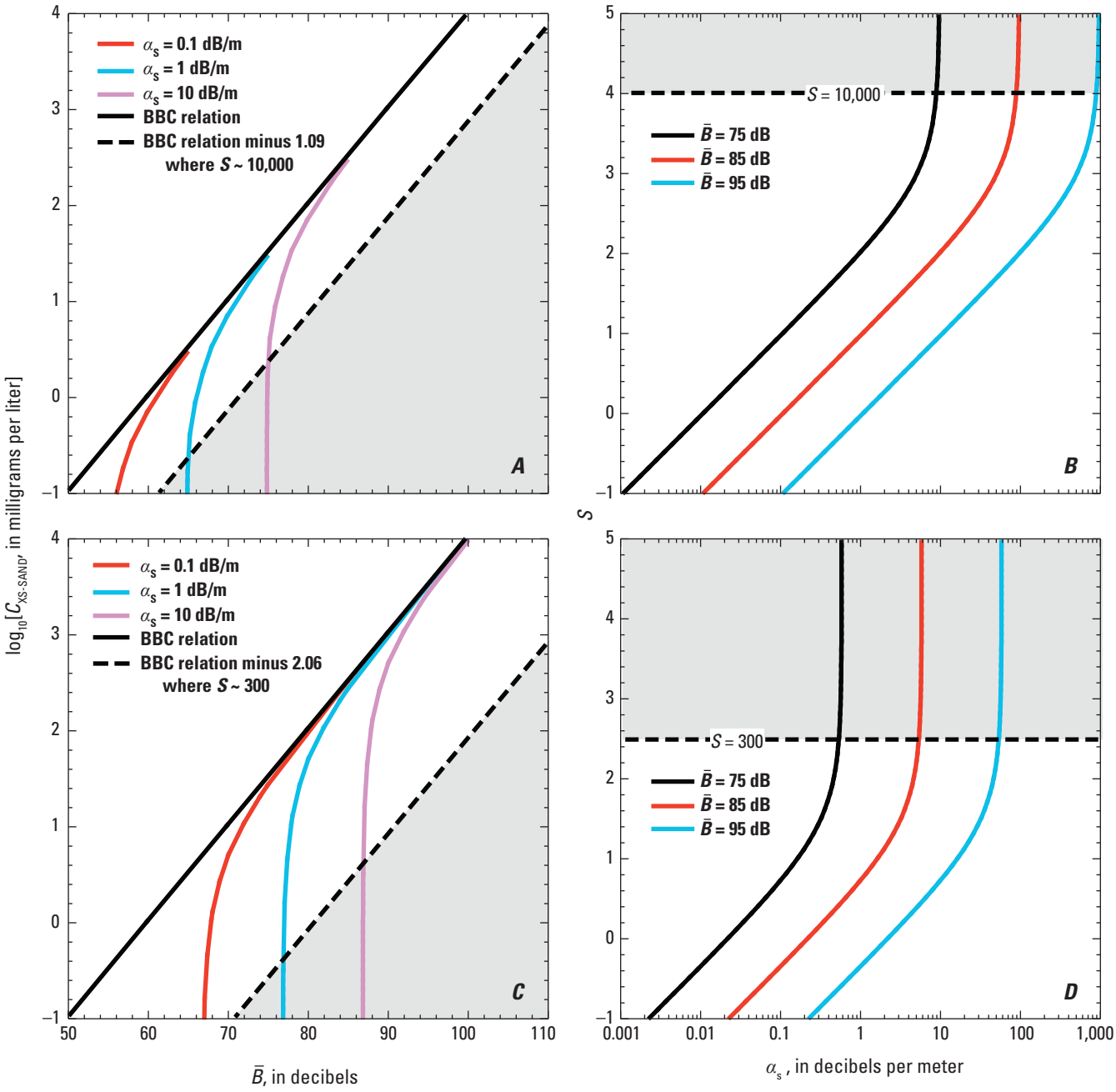

Figure 16. Behavior of theoretical relations between $\bar{B}$ and $\log_{10}(C_{XS\text{-}SAND})$ for different values of α_S and behavior of theoretical relations between α_S and $\log_{10}(S)$ for different values of $\bar{B}$ for different grain-size distributions of suspended silt and clay at the 1-MHz acoustic frequency. The gray shaded regions indicate the regions of "backscatter masking" resulting from relatively high concentrations of suspended silt and clay. The suspended-sand grain-size distribution used to develop these relations has D_{50}=0.125 mm and σ_G=0.63ϕ; the suspended-silt-and-clay grain-size distributions used to develop these relations all have a density of 2,650 kg/m^3 and σ_G=3ϕ. The BBC relation has a slope of 0.1 and a y-intercept of –6 in all cases. ***A***, $\text{Log}_{10}(C_{XS\text{-}SAND})$ plotted as a function of $\bar{B}$ for the case where the D_{50} of the silt and clay is 0.0001 mm. Shown are the BBC relation and the relations between $\bar{B}$ and $\log_{10}(C_{XS\text{-}SAND})$ for the cases where α_S=0.1, 1.0, and 10 dB/m. These relations between $\bar{B}$ and $\log_{10}(C_{XS\text{-}SAND})$ are near vertical when S exceeds ~10,000. ***B***, $\text{Log}_{10}(S)$ plotted as a function of α_S for the case depicted in ***A***. Shown are the relations between α_S and $\log_{10}(S)$ for the cases where $\bar{B}$=75, 85, and 95 dB. These relations are also near vertical when S exceeds ~10,000. ***C***, $\text{Log}_{10}(C_{XS\text{-}SAND})$ plotted as a function of $\bar{B}$ for the case where the D_{50} of the silt and clay is 0.001 mm. Shown are the BBC relation and the relations between $\bar{B}$ and $\log_{10}(C_{XS\text{-}SAND})$ for the cases where α_S=0.1, 1.0, and 10 dB/m. These relations between and $\log_{10}(C_{XS\text{-}SAND})$ are near vertical when S exceeds ~300. ***D***, $\text{Log}_{10}(S)$ plotted as a function of α_S for the case depicted in ***C***. Shown are the relations between α_S and $\log_{10}(S)$ for the cases where $\bar{B}$=75, 85, and 95 dB. These relations are also near vertical when S exceeds ~300.

As a result of "backscatter masking" by relatively high $C_{XS\text{-}SILT\text{-}CLAY}$, relations between $\overline{B}$ and $\log_{10}(C_{XS\text{-}SAND})$ at constant α_S become extremely steep at lower values of $\log_{10}(C_{XS\text{-}SAND})$, making it problematic to accurately solve for $\log_{10}(C_{XS\text{-}SAND})$ when S is relatively high. The "steepness" transition in these relations occurs at increasing values of S as the D_{50} of the silt and clay decreases. For the 0.0001-mm silt-and-clay-D_{50} case depicted in figures 16*A–B*, relations between $\overline{B}$ and $\log_{10}(C_{XS\text{-}SAND})$ at constant α_S and relations between α_S and $\log_{10}(S)$ at constant $\overline{B}$ become near vertical when S exceeds ~10,000. In figure16*A*, S exceeds 10,000 when $\log_{10}(C_{XS\text{-}SAND})$ is less than that predicted by the BBC relation minus ~1.09. Similarly, for the 0.001 mm silt-and-clay-D_{50} case depicted in figures 16*C–D*, relations between $\overline{B}$ and $\log_{10}(C_{XS\text{-}SAND})$ at constant α_S and relations between α_S and $\log_{10}(S)$ at constant $\overline{B}$ become near vertical when S exceeds ~300. In figure 16*C*, S exceeds 300 when $\log_{10}(C_{XS\text{-}SAND})$ is less than that predicted by the BBC relation minus ~2.06. When relatively strong correlation exists between the discharge of water and $C_{XS\text{-}SAND}$, application of discharge-weighting factors may allow estimation of $\log_{10}(C_{XS\text{-}SAND})$ under the conditions of backscatter masking at high values of S (see appendix 6).

Theoretical relations between α_S and $\log_{10}(S)$ at constant $\overline{B}$ typically agree well with measurements when the BBC relation does not shift with changing water discharge (a problem described in appendix 6). Examples of good agreement between theoretical and measured relations between α_S and $\log_{10}(S)$ over the 86-88-dB range in $\overline{B}$ at the CR87 study site are provided in figure 17. This particular 2-dB range in $\overline{B}$ was chosen for this example because, at both the 1- and 2-MHz frequencies, this range contains a relatively large number of both EDI and cross-section-calibrated pump measurements over a relatively large range in α_S.

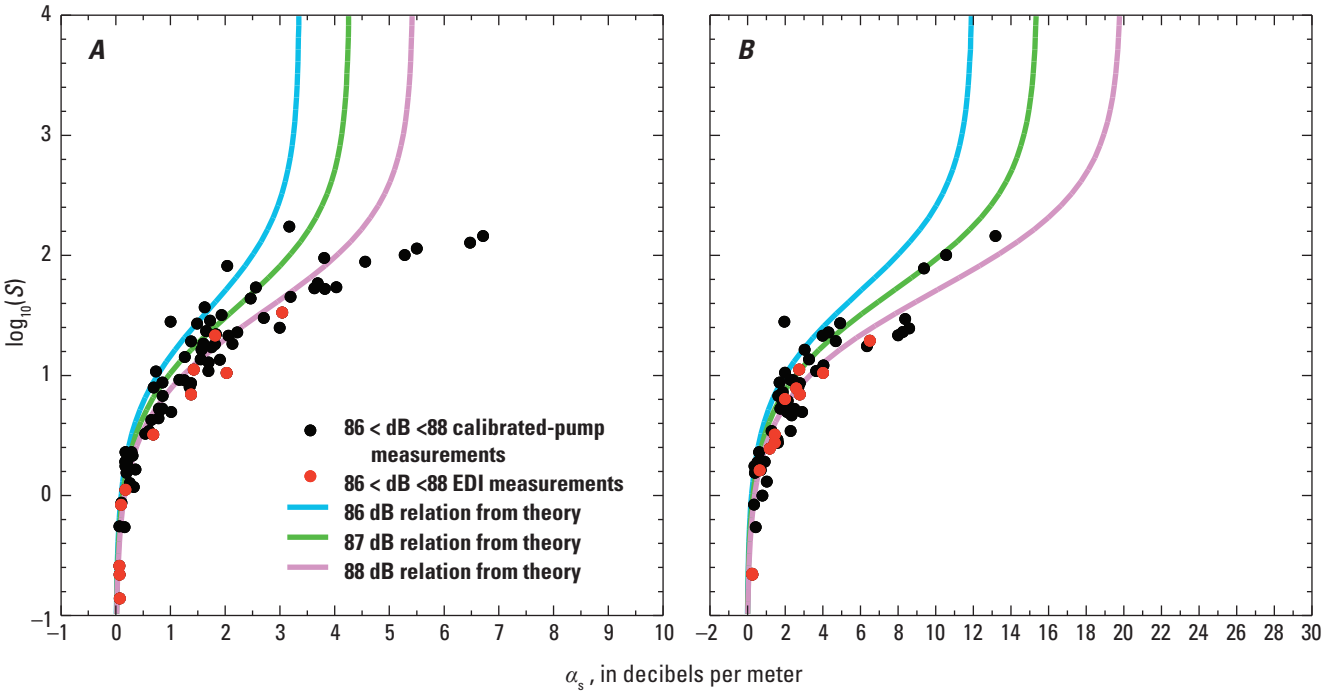

Figure 17. Examples of theoretical and measured relations between α_S and $\log_{10}(S)$ for the 86- to 88-dB range in $\overline{B}$ at the CR87 study site for the (***A***) 1-MHz and (***B***) 2-MHz acoustic-Doppler profilers (ADPs). *A* 2-dB range in $\overline{B}$ was chosen for these comparisons because of the ~2 percent estimated error in measurements of $\overline{B}$. Measurements depicted are from the same period used to develop the BBC relations in figure 11. Theoretical relations between α_S and $\log_{10}(S)$ were derived using (1) regression-determined slopes and intercepts of the BBC relations, (2) measured typical suspended-sand grain-size distribution with $D_{50\text{-}XS\text{-}SAND\text{-}REF}$=0.125 mm and σ_G=0.63ϕ, (3) estimated typical suspended-silt-and-clay grain-size distribution with D_{50}=0.0008 mm, σ_G=3ϕ, and density of 2,500 kg/m^3, and (4) α_S estimated using the empirical relations between α_S and $C_{XS\text{-}SILT\text{-}CLAY}$ in figure 6.

Procedure for Applying Method

Calibration Procedure for Each Single-Frequency ADP in an Array

Development of cross-section calibrations for each single-frequency ADP in the multi-frequency ADP arrays is a 13-step process described in detail in appendix 7. The outcomes of this process are single-frequency acoustical estimates of $C_{XS\text{-}SILT\text{-}CLAY}$ and $C_{XS\text{-}SAND}$. Because of how changes in suspended-sediment concentration and grain size combine to affect *TS* at each frequency, the single-frequency estimates of $C_{XS\text{-}SAND}$ will be grain-size biased. These biases will be minimized by the *RUTS* method (described in the next section) that is used to combine single-frequency $C_{XS\text{-}SAND}$ estimates into multi-frequency measurements of $C_{XS\text{-}SAND}$ and $D_{50\text{-}XS\text{-}SAND}$. The essence of the calibration procedure is as follows: (1) equation 27 serves as the basis for relating the acoustic attenuation measurements to $C_{XS\text{-}SILT\text{-}CLAY}$, and (2) equations 27, 60, and 66 are solved together to allow subtraction of B' from $\overline{B}$ thus allowing single-frequency acoustic-backscatter measurements to be used to estimate the value of $C_{XS\text{-}SAND}$ that would be present if $D_{50\text{-}XS\text{-}SAND}$ were equal to $D_{50\text{-}XS\text{-}SAND\text{-}REF}$.

Multi-Frequency *RUTS*-Based Calculation of $C_{XS\text{-}SAND}$ and $D_{50\text{-}XS\text{-}SAND}$ Using the Single-Frequency Estimates of $C_{XS\text{-}SAND}$

The *RUTS* associated with each frequency forms the basis for calculating $C_{XS\text{-}SAND}$ and $D_{50\text{-}XS\text{-}SAND}$. These calculations draw on the theoretical result that, for a given sorting of suspended sand and at the 600-kHz to 2-MHz range of frequencies used in this study, acoustic backscatter at lower frequencies is more affected by changes in $D_{50\text{-}XS\text{-}SAND}$ than is backscatter at higher frequencies. Inputs to these calculations are the single-frequency estimates of $C_{XS\text{-}SAND}$ produced by the procedure described in the previous section, and the theoretical *RUTS* at each frequency (for example, fig. 10). The difference in the values of $\overline{B}$ measured at two frequencies (corrected for B'), the theoretical *RUTS* relations, and the BBC relations for the two different-frequency ADPs are then used to calculate values of $D_{50\text{-}XS\text{-}SAND}$ and $C_{XS\text{-}SAND}$ that satisfy the constraint that the $\overline{B}$ measured at each frequency (corrected for B') is associated with the same $C_{XS\text{-}SAND}$. The detailed procedure for the multi-frequency *RUTS*-based calculation of $C_{XS\text{-}SAND}$ and $D_{50\text{-}XS\text{-}SAND}$ is provided in appendix 8.

Results

The two-frequency attenuation-based acoustical measurements of $C_{XS\text{-}SILT\text{-}CLAY}$ and the two-frequency *RUTS*-based acoustical measurements $C_{XS\text{-}SAND}$ and $D_{50\text{-}XS\text{-}SAND}$ compare well with the physical measurements of these quantities at the Colorado River and Rio Grande study sites, with better agreement occurring at those study sites with less distance between the calibration cross section and the ADP arrays. In figures 18*A–C*, the acoustical and physical measurements are plotted in a format showing predicted (acoustical) versus observed (physical), segregated by river, in-sample versus out-of-sample data, and longitudinal distance between the calibration cross section and the ADP array (Colorado River study sites with this distance ≤200 m are grouped as "Colorado River"). Data from the one study site, CR61, with a ~750-m longitudinal distance between the calibration cross section and ADPs are plotted separately. Additional versions of figures 18*A–C* are provided in appendix 9 in which these measurements are also segregated by study site. We define "in-sample" data as data that were used to calibrate either one or both of the ADPs at a study site. Similarly, we define "out-of-sample" data as data that were not used in any calibration. The out-of-sample data depicted in figures 18*A–C* are all from the CR87 study site. The in-sample and out-of-sample data from the CR87 study site are analyzed in the following error-analysis section of this report to evaluate whether there is a significant difference between in- and out-of-sample relative errors. Also plotted in figures 18*A–C* are the lines of perfect agreement between the physical and acoustical measurements and the best-fit log-linear regressions fit to all of the data plotted in each figure panel (for the study sites with ≤200-m longitudinal distance between the calibration cross section and the ADP array). For brevity, time-series plots comparing the acoustical and physical measurements are not provided in this report; user-interactive versions of such plots can readily be made at http://www.gcmrc.gov/discharge_qw_sediment/ or http://cida.usgs.gov/gcmrc/discharge_qw_sediment/.

In the comparisons of acoustical and physical measurements of $C_{XS\text{-}SILT\text{-}CLAY}$ and $C_{XS\text{-}SAND}$ in figures 18*A–B*, the best-fit log-linear regressions plot extremely close to the lines of perfect agreement. This result suggests that, over the four orders of magnitude in sediment concentration plotted in figures 18*A–B*, the methods described in this report result in unbiased acoustical measurements of both $C_{XS\text{-}SILT\text{-}CLAY}$ and $C_{XS\text{-}SAND}$ (a result to be further tested in subsequent error-analysis sections of this report). In figure 18*A*, the acoustical and physical measurements of $C_{XS\text{-}SILT\text{-}CLAY}$ are in good agreement over the range from ~100 mg/L to ~20,000 mg/L; in figure 18*B*, the acoustical and physical measurements of C_{SAND} are in good agreement over the range from ~2 mg/L to ~5,000 mg/L. Though not shown in figure 18*A* because the physical measurements are calibrated-pump measurements, acoustical and calibrated-pump measurements of $C_{XS\text{-}SILT\text{-}CLAY}$ have been found to agree well at concentrations as high as ~30,000 mg/L on both the Colorado River and Rio Grande.

Although the closeness of the lines of perfect agreement and best-fit log-linear regressions suggests strongly that the acoustical measurements are unbiased, the presence

of reasonably large variance about the lines of perfect agreement indicates that these measurements are subject to reasonably large time-varying error (evaluated in subsequent error-analysis sections of this report). In addition, the variance about the lines of perfect agreement is larger, especially for $C_{XS\text{-}SAND}$ (fig. 18*B*) and $D_{50\text{-}XS\text{-}SAND}$ (fig. 18*C*) in the case where the longitudinal distance between the calibration cross section and the ADP array is much greater than 200 m (for example, at the CR61 study site where the calibration cross section is ~750 m downstream of the ADPs). This result suggests strongly that time-varying error in acoustical measurements of both $C_{XS\text{-}SAND}$ and $D_{50\text{-}XS\text{-}SAND}$ increases with increasing distance between the calibration cross section and the ADP array, a point that will be revisited below.

For both $C_{XS\text{-}SILT\text{-}CLAY}$ and $C_{XS\text{-}SAND}$, the log-transformed variance about the lines of perfect agreement decreases significantly with increasing concentration. In the case of $C_{XS\text{-}SAND}$, this decrease in variance is gradual, whereas in the case of $C_{XS\text{-}SILT\text{-}CLAY}$, this decrease in variance is rapid between concentrations of 1 and 100 mg/L and more gradual between concentrations of 100 and 20,000 mg/L. These negative correlations between concentration and the log-transformed variance about the lines of perfect agreement indicate that the time-varying relative errors in both the acoustical measurements of $C_{XS\text{-}SILT\text{-}CLAY}$ and $C_{XS\text{-}SAND}$ decrease with increasing concentration.

Although still reasonably good, the agreement between the acoustical and physical measurements of $D_{50\text{-}XS\text{-}SAND}$ depicted in figure 18*C* is not as good as the agreement between the acoustical and physical concentration measurements depicted in figures 18*A–B*. Unlike in the cases of $C_{XS\text{-}SILT\text{-}CLAY}$ or $C_{XS\text{-}SAND}$, the best-fit log-linear regression fit to the $D_{50\text{-}XS\text{-}SAND}$ data from all study sites cross-cuts the line of perfect agreement at a low angle. This result suggests the presence of a small grain-size-dependent bias in the acoustical measurements of $D_{50\text{-}XS\text{-}SAND}$ (evaluated in subsequent error-analysis sections of this report). At only the CR30 study site does the best-fit log-linear regression plot close to the line of perfect agreement. Because the CR30 study site is the site with the largest EWI-measured range in $D_{50\text{-}XS\text{-}SAND}$, however, the detection of the apparent grain-size-dependent bias in the acoustical measurements of $D_{50\text{-}XS\text{-}SAND}$ at the other study sites could possibly be an artifact of the relatively small measured range in $D_{50\text{-}XS\text{-}SAND}$ at these sites. Although the variance about the line of perfect agreement in figure 18*C* appears larger than in figures 18*A–B*, this is a visual artifact of differences in scale between the figure panels; five orders of magnitude are plotted in figures 18*A–B*, whereas less than one order of magnitude is plotted in figure 18*C*. In reality, the time-varying relative error associated with the variance about the line of perfect agreement in figure 18*C* is smaller than in figures 18*A–B*, a result further evaluated below.

Comparison of the two- and three-frequency acoustical measurements with the physical measurements of $C_{XS\text{-}SAND}$ in figure 18*D* indicate that use of the three-frequency *RUTS* method does not substantially improve the results relative to those obtainable through use of the two-frequency *RUTS* method, likely because of the small difference between the *RUTS* at 600 kHz and 1MHz in figure 9 for the suspended-sand grain-size distribution with assumed constant sorting (in this case, constant σ_G=0.63ϕ). The data associated with each version of the *RUTS* method essentially plot on top of each other (except in a few cases) and the best-fit log-linear regressions associated with each version of the *RUTS* method plot on top of each other in figure 18*D*. In slight contrast to the $C_{XS\text{-}SAND}$ results, addition of the third frequency does result in some improvement in the acoustical measurements of $D_{50\text{-}XS\text{-}SAND}$ in figure 18*E*. These results indicate only minor improvement in either bias or time-varying error associated with adding the third frequency to the *RUTS*-based calculations. If the σ_G of the suspended-sand grain size distribution and, therefore, the form function and *RUTS* were allowed to vary, iterative solution for $C_{XS\text{-}SAND}$, $D_{50\text{-}XS\text{-}SAND}$, and σ_G of the suspended sand using three acoustic frequencies could possibly improve the results, but this possibility has not yet been tested.

Figure 18. (**following page**) Predicted versus observed plots for the equal-discharge increment (EDI) or equal-width increment (EWI) and acoustical measurements of $C_{XS\text{-}SILT\text{-}CLAY}$, $C_{XS\text{-}SAND}$, and $D_{50\text{-}XS\text{-}SAND}$. In each figure panel, the solid black line is the line of perfect agreement; *n* is the number of observations; horizontal error bars indicate the 95-percent-confidence-level combined field and laboratory-processing error in the EDI or EWI measurement. ***A***, Predicted versus observed plot for $C_{XS\text{-}SILT\text{-}CLAY}$. Solid green line is the best-fit log-linear regression fit to the data from all study sites in ***A–C*** with ≤200-m longitudinal distance between the calibration cross section and the acoustic-Doppler profiler (ADP) array. Colorado River data are segregated into in-sample and out-of-sample data in plots ***A–C***. ***B***, Predicted versus observed plot for $C_{XS\text{-}SAND}$. ***C***, Predicted versus observed plot for $D_{50\text{-}XS\text{-}SAND}$. Dashed green line is the best-fit log-linear regression fit to the data from only the CR30 study site (the study site with the largest range in EDI- or EWI-measured $D_{50\text{-}XS\text{-}SAND}$). ***D***, Predicted versus observed plot for $C_{XS\text{-}SAND}$ for the standard two-frequency *RUTS* method and the three-frequency *RUTS* method at the CR87 study site for the 132 measurements common to both methods. Solid blue line is the best-fit log-linear regression fit to the two-frequency data, dashed red line is the best-fit log-linear regression fit to the three-frequency data in ***D–E***. ***E***, Predicted versus observed plot for $D_{50\text{-}XS\text{-}SAND}$ for the standard two-frequency *RUTS* method and the three-frequency *RUTS* method at the CR87 study site for the 132 measurements common to both methods.

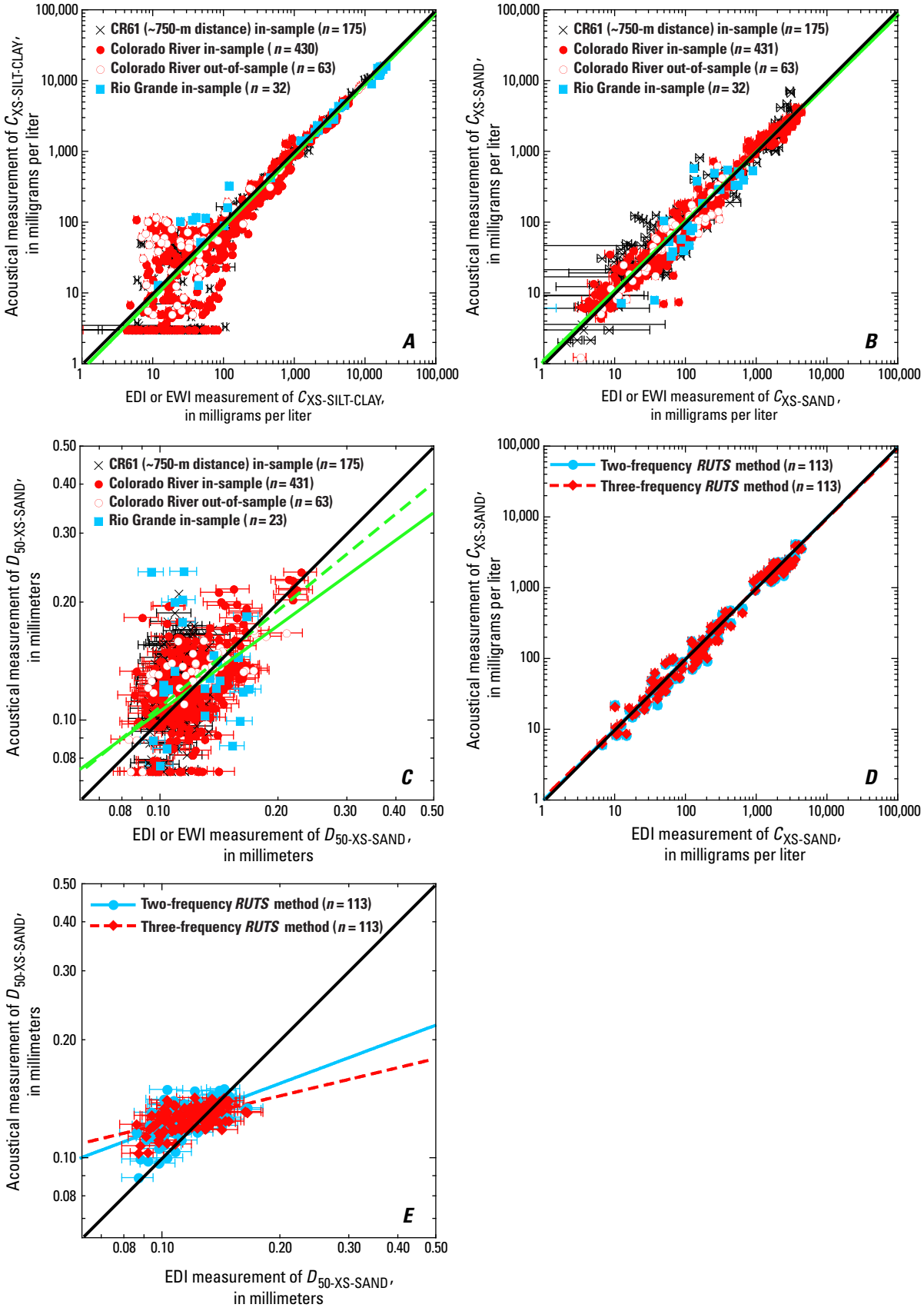
CR61 (~750-m distance) in-sample (n = 175)
Colorado River in-sample (n = 430)
Colorado River out-of-sample (n = 63)
Rio Grande in-sample (n = 32)
Acoustical measurement of $C_{XS\text{-}SILT\text{-}CLAY}$, in milligrams per liter
EDI or EWI measurement of $C_{XS\text{-}SILT\text{-}CLAY}$, in milligrams per liter
A
CR61 (~750-m distance) in-sample (n = 175)
Colorado River in-sample (n = 431)
Colorado River out-of-sample (n = 63)
Rio Grande in-sample (n = 32)
Acoustical measurement of $C_{XS\text{-}SAND}$, in milligrams per liter
EDI or EWI measurement of $C_{XS\text{-}SAND}$, in milligrams per liter
B
CR61 (~750-m distance) in-sample (n = 175)
Colorado River in-sample (n = 431)
Colorado River out-of-sample (n = 63)
Rio Grande in-sample (n = 23)
Acoustical measurement of $D_{50\text{-}XS\text{-}SAND}$, in millimeters
EDI or EWI measurement of $D_{50\text{-}XS\text{-}SAND}$, in millimeters
C
Two-frequency RUTS method (n = 113)
Three-frequency RUTS method (n = 113)
Acoustical measurement of $C_{XS\text{-}SAND}$, in milligrams per liter
EDI measurement of $C_{XS\text{-}SAND}$, in milligrams per liter
D
Two-frequency RUTS method (n = 113)
Three-frequency RUTS method (n = 113)
Acoustical measurement of $D_{50\text{-}XS\text{-}SAND}$, in millimeters
EDI measurement of $D_{50\text{-}XS\text{-}SAND}$, in millimeters
E

Figure 18.

Introduction to the Analyses of Bias and Error

Measurements of suspended-sediment concentration, by whatever means, are often used to quantify sediment loads and sediment budgets for rivers and estuaries (for example, Topping and others 2000a, 2010; Wright and Schoellhamer, 2005; Grams and others 2013; Shellenbarger and others 2013). Suspended-sediment flux through a cross section (that is, sediment load) is the product of measurements of water discharge and suspended-sediment concentration, and the difference in flux between the upstream and downstream cross sections bounding a river reach forms the basis for the sediment budget for that reach. Suspended-sediment fluxes through the cross sections bounding a river reach are typically much larger than the changes in sediment storage in that reach (especially over years to decades). Therefore, a sediment-budget calculation often involves computing relatively small differences in flux (the change in sediment storage) between two relatively large numbers (the flux at the upstream and downstream sites). Thus, knowing the amount of bias and error in sediment-flux calculations at individual river cross sections is critical for evaluating sediment-budget uncertainty.

Several processes contribute to the overall bias and (or) time-varying error in acoustical suspended-sediment measurements made using side-looking ADPs. On the basis of the work presented in the previous sections of this report, two of the largest sources of bias and time-varying error are likely: (1) the contribution of silt- and clay-sized sediment to backscatter, and (2) changes in the grain-size distribution of suspended sand. In addition, bias and time-varying error arises from the fact that side-looking ADPs collect data in only a part of a river cross section, and that embedded within the ADP-calibration process is the requirement of a stable relation between the concentration and grain-size distribution in this ensonified part of the cross section and the concentration and grain-size distribution in the entire river cross section. Topping and others (2011) showed that such relations are not necessarily unique and observed that, at some of the same sites used in this study, cross-stream spatial structures in both suspended-silt-and-clay concentration and suspended-sand concentration could persist in a river cross section for many hours before evolving into other spatial structures that would then persist for many additional hours. Because this process of change in the lateral distribution of suspended sediment was observed to occur at essentially constant discharge, this process produces short-term shifts in calibration relations that are not correlated with water discharge, and therefore cannot be corrected using the methods described in appendix 6. Given the length of time that such structures can persist and their effect on suspended-sediment concentrations and grain-size distributions in the ensonified part of the cross section, the time-varying errors in acoustical suspended sediment measurements made using side-looking ADPs can be autocorrelated. Moreover, these changes in the spatial structure of concentration and grain size are increasingly important in cases where the longitudinal distance between the ADP array and the calibration cross section is large.

In the remaining sections of this report, we evaluate the biases and errors associated with the single- and two-frequency acoustical methods developed above with respect to these three processes, that is, silt-and-clay contributions to backscatter, changes in sand grain size, and temporal variability in the spatial structure of concentration and grain size in the cross section. In addition, we compare the biases associated with suspended-sand concentrations measured using the two-frequency *RUTS* method with suspended-sand concentrations estimated using simpler single-frequency methods, including those that do not take into account the backscatter from silt and clay.

Error Analysis

To quantify biases and time-varying errors in the ADP-calibration methods, analyses were conducted to:

(1) compare in- and out-of-sample relative errors;

(2) compare the relative bias in $C_{\text{XS-SAND}}$ calculated by the two-frequency *RUTS* method to the relative biases in single-frequency estimates of $C_{\text{XS-SAND}}$, with and without inclusion of the effects of silt and clay on backscatter;

(3) detect any dependence on concentration or grain size of the relative errors in the two-frequency acoustical measurements of $C_{\text{XS-SILT-CLAY}}$, $C_{\text{XS-SAND}}$, and $D_{\text{50-XS-SAND}}$;

(4) remove the errors associated with EDI or EWI measurements (combined field and laboratory) to thereby calculate the "true" errors associated with only the acoustical measurements; and

(5) address the likely importance of changes in sediment-concentration relations between the ensonified part and the entire cross section (that is, spatial structure error).

Because the errors associated with EDI and EWI measurements are much smaller than those associated with calibrated-pump measurements, the errors associated with acoustical suspended-sediment measurements were calculated using only EDI and EWI measurements. In these analyses, the relative error, given in percent, in each acoustical measurement of concentration or D_{50} is therefore defined as

$$\text{relative error} = 100\frac{(a-b)}{b} \tag{67}$$

where

a is the acoustical measurement, and
b is the paired EDI or EWI measurement.

Because it neglects the fact that the EDI or EWI measurements are not without error (Topping and others, 2011), the error

calculated by equation 67 is referred to as an apparent error that is slightly larger than the true error associated with the acoustical method only.

As used in this report, the terms "error" or "absolute error" have magnitude and sign, and are reported in units of concentration or grain size. In this usage, the "absolute error" is not equivalent to the "absolute value of the error" because absolute error can be positive or negative. The term "relative error" has relative magnitude and sign, and is reported in units of percent (as in equation 67). The central tendency of the distribution of relative error is referred to as the relative bias. If the distribution of relative error is symmetric, the best measure of the central tendency is the mean value; if the distribution of relative error is skewed (which may be the case, as described in the next section), the best measure of the central tendency is the median value. If the distribution of relative error in either concentration or grain size varies as a function of either concentration or grain size (for example, larger error at lower concentration), then the relative bias could vary with concentration or grain size, as well. The part of the relative error that varies over time about the relative bias is referred to as the time-varying relative error. The time-varying error is the relative error minus the relative bias. Thus, for an unbiased measurement, which would have a relative bias of zero, the relative error calculated by equation 67 is the time-varying relative error associated with that individual measurement. If a distribution of relative error can be approximated as normally distributed about the relative bias, then the 68-percent-confidence-level time-varying relative error associated with an individual measurement is, by definition, the standard deviation of the distribution of the relative error. By extension, the 95-percent-confidence-level time-varying relative error is then, by definition, 1.96 times the standard deviation of the distribution of relative error. These time-varying relative errors may or may not be random. If a time-varying relative error is random, then it will decay to zero as a function of $1/\sqrt{n}$, where n is the number of observations. However, if a time-varying error is positively autocorrelated, then it will decay at a slower rate.

Comparison of In-Sample and Out-of-Sample Relative Errors

For any instrument that requires field calibration, out-of-sample errors tend to be greater than in-sample errors because the range of conditions included in a calibration dataset is typically not as broad as the full range of conditions that occurs in nature. In this section, analyses are conducted to determine whether significant differences exist between the in- and out-of-sample relative errors in the two-frequency acoustical measurements of $C_{\text{XS-SILT-CLAY}}$, $C_{\text{XS-SAND}}$, and $D_{\text{50-XS-SAND}}$. Then, for any case where a significant difference between the in- and out-of-sample errors is detected, a second analysis is conducted to estimate the relative magnitude of the difference between these errors. For these analyses to be meaningful, relatively large numbers of concurrent acoustical measurements and EDI or EWI measurements must be present in both the (in-sample) calibration and (out-of-sample) calibration-verification periods at a study site. Unfortunately, the only longer-term study site that met this criterion was the CR87 study site. Data from the other longer-term study sites (that is, CR30, CR61, and CR225) could not be segregated into in-sample and out-of-sample data with sufficient numbers of observations in each category for several reasons. First, repairs and (or) replacements of ADPs at two of these study sites (CR61 and CR225) required modifications to BBC relations. Second, large changes in the relations between the suspended-sand conditions in the ensonified part of the cross section and the suspended-sand conditions in the entire calibration cross section at two of these study sites (CR30 and CR61) also required modifications to BBC relations. Both of these reasons prevented data collection over time periods of sufficient duration to calculate meaningful out-of-sample errors for $C_{\text{XS-SAND}}$ or $D_{\text{50-XS-SAND}}$ at these study sites.

Distributions of relative error in suspended-sediment concentration and (or) grain size are typically not normal, and, in many cases, are right skewed. This right, or positive, skewness arises because distributions of relative error have a lower bound of –100 percent but have no upper bound (meaning >100 percent positive relative error is possible). Relative errors in acoustical measurements of $C_{\text{XS-SILT-CLAY}}$ and $C_{\text{XS-SAND}}$ calculated by equation 67 can never be less than –100 percent (because concentration is always positive), and relative errors in acoustical measurements of $D_{\text{50-XS-SAND}}$ calculated by equation 67 are additionally limited because acoustical measurements of $D_{\text{50-XS-SAND}}$ are never allowed to be smaller than 0.074 mm by the *RUTS* method. The better measure of the central tendency in such a skewed distribution is the median and not the mean. Thus, herein we typically use the median value to characterize the central value of distributions of relative error (relative bias). In addition, because distributions of error are typically not normal, a statistical test that does not assume normality is used to evaluate whether distributions of in-sample and out-of-sample relative error are significantly different; the test used is the Wilcoxon-Mann-Whitney test (Mann and Whitney, 1947).

At the CR87 study site, Wilcoxon-Mann-Whitney tests indicate that the in-sample and out-of-sample distributions of relative error in the acoustical measurements of $C_{\text{XS-SAND}}$ and $D_{\text{50-XS-SAND}}$ are not significantly different at the p_{SIG}=0.05 critical level, but that the in-sample and out-of-sample distributions of relative error in the acoustical measurements of $C_{\text{XS-SILT-CLAY}}$ are significantly different. The in- and out-of-sample relative error distributions for acoustically measured $C_{\text{XS-SAND}}$ and $D_{\text{50-XS-SAND}}$ are indistinguishable at the p_{SIG}=0.75 and 0.72 levels of significance, respectively. In contrast, for acoustically measured $C_{\text{XS-SILT-CLAY}}$, the in- and out-of-sample relative error distributions are significantly different at only the p_{SIG}=0.0022 level, with most of this difference occurring at $C_{\text{XS-SILT-CLAY}}$<50 mg/L. n is 159 in each of the in-sample relative-error datasets and n is 63 in each of the out-of-sample relative-error datasets.

Estimation of the magnitude of the statistically significant difference between the in- and out-of-sample relative errors in the acoustical measurements of $C_{XS\text{-}SILT\text{-}CLAY}$ is possible through comparison of these distributions of relative error. Both of these distributions are highly right-skewed (in-sample skewness=5.6, out-of-sample skewness=2.1) with large positive kurtosis (in-sample kurtosis=39.4, out-of-sample kurtosis=4.0). Thus, both of these distributions of relative error are not normal. In a Gaussian normal distribution of relative error with zero bias, the 68-percent-confidence-level relative error is equivalent to the standard deviation of that distribution. However, as these two distributions of relative error are not at all normal, the standard deviations of these distributions can only be taken as an index of error and not assigned a confidence level. Therefore, because the standard deviation of the out-of-sample relative errors in $C_{XS\text{-}SILT\text{-}CLAY}$ is ~32 percent larger than the standard deviation of the in-sample relative errors, and most of this difference occurs at lower $C_{XS\text{-}SILT\text{-}CLAY}$, it is likely that the 68-percent-confidence-level out-of-sample relative error is slightly larger than the 68-percent-confidence-level in-sample relative error. Unfortunately, it is impossible to generalize on the basis of this result from a single study site because the difference in magnitude between in-sample and out-of-sample relative errors at any given study site will depend on the breadth of the range of suspended-sediment conditions included in the development of the calibrations for the different-frequency ADPs. It is, however, likely prudent to generally assume that out-of-sample relative errors will be at least slightly larger than in-sample relative errors.

Because no statistically significant differences between the in- and out-of-sample relative errors in the acoustical measurements of $C_{XS\text{-}SAND}$ and $D_{50\text{-}XS\text{-}SAND}$ were detected at the CR87 study site, and the statistically significant difference between the in- and out-of-sample relative errors in the acoustical measurements of $C_{XS\text{-}SILT\text{-}CLAY}$ at this study site is relatively small (~32 percent), the below analyses of relative error proceed by combining the in- and out-of-sample error datasets into a single error dataset at each study site. One benefit in this approach is that the single datasets have greater numbers of observations than if in- and out-of-sample datasets were analyzed separately. The other benefit in this approach is that combining the relative error data from all of the study sites allows the development of generalized error relations.

Comparison of Relative Biases in Acoustical Measurements of Suspended-Sand Concentration Made Using Different Methods

To determine the effect on relative bias of using different acoustical methods, the median values of the relative errors in the acoustical measurements of $C_{XS\text{-}SAND}$ were compared at each study site using five methods: (1) the two-frequency *RUTS* method, (2) the 2-MHz single-frequency method neglecting B' (that is, neglecting the backscatter from silt and clay), (3) the 2-MHz single-frequency method including B', (4) the 1-MHz single-frequency method neglecting B', and (5) the 1-MHz single-frequency method including B'. For simplicity, all data at each study site were combined in this analysis and the effects of any dependencies of relative bias on either $C_{XS\text{-}SAND}$ or $D_{50\text{-}XS\text{-}SAND}$ were excluded. Thus, the method associated with the lowest absolute value of the median relative error in this analysis may not ultimately be the most accurate method because the relative error could vary as a function of $C_{XS\text{-}SAND}$ or $D_{50\text{-}XS\text{-}SAND}$. This issue is addressed below.

When any dependencies of relative error on concentration or $D_{50\text{-}XS\text{-}SAND}$ are excluded, the methods that are generally associated with the least relative bias are the two-frequency *RUTS* method, and the 2- and 1-MHz single-frequency methods including B' (table 2). As shown in table 2, the method that is subject to the greatest relative bias is the 1-MHz single-frequency method neglecting B'. We recommend that this method never be used unless it can be definitively established that silt-and-clay does not contribute to backscatter at the site of interest. In order of decreasing absolute value, the average relative bias from the Colorado River and Rio Grande study sites (EDI and EWI cases only) depicted in table 2 are: the 1-MHz single-frequency method neglecting B' (+112.8 percent bias), the 2-MHz single-frequency method neglecting B' (+69.9 percent bias), the 2-MHz single-frequency method including B' (–10.6 percent bias), the 1-MHz single-frequency method including B' (+9.6 percent bias), and the two-frequency *RUTS* method (–3.4 percent bias). Among only the Colorado River study sites (which have many more observations than the Rio Grande study sites), the rankings for the EDI and EWI cases are identical (but with smaller absolute values of average relative bias): the 1-MHz single-frequency method neglecting B' (+13.4 percent bias), the 2-MHz single-frequency method neglecting B' (+6.1 percent bias), the 2-MHz single-frequency method including B' (–2.7 percent bias), the 1-MHz single-frequency method including B' (1.2 percent bias), and the two-frequency *RUTS* method (+1.0 percent bias).

Inclusion of the effect of the backscatter from silt and clay results in substantial reductions in the relative errors in the single-frequency acoustical estimates of $C_{XS\text{-}SAND}$ at all study sites on the Colorado River and Rio Grande. As expected on the basis of theory, this reduction in error is greatest for the cases with the largest positive relative errors in the single-frequency acoustical estimate of $C_{XS\text{-}SAND}$. For example, among the 99 paired acoustical and calibrated-pump measurements at the RG-RGV study site, the maximum relative error in the acoustical measurements of $C_{XS\text{-}SAND}$ when using the 1-MHz single-frequency method neglecting B' is +66,600 percent, which decreases to +364 percent upon inclusion of the effects of B'. Furthermore, among the 173 paired acoustical and EWI measurements at the CR30 study site, the maximum relative error in the

Table 2. Effect of using different acoustical methods on the relative bias in acoustical measurements of $C_{XS\text{-}SAND}$.

Study site and physical measurement type	*n*	Range in $D_{50\text{-}XS\text{-}SAND}$ (in mm)	Median relative error, that is, relative bias, in acoustical measurements of $C_{XS\text{-}SAND}$ (in percent)				
			2-frequency *RUTS* method	2-MHz frequency		1-MHz frequency	
				B' neglected	B' included	B' neglected	B' included
CR30 EWI	173	0.09–0.23	–5.1	8.3	–3.0	30.7	11.5
CR61 EWI	175	0.09–0.14	6.5	7.1	–1.1	2.8	–7.7
CR87 EDI	222	0.08–0.21	1.3	0.0	–5.8	6.8	–0.8
CR225 EDI	99	0.09–0.15	1.1	9.1	–1.0	13.1	1.7
RG-CAS EWI	25	0.07–0.17	–9.3	251.5	–9.3	469.4	35.6
RG-CAS pump	243	0.07–0.21	–4.5	138.9	1.8	347.8	–4.2
RG-RGV EWI	7	0.10–0.14	–14.7	143.5	8.6	153.8	17.0
RG-RGV pump	99	0.08–0.18	–67.1	644.0	–59.5	1,703.4	–17.4
Average values among all six EDI and EWI cases			–3.4	69.9	–10.6	112.8	9.6
Average values among only the EDI and EWI cases at the Colorado River study sites			1.0	6.1	–2.7	13.4	1.2

acoustical measurements of $C_{XS\text{-}SAND}$ when using the 2-MHz single-frequency method neglecting B' is +427 percent, which decreases to +157 percent upon inclusion of the effects of B'. These large reductions in the relative errors on the right tail of the error distribution are so great that they also generally cause reductions in the central tendencies of the distributions of relative error; that is, they generally cause reductions in the relative bias. In most of the cases depicted in table 2, at both the 2-MHz and 1-MHz frequencies, inclusion of the effect of the backscatter from silt and clay results in a substantial reduction in relative bias. Although the reduction in relative bias is greater at the two Rio Grande study sites, where the average value of S (that is, the ratio of suspended-silt-and-clay concentration to suspended-sand concentration) is much greater than at the four Colorado River study sites, inclusion of the effect of the backscatter from silt and clay typically causes reductions in the relative biases at the Colorado River study sites as well. Thus, it may be necessary, in general, to account for the contribution of silt and clay to backscatter when using side-looking ADPs to measure suspended-sand concentrations. At minimum, the contribution of silt and clay to backscatter must be evaluated at a given site before a particular acoustical method can be selected.

Additional analyses were conducted to determine whether the relative biases reported in table 2 were constant or varied as a function of $D_{50\text{-}XS\text{-}SAND}$. In these analyses, the effects of B' were included in all single-frequency measurements of $C_{XS\text{-}SAND}$. At the two study sites with the largest ranges in $D_{50\text{-}XS\text{-}SAND}$, the CR30 and CR87 study sites, only the two-frequency *RUTS* method was found to produce measurements of $C_{XS\text{-}SAND}$ that were unbiased as a function of changing $D_{50\text{-}XS\text{-}SAND}$ (fig. 19). Both the 1- and 2-MHz single-frequency methods resulted in relative errors in the acoustical measurements of $C_{XS\text{-}SAND}$ that were significantly and positively correlated with $D_{50\text{-}XS\text{-}SAND}$. The best-fit linear regressions fit to the relative errors depicted in figure 19 approximate the behavior of the relative bias in the acoustical measurements of $C_{XS\text{-}SAND}$ as a function of $D_{50\text{-}XS\text{-}SAND}$. At both the CR30 and CR87 study sites, the relative bias in 1-MHz single-frequency measurements of $C_{XS\text{-}SAND}$ varied much more strongly as a function of $D_{50\text{-}XS\text{-}SAND}$ than did the relative bias in 2-MHz single-frequency measurements of $C_{XS\text{-}SAND}$. These results are expected on the basis of the theory and analyses presented in the "Theoretical Framework" section above; that is, the higher frequency instrument is less sensitive to grain-size effects.

Similar analyses conducted at the other study sites with much smaller ranges in $D_{50\text{-}XS\text{-}SAND}$ found little dependence of bias in the acoustical measurements of $C_{XS\text{-}SAND}$, regardless of whether the 2-frequency *RUTS* method or the 1- or 2-MHz single-frequency methods were used. Thus, because the relative biases in acoustical measurements of $C_{XS\text{-}SAND}$ reported in table 2 are similar for the two-frequency *RUTS* method and 2-MHz single-frequency method including B', either of these methods can likely be used to produce acoustical measurements of $C_{XS\text{-}SAND}$ with acceptably low levels of bias if the range in $D_{50\text{-}XS\text{-}SAND}$ is known independently beforehand at a given study site to be small (that is, approximately $\leq 0.5\phi$). However, if the range in $D_{50\text{-}XS\text{-}SAND}$ at a given study site is relatively large (that is, approximately $\geq 1\phi$), two acoustic frequencies are likely required to produce acoustical measurements of $C_{XS\text{-}SAND}$ that are not biased by changes in $D_{50\text{-}XS\text{-}SAND}$.

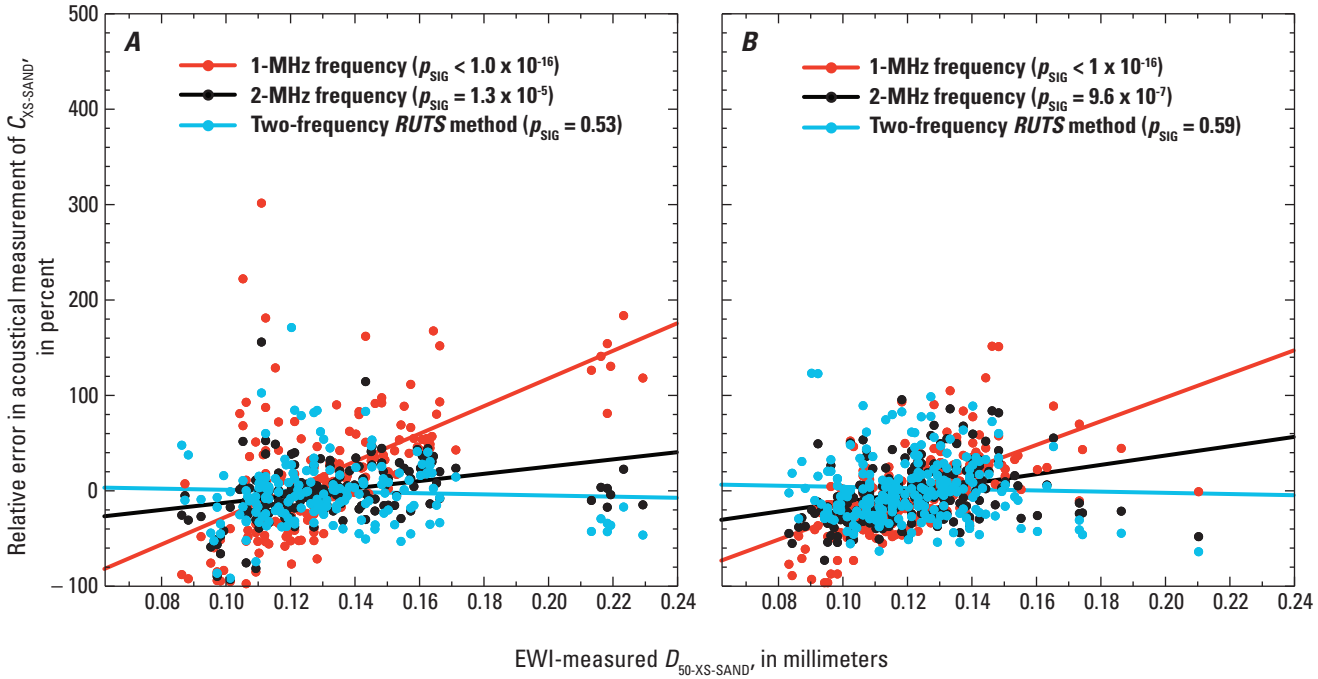

Figure 19. Relative errors in single-frequency and two-frequency acoustical measurements of $C_{XS-SAND}$ at the (***A***) CR30 and (***B***) CR87 study sites plotted as a function of $D_{50-XS-SAND}$. F-tests conducted on the least-squares linear regressions fit to these relative errors indicate significant positive correlations (at the p_{SIG}=0.05 critical level) between $D_{50-XS-SAND}$ and error for both the 1- and 2-MHz single-frequency measurements of $C_{XS-SAND}$, but no significant correlation between $D_{50-XS-SAND}$ and error for the two-frequency measurements. At both study sites, the significant relation between $D_{50-XS-SAND}$ and error is much steeper at the 1-MHz frequency than at the 2-MHz frequency. These results indicate the presence of grain-size-driven bias in the single-frequency measurements of $C_{XS-SAND}$ that is larger at the lower frequency, as expected on the basis of the theoretical behavior of the *RUTS* depicted in figures 9 and 10.

The choice of one versus two-frequency ADP deployments for measuring $C_{XS-SAND}$ depends on site-specific sand grain-size information, as well as the acceptable levels of bias for a given study. Analyses of the suspended-sand grain-size distributions in the database of 22 rivers (from all parts of the United States) assembled by Wright and others (2010) indicate that 36 percent of the rivers (n=8) fall within the $-1\sigma_G$ to $+1\sigma_G$ range in $D_{50-XS-SAND}$ between 0.5ϕ and 1ϕ, where it is unclear if one or two acoustic frequencies are required to produce unbiased acoustical measurements of $C_{XS-SAND}$; 32 percent (n=7) of the rivers had ranges in $D_{50-XS-SAND}$<0.5ϕ; and 32 percent (n=7) of the rivers had ranges in $D_{50-XS-SAND}$ exceeding 1ϕ. These results suggest that, for the majority of rivers, single-frequency ADP deployments will be subject to some level of bias in measurements of $C_{XS-SAND}$ owing to changes in the suspended-sand grain-size distribution. Because the average relative biases reported at the bottom of table 2 for the 2-frequency *RUTS* method, and the 2-MHz single-frequency method that includes B' are much smaller than the absolute values of the relative errors analyzed in the next section of this report, both of these methods do provide relatively unbiased acoustical measurements of $C_{XS-SAND}$ so long as the range in $D_{50-XS-SAND}$ is small. In cases where the range in $D_{50-XS-SAND}$ is not small or not known independently beforehand, two acoustic frequencies are required for unbiased acoustical measurements of $C_{XS-SAND}$.

Dependence of Relative Errors in Acoustical Measurements of Concentration and Median Grain Size on Either Concentration or Grain Size

Analyses were conducted to determine whether the errors in the two-frequency acoustical measurements are independent of changes in concentration or $D_{50-XS-SAND}$. These analyses consisted of conducting F-tests on least-squares linear regressions relating $C_{XS-SILT-CLAY}$, $C_{XS-SAND}$, and $D_{50-XS-SAND}$ to the relative errors in the acoustical measurements of these quantities to determine whether significant trends were present in the relative errors as a function of either concentration or grain size. The results from these analyses should be taken as somewhat approximate because most of the analyzed data are heteroscedastic, with much greater variance owing to larger right skewness in the lower part of the domain in either concentration or grain size, especially in the case of the relative errors in the acoustical measurements of $C_{XS-SILT-CLAY}$

(as discussed above, in the "Results" section). F-tests were first conducted to determine whether the relative errors in the acoustical measurements of $C_{XS\text{-}SILT\text{-}CLAY}$ significantly depend on the physically measured $C_{XS\text{-}SILT\text{-}CLAY}$. F-tests were then conducted to determine whether the relative errors in the acoustical measurements of $C_{XS\text{-}SAND}$ and $D_{50\text{-}XS\text{-}SAND}$ significantly depend on either the physically measured $C_{XS\text{-}SAND}$ or $D_{50\text{-}XS\text{-}SAND}$. Detection of a significant trend by these analyses would indicate that the central tendency of the distribution of relative error in the acoustical measurements varies systematically over the domain in concentration or grain size. Because the central tendency of the distribution of relative error is the relative bias, the presence of significant trends thus indicate the presence of a bias in the acoustical measurements driven by either changes in concentration or grain size. Results from these F-tests are reported in table 3.

In general, the results from the F-tests summarized in table 3 indicate that the central tendencies of the distributions of relative error in the acoustical measurements of $C_{XS\text{-}SILT\text{-}CLAY}$ and $C_{XS\text{-}SAND}$ do not significantly depend on concentration or grain size, and the distributions of relative error in the acoustical measurements of $D_{50\text{-}XS\text{-}SAND}$ do not significantly depend on concentration. These results therefore indicate that changes in $C_{XS\text{-}SILT\text{-}CLAY}$ do not cause a concentration-driven relative bias in the acoustical measurements of $C_{XS\text{-}SILT\text{-}CLAY}$, and that changes in $C_{XS\text{-}SAND}$ do not cause a concentration-driven relative bias in the acoustical measurements of $C_{XS\text{-}SAND}$. Furthermore, these results indicate that changes in $D_{50\text{-}XS\text{-}SAND}$ do not generally cause a grain-size-driven relative bias in the acoustical measurements of $C_{XS\text{-}SAND}$, and that changes in $C_{XS\text{-}SAND}$ do not generally cause a concentration-driven relative bias in the acoustical measurements of $D_{50\text{-}XS\text{-}SAND}$ made using the two-frequency *RUTS* method.

The results in table 3 do not indicate, however, that the distributions of relative error in the acoustical measurements of $C_{XS\text{-}SILT\text{-}CLAY}$ and $C_{XS\text{-}SAND}$ do not vary systematically as a function of concentration. As shown in figure 20, the distributions of relative error in the acoustical measurements of both $C_{XS\text{-}SILT\text{-}CLAY}$ and $C_{XS\text{-}SAND}$ are highly heteroscedastic, with much larger variance and right skewness in the lower parts of the domains in $C_{XS\text{-}SILT\text{-}CLAY}$ and $C_{XS\text{-}SAND}$. Only as $C_{XS\text{-}SILT\text{-}CLAY}$ exceeds ~40 mg/L and $C_{XS\text{-}SAND}$ exceeds ~15 mg/L is the right skewness reduced such that the distributions of relative error in the acoustical measurements in $C_{XS\text{-}SILT\text{-}CLAY}$ and $C_{XS\text{-}SAND}$ become approximately symmetric about zero. Thus, owing to the large right skewness at lower concentrations, the acoustical measurements of $C_{XS\text{-}SILT\text{-}CLAY}$ are only unbiased when $C_{XS\text{-}SILT\text{-}CLAY}$>~40 mg/L and two frequency *RUTS* measurements of $C_{XS\text{-}SAND}$ are only unbiased when $C_{XS\text{-}SAND}$>~15 mg/L. Because the variance (and

Table 3. Levels of significance (p_{SIG}) associated with F-tests conducted to determine whether relative errors in the acoustical suspended-sediment measurements depend significantly on concentration or sand median grain size ($D_{50\text{-}XS\text{-}SAND}$).

[Dependencies that are significant at the p_{SIG}=0.05 critical level are indicated in bold type; the positive or negative trend of each significant relation is indicated in parentheses. The number of observations, *n*, associated with each p_{SIG} value is indicated in parentheses. There are fewer observations associated with $D_{50\text{-}XS\text{-}SAND}$ at the RG-CAS and RG-RGV study sites because some suspended-sediment samples had insufficient sand mass for laboratory grain-size analysis. EWI, equal-width increment; EDI, equal-discharge increment; $C_{XS\text{-}SAND}$, velocity-weighted suspended-sand concentration in river cross section]

Study site and physical measurement type	p_{SIG} value associated with…				
	Dependence of relative error in acoustical $C_{XS\text{-}SILT\text{-}CLAY}$ on physical $C_{XS\text{-}SILT\text{-}CLAY}$	Dependence of relative error in acoustical $C_{XS\text{-}SAND}$ on physical $C_{XS\text{-}SAND}$	Dependence of relative error in acoustical $C_{XS\text{-}SAND}$ on physical $D_{50\text{-}XS\text{-}SAND}$	Dependence of relative error in acoustical $D_{50\text{-}XS\text{-}SAND}$ on physical $C_{XS\text{-}SAND}$	Dependence of relative error in acoustical $D_{50\text{-}XS\text{-}SAND}$ on physical $D_{50\text{-}XS\text{-}SAND}$
CR30 EWI	0.59 (*n*=172)	0.12 (*n*=173)	[1]0.53 (*n*=173)	**0.00054(–)** (*n*=173)	**0.018(–)** (*n*=173)
CR61 EWI	0.74 (*n*=175)	0.090 (*n*=175)	**1.5×10^{-7}(–)** (*n*=175)	0.31 (*n*=175)	0.23 (*n*=175)
CR87 EDI	0.063 (*n*=222)	0.12 (*n*=222)	[1]0.59 (*n*=222)	0.99 (*n*=222)	**$<1\times10^{-16}$(–)** (*n*=222)
CR225 EDI	0.41 (*n*=99)	0.13 (*n*=99)	0.52 (*n*=99)	0.75 (*n*=99)	**3.4×10^{-9}(–)** (*n*=99)
RG-CAS EWI	0.11 (*n*=25)	0.25 (*n*=25)	0.61 (*n*=17)	0.28 (*n*=17)	**0.0070(–)** (*n*=17)
RG-RGV EWI	0.21 (*n*=7)	0.42 (*n*=7)	0.39 (*n*=6)	0.12 (*n*=6)	0.89 (*n*=6)

[1]These analyses are depicted in figure 19.

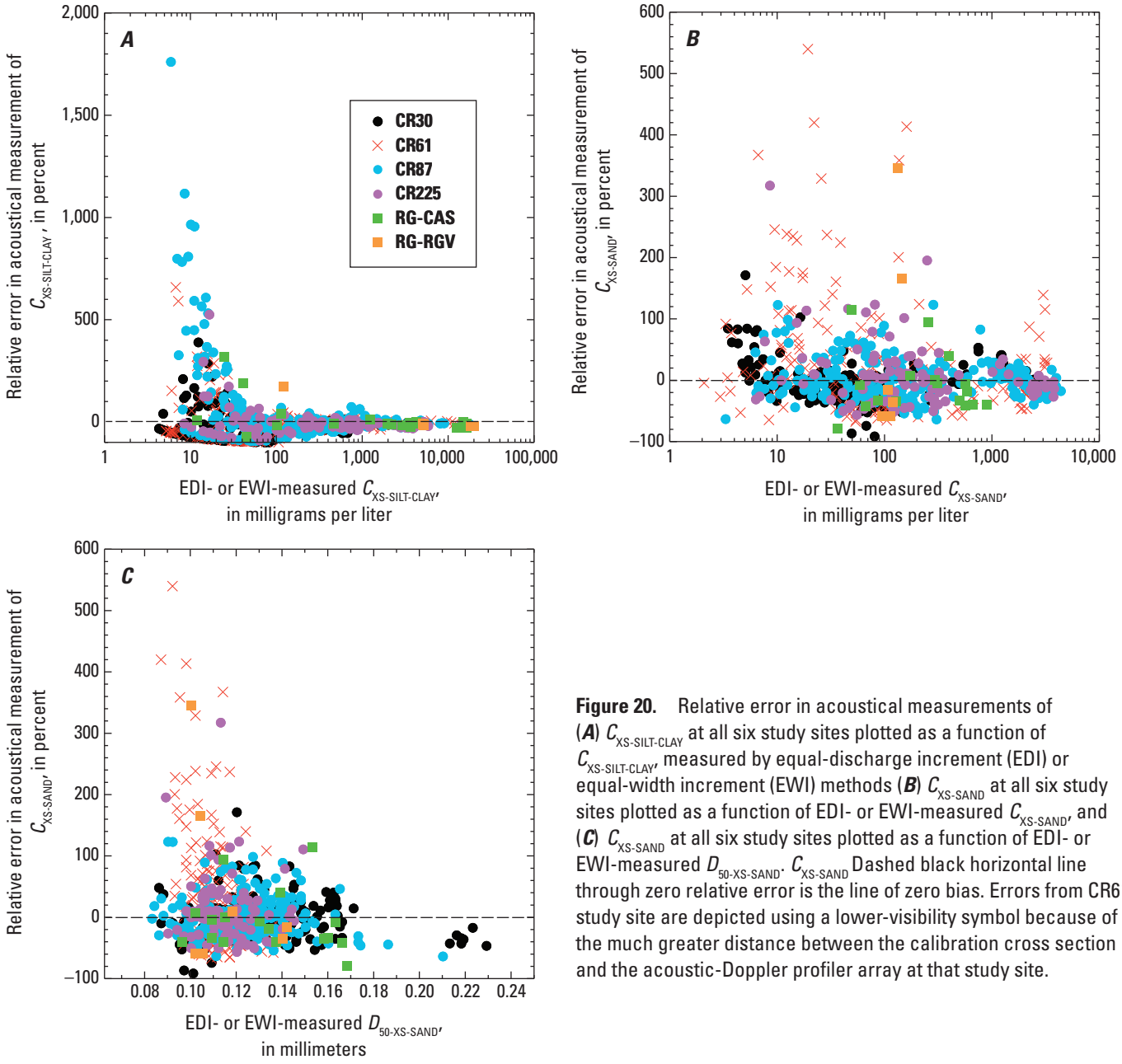

Figure 20. Relative error in acoustical measurements of (***A***) $C_{XS\text{-}SILT\text{-}CLAY}$ at all six study sites plotted as a function of $C_{XS\text{-}SILT\text{-}CLAY}$, measured by equal-discharge increment (EDI) or equal-width increment (EWI) methods (***B***) $C_{XS\text{-}SAND}$ at all six study sites plotted as a function of EDI- or EWI-measured $C_{XS\text{-}SAND}$, and (***C***) $C_{XS\text{-}SAND}$ at all six study sites plotted as a function of EDI- or EWI-measured $D_{50\text{-}XS\text{-}SAND}$. $C_{XS\text{-}SAND}$ Dashed black horizontal line through zero relative error is the line of zero bias. Errors from CR61 study site are depicted using a lower-visibility symbol because of the much greater distance between the calibration cross section and the acoustic-Doppler profiler array at that study site.

therefore the standard deviation) in both of these cases decreases with increasing concentration, these results indicate that the 68-percent- and 95-percent-confidence-level time-varying relative errors in the acoustical measurements of $C_{XS\text{-}SILT\text{-}CLAY}$ and $C_{XS\text{-}SAND}$ significantly decrease with increasing concentration. These negative correlations between concentration and the time-varying relative error in concentration likely arise from the process described by equation 11 in Thorne and Hanes (2002), where increases in suspended-sediment concentration result in a greater number of randomly distributed particles generating the acoustic return, thus reducing the error in the estimation of suspended-sediment concentration during a single acoustical measurement made over a fixed duration. The 68-percent- and 95-percent-confidence-level time-varying relative errors in the acoustical measurements of $C_{XS\text{-}SILT\text{-}CLAY}$ and $C_{XS\text{-}SAND}$ are estimated in the next section of this report.

In addition to the negative correlation between concentration and the variance in the distributions of relative error in the acoustical measurements of $C_{XS\text{-}SAND}$, the variance in the relative error in the acoustical measurements of $C_{XS\text{-}SAND}$ at the CR61 study site is generally larger across the entire domain than at the other study sites on the Colorado River and Rio Grande. This larger variance in relative error, and therefore larger time-varying relative error, likely arises from the fact that the longitudinal distance between the calibration

cross section and the ADP array is much greater at the CR61 study site than it is at any other study site. At the CR61 study site, the ADPs are located ~750 m upstream from the calibration cross section. This distance is much smaller at all of the other study sites, where it ranges from 0 to 200 m. Because of the large distance between the calibration cross section and the ADPs at the CR61 study site, there is a risk that, during some time periods, the suspended-sediment characteristics within the ensonified volume could be less correlated with those in the calibration cross section, thus leading to the much larger variance in the relative errors in the acoustical measurements of $C_{XS\text{-}SAND}$ at this study site.

Although the relative bias in the acoustical measurements of $D_{50\text{-}XS\text{-}SAND}$ does not generally depend on $C_{XS\text{-}SAND}$, in two-thirds of the cases summarized in table 3 it does depend on $D_{50\text{-}XS\text{-}SAND}$. In all cases where these dependencies exist, the correlation is negative, meaning that as the EDI- or EWI-measured values of $D_{50\text{-}XS\text{-}SAND}$ increase, the relative bias in the acoustical measurements of $D_{50\text{-}XS\text{-}SAND}$ becomes more negative (fig. 21*A*). In these cases, there is a tendency for the acoustical measurements of $D_{50\text{-}XS\text{-}SAND}$ to be slightly high at low values of the EDI or EWI-measured $D_{50\text{-}XS\text{-}SAND}$, and a tendency for the acoustical measurements of $D_{50\text{-}XS\text{-}SAND}$ to be slightly low at high values of the EDI or EWI-measured $D_{50\text{-}XS\text{-}SAND}$. When the acoustical measurements of $D_{50\text{-}XS\text{-}SAND}$ approach the value of $D_{50\text{-}XS\text{-}SAND\text{-}REF}$ used in the development of the BBC relations, the slight positive or negative bias in the acoustical measurements of $D_{50\text{-}XS\text{-}SAND}$ vanishes.

The negative correlation between $D_{50\text{-}XS\text{-}SAND}$ and the relative bias in the acoustical measurements of $D_{50\text{-}XS\text{-}SAND}$ is strongest at the RG-CAS, CR87, and CR225 study sites (in decreasing order of correlation strength). This negative correlation is extremely weak at the CR30 study site (R^2=0.032), and no significant correlation is present at the CR61 and RG-RGV study sites. A potential cause of this negative correlation could be the imposed lower bound on error. Because the acoustical measurements of $D_{50\text{-}XS\text{-}SAND}$ are never allowed to be smaller than 0.074 mm by the *RUTS* method, large negative relative errors in $D_{50\text{-}XS\text{-}SAND}$ are precluded at lower $D_{50\text{-}XS\text{-}SAND}$ values (fig. 21*A*). Because of this imposed lower bound, there is right skewness in the distribution of relative error at lower values of $D_{50\text{-}XS\text{-}SAND}$ such that there is a much greater likelihood that the relative errors in the acoustical measurements of $D_{50\text{-}XS\text{-}SAND}$ will be positive at lower values of the EDI- or EWI-measured $D_{50\text{-}XS\text{-}SAND}$. In any case, because the negative correlation is not always present,

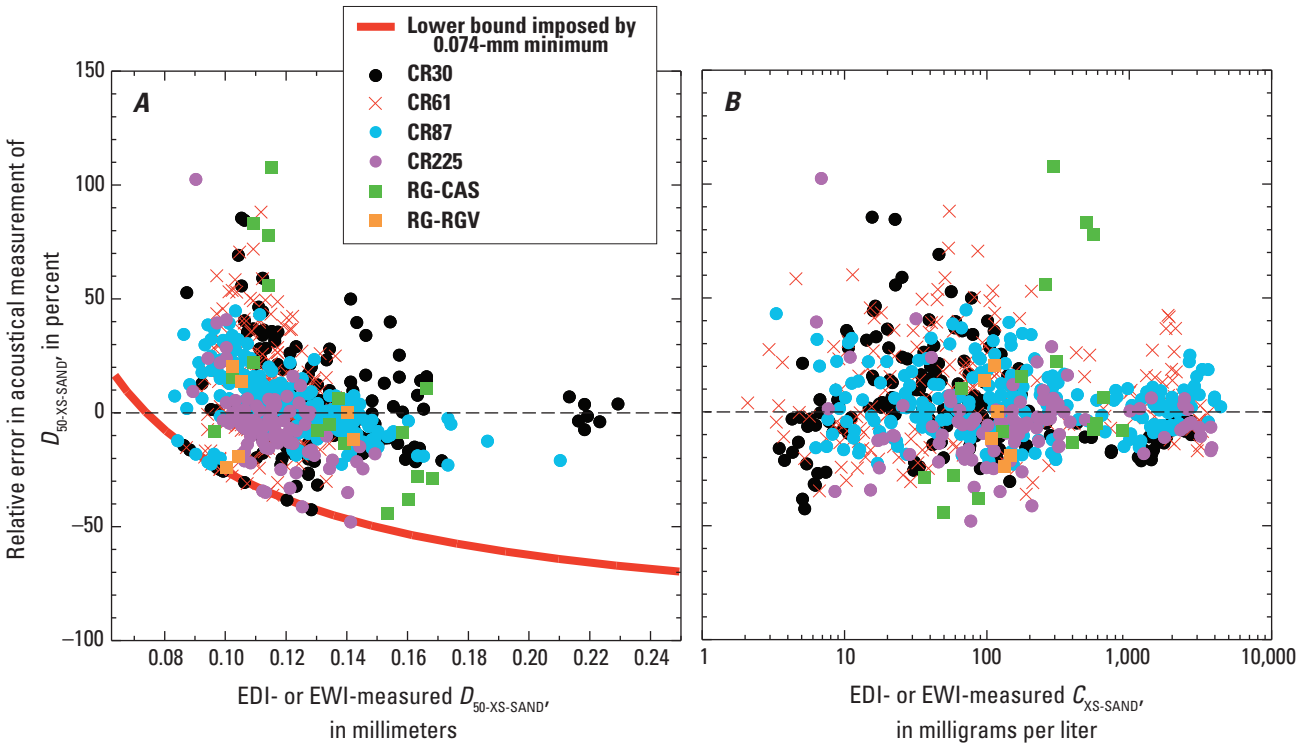

Figure 21. Relative error in acoustical measurements of $D_{50\text{-}XS\text{-}SAND}$ at all six study sites plotted as a function of (***A***) $D_{50\text{-}XS\text{-}SAND}$ measured by equal-discharge increment (EDI) or equal-width increment (EWI) methods, and (***B***) EDI- or EWI-measured $C_{XS\text{-}SAND}$. Dashed black horizontal line through zero relative error is the line of zero bias. Also shown in ***A*** is the lower bound on relative error in acoustical measurements of $D_{50\text{-}XS\text{-}SAND}$ imposed by the condition that acoustical measurements of $D_{50\text{-}XS\text{-}SAND}$ <0.074 mm are precluded. Errors from CR61 study site are depicted using a lower-visibility symbol because of the much greater distance between the calibration cross section and the acoustic-Doppler profiler array at that study site.

and when present, it tends to be relatively small, we make no attempt to remove it. Thus, its effects are included within the 68-percent- and 95-percent-confidence level time-varying relative errors in the acoustical measurements of $D_{50\text{-XS-SAND}}$ estimated in the next section of this report.

Unlike the high degree of heteroscedasticity in the distributions of relative error in the acoustical measurements of $C_{\text{XS-SILT-CLAY}}$ and $C_{\text{XS-SAND}}$ over their respective domains, the distribution of relative error in the acoustic measurements of $D_{50\text{-XS-SAND}}$ is almost homoscedastic over the domain in $C_{\text{XS-SAND}}$, especially when data from the CR61 study site are excluded (fig. 21*B*). Thus, in addition to the relative bias in the acoustical measurements of $D_{50\text{-XS-SAND}}$ not being correlated with $C_{\text{XS-SAND}}$, there is also minimal dependence of the time-varying relative errors in the acoustical measurements of $D_{50\text{-XS-SAND}}$ on $C_{\text{XS-SAND}}$. Furthermore, because the distribution of relative error in the acoustical measurements of $D_{50\text{-XS-SAND}}$ is approximately symmetric about zero when plotted as a function of $C_{\text{XS-SAND}}$, the acoustical measurements of $D_{50\text{-XS-SAND}}$ can be treated as relatively unbiased as a function of concentration. These results provide further justification for not including the sometimes-present, grain-size-correlated relative bias in the acoustical measurements of $D_{50\text{-XS-SAND}}$ within the estimations of the 68-percent- and 95-percent-confidence level time-varying relative errors in the next section of this report.

Estimation of the 68-Percent- and 95-Percent-Confidence-Level Time-Varying Relative Errors in Individual Acoustical Measurements

Data from the five study sites that have calibration cross sections within 200 m of the ADP arrays were used to estimate the generalized 68-percent- and 95-percent-confidence level true relative errors in the acoustical measurements of $C_{\text{XS-SILT-CLAY}}$, $C_{\text{XS-SAND}}$, and $D_{50\text{-XS-SAND}}$. In essence, this analysis was conducted to provide an estimate of the magnitude of the error bar associated with each acoustical measurement. The errors calculated in this analysis are referred to as true relative errors because field and laboratory-processing errors associated with the EDI or EWI measurements are accounted for. All other errors reported herein, referred to as apparent relative errors, were calculated with the assumption of zero error in the EDI or EWI measurements. This assumption is acceptable for the other analyses because errors in the EDI and EWI measurements are typically much smaller than those in the acoustical measurements. However, because error is present in the EDI and EWI measurements (for example, Topping and others, 2010, 2011), the error associated with the EDI or EWI measurements must be accounted for to yield true error in the acoustical measurements.

As described in the "Introduction to the Analyses of Bias and Error" section, time-varying errors in the acoustical measurements arise from two processes: (1) error in the acoustical measurements of the suspended sediment within the volume ensonified by the acoustic beams, and (2) error arising from slow variation in relations between the suspended sediment within just the ensonified part of the cross section and the suspended sediment in the entire cross section. The first source of error is likely random to the extent that biases in the acoustical measurements produced by changes in the suspended-sediment grain-size distribution are minimized by the *RUTS* method. The second source of error may either be random or non-random, as discussed in the next section of this report. The 200-m longitudinal-distance limit was chosen so that the generalized errors estimated in this section of the report would be based on the errors at only those study sites where the influence of the second part of the two-part error is minimized; that is, at study sites where the volume ensonified by the acoustic beams is located either within or, at least, near the calibration cross section. In the best-case scenario where the ADPs are located within the calibration cross section (for example, the CR30 and RG-RGV study sites), the volume ensonified by the acoustic beams is an actual subsample of the calibration cross section. In this case, the correlation between the suspended-sediment characteristics within just the ensonified volume and within the entire cross section should be the highest possible and vary the least over time. The study sites therefore chosen for inclusion in this analysis are the CR30 (0 m from calibration cross section), CR87 (200 m from calibration cross section), CR225 (130 m), RG-CAS (50 m), and RG-RGV (0 m) study sites.

For relative errors to be calculated using equation 67, the denominator, b, must be known. An inconvenient fact that needs to be addressed before proceeding, therefore, is that although relative error equations must include a dependence on $C_{\text{XS-SILT-CLAY}}$, $C_{\text{XS-SAND}}$, or $D_{50\text{-XS-SAND}}$, these parameters cannot be known independently before any acoustical measurement. The solution of this problem is that, because acoustical and EDI or EWI measurements of $C_{\text{XS-SILT-CLAY}}$, $C_{\text{XS-SAND}}$, and $D_{50\text{-XS-SAND}}$ are strongly correlated (for example, figure 18), equation 67 can be approximated for this analysis as

$$\text{proxy relative error} = 100\frac{(a-b)}{a}, \qquad (68)$$

where

a is the acoustical measurement, and
b is the EDI or EWI measurement.

In other words, to solve this problem, we have used the strong correlation between the physical and acoustical measurements to allow approximating the unknown b (the EDI or EWI measurement) in the denominator of equation 67 with the known a (the acoustical measurement) in the denominator of equation 68. Making this approximation allows relative errors to be calculated using equations fit to the data from the CR30, CR87, CR225, RG-CAS, and RG-RGV study sites. These equations allow estimation of relative errors on the basis of only the acoustical measurements, without requiring additional information.

In cases where measurements are unbiased and the proxy relative errors calculated by equation 68 comprise a Gaussian normal distribution, the 68-percent-confidence-level time-varying relative error will be equal to the absolute value of the standard deviation of the distribution of relative errors calculated by equation 68, and the 95-percent-confidence-level time-varying relative error will be equal to 1.96 times this quantity. In reality, because relative errors calculated by equation 67 tend to be right-skewed because of imposed lower bounds (described above), proxy relative errors calculated by equation 68 tend to be left-skewed. Because of the skewness (which tends to be more prevalent at lower values of concentration and $D_{50\text{-XS-SAND}}$), the Gaussian-normal approximation for calculating the 68-percent-confidence-level time-varying relative error is not quite accurate, but for the purposes of this analysis is used anyways. The ramifications of making this Gaussian-normal approximation will be described below.

The time-varying relative errors in the acoustical measurements, and their relation to concentration, were evaluated following a seven-step procedure:

(1) Proxy relative errors in the acoustical measurements of $C_{\text{XS-SILT-CLAY}}$ and $C_{\text{XS-SAND}}$ were calculated using equation 68 for the pooled data from the CR30, CR87, CR225, RG-CAS, and RG-RGV study sites.

(2) These relative errors were segregated into $C_{\text{XS-SILT-CLAY}}$ or $C_{\text{XS-SAND}}$ bins centered on 1-mg/L increments over the entire range of the acoustical measurements of $C_{\text{XS-SILT-CLAY}}$ or $C_{\text{XS-SAND}}$ associated with concurrent EDI or EWI measurements in the pooled dataset. The bounds on these bins were ±20 percent of the central concentration in each bin.

(3) In each bin where 20 or more observations were present, the sample standard deviation (σ) was calculated relative to an imposed mean of zero. Twenty observations was determined to be the minimum number needed to calculate a sample standard deviation that is a reasonably accurate approximation of the population standard deviation. For example, when n=20 and data are randomly selected from a Gaussian-normal distribution, the 95-percent confidence interval associated with the population standard deviation ranges from 0.76σ to 1.46σ (Sheskin, 2003).

(4) Power-law fits were applied relating either $C_{\text{XS-SILT-CLAY}}$ or $C_{\text{XS-SAND}}$ (as appropriate) to σ of the binned error distributions for the cases that satisfy the condition in step 3 (fig. 22).

(5) 68-percent-confidence-level true relative errors in the acoustical measurements of $C_{\text{XS-SILT-CLAY}}$ and $C_{\text{XS-SAND}}$ were estimated by subtracting out the EWI/EDI errors in quadrature using the following equation:

$$E_{68\text{-ABS}} = \sqrt{E^2_{\text{FIT-ABS}} - E^2_{(\text{EDI-EWI})68\text{-ABS}}}\ , \qquad (69)$$

where

$E_{68\text{-ABS}}$ is the absolute form (in mg/L) of the 68-percent-confidence level true error in the acoustical measurements of either $C_{\text{XS-SILT-CLAY}}$ and $C_{\text{XS-SAND}}$,

$E_{68\text{-FIT-ABS}}$ is the absolute form (in mg/L) of the power law fit to σ of the proxy relative error in step 4, and

$E_{(\text{EDI-EWI})68\text{-ABS}}$ is the absolute form (in mg/L) of the 68-percent-confidence-level combined field and laboratory-processing error in the concurrent EDI or EWI measurement (after Topping and others, 2010, 2011).

$E_{68\text{-ABS}}$ was then converted to the proxy relative form (E_{68}) by dividing by the acoustical measurement of $C_{\text{XS-SILT-CLAY}}$ or $C_{\text{XS-SAND}}$, as appropriate, and multiplying by 100 percent.

(6) 95-percent-confidence level true relative errors in the acoustical measurements of $C_{\text{XS-SILT-CLAY}}$ and $C_{\text{XS-SAND}}$ were estimated using a version of equation 69 in which all three 68-percent-confidence-level errors were replaced by 95-percent-confidence-level errors.

(7) Power-law fits relating $C_{\text{XS-SILT-CLAY}}$ or $C_{\text{XS-SAND}}$ (as appropriate) to E_{68} and E_{95} were then calculated to result in estimations of the true time-varying relative errors in the acoustical measurements that can be calculated on the basis of the acoustical measurements of either $C_{\text{XS-SILT-CLAY}}$ or $C_{\text{XS-SAND}}$ (fig. 22). As a result of the binning and filtering processes in steps 2 through 6, the R^2 values associated with these power-law fits are exceptionally high.

Because the 68-percent- and 95-percent-confidence-level relative errors in the acoustical measurements of $D_{50\text{-XS-SAND}}$ are invariant as a function of $D_{50\text{-XS-SAND}}$, a simpler version of the above 7-step process was used to estimate the true time-varying relative errors in the acoustical measurements of $D_{50\text{-XS-SAND}}$. In this simpler process, steps 1–3 in the above procedure were combined into one step where σ was calculated on the basis of all proxy relative errors in the pooled dataset (instead of binning the errors), step 4 in the above procedure was not needed, and steps 5–7 were followed as described above.

As shown in figure 22, at low concentrations, true time-varying relative errors in individual acoustical measurements of $C_{\text{XS-SILT-CLAY}}$ and $C_{\text{XS-SAND}}$ are extremely large, whereas at high concentrations, the errors in the acoustical measurements of $C_{\text{XS-SILT-CLAY}}$ and $C_{\text{XS-SAND}}$ are similar to those associated with EDI and EWI measurements. The true errors in the acoustical measurements of $D_{50\text{-XS-SAND}}$ are roughly

2 to 3 times larger than those associated with EDI and EWI measurements. Even though the 68-percent- and 95-percent-confidence-level errors in the acoustical measurements plotted in figure 22 may seem large, it is important to note that these errors are associated with single acoustical measurements of $C_{\text{XS-SILT-CLAY}}$, $C_{\text{XS-SAND}}$, or $D_{\text{50-XS-SAND}}$, just as the errors associated with the EDI and EWI measurements are the errors associated with single EDI or EWI measurements. If these time-varying errors are random (investigated in the next section of this report), they will decay as a function of $1/\sqrt{n}$, where n is the number of acoustical measurements. Thus, the random error in a quantity measured at 15-minute intervals can effectively decrease tenfold over the course of one day such that, under approximately constant sediment conditions, a ±100-percent random error will decay to roughly a ±10-percent error in the daily average after 96 measurements at 15-minute intervals have been made.

Skewness in the distributions of relative error arising from the imposed lower bounds produces two important effects in the results plotted in figure 22. First, the true proxy errors based on a normal distribution plotted in figure 22 are slight overestimates of the error on one tail of the distribution, but slight underestimates of the error on the other tail of the distribution. This result is acceptable because one does not know independently whether the time-varying error associated with any individual acoustical measurement of $C_{\text{XS-SILT-CLAY}}$, $C_{\text{XS-SAND}}$, or $D_{\text{50-XS-SAND}}$ is positive or negative. Second, if the distribution of relative error in concentration were truly a normal distribution with no imposed bounds, relative errors exceeding ±100 percent would be impossible because the distribution would be symmetric, and it is impossible to have errors less than –100 percent. Because the skewness is largest at the lowest concentrations, 68-percent- and 95-percent-confidence-level relative errors exceeding ±100 percent are predicted at low concentrations (fig. 22*A–D*). When errors exceeding ±100 percent are predicted, the largest negative error allowed is capped at –100 percent. The lower bound on the negative errors in the acoustical measurements of $D_{\text{50-XS-SAND}}$ arising from the imposed constraint of $D_{\text{50-XS-SAND}} \geq 0.074$ mm has a more complicated influence on the allowed range of negative errors, which is best described graphically (see fig. 22*E–F*).

Importance of Errors from Slow Changes in the Spatial Structure of Suspended Sediment in the River Cross Section

Spatial structures in both suspended-sand and suspended-silt-and-clay concentration can evolve slowly over hours to days in a river cross section (Topping and others, 2011). At both the CR30 and CR61 study sites, the lateral distribution of suspended silt and clay and suspended sand were both observed by Topping and others (2011) to be stable for large fractions of a day before evolving into different lateral distributions that were then sometimes stable over similar timescales. These slow changes in the spatial structure of the suspended sediment were observed to occur at relatively constant discharge. On the basis of Rubin and others (2001), Topping and others (2011) interpreted this behavior to arise from relatively slow changes in the lateral distribution of suspendable bed sediment, which is, in turn, produced by the relatively slow downstream migration of irregular dunes within patches of sand on the gravel bed. It is also possible that these slow changes in the lateral distribution of suspended sediment were produced by the downstream migration of the patches of sand on the bed. The existence of such slow changes in the lateral distribution of suspended sediment in a river cross section indicates that $C_{\text{SILT-CLAY}}$ and C_{SAND} will likely not be constant within the ensonified part of the cross

Figure 22. (**folllowing page**) Six plots showing 68-percent- and 95-percent-confidence-level relative errors in individual acoustical suspended-sediment measurements and in individual equal-discharge increment (EDI) or equal-width increment (EWI) measurements plotted as a function of the acoustical suspended-sediment measurements. These errors can have positive or negative sign. E_{68} is the power-law relation of step 7 (of the analysis of time-varying relative errors, described above in text) that is fit to the calculated 68-percent-confidence-level true proxy relative errors in the acoustical measurements; E_{95} is the power-law relation fit, in step 7, to the calculated 95-percent-confidence-level true proxy relative errors in the acoustical measurements. As described in the text, the exceptionally high R^2 values associated with the E_{68} and E_{95} power-law fits result from the binning and filtering processes in steps 2 through 6 of the 7-step error-calculation procedure. $E_{68\text{-FIT}}$ is the power-law relation fit, in step 4, to the standard deviation (σ) of the proxy relative errors in the acoustical measurements. Solid red lines indicate the largest possible negative value of these errors. ***A***, 68-percent-confidence-level proxy errors in $C_{\text{XS-SILT-CLAY}}$ plotted as a function of acoustical measurements of $C_{\text{XS-SILT-CLAY}}$. ***B***, 95-percent-confidence-level proxy errors in $C_{\text{XS-SILT-CLAY}}$ plotted as a function of acoustical measurements of $C_{\text{XS-SILT-CLAY}}$. ***C***, 68-percent-confidence-level proxy errors in $C_{\text{XS-SAND}}$ plotted as a function of acoustical measurements of $C_{\text{XS-SAND}}$. ***D***, 95-percent-confidence-level proxy errors in $C_{\text{XS-SAND}}$ plotted as a function of acoustical measurements of $C_{\text{XS-SAND}}$. ***E***, 68-percent-confidence-level proxy errors in $D_{\text{50-XS-SAND}}$ plotted as a function of acoustical measurements of $D_{\text{50-XS-SAND}}$. ***F***, 95-percent-confidence-level proxy errors in $D_{\text{50-XS-SAND}}$ plotted as a function of acoustical measurements of $D_{\text{50-XS-SAND}}$. So that their magnitudes could be directly compared with the magnitudes of the proxy relative errors in the acoustical measurements, the 68-percent- and 95-percent-confidence-level relative errors in the EDI and EWI measurements depicted in these plots were converted to errors calculated relative to their associated acoustical measurement. This operation was done by dividing the 68-percent- and 95-percent-confidence level absolute errors in the EDI and EWI measurements by the concurrent acoustical measurement of concentration or median grain size, and then multiplying by 100 percent.

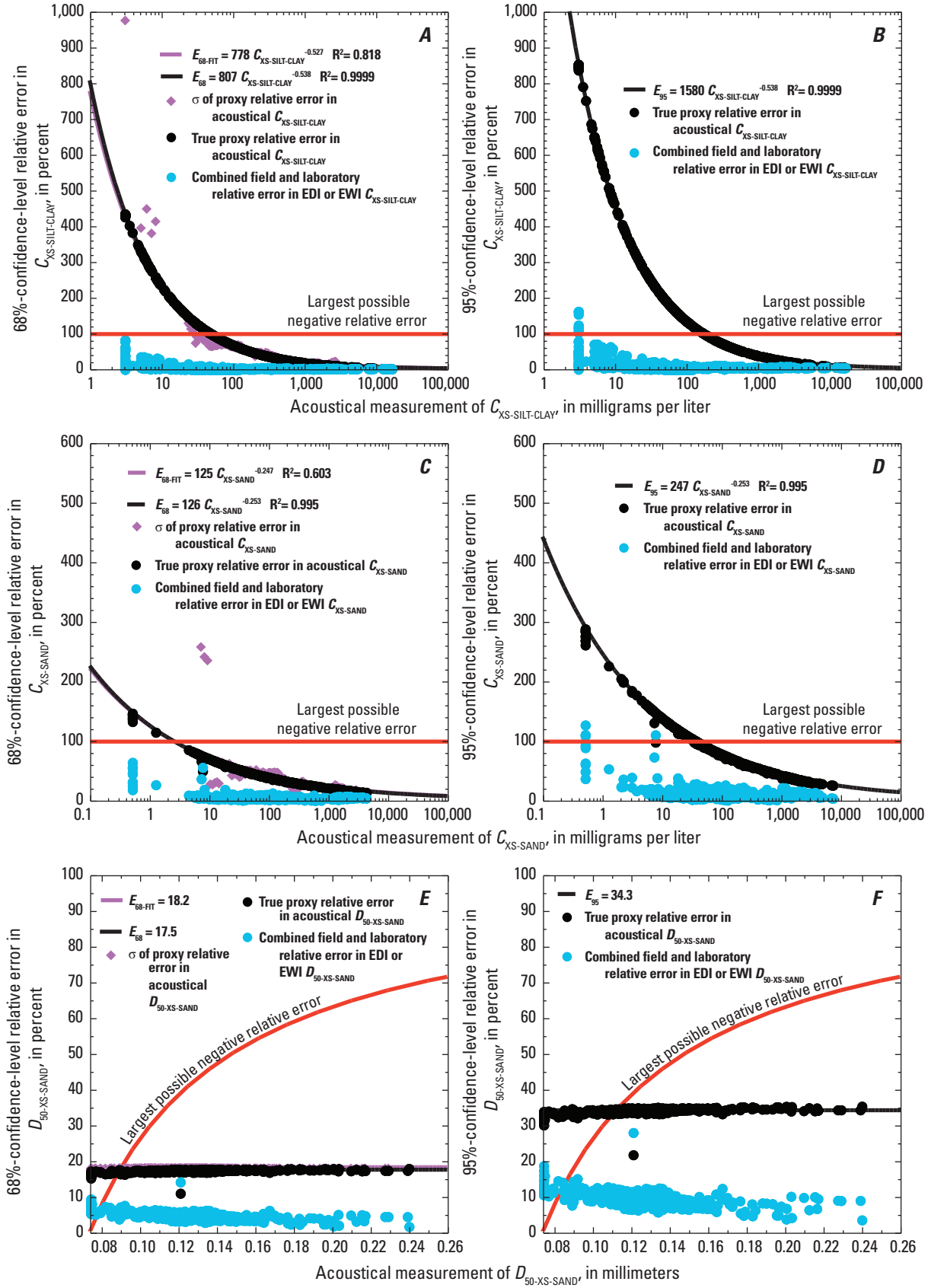
A
$E_{68\text{-FIT}} = 778\ C_{XS\text{-SILT-CLAY}}^{-0.527}$ $R^2 = 0.818$
$E_{68} = 807\ C_{XS\text{-SILT-CLAY}}^{-0.538}$ $R^2 = 0.9999$
σ of proxy relative error in acoustical $C_{XS\text{-SILT-CLAY}}$
True proxy relative error in acoustical $C_{XS\text{-SILT-CLAY}}$
Combined field and laboratory relative error in EDI or EWI $C_{XS\text{-SILT-CLAY}}$
Largest possible negative relative error
68%-confidence-level relative error in $C_{XS\text{-SILT-CLAY}}$, in percent
B
$E_{95} = 1580\ C_{XS\text{-SILT-CLAY}}^{-0.538}$ $R^2 = 0.9999$
True proxy relative error in acoustical $C_{XS\text{-SILT-CLAY}}$
Combined field and laboratory relative error in EDI or EWI $C_{XS\text{-SILT-CLAY}}$
Largest possible negative relative error
95%-confidence-level relative error in $C_{XS\text{-SILT-CLAY}}$, in percent
Acoustical measurement of $C_{XS\text{-SILT-CLAY}}$, in milligrams per liter
C
$E_{68\text{-FIT}} = 125\ C_{XS\text{-SAND}}^{-0.247}$ $R^2 = 0.603$
$E_{68} = 126\ C_{XS\text{-SAND}}^{-0.253}$ $R^2 = 0.995$
σ of proxy relative error in acoustical $C_{XS\text{-SAND}}$
True proxy relative error in acoustical $C_{XS\text{-SAND}}$
Combined field and laboratory relative error in EDI or EWI $C_{XS\text{-SAND}}$
Largest possible negative relative error
68%-confidence-level relative error in $C_{XS\text{-SAND}}$, in percent
D
$E_{95} = 247\ C_{XS\text{-SAND}}^{-0.253}$ $R^2 = 0.995$
True proxy relative error in acoustical $C_{XS\text{-SAND}}$
Combined field and laboratory relative error in EDI or EWI $C_{XS\text{-SAND}}$
Largest possible negative relative error
95%-confidence-level relative error in $C_{XS\text{-SAND}}$, in percent
Acoustical measurement of $C_{XS\text{-SAND}}$, in milligrams per liter
E
$E_{68\text{-FIT}} = 18.2$
$E_{68} = 17.5$
σ of proxy relative error in acoustical $D_{50\text{-XS-SAND}}$
True proxy relative error in acoustical $D_{50\text{-XS-SAND}}$
Combined field and laboratory relative error in EDI or EWI $D_{50\text{-XS-SAND}}$
Largest possible negative relative error
68%-confidence-level relative error in $D_{50\text{-XS-SAND}}$, in percent
F
$E_{95} = 34.3$
True proxy relative error in acoustical $D_{50\text{-XS-SAND}}$
Combined field and laboratory relative error in EDI or EWI $D_{50\text{-XS-SAND}}$
Largest possible negative relative error
95%-confidence-level relative error in $D_{50\text{-XS-SAND}}$, in percent
Acoustical measurement of $D_{50\text{-XS-SAND}}$, in millimeters

Figure 22.

section, even when the discharge of water, $C_{XS\text{-}SILT\text{-}CLAY}$, and $C_{XS\text{-}SAND}$ remain constant over time. Furthermore, the existence of changes in the lateral distribution of suspended sediment over timescales of a day suggest that slower changes in the lateral distribution are also possible. These changes will result in slowly varying, positively correlated errors in the acoustical measurements of $C_{XS\text{-}SILT\text{-}CLAY}$ and $C_{XS\text{-}SAND}$ that behave as biases over timescales smaller than those associated with the changes in the lateral distribution of suspended sediment. Positively correlated errors in acoustical measurements of $C_{XS\text{-}SILT\text{-}CLAY}$ or $C_{XS\text{-}SAND}$ arising from only slow changes in the lateral distribution of suspended sediment in the cross section will depend on the error associated with the previous measurement (that is, autocorrelation) and be independent of water discharge, suspended-sediment concentration, and the grain-size distribution of the suspended sand.

Slowly varying, correlated time-varying errors can be distinguished from random errors through analyses of temporal autocorrelation (Durbin and Watson, 1950, 1951; Anderson, 1971; Box and Jenkins, 1976). Autocorrelation analysis provides insight into whether the sign of a time-varying error remains positive or negative among sequential measurements for durations different than those expected for a random error. The case where errors are positively correlated is commonly referred to as having positive serial correlation. Positive serial correlation is a serial correlation in which the occurrence of a positive error in one measurement increases the likelihood of a positive error in the next measurement, and in which the occurrence of a negative error in one measurement increases the likelihood of a negative error in the next measurement. Conversely, the case where errors are negatively correlated is commonly referred to as having negative serial correlation. Negative serial correlation is a serial correlation in which the occurrence of a positive error in one measurement increases the likelihood of a negative error in the next measurement, and in which the occurrence of a negative error in one measurement increases the likelihood of a positive error in the next measurement. Positive serial correlation leads to errors that are larger than those predicted by the formula for the standard error of the mean, and negative serial correlation leads to errors that are smaller than those predicted by the standard formula for the standard error of the mean (Dunlop, 1994; Bence, 1995; Quinn and Keough, 2003). The ramifications of serial correlation on error are that positively correlated errors, that is, positive serial correlation, will lead to errors that decay in absolute value toward zero more slowly than expected on the basis of the standard error formula as more observations are made. Similarly, negative serial correlation will lead to errors that decay in absolute value toward zero more quickly than expected on the basis of the standard error formula as more observations are made (Topping and others, 2011).

The first step in this analysis was to determine whether, on average, the time-varying relative errors in the acoustical measurements of $C_{XS\text{-}SILT\text{-}CLAY}$ and $C_{XS\text{-}SAND}$ were independent of water discharge, suspended-sediment concentration, and the grain-size distribution of the suspended sand. If the time-varying errors in the acoustical measurements were found to be independent of these parameters, then the most likely dominant source of the time-varying error would be the observed slow variation in the lateral distribution of suspended sediment in the cross section. F-tests were used in these correlation analyses, as described below. Given that the relative errors in the acoustical measurements of $C_{XS\text{-}SILT\text{-}CLAY}$ and $C_{XS\text{-}SAND}$ were found to be largely independent of water discharge, sediment concentration, and grain size, the second step in this analysis was to use autocorrelation plots (Box and Jenkins, 1976) to determine whether the time-varying relative errors exhibited serial correlation between successive acoustical measurements. In cases of significant positive serial correlation, these plots will exhibit consecutive values of positive autocorrelation in excess of the positive 95-percent-confidence band associated with random processes for contiguous lags >0. Likewise, in cases of significant negative serial correlation, these plots will exhibit consecutive values of negative autocorrelation in excess of the negative 95-percent-confidence band associated with random processes for contiguous lags >0. In contrast, random errors in acoustical measurements of $C_{XS\text{-}SILT\text{-}CLAY}$ or $C_{XS\text{-}SAND}$ will exhibit no significant autocorrelation for non-zero lags.

Meaningful analyses of correlation and autocorrelation in the relative errors require a large number of suspended-sediment measurements made using a method that is much more accurate than the *RUTS* acoustical method. The only measurement techniques that meet this criterion are the EDI and EWI method (Topping and others, 2011), and the only four study sites with sufficient numbers of EDI or EWI measurements for these analyses are the CR30, CR61, CR87, and CR225 study sites. Ideally, the measurements used to calculate the error analyzed for autocorrelation would be made at evenly spaced intervals similar to the 15-minute interval of the acoustical measurements. This condition is, of course, impossible. Several EDI measurements are typically made over 1–2 days every 2 months at the CR87 and CR225 study sites, 8 EWI measurements are typically made over 2 days every 6 months at the CR30 and CR61 study sites, with a larger number of EDI or EWI measurements clustered at all study sites during discrete high-discharge periods. If it were possible to make highly accurate suspended-sediment measurements at 15-minute intervals, there would be no need for this study.

Although the EDI or EWI measurement programs at these study sites are nonrandom with the distribution of the interval between measurements being highly right-skewed, this nonrandom sampling design does not adversely affect the autocorrelation analyses. An evenly spaced, random, or nonrandom sampling of a time series will yield similar results so long as the number of observations is sufficiently large. Autocorrelation plots appear similar when the time series analyzed is random regardless of whether the sampling

scheme is evenly spaced, random, or nonrandom. Thus, detection of nonrandom error behavior is possible using the autocorrelation-plot method regardless of whether the sampling scheme is nonrandom (as it is in this study).

The results from the correlation analyses were partially presented in table 3, with the remaining parts of these analyses presented in text below; the results from the autocorrelation analyses are presented in table 4. Both the correlation and autocorrelation analyses were conducted on the apparent relative errors calculated using equation 67. F-tests were used to determine whether significant correlations existed between the relative errors in the acoustical sediment-concentration measurements and water discharge, $C_{XS\text{-}SILT\text{-}CLAY}$, $C_{XS\text{-}SAND}$, or $D_{50\text{-}XS\text{-}SAND}$ (see table 3).

The results summarized previously in table 3 indicate that the relative errors in the acoustical measurements of $C_{XS\text{-}SILT\text{-}CLAY}$ are typically uncorrelated with $C_{XS\text{-}SILT\text{-}CLAY}$, and the acoustical measurements of $C_{XS\text{-}SAND}$ are typically uncorrelated with $C_{XS\text{-}SAND}$ and $D_{50\text{-}XS\text{-}SAND}$. F-tests used to detect significant correlations between water discharge (Q) and the relative errors in the acoustical measurements of $C_{XS\text{-}SILT\text{-}CLAY}$ and $C_{XS\text{-}SAND}$ yield slightly different results, with the relative errors in the acoustical measurements of $C_{XS\text{-}SILT\text{-}CLAY}$ and $C_{XS\text{-}SAND}$ being slightly more dependent on Q than they are on concentration or grain size. However, although significant correlations between Q and relative error in the acoustical measurements occur at several of the Colorado River study sites, these significant correlations are extremely weak, with R^2 values <0.05. Relative errors in the acoustical measurements of $C_{XS\text{-}SILT\text{-}CLAY}$ were found to depend on Q at the p_{SIG}=0.037 level at the CR30 study site, and at the p_{SIG}=0.0011 level at the CR87 study site. Relative errors in the acoustical measurements of $C_{XS\text{-}SAND}$ were found to depend on Q at the p_{SIG}=0.0034 level at only the CR61 study site. In these three cases, as in the few cases of significant correlations between $C_{XS\text{-}SILT\text{-}CLAY}$, $C_{XS\text{-}SAND}$, or $D_{50\text{-}XS\text{-}SAND}$ and the relative errors in the acoustical measurements of $C_{XS\text{-}SILT\text{-}CLAY}$ and $C_{XS\text{-}SAND}$ presented in table 3, the relative errors in the acoustical measurements of $C_{XS\text{-}SILT\text{-}CLAY}$ and $C_{XS\text{-}SAND}$ are slightly negatively correlated with Q, meaning the relative errors become slightly more negative with increasing Q.

The results from the autocorrelation analyses indicate that, of the four study sites, only at the CR225 study site do the errors in the acoustical measurements of $C_{XS\text{-}SILT\text{-}CLAY}$ and $C_{XS\text{-}SAND}$ appear to be completely random (table 4). At the other three study sites, significant positive autocorrelation exists in the relative errors in acoustically measured $C_{XS\text{-}SILT\text{-}CLAY}$ and $C_{XS\text{-}SAND}$, and these positive autocorrelations persist for multiple lags (figs. 23–24). Positive autocorrelation is most persistent at the CR61 study site for the case of the relative error in the acoustical measurements of $C_{XS\text{-}SAND}$ (fig. 24*B*), perhaps again because of the much greater distance between the calibration cross section and the ADP array at that study site. Because the distribution of the intervals between the sequential EDI or EWI measurements at the study sites are highly right skewed (that is, there are distinct clusters of measurements at monthly to semi-annual time steps), the median value reported in table 4 is a better measure than the mean value for the timescale associated with each lag in the autocorrelation analyses. Thus, the relative errors in acoustical measurements of $C_{XS\text{-}SILT\text{-}CLAY}$ are typically nonrandom for durations exceeding ~7 hours at CR30, ~16 hours at CR61, and 1.4 days at CR87, and the relative errors in acoustical measurements of $C_{XS\text{-}SAND}$ are typically nonrandom for durations exceeding ~14 hours at CR30, 6 hours at CR61, and 2.1 days at CR87.

Table 4. Results from autocorrelation analyses conducted on relative errors in acoustical measurements of suspended-sediment concentration ($C_{XS\text{-}SILT\text{-}CLAY}$ and $C_{XS\text{-}SAND}$).

Study site	*n*	Central tendency of the interval between sequential EDI or EWI measurements, that is, the variable time step of each lag, expressed as the:		Number of contiguous lags >0 where the autocorrelation in the relative errors in acoustical measurements exceeds the positive 95-percent-confidence band for:	
		Mean number of days	Median number of days	$C_{XS\text{-}SILT\text{-}CLAY}$	$C_{XS\text{-}SAND}$
CR30	172	13.84	0.15	3	4
CR61	175	12.57	0.13	6	5
CR87	224	15.15	0.70	3	4
CR225	99	23.34	0.76	0	0

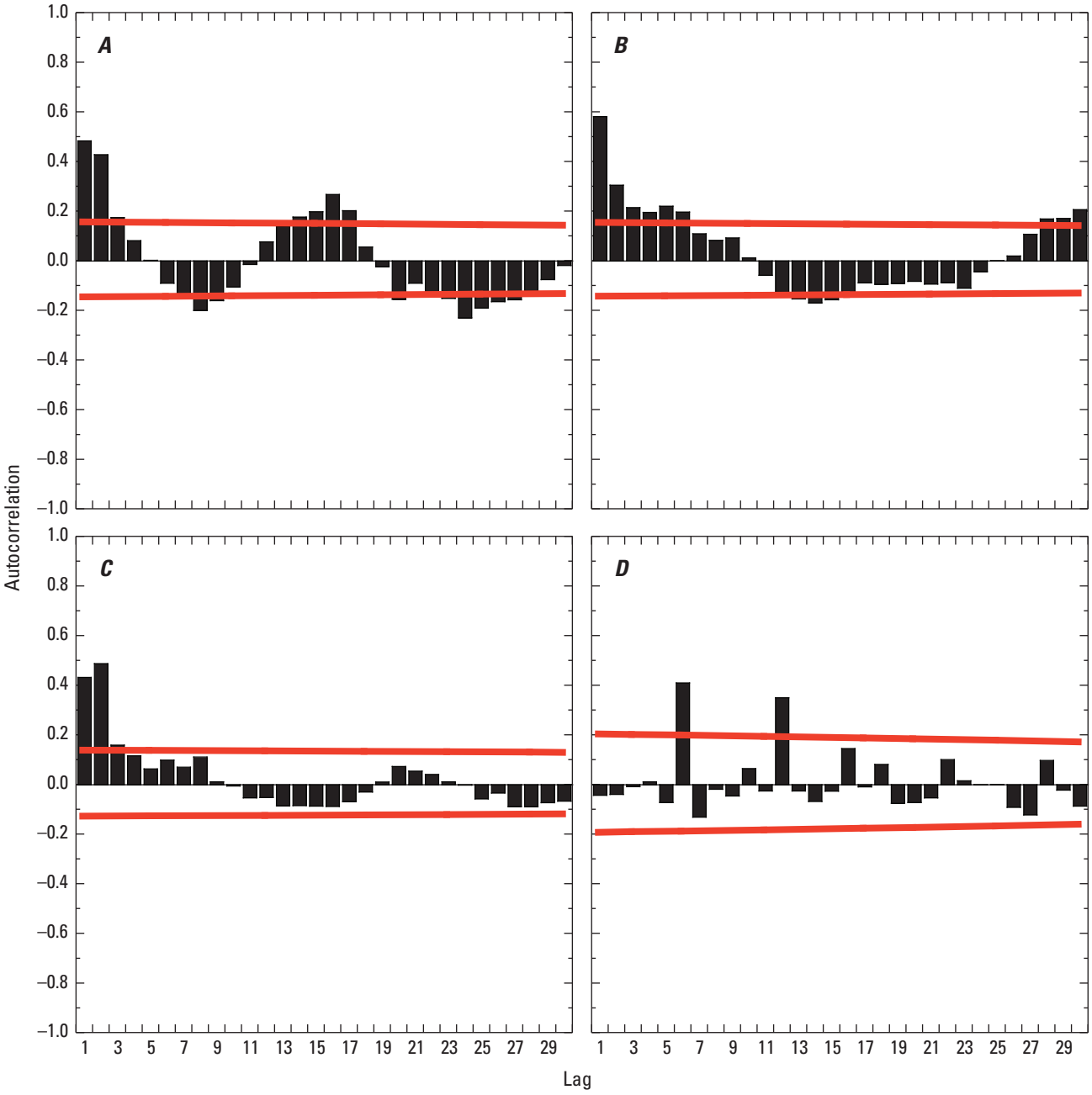

Figure 23. Autocorrelation in the relative errors associated with acoustical measurements of $C_{XS\text{-}SILT\text{-}CLAY}$ at the (***A***) CR30, (***B***) CR61, (***C***) CR87, and (***D***) CR225 study sites. Relative errors exhibit random behavior at only the CR225 site; relative errors exhibit varying degrees of positive autocorrelation at the other 4 study sites. Red lines are the 95-percent-confidence bands (Box and Jenkins, 1976). Lag refers to the nonuniform temporal spacing between successive equal-discharge-increment or equal-width-increment measurements; see text and table 4 for the estimated duration of a lag at each study site.

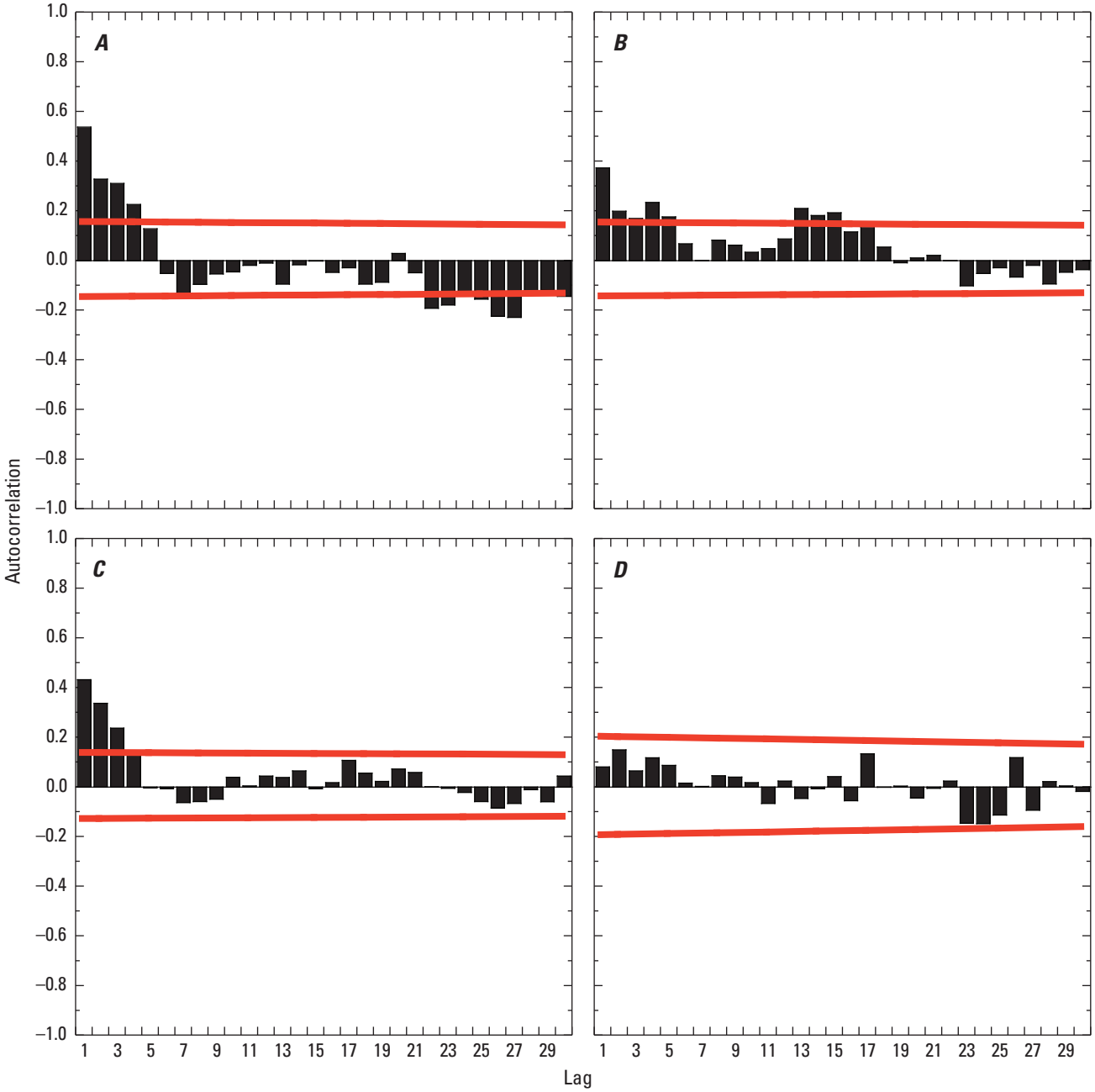

Figure 24. Autocorrelation in the relative errors associated with acoustical measurements of $C_{XS\text{-}SAND}$ at the (***A***) CR30, (***B***) CR61, (***C***) CR87, and (***D***) CR225 study sites. Relative errors exhibit random behavior at only the CR225 site; relative errors exhibit varying degrees of positive autocorrelation at the other four study sites. Red lines are the 95-percent-confidence bands (Box and Jenkins, 1976). Lag refers to the non-uniform temporal spacing between successive equal-discharge-increment or equal-width-increment measurements; see text and table 4 for the estimated duration of a lag at each study site.

These timescales of nonrandom behavior in the acoustical measurements are consistent with the >4 to <24-hour timescale reported for the physical measurements in Topping and others (2011) over which stable spatial structures in the lateral distribution of suspended silt and clay and suspended sand were observed to persist in river cross sections. Therefore, it is plausible that the positive autocorrelation in these errors does arise from the slow evolution of the lateral distribution of suspended sediment in a river cross section. Recalculation of the 68-percent- and 95-percent-confidence-level errors in the preceding section by segregating the data from the CR225 study site from the data from the CR30 and CR87 study sites indicates, however, that little difference exists in the magnitudes of these errors when random or nonrandom error behavior is suggested by autocorrelation analyses. Therefore, the presence of nonrandom error behavior at a study site does not necessarily indicate the presence of larger time-varying relative error, but rather only that the time-varying error may require a larger number of observations to decay.

The presence of positive autocorrelation in the errors indicates that a substantial number (perhaps many more than 100) of acoustical measurements of $C_{\text{XS-SILT-CLAY}}$ or $C_{\text{XS-SAND}}$ are required before the errors in time-averaged quantities decay to acceptably small values. Random errors will decay as a function of $1/\sqrt{n}$, whereas positively correlated errors will decay as a function of $1/n^x$ where $x<0.5$. For example, in the random case, a ±50 percent 95-percent-confidence level relative error will decay to an error of approximately ±5 percent after 96 observations (one day of 15-minute measurements). However, in the nonrandom case, many hours to days of 15-minute observations are likely required before any substantial decay in the error associated with the time average of the measurements is realized.

Therefore, although random behavior in the errors in the acoustical measurements of $C_{\text{XS-SILT-CLAY}}$ and $C_{\text{XS-SAND}}$ are possible (for example, at CR225), it is perhaps safer to assume nonrandom behavior of the errors at a study site (for example, CR30, CR61, and CR87) until proven otherwise by comparison with EDI or EWI measurements. Finally, it is important to reiterate that nonrandom behavior in the errors in the acoustical measurements of $C_{\text{XS-SILT-CLAY}}$ and $C_{\text{XS-SAND}}$ most likely arises not because of error in the acoustical measurements themselves but, rather, because the ADP samples only a part of the entire river cross section.

Conclusions

The two-frequency *RUTS* method presented herein for processing ADP data allows for reasonably accurate, unbiased, 15-minute acoustical measurements of $C_{\text{XS-SILT-CLAY}}$, $C_{\text{XS-SAND}}$, and $D_{\text{50-XS-SAND}}$ to be made over long timescales. Multi-frequency arrays of single-frequency ADPs, with data processed using the *RUTS* method, have been continuously deployed for over a decade at most of the study sites in this report. The power of the *RUTS* method arises from the fact that it is based on the physics of sound scattering by small particles. Acoustical theory forms the basis for all aspects of the ADP-calibration procedure. Empiricism is used only in the development of the relations between the suspended-sediment conditions within the ensonified part of the river cross section "sampled" by the acoustic beams to the suspended-sediment conditions in the entire cross section.

In most situations over the range of acoustic frequencies tested in our study, 600 kHz to 2 MHz, acoustic attenuation was caused primarily by silt-and-clay-sized sediment, whereas acoustic backscatter resulted from sand-, silt-, and clay-sized sediment. Only when $C_{\text{XS-SILT-CLAY}}$ is smaller than roughly twice $C_{\text{XS-SAND}}$ can acoustic backscatter be accurately related to only sand-size sediment. Thus, in rivers where a large range in $C_{\text{XS-SILT-CLAY}}$ is possible for any given value of $C_{\text{XS-SAND}}$, accounting for the acoustic backscatter from silt and clay is required to produce acoustical measurements of $C_{\text{XS-SAND}}$ with acceptably low levels of bias. Positive relative biases in the acoustical measurements of $C_{\text{XS-SAND}}$ will be produced if the backscatter from silt-and-clay-sized sediment is neglected (a common practice in the recent literature). In cases where the backscatter from silt and clay is incorrectly assigned to sand-size sediment, positive relative biases in the acoustical measurements of $C_{\text{XS-SAND}}$ of many hundreds of percent are common and many thousands to tens of thousands of percent are possible. This result is supported by the target-strength theory for different grain-size distributions, and is independent of the acoustic frequencies used in this study.

Changes in the grain-size distribution of the suspended sand can greatly affect acoustic backscatter. At any given constant $C_{\text{XS-SAND}}$, coarser grain-size distributions of suspended sand will result in much more backscatter than finer grain-size distributions of suspended sand. Because of the theoretical behavior of the *RUTS*, this grain-size effect causes larger changes in acoustic backscatter at lower frequencies than at high frequencies. Therefore, in cases where the grain-size distribution of the suspended sand is not constant, two acoustic frequencies are required for acoustical measurements of $C_{\text{XS-SAND}}$ that are not grain-size biased. Addition of a third frequency did not substantially improve the two-frequency measurements of $C_{\text{XS-SAND}}$ and only slightly improved the two-frequency measurements of $D_{\text{50-XS-SAND}}$ in our study. If single-frequency measurements of acoustic backscatter are to be used to calculate $C_{\text{XS-SAND}}$, these measurements should not be made at acoustic frequencies much less than ~2 MHz. Substantial grain-size-driven bias in single-frequency acoustical measurements of $C_{\text{XS-SAND}}$ is always present at these lower frequencies. Only in cases where the variation in $D_{\text{50-XS-SAND}}$ is less than ~0.5ϕ are reasonably unbiased single-frequency acoustical measurements of $C_{\text{XS-SAND}}$ possible, but only when the 2-MHz frequency is used to make these measurements. These results are supported by the theoretical behavior of target strength at different acoustic frequencies.

Time-varying relative errors in the acoustical measurements of $C_{\text{XS-SILT-CLAY}}$ and $C_{\text{XS-SAND}}$ decrease as a function of increasing concentration, as expected on the basis of Thorne and Hanes (2002). Although these errors are much larger than the combined field and laboratory-processing errors associated with EDI or EWI measurements at lower concentrations, they decrease to become similar to EDI or EWI errors at the higher concentrations measured in this study. Because of the right skewness in distributions of relative error, time-varying relative errors in excess of 100 percent are possible at the lowest concentrations. The estimated 68-percent-confidence-level time-varying relative error in the acoustical measurements of $C_{\text{XS-SILT-CLAY}}$ decreases from ±50 percent to ±10 percent as $C_{\text{XS-SILT-CLAY}}$ increases from ~180 to ~3,500 mg/L. Similarly, the estimated 68-percent-confidence-level time-varying relative error in the acoustical measurements of $C_{\text{XS-SAND}}$ decreases from ±50 percent to ±15 percent as $C_{\text{XS-SAND}}$ increases from ~39 to ~4,500 mg/L.

The behavior of the relative error in the acoustical measurements of $D_{\text{50-XS-SAND}}$ is slightly more complicated than the behavior of errors in concentration. The acoustical measurements of $C_{\text{XS-SAND}}$ are generally unbiased with respect to changes in either the concentration or the grain-size distribution of the suspended sand. Although the acoustical measurements of $D_{\text{50-XS-SAND}}$ are unbiased with respect to changes in $C_{\text{XS-SAND}}$, there is a tendency for these measurements to be slightly biased as a function of changes in $D_{\text{50-XS-SAND}}$. In essence, at most of the study sites there is a tendency for the acoustical measurements of $D_{\text{50-XS-SAND}}$ to be slightly low when the suspended sand is relatively coarse and for these measurements to be slightly high when the suspended sand is relatively fine. As $D_{\text{50-XS-SAND}}$ approaches the $D_{\text{50-XS-SAND-REF}}$ used in the ADP calibrations, the acoustical measurements of $D_{\text{50-XS-SAND}}$ become essentially unbiased. As it is impossible to know independently how coarse or fine the suspended-sand grain-size distribution is during an acoustical measurement (which would allow for a bias correction), we chose to include this small bias within the calculation of the time-varying relative error. Largely as a result of the inclusion of this small grain-size-driven bias, the time-varying relative error in the acoustical measurements of $D_{\text{50-XS-SAND}}$ is much larger than the combined field and laboratory-processing errors associated with EDI or EWI measurements. The 68-percent-confidence-level time-varying relative error in the acoustical measurements of $D_{\text{50-XS-SAND}}$ is roughly ±18 percent.

Because there is a general tendency for positive autocorrelation to exist in the time-varying relative errors, the errors in time-averaged acoustical measurements of either $C_{\text{XS-SILT-CLAY}}$ or $C_{\text{XS-SAND}}$ do not decay as fast as if these errors were random. The behaviors of the time-varying errors in $C_{\text{XS-SILT-CLAY}}$ and $C_{\text{XS-SAND}}$ were completely random at only one of the four study sites where sufficient data existed to conduct an autocorrelation analysis. When time-varying errors are random, these errors in a time-averaged quantity decrease as a function of $1/\sqrt{n}$. Thus, at the one study site where the autocorrelation analyses indicated only random error behavior, the time-varying relative errors in the 15-minute acoustical measurements of $C_{\text{XS-SILT-CLAY}}$ or $C_{\text{XS-SAND}}$ would decrease roughly tenfold over the course of a day (after 96 measurements have been made), under conditions of constant concentration. At the other study sites exhibiting nonrandom error behavior, however, it would take much longer (likely at least several days depending on the timescale of the nonrandom errors) for these errors to decay to similarly small values. Recognition of whether positive autocorrelation exists in the time-varying errors at a study site is important because it provides information on the timescale over which the errors in sediment loads calculated using the acoustical measurements decay to acceptably small values, and thus sets limits on the timescales associated with the calculation of accurate sediment budgets.

The source of positive autocorrelation in time-varying error is not likely the acoustical measurements themselves, but rather, the presence of spatial structures in both suspended-sand and suspended-silt-and-clay concentration that evolve slowly over time in a river cross section (for example, Topping and others, 2011). This slow variation in the lateral distribution of suspended sediment results in variation in the relation between the suspended sediment within the ensonified part of the cross section and the suspended sediment in the entire river cross section. Because the ADP calibrations are constant over time, this effect produces the slower-than-random time-varying error behavior. Because of its likely source, this nonrandom error behavior is likely to be present in any method that relies on suspended-sediment measurements made within a subsample of an entire river cross section (for example, automatic-pump, optical, and LISST methods). Furthermore, because the ADP beams effectively sample the suspended-sediment conditions within a larger part of the river cross section than do any of these other methods that measure the suspended-sediment conditions at only a point in the cross section, the nonrandom time-varying errors in the acoustical measurements of $C_{\text{XS-SILT-CLAY}}$, $C_{\text{XS-SAND}}$, and $D_{\text{50-XS-SAND}}$ are expected to be smaller than errors associated with any of the point methods.

Finally, although both the random and nonrandom relative errors in the acoustical measurements decay to relatively small values as more measurements are made, sediment loads calculated on the basis of acoustical measurements are still subject to small potential biases in EDI/EWI measurements (Topping and others, 2010) because the acoustical measurements are calibrated to the EDI/EWI measurements. However, because (1) it is typically not standard to make more than one or two EDI or EWI measurements on any given day, (2) it is certainly not typical to make many EDI or EWI measurements over consecutive days, and (3) the suspended-sediment conditions can change substantially in a river over minutes to hours, long-term sediment loads calculated on the basis of the acoustical measurements described herein will be much more accurate than loads calculated on the basis of a relatively sparse EDI- or EWI-measurement program using interpolation to estimate concentrations between the times of the sparse measurements.

Acknowledgments

Funding for this study was provided by the Department of the Interior's Glen Canyon Dam Adaptive Management Program administered by the Bureau of Reclamation; by the U.S. Geological Survey Southwest Biological Science Center; by the National Park Service; by the Commission for Environmental Cooperation (funded by the North American Free Trade Agreement); by the Utah State University Watershed Sciences Department; and by the Federal Interagency Sedimentation Project. Ted Melis played a key role in getting this study established. Ron Griffiths and David Dean both played substantial roles in maintaining the instrumentation described in this report and in processing the acoustical data. Ron Griffiths, Tom Sabol, Nick Voichick, David Dean, and Hunter Edwards played critical roles in collecting the physical suspended-sediment samples used in the ADP calibration and verification process. David Schoellhamer provided thoughtful and helpful comments on an earlier condensed draft of this paper. Daniel Buscombe, Francisco Pedocchi, and Mark Landers provided insightful reviews that greatly improved the quality of this report. All data used in this report can be obtained at http://www.gcmrc.gov/discharge_qw_sediment/, http://cida.usgs.gov/gcmrc/discharge_qw_sediment/, or from the authors.

References Cited

Agrawal, Y.C., and Pottsmith, H.C., 1994, Laser diffraction particle sizing in STRESS: Continental Shelf Research, v. 14, no. 10/11, p. 1101–1121, doi:10.1016/0278-4343(94)90030-2.

Agrawal, Y.C., and Pottsmith, H. C., 2000, Instruments for particle size and settling velocity observations in sediment transport: Marine Geology, v. 168, p. 89–114, doi:10.1016/S0025-3227(00)00044-X.

Ainslie M.A., and McColm J.G., 1998, A simplified formula for viscous and chemical absorption in sea water: Journal of the Acoustical Society of America, v. 103, no. 3, p. 1671–1672, doi:10.1121/1.421258.

Anderson, T.W., 1971, The statistical analysis of time series: New York, Wiley and Sons, Inc., 704 p.

Anderson, V.C., 1950, Sound scattering from a fluid sphere: Journal of the Acoustical Society of America, v. 22, no. 4, p. 426–431, doi:10.1121/1.1906621.

Anima, R. J., Marlow, M. S., Rubin, D. M., and Hogg, D. J., 1998, Comparison of sand distribution between April 1994 and June 1996 along six reaches of the Colorado River in Grand Canyon, Arizona: U.S. Geological Survey Open-File Report 98–141, 33 p.

Bence, J.R., 1995, Analysis of short time series; Correcting for autocorrelation: Ecology, v. 76, no. 2, p. 628–639, doi:10.2307/1941218.

Beverage, J.P., and Culbertson, J.K., 1964, Hyperconcentrations of suspended sediment: Journal of the Hydraulics Division, Proceedings of the American Society of Civil Engineers, v. 90, n. 6, p. 117–128.

Box, G.E.P., and Jenkins, G.M., 1976, Time series analysis; Forecasting and control, 2d ed.: San Francisco, Calif., Holden-Day, 575 p.

Buscombe, D., Grams, P.E., and Kaplinski, M.A., 2014, Characterizing riverbed sediment using high-frequency acoustics; 2. Scattering signatures of Colorado River bed sediment in Marble and Grand Canyons: Journal of Geophysical Research—Earth Surface, v. 119, p. 2692–2710, doi:10.1002/2014JF003191.

Cohn, T.A., 1995, Recent advances in statistical methods for the estimation of sediment and nutrient transport in rivers, *in* Pielke, R.A., ed., Contributions in Hydrology, U.S. National Report to the International Union of Geodesy and Geophysics, 1991–1994: Reviews of Geophysics, v. 33, no. S2, p. 1117–1123, doi:10.1029/95RG00292.

Cohn, T.A., DeLong, L.J., Gilroy, E.J., Hirsch, R.M., and Wells, D.K., 1989, Estimating constituent loads: Water Resources Research, v. 25, no. 5, p. 937–942, doi:10.1029/WR025i005p00937.

Colby, B. R., 1964, Scour and fill in sand-bed streams: U.S. Geological Survey Professional Paper 462-D, 32 p.

Conner, C.S., and De Visser, A.M., 1992, A laboratory investigation of particle size effects on an optical backscatterance sensor: Marine Geology, v. 108, no. 2, p. 51–159, doi:10.1016/0025-3227(92)90169-I

Curran, K.J., Hill, P.S., Milligan, T.G., Mikkelsen, O.A., Law, B.A., Durrieu de Madron, X., and Bourrin, F., 2007, Settling velocity, effective density, and mass composition of suspended sediment in a coastal bottom boundary layer, Gulf of Lions, France: Continental Shelf Research, v. 27, no. 10–11, p. 1408–1421, doi:10.1016/j.csr.2007.01.014.

Deer, W.A., Howie, R.A., and Zussman, J., 1966, An introduction to the rock-forming minerals: Essex, England, Longmans, 528 p.

Deines, K.L., 1999, Backscatter estimation using broadband acoustic Doppler current profilers, *in* Anderson, S.P., Terray, E.A., Rizoli White, J.A., and Williams, A.J., III, eds., Proceedings of the IEEE Sixth Working Conference on Current Measurement: Institute of Electrical and Electronics Engineers, p. 249–253, doi:10.1109/CCM.1999.755249.

DeWit, C.T., and Arens, P.R., 1950, Moisture content and density of some clay minerals and some remarks on the hydration pattern of clay: Transactions of the 4th International Congress of Soil Science, v. 2, p. 59–62.

Dinehart, R.L., 1998, Sediment transport at gaging stations near Mount St. Helens, Washington, 1980–90; Data collection and analysis: U.S. Geological Survey Professional Paper 1573, 105 p.

Downing, A., Thorne, P.D., and Vincent, C.E., 1995, Backscattering from a suspension in the near field of a piston transducer: Journal of the Acoustical Society of America, v. 97, no. 3, p. 1614–1620, doi:10.1121/1.412100.

Dunlop, D.D., 1994, Regression for longitudinal data; a bridge from least squares regression: American Statistician, v. 48, p. 299–303.

Durbin, J., and Watson, G.S., 1950, Testing for serial correlation in least squares regression; I: Biometrika, v. 37, no. 3/4, p. 409–428, doi:10.1093/biomet/37.3-4.409.

Durbin, J., and Watson, G.S., 1951, Testing for serial correlation in least squares regression; II: Biometrika, v. 38, no. 1/2, p. 159–177, doi:10.1093/biomet/38.1-2.159.

Dyer, K.R., and Manning, A.J., 1999, Observation of the size, settling velocity and effective density of flocs, and their fractal dimensions: Journal of Sea Research, v. 41, no. 1–2, p. 87–95, doi:10.1016/S1385-1101(98)00036-7.

EdgeTech, 2005, Application note—Sidescan sonar beamwidth, ver. 1.2: EdgeTech Resource Center, 6 p., accessed on September 14, 2015, at http://www.edgetech.com/pdfs/ut/app_note_beamwidth.pdf.

Edwards, T.K., and Glysson, G.D., 1999, Field methods for measurement of fluvial sediment: Techniques of Water-Resources Investigations of the U.S. Geological Survey, book 3, chap. C2, 89 p.

Flammer, G.H., 1962, Ultrasonic measurement of suspended sediment: U.S. Geological Survey Bulletin 1141-A, 48 p.

Flammer, G.H., Stauffer, N.E., Jr., and Liu, E.Y., 1969, The effect of sediment properties on the attenuation of an ultrasonic plane wave: Utah State University, College of Engineering, Utah Water Research Laboratory PREC 30-1, 15 p.

Gartner, J.W., 2004, Estimating suspended solids concentrations from backscatter intensity measured by acoustic Doppler current profiler in San Francisco Bay, California: Marine Geology, v. 211, p. 169–187, doi:10.1016/j.margeo.2004.07.001.

Gartner, J.W., and Carder, K.L., 1979, A method to determine specific gravity of suspended particles using an electronic particle counter: Journal of Sedimentary Petrology, v. 49, no. 2, p. 631–633.

Gartner, J.W., and Wright, S.A., 2010, Section 1.2.5, Acoustic backscatter, *in* Gray, J.R., and Gartner, J.W., eds., Surrogate technologies for monitoring suspended-sediment transport in rivers, chap. 1 *of* Poleto, C., and Charlesworth, S., eds., Sedimentology of Aqueous Systems: London, U.K., Wiley-Blackwell, p. 28–34.

Gelfenbaum, G., and Smith, J.D., 1986, Experimental evaluation of a generalized suspended-sediment transport theory, *in* Knight, R.J., and McLean, J.R., eds., Shelf sands and sandstones: Canadian Society of Petroleum Geologists, Memoir II, p. 133–144.

Glysson, G.D., Gray, J.R., and Schwarz, G.E., 2001, Comparison of load estimates using total suspended solids and suspended sediment data, *in* Phelps, D., and Sehlke, G., eds., Bridging the gap—Meeting the world's water and environmental resources challenges: American Society of Civil Engineers, Proceedings of the World Water and Environmental Resources Congress, 2001, doi: 10.1061/40569(2001)123.

Grams, P.E., Topping, D.J., Schmidt, J.C., Hazel, J.E., Jr., and Kaplinski, M., 2013, Linking morphodynamic response with sediment mass balance on the Colorado River in Marble Canyon—Issues of scale, geomorphic setting, and sampling design: Journal of Geophysical Research Earth Surface, v. 118, p. 361–381, doi:10.1002/jgrf.20050.

Gray, J.R., and Gartner, J.W., 2009, Technological advances in suspended-sediment surrogate monitoring: Water Resources Research, v. 45, W00D29, 20 p., doi:10.1029/2008WR007063.

Gray, J.R., and Simoes, F.J.M., 2008, Estimating sediment discharge, appendix D *in* Garcia, M.H., ed., Sedimentation Engineering—Processes, Measurements, Modeling, and Practice: American Society of Civil Engineers Manuals and Reports on Engineering Practice, v. 110, p. 1067–1088.

Griffiths, R.E., Topping, D.J., Andrews, T., Bennett, G.E., Sabol, T.A., and Melis, T.S., 2012, Design and maintenance of a network for collecting high-resolution suspended-sediment data at remote locations on rivers, with examples from the Colorado River: U.S. Geological Survey Techniques and Methods, book 8, chapter C2, 44 p.

Hanes, D.M., 2012, On the possibility of single-frequency acoustic measurement of sand and clay concentrations in uniform suspensions: Continental Shelf Research, v. 46, p. 64–66, doi:10.1016/j.csr.2011.10.008.

Hanes, D.M., 2013, Erratum to ‘‘On the possibility of single-frequency acoustic measurement of sand and clay concentrations in uniform suspensions’’ [Continental Shelf Research, v. 46, doi:10.1016/j.csr.2011.10.008,2012]: Continental Shelf Research, v. 54, p. 117–118, doi:10.1016/j.csr.2012.10.003.

Hay, A.E., 1983, On the remote acoustic detection of suspended sediment at long wavelengths: Journal of Geophysical Research, v. 88, no. C12, p. 7525–7542, doi:10.1029/JC088iC12p07525.

Hay, A.E., 1991, Sound scattering from a particle-laden, turbulent jet: Journal of the Acoustical Society of America, v. 90, no. 4, p. 2055–2074, doi:10.1121/1.401633.

Hay, A.E., and Sheng, J., 1992, Vertical profiles of suspended sand concentration and size from multifrequency acoustic backscatter: Journal of Geophysical Research, v. 97, no. C10, p. 15,661–15,677, doi:10.1029/92JC01240.

He, C., and Hay, A.E., 1993, Broadband measurements of the acoustic scattering cross section of sand particles in suspension: Journal of the Acoustical Society of America, v. 94, no. 4, p. 2247–2254, doi:10.1121/1.407496.

Heidel, S.G., 1956, The progressive lag of sediment concentration with flood waves: American Geophysical Union Transactions, v. 37, no. 1, p. 56–66.

Henry, C.D., Price, J.G., and Miser, D.E., 1989, Geology and tertiary igneous activity of the Hen Egg Mountain and Christmas Mountains quadrangles, Big Bend region, Trans-Pecos Texas: University of Texas at Austin Bureau of Economic Geology, Report of Investigations 183, 105 p.

Hickling, R., 1962, Analysis of echoes from a solid elastic sphere in water: Journal of the Acoustical Society of America, v. 34, no. 10, p. 1582–1592, doi:10.1121/1.1909055.

Hill, P.S., Voulgaris, G., and Trowbridge, J.H., 2001, Controls on floc size in a continental shelf bottom boundary layer: Journal of Geophysical Research: Oceans, v. 106, no. C5, p. 9543–9549, doi:0.1029/2000JC900102.

Iorns, W.V., Hembree, C.H., Phoenix, D.A., and Oakland, G.L., 1964, Water resources of the Upper Colorado River Basin–Basic data: U.S. Geological Survey Professional Paper 442, 1036 p. and 12 plates.

Julien, P.Y., and Klaassen, G.J., 1995, Sand-dune geometry of large rivers during floods: Journal of Hydraulic Engineering, v. 121, no. 9, p. 657–663, doi:10.1061/(ASCE)07339429(1995)121:9(657).

Julien, P.Y., Klaassen, G.J., Ten Brinke, W.B.M., and Wilbers, A.W.E., 2002, Case study—Bed resistance of Rhine River during 1998 flood: Journal of Hydraulic Engineering, v. 128, no. 12, p. 1042–1050, doi:10.1061/(ASCE)0733-9429(2002)128:12(1042).

Kino, G.S., 1987, Acoustic Waves—Devices, imaging, and analog signal processing: Englewood Cliffs, New Jersey, Prentice Hall, 601 p.

Kleinhans, M.G., Wilbers, A.W.E, and ten Brinke, W.B.M., 2007, Opposite hysteresis of sand and gravel transport upstream and downstream of a bifurcation during a flood in the Rhine River, the Netherlands: Netherlands Journal of Geosciences, v. 86, no. 3, p. 273–285.

Krumbein, W.C., 1936, Application of logarithmic moments to size frequency distributions of sediments: Journal of Sedimentary Petrology, v. 6, no. 1, p. 35–47.

Lamb, H., 1945, Hydrodynamics, 6th ed.: New York, Dover Publications, 738 p.

Latosinksi, F.G., Szupiany, R.N., Garcia, C.M., Guerrero, M, and Amsler, M.L., 2014, Estimation of concentration and load of suspended bed sediment in a large river by means of acoustic doppler technology: Journal of Hydraulic Engineering, v. 140, no. 7, 15 p., doi:10.1061/(ASCE)HY.1943-7900.0000859.

Lockwood, J.C., and Willette, J.G., 1973, High-speed method for computing the exact solution for the pressure variations in the nearfield of a baffled piston: Journal of the Acoustical Society of America, v. 53, no. 3, p. 735–741, doi:10.1121/1.1913385.

Lohrmann, A., 2001, Monitoring sediment concentration with acoustic backscattering instruments: Nortek Technical Note No. 3, 5 p., accessed on March 12, 2014, at http://www.nortekusa.com/usa/knowledge-center/technical-notes.

MacDonald, I.T., Vincent, C.E., Thorne, P.D., and Moate, B.D., 2013, Acoustic scattering from a suspension of flocculated sediments: Journal of Geophysical Research: Oceans, v. 118, no. 5, p. 2581–2594, doi:10.1002/jgrc.20197.

Mann, H.B., and Whitney, D.R., 1947, On a test of whether one of two random variables is stochastically larger than the other: Annals of Mathematical Statistics, v. 18, no. 1, p. 50–60, doi:10.1214/aoms/1177730491.

McLean, S.R., 1991, Stratification effects due to suspended sediments *in* Proceedings of the International Symposium on the Transport of Suspended Sediment and its Mathematical Modeling: International Association for Hydro-Environment Engineering and Research, p. 145–164.

McLean, S.R., 1992, On the calculation of suspended load for noncohesive sediments: Journal of Geophysical Research: Oceans, v. 97, no. C4, p. 5759–5770, doi:10.1029/91JC02933.

Medwin, H., and Clay, C.S, 1997, Fundamentals of acoustical oceanography: New York, Academic Press, 712 p.

Melis, T.S., Topping, D.J., and Rubin, D.M., 2002, Testing laser-based sensors for continuous, in-situ monitoring of suspended sediment in the Colorado River, Grand Canyon, Arizona, *in* appendix 2 *of* Gray, J.R., and Glysson, G.D., eds., Proceedings of the Federal interagency workshop on turbidity and other sediment surrogates, April 30-May 2, 2002, Reno, Nevada: U.S. Geological Survey Circular 1250.

Melis, T.S., Topping, D.J., and Rubin, D.M., 2003, Testing laser-based sensors for continuous in situ monitoring of suspended sediment in the Colorado River, Arizona, *in* Bogen, J., Fergus, T., and Walling D.E., eds., Erosion and sediment transport measurement in rivers; technological and methodological advances: International Association of Hydrological Sciences Publication 283, p. 21–27.

Moore, S.A., and Hay, A.E., 2009, Angular scattering of sound from solid particles in turbulent suspension: Journal of the Acoustical Society of America, v. 126, no. 3, p. 1046–1056, doi:10.1121/1.3180696.

Moore, S.A., Le Coz, J., Hurther, D., and Paquier, A., 2013, Using multi-frequency acoustic attenuation to monitor grain size and concentration of suspended sediment in rivers: Journal of the Acoustical Society of America, v. 33, no. 4, p. 1959–1970, doi:10.1121/1.4792645.

Morse, P.M., 1948, Vibration and sound, 2d ed.: New York, McGraw-Hill, 468 p.

Mouraenko, O.A., 2004, Acoustic measurement techniques for suspended sediments and bedforms: Gainesville, University of Florida, Ph.D. dissertation, 150 p., accessed on November 3, 2015, at http://etd.fcla.edu/UF/UFE0008389/mouraenko_o.pdf.

National Defense Research Committee [NDRC], 1946, Principles and applications of underwater sound: Summary Technical Report of Division 6, v. 7: Washington, D.C., Department of the Navy, Office of Scientific Research and Development, 295 p.

Nortek, 2002, EasyQ River Flow Monitor User Manual: Sandvika, Norway, Nortek AS Document no. N3009-100, revision C, 56 p., accessed on April 26, 2010, at http://www.nortekusa.com/lib/manuals/easyq.

Nortek, 2008, Aquadopp Current Profiler User Guide: Rud, Norway, Nortek AS Document no. N3009-103, revision C, 84 p., accessed on April 26, 2010, at http://www.nortekusa.com/lib/manuals/aquadopp-profiler.

Nortek, 2013, Comprehensive Manual, December 2013: Rud, Norway, Nortek AS, 138 p., accessed on October 14, 2015, at www.nortek-as.com/lib/manuals/the-comprehensive-manual.

Osterkamp, W.R., and Parker, R.S., 1991, Sediment monitoring in the United States *in* Kuo, Y.-H., and Fan, S.-s., eds., Proceedings of the Fifth Federal Interagency Sedimentation Conference, 1991: Interagency Committee on Water Resources, Subcommittee on Sedimentation, v. 1, p. 1-15–1-23.

OTT, 2014, Quick Reference—Side Looking Doppler—OTT SLD: Kempten, Germany, OTT Hydromet, accessed on December 8, 2015, at http://www.ott.com/en-us/nc/resources/.

Porterfield, G., 1972, Computation of fluvial sediment discharge: U.S. Geological Survey Techniques of Water-Resources Investigations, book 3, chapter C3, 66 p.

Quinn, G.P., and Keough, M.J., 2003, Experimental design and data analysis for biologists: New York, Cambridge University Press, 537 p.

Rasmussen, P.P., Gray, J.R., Glysson, G.D., and Ziegler, A.C., 2009, Guidelines and procedures for computing time-series suspended-sediment concentrations and loads from in-stream turbidity-sensor and streamflow data: U.S. Geological Survey Techniques and Methods, book 3, chapter C4, 53 p.

Rayleigh, B., Strutt, J.W., 1896, Theory of sound, volume 2: New York, Macmillan and Co., 504 p., accessed on March, 13, 2014, at http://books.google.com/books?id=Zm9LAAAAMAAJ&pg=PR5&source=gbs_selected_pages&cad=3#v=onepage&q&f=false.

Reichel, G., and Nachtnebel, H.P., 1994, Suspended sediment monitoring in a fluvial environment—advantages and limitations applying an acoustic Doppler current profile: Water Research, v. 28, no. 4, p. 751–761, doi:10.1016/0043-1354(94)90083-3.

Reverberation Group, University of California Division of War Research, 1943, The discrimination of transducers against reverberation: University of California Division of War Research Report no. U75, file 01.40, National Defense Research Committee Division 6 - Section 6.1, 14 p., accessed on September 17, 2015, at http://escholarship.org/uc/item/3fn5n0rj.

Rouhnia, M., Keyvani, A., and Strom, K., 2014, Do changes in the size of mud flocs affect the acoustic backscatter values recorded by a Vector ADV?: Continental Shelf Research, v. 84, p. 84–92, doi:10.1016/j.csr.2014.05.015.

Rubin, D.M., Nelson, J.M., and Topping, D.J., 1998, Relation of inversely graded deposits to suspended-sediment grain-size evolution during the 1996 Flood Experiment in Grand Canyon: Geology, v. 26, p. 99–102, doi:10.1130/0091-7613(1998)026<0099:ROIGDT>2.3.CO;2.

Rubin, D.M., Tate, G.M., Topping, D.J., and Anima, R.A., 2001, Use of rotating side-scan sonar to measure bedload *in* Proceedings of the Seventh Federal Interagency Sedimentation Conference: Interagency Committee on Water Resources, Subcommittee on Sedimentation, v. 1, p. III-139–III-143.

Rubin, D.J., Topping, D.J., Chezar, H., Hazel, J.E., Schmidt, J.C., Breedlove, M., Melis, T.S., and Grams, P.E., 2010, 20,000 grain-size observations from the bed of the Colorado River, and implications for sediment transport through Grand Canyon *in* Proceedings of the 2nd Joint Federal Interagency Conference (9th Federal Interagency Sedimentation Conference and 4th Federal Interagency Hydrologic Modeling Conference on Sedimentation and Hydrologic Modeling): Advisory Committee on Water Information, Subcommittees on Hydrology and Sedimentation.

Sabol, T.A., and Topping, D.J., 2013, Evaluation of intake efficiencies and associated sediment-concentration errors in US D-77 bag-type and US D-96-type depth-integrating suspended-sediment samplers: U.S. Geological Survey Scientific Investigations Report 2012–5208, 88 p., http://dx.doi.org/10.3133/sir20125208.

Schaafsma, A.S., and Hay, A.E., 1997, Attenuation in suspensions of irregularly shaped sediment particles—a two-parameter equivalent spherical scatterer model: Journal of the Acoustical Society of America, v. 102, no. 3, p. 1485–1502, doi:10.1121/1.420063.

Schmidt, J.C., 1990, Recirculating flow and sedimentation in the Colorado River in Grand Canyon, Arizona: Journal of Geology, v. 98, p. 709–724.

Schmidt, J.C., and Graf, J.B., 1990, Aggradation and degradation of alluvial sand deposits, 1965 to 1986, Colorado River, Grand Canyon National Park, Arizona: U.S. Geological Survey Professional Paper 1493, 74 p.

Schmidt, J.C., Topping, D.J., Rubin, D.M., Hazel, J.E., Jr., Kaplinski, M., Wiele, S.M., and Goeking, S.A., 2007, Streamflow and sediment data collected to determine the effects of low summer steady flows and habitat maintenance flows in 2000 on the Colorado River between Lees Ferry and Bright Angel Creek, Arizona: U.S. Geological Survey Open-File Report 2007–1268, 79 p.

Schoellhamer, D.H., 2001, Continuous monitoring of suspended sediment in rivers by use of optical sensors *in* Proceedings of the Seventh Federal Interagency Sedimentation Conference: Interagency Committee on Water Resources, Subcommittee on Sedimentation, v. 1, p. III-160–III-167.

Schoellhamer, D.H., and Wright, S.A., 2003, Continuous measurement of suspended-sediment discharge in rivers by use of optical backscatterance sensors, *in* Bogen, J., Fergus, T., and Walling, D.E., eds., Erosion and sediment transport measurement in rivers; technological and methodological advances: International Association of Hydrological Sciences Publication 283, p. 28–36.

Schulkin, M., and Marsh, H.W., 1962, Sound absorption in sea water: Journal of the Acoustical Society of America, v. 34, p. 864–865, doi:10.1121/1.1918213.

Scott, C.H., and Stephens, H.D., 1966, Special sediment investigations—Mississippi River at St. Louis, Missouri, 1961–63: U.S. Geological Survey Water-Supply Paper 1819-J, 35 p. and 3 plates.

Sequoia Scientific, 2010, LISST-25X, Constant calibration suspended sediment sensor showing true volume concentration and mean diameter: Sequoia Scientific technical document, accessed on May 3, 2010, at http://sequoiasci.com/downloads/LISST-25X.pdf.

Shellenbarger, G.G., Wright, S.A., and Schoellhamer, D.H., 2013, A sediment budget for the southern reach in San Francisco Bay, CA—Implications for habitat restoration: Marine Geology, v. 345, p. 281–293, doi:10.1016/j.margeo.2013.05.007.

Sheng, J., and Hay, A.E., 1988, An examination of the spherical scatterer approximation in aqueous suspensions of sand: Journal of the Acoustical Society of America, v. 83, no. 2, p. 598–610, doi:10.1121/1.396153.

Sheskin, D.J., 2003, Handbook of Parametric and Nonparametric Statistical Procedures, 3d ed.: New York, Chapman and Hall/CRC, 1,195 p.

Shimizu, Y., Giri, S., Yamaguchi, S., and Nelson, J., 2009, Numerical simulation of dune-flat bed transition and stage-discharge relationship with hysteresis effect: Water Resources Research, v. 45, W04429, 14 p., doi:10.1029/2008WR006830.

Simmonds, J., and McLennan, D., 2005, Fisheries acoustics—Theory and practice, 2d ed.: Oxford, U.K., Blackwell Science Limited, 456 p.

Stanton, T.K., and Chu, D., 2008, Calibration of broadband active acoustic systems using a single spherical target: Journal of the Acoustical Society of America, v. 124, no. 1, p. 128–136, doi:10.1121/1.2917387.

Stevens, J.B., 1969, Geology of the Castolon area, Big Bend National Park, Brewster County, Texas: Austin, University of Texas, Ph.D. dissertation, 258 p.

Sutherland, T.F., Lane, P.M., Amos, C.L., and Downing, J., 2000, The calibration of optical backscatter sensors for suspended sediment of varying darkness levels: Marine Geology, v. 162, no. 2–4, p. 587–597, doi:10.1016/S0025-3227(99)00080-8.

Thevenot, M.M., Prickett, T.L., and Kraus, N.C., 1992, Tylers Beach, Virginia, Dredged material plume monitoring project 27 September to 4 October 1991: U.S. Army Corps of Engineers Dredging Research Program Technical Report DRP-92-7, 204 p.

Thorne, P.D., and Buckingham, M.J., 2004, Measurements of scattering by suspensions of irregularly shaped sand particles and comparison with a single parameter modified sphere model: Journal of the Acoustical Society of America, v. 116, no. 5, p. 2876–2889, doi:10.1121/1.1808458.

Thorne, P.D., and Campbell, S.C., 1992, Backscattering by a suspension of spheres: Journal of the Acoustical Society of America, v. 92, no. 2, p. 978–986, doi:10.1121/1.403967.

Thorne, P.D., and Hanes, D.M., 2002, A review of acoustic measurements of small-scale sediment processes: Continental Shelf Research, v. 22, no. 4, p. 603–632, doi:10.1016/S0278-4343(01)00101-7.

Thorne, P.D., and Hardcastle, P.J., 1997, Acoustic measurements of suspended sediments in turbulent currents and comparison with in-situ samples: Journal of the Acoustical Society of America, v. 101, no. 5, p. 2603–2614, doi:10.1121/1.418501.

Thorne, P.D., Hardcastle, P.J., and Soulsby, R.L., 1993, Analysis of acoustic measurements of suspended sediments: Journal of Geophysical Research, v. 98, n. C1, p. 899–910, doi:10.1029/92JC01855.

Thorne, P.D., MacDonald, I.T., and Vincent, C.E., 2014, Modelling acoustic scattering by suspended flocculating sediments: Continental Shelf Research, v. 88, p. 81–92, doi:10.1016/j.csr.2014.07.003.

Thorne, P.D., and Meral, R., 2008, Formulations for the scattering properties of suspended sandy sediments for use in the application of acoustics to sediment transport processes: Continental Shelf Research, v. 28, no. 2, p. 309–317, doi:10.1016/j.csr.2007.08.002.

Thorne, P.D., Sun, S., Zhang, J., Bjorno, I., and Mazoyer, T., 1997, Measurements and analysis of acoustic backscattering by elastic cubes and irregular polyhedral: Journal of the Acoustical Society of America, v. 102, no. 5, p. 2705–2713, doi:10.1121/1.420324.

Thorne, P.D., Waters, K.R., and Brudner, T.J., 1995, Acoustic measurements of scattering by objects of irregular shape: Journal of the Acoustical Society of America, v. 97, no. 1, p. 242–251, doi:10.1121/1.413109.

Topping, D.J., Melis, T.S., Rubin, D.M., and Wright, S.A., 2004, High-resolution monitoring of suspended-sediment concentration and grain size in the Colorado River in Grand Canyon using a laser-acoustic system, *in* Hu, C., and Tan, Y., eds., Proceedings of the 9th International Symposium on River Sedimentation: Beijing, China, Tsinghua University Press, p. 2507–2514.

Topping, D.J., Rubin, D.M., Grams, P.E., Griffiths, R.E., Sabol, T.A., Voichick, N., Tusso, R.B., Vanaman, K.M., and McDonald, R.R., 2010, Sediment transport during three controlled-flood experiments on the Colorado River downstream from Glen Canyon Dam, with implications for eddy-sandbar deposition in Grand Canyon National Park: U.S. Geological Survey Open-File Report 2010–1128, 111 p.

Topping, D.J., Rubin, D.M., and Melis, T.S., 2007a, Coupled changes in sand grain size and sand transport driven by changes in the upstream supply of sand in the Colorado River—relative importance of changes in bed-sand grain size and bed-sand area: Sedimentary Geology, v. 202, no. 3, p. 538–561, doi:10.1016/j.sedgeo.2007.03.016.

Topping, D.J., Rubin, D.M., Nelson, J.M., Kinzel, P.J., III, and Bennett, J.P., 1999, Linkage between grain-size evolution and sediment depletion during Colorado River floods, *in* Webb, R.H., Schmidt, J.C., Marzolf, G.R., and Valdez R.A., eds., The 1996 controlled flood in Grand Canyon: Washington, D.C, American Geophysical Union, Geophysical Monograph 110, p. 71–98.

Topping, D.J., Rubin, D.M., Nelson, J.M., Kinzel, P.J., III, and Corson, I.C., 2000b, Colorado River sediment transport 2—Systematic bed-elevation and grain-size effects of sand supply limitation: Water Resources Research, v. 36, no. 2, p. 543–570, doi:10.1029/1999WR900286.

Topping, D.J., Rubin, D.M., and Vierra, Jr., L.E., 2000a, Colorado River sediment transport 1—Natural sediment supply limitation and the influence of Glen Canyon Dam: Water Resources Research, v. 36, no. 2, p. 515–542, doi:10.1029/1999WR900285.

Topping, D.J., Rubin, D.M., Wright, S.A., and Melis, T.S., 2011, Field evaluation of the error arising from inadequate time averaging in the standard use of depth-integrating suspended-sediment samplers: U.S. Geological Survey Professional Paper 1774, 95 p.

Topping, D.J., Wright, S.A., Melis, T.S., and Rubin, D.M., 2006, High-resolution monitoring of suspended-sediment concentration and grain size in the Colorado River using laser-diffraction instruments and a three-frequency acoustic system, *in* Proceedings of the Eighth Federal Interagency Sedimentation Conference: Advisory Committee on Water Information, Subcommittee on Sedimentation, CD-ROM, ISBN 0-9779007-1-1.

Topping, D.J., Wright, S.A., Melis, T.S., and Rubin, D.M., 2007b, High-resolution measurements of suspended-sediment concentration and grain size in the Colorado River in Grand Canyon using a multi-frequency acoustic system, *in* Proceedings of the Tenth International Symposium on River Sedimentation: Moscow State University, p. 330–339, ISBN 978-5-89575-124-4, 978-5-89575-127-5.

Udden, J.A., 1907, A sketch of the geology of the Chisos country, Brewster County, Texas: Bulletin of the University of Texas, no. 93, scientific series 11, 101 p., accessed November 13, 2015, at https://books.google.com/books?id=K_pDAQAAMAAJ&pg=RA3-PA75&dq=chisos+chlorite&hl=en&sa=X&ved=0CD4Q6AEwBmoVChMI3LDOzceOyQIVVNRjCh30Agly#v=onepage&q=chisos%20chlorite&f=false.

U.S. Geological Survey, 2011a, Water quality samples for the nation, USGS, 11457500, Sacramento River at Sacramento, California: U.S. Geological Survey National Water Quality Information System, accessed on August 1, 2011, at http://nwis.waterdata.usgs.gov/nwis/qwdata/?site_no=11447500&agency_cd=USGS&amp.

U.S. Geological Survey, 2011b, Water quality samples for the nation, USGS, 07010000, Mississippi River at St. Louis, Missouri: U.S. Geological Survey National Water Quality Information System accessed on August 1, 2011, at http://nwis.waterdata.usgs.gov/nwis/qwdata/?site_no=07010000&agency_cd=USGS&amp.

Urick, R.J., 1948, The absorption of sound in suspensions of irregular particles: Journal of the Acoustical Society of America, v. 20, no. 3, p. 283–289, doi:10.1121/1.1906373.

Urick, R.J., 1962, Generalized form of the sonar equations: Journal of the Acoustical Society of America, v. 34, no. 5, p. 547–550, doi:10.1121/1.1918166.

Urick, R.J., 1975, Principles of underwater sound for engineers: New York, McGraw Hill, 384 p.

Voichick, N., and Topping, D.J., 2014, Extending the turbidity record—Making additional use of continuous data from turbidity, acoustic-Doppler, and laser diffraction instruments, and suspended-sediment samples in the Colorado River in Grand Canyon: U.S. Geological Survey Scientific Investigations Report 2014–5097, 31 p.

Wall, G.R., Nystrom, E.A., and Litten, S., 2006, Use of an ADCP to compute suspended-sediment discharge in the tidal Hudson River, New York: U.S. Geological Survey Scientific Investigations Report 2006–5055, 26 p.

West Texas Geological Society, 1972, Geology of the Big Bend area, Texas—Field trip guidebook with road log and papers on natural history of the area: Midland, Texas, Issue 72, Part 59, 248 p.

Wood, M.S., and Teasdale, G. N., 2013, Use of surrogate technologies to estimate suspended sediment in the Clearwater River, Idaho, and Snake River, Washington, 2008–10: U.S. Geological Survey Scientific Investigations Report 2013–5052, 29 p.

Wright, S., and Parker, G., 2004, Density stratification effects in sand-bed rivers: Journal of Hydraulic Engineering, v. 130, no. 8, p. 783–795, doi:10.1061/(ASCE)0733-9429(2004)130:8(783).

Wright, S.A. and Schoellhamer, D.H., 2005, Estimating sediment budgets at the interface between rivers and estuaries with application to the Sacramento-San Joaquin River Delta: Water Resources Research, v. 41, W09428, 17 p., doi:10.1029/2004WR003753.

Wright, S.A., Topping, D.J., and Williams, C.A., 2010, Discriminating silt-and-clay from suspended-sand in rivers using side-looking acoustic profilers *in* Proceedings of the 2nd Joint Federal Interagency Conference (9th Federal Interagency Sedimentation Conference and 4th Federal Interagency Hydrologic Modeling Conference on Sedimentation and Hydrologic Modeling): Advisory Committee on Water Information, Subcommittees on Hydrology and Sedimentation.

Appendixes 1–9

Appendix 1. Example Illustrating how Transmit-Pulse, Blanking, and Receive-Window Durations Together Determine the Locations and Sizes of the Measurement Cells

The following hypothetical example is used to more completely describe how the transmit-pulse, blanking, and receive-window durations together determine the locations and sizes of the measurement cells along an acoustic beam. This example consists of a transmit-pulse length of 0.44 m, followed by a blanking distance of 0.22 m, and two sequential receive windows of 0.44 m in length. These spatial magnitudes were chosen for this hypothetical example because they are the magnitudes of the transmit-pulse length, blanking distance, and receive-window lengths used by the 1-MHz EasyQ and SLD ADPs operating in diagnostics mode. In shallow, fresh water, at 20 ºC, the speed of sound is 1,480 m/s. Under these conditions, the above spatial magnitudes therefore equate to a transmit-pulse duration of 0.00030 s, blanking duration of 0.00030 s, and receive-window durations of 0.00059 s. In this example, the first 0.44-m-long receive window therefore begins 0.00030 s after the end of the transmit pulse and extends to 0.00089 s after the end of the transmit pulse. Similarly, the second 0.44-m-long receive window begins 0.00089 s after the end of the transmit pulse and extends to 0.00148 s after the end of the transmit pulse.

By virtue of the convolution of the 0.44-m-long transmit pulse and receive window, at the beginning of the first receive window the transducer is able to detect sound backscattered from particles located between 0.22 and 0.66 m from the transducer. The smaller of these two distances (0.22 m) arises from the interaction of the end of the transmit pulse with the beginning of the receive window, whereas the larger of these two distances (0.66 m) arises from the interaction of the beginning of the transmit pulse with the beginning of the receive window. At the end of the first receive window the transducer is able to detect sound backscattered from particles located between 0.66 and 1.1 m from the transducer. The smaller of these two distances (0.66 m) arises from the interaction of the end of the transmit pulse with the end of the receive window, whereas the larger of these two distances (1.1 m) arises from the interaction of the beginning of the transmit pulse with the end of the receive window. The cell associated with the first receive window therefore extends from 0.22 to 1.1 m from the transducer, and most of the detected backscatter is from the part of the cell located between 0.44 and 0.88 m from the transducer. Likewise, at the beginning of the second receive window the transducer is able to detect sound backscattered from particles located between 0.66 and 1.1 m from the transducer; at the end of the second receive window the transducer is able to detect sound backscattered from particles located between 1.1 and 1.44 m from the transducer. The cell associated with the second receive window therefore extends from 0.66 to 1.44 m from the transducer, and most of the detected backscatter is from the part of the cell located between 0.88 and 1.22 m from the transducer. This example illustrates that, in addition to it producing measurement cells wherein most of the backscatter is from particles located in the central 50 percent of each cell, the triangular-weighting function arising from the convolution of equal-length transmit pulse and receive windows also produces 50 percent overlap between sequential measurement cells (Nortek, 2013).

Appendix 2. Calibration Measurements, ADP-Array Configurations, and the Distance Between the Calibration Cross Section and the ADP Arrays at Each Study Site

The EDI sample-collection method was used in the ADP calibrations at the two study sites with previously determined, well-known lateral distribution of discharge within the measurement cross sections, that is, the CR87 and CR225 study sites, whereas the EWI sample-collection method was used at the other study sites. Suspended-sediment measurements made with either method are identical when done properly. Depending on the river and cross section, the EWI method may require collection of cumulatively more water and more sampling verticals than the EDI method. Spatial and temporal field errors associated with EDI and EWI measurements are described in Topping and others (2011); laboratory-processing errors associated with all physical suspended-sediment samples are based on methods in Topping and others (2010); field errors associated with suspended-sediment measurements made using cross-section calibrated automatic pump samplers are estimated using an analysis currently being prepared for publication. At the Colorado River study sites, EDI measurements at the CR87 and CR225 study sites were made from a cableway, whereas EWI measurements at the CR30 and CR61 study sites were made from a boat deployed under a tagline. EWI measurements at the Rio Grande study sites were made under a tagline, from a boat at higher discharge and by wading at lower discharge.

At the CR87, CR225, RG-CAS, and RG-RGV study sites, the ADPs of different frequency are located adjacent to one another within the same array. At the CR30 study site, the 1- and 2-MHz ADPs are mounted on the same side of the river, 30 m apart; at the CR61 study site, because the banks are unsuitable for attaching multiple ADPs to the same mount, the 1- and 2-MHz ADPs are mounted on opposite sides of the river; one ADP is located 60 m upstream of the other.

At the CR30 and RG-RGV study sites, the ADP arrays are located within the calibration cross section. At the RG-CAS study site, the calibration cross section is located ~50 m downstream from the ADP array; at the CR225 study site, the calibration cross section is located ~130 m downstream from the ADP array; at the CR87 study site, the calibration cross section is located ~200 m downstream from the ADP array; at the CR61 site, the calibration cross section is located ~750 m downstream from the ADPs at the former location of a USGS cableway (Griffiths and others, 2012). This exceptionally large, and undesirable, longitudinal distance between the ADP array and the calibration cross section at the CR61 site originated from the desire to continue making EWI measurements at the cross section where a large number of historical suspended-sediment measurements were made by the USGS. Unfortunately, no suitable mounting locations could be found on the riverbank for the ADPs near the former location of the USGS cableway because of poor bank material, spatially nonuniform flow in the river, or proximity to a downstream tributary (the Little Colorado River) that episodically backwaters the former location of the cableway.

Appendix 3. Effect of the Downing and Others (1995) Empirical Near-Field Correction

Within the near-field region of a circular piston transducer, the pressure field is extremely complicated. In the near-field region in front of the transducer, there is a central zone of higher pressure surrounded by multiple rings of slightly lower pressure; the number of these rings increases with the ratio of a_T/λ (figs. 7–8 in Lockwood and Willette, 1973), where a_T is the transducer radius and λ is the acoustic wavelength. Along the axis of the transducer, the pressure amplitude is an oscillating function of range that reaches a maximum at the critical, that is, Fresnel, distance $r_C=a_T^2/\lambda$ (Kino, 1987). Beyond this distance, the pressure decays monotonically into the far field as a function of range and the spreading losses are spherical (Lockwood and Willette, 1973; Medwin and Clay, 1997).

On the basis of laboratory experiments in a suspension tank conducted using 5 circular piston transducers operating over the 1- to 5-MHz range in acoustic frequency, Downing and others (1995) developed an empirical correction to account for nonspherical spreading losses in the near-field region. The form of this correction is:

$$\psi_{NF}=\frac{1+1.35\left(r/r_D\right)+\left(2.5\left(r/r_D\right)\right)^{3.2}}{1.35\left(r/r_D\right)+\left(2.5\left(r/r_D\right)\right)^{3.2}} \qquad (3\text{-}1)$$

where

r is the axial distance, that is, range from the transducer in m, and

r_D is a larger critical distance defined as $r_D=\pi r_C$.

This correction is largest at $r=0$ and decreases to 1 at $r\geq r_D$. The larger critical distance of r_D used by Downing and others (1995) is defined in the acoustical literature as the safe distance beyond which there is no doubt that the pressure decays as $1/r$ (Medwin and Clay, 1997). Because the Downing and others (1995) empirical correction applies at distances greater than r_C and less than r_D, where the pressure likely decays as $1/r$, there is a possibility that it may correct data that do not need to be corrected.

The Downing and others (1995) empirical near-field correction has gained acceptance within the literature of those using commercially available acoustic-Doppler current profilers (ADCPs) and ADPs (for example, Wall and others, 2006; Wood and Teasdale, 2013; Latosinski and others, 2014) even though it was developed under very different conditions than those associated with acoustical measurements made by ADCPs and ADPs. Downing and others (1995) reported transmit-pulse durations of ~0.000014 s and measurement cells of ~0.01 m. Assuming a speed of sound of 1,480 m/s, the transmit-pulse duration of ~0.000014 s corresponds to a transmit-pulse length of ~0.02 m. In the Downing and others (1995) experiments, each time-averaged acoustical measurement consisted of somewhat more than 100 pings. In contrast, the transducers in the ADPs used in this study have transmit-pulse lengths that range from 0.22 to 0.55 m and nominal measurement cells that range in size from 0.22 to 0.55 m. Each time-averaged acoustical measurement made by the ADPs in this study consists of an average of between 960 to 2,880 pings.

Figure 3-1. (**following page**) Examples of measurements of the relative backscatter, *B*, made with and without the Downing and others (1995) empirical near-field correction. Shown in each figure panel are the values of r_C and r_D for each ADP. The values of *B* shown are those averaged between the two horizontal beams. Because inclusion of the Downing and others (1995) correction affects the calculations of the sediment attenuation coefficient, and therefore affects the calculated values of *B* in each cell, use of the Downing and others (1995) correction may substantially affect the values of *B* in each cell when the correction of data within the region between r_C and r_n is particularly large. ***A***, Measurements of *B* made with a Nortek 1-MHz EasyQ at the CR87 study site at 4:32 MST on December 7, 2011; no measurement cells on this ADP fall within the region between r_C and r_D. ***B***, Measurements of *B* made with a Nortek 2-MHz EasyQ at the CR87 study site at 4:35 MST on December 7, 2011; two measurement cells on this ADP fall within the region between r_C and r_D. ***C***, Measurements of *B* made with a Nortek 1-MHz EasyQ at the CR87 study site at 2:35 MST on September 29, 2009; no measurement cells on this ADP fall within the region between r_C and r_D. ***D***, Measurements of *B* made with a Nortek 2-MHz EasyQ at the CR87 study site at 4:35 MST on September 29, 2009; two measurement cells on this ADP fall within the region between r_C and r_D. ***E***, Measurements of *B* made with the OTT 1-MHz SLD at the RG-RGV study site at 4:04 CST on July 16, 2011; one measurement cell on this ADP falls within the region between r_C and r_D. ***F***, Measurements of *B* made with an OTT 2-MHz SLD at the RG-RGV study site at 4:04 CST on July 16, 2011; one measurement cell on this ADP falls within the region between r_C and r_D. ***G***, Measurements of *B* made with an OTT 1-MHz SLD at the RG-RGV study site at 16:04 CST on July 15, 2012; one measurement cell on this ADP falls within the region between r_C and r_D. ***H***, Measurements of *B* made with a Nortek 2-MHz EasyQ at the RG-RGV study site at 16:04 CST on July 15, 2012; two measurement cells on this ADP fall within the region between r_C and r_D. ***I***, Measurements of *B* made with an OTT 1-MHz SLD at the RG-RGV study site at 22:49 CST on July 14, 2012; one measurement cell on this ADP falls within the region between r_C and r_D. ***J***, Measurements of *B* made with a Nortek 2-MHz EasyQ at the RG-RGV study site at 22:49 CST on July 14, 2012; two measurement cells on this ADP fall within the region between r_C and r_D.

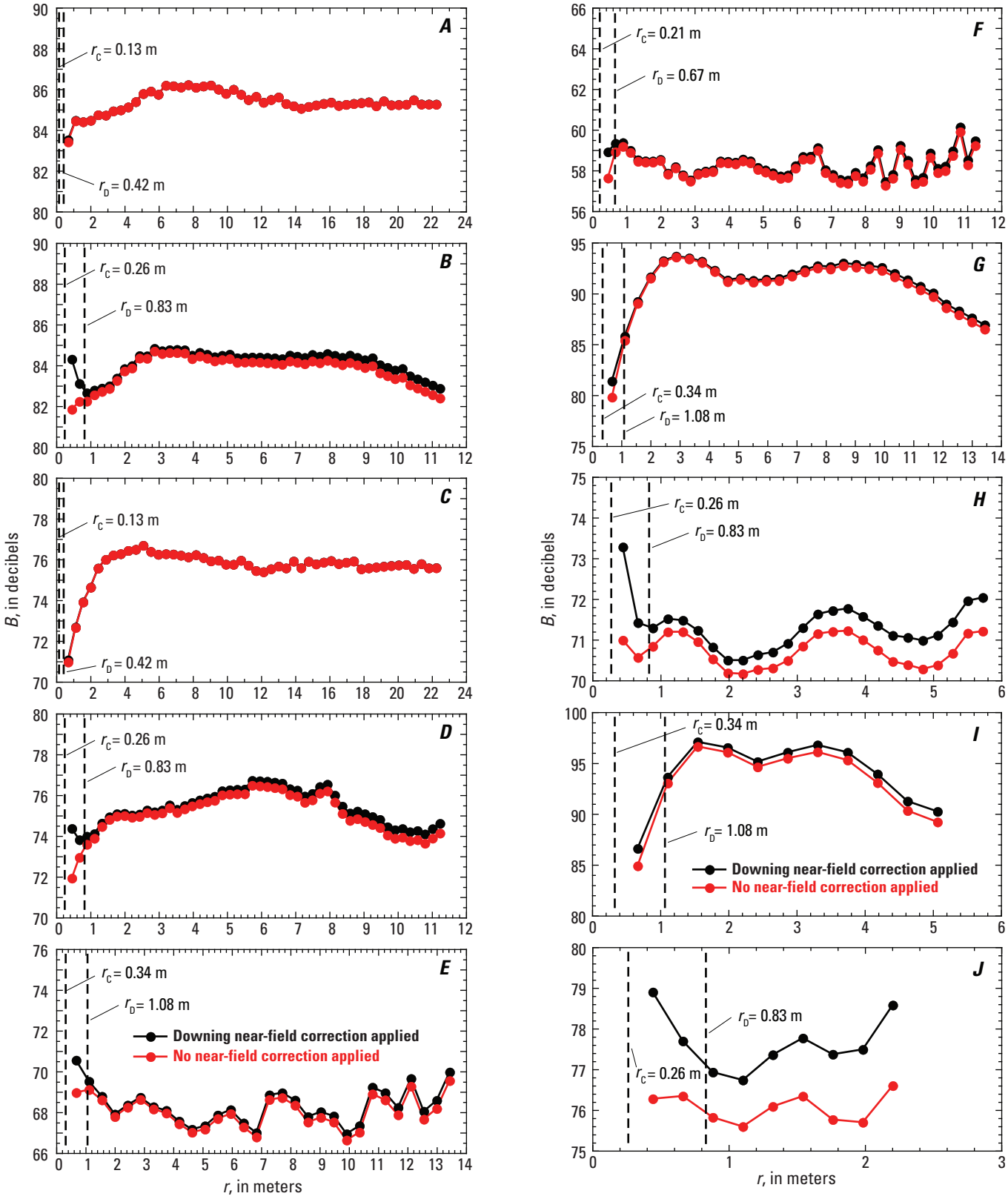
A
r_C = 0.13 m
r_D = 0.42 m
B
r_C = 0.26 m
r_D = 0.83 m
C
r_C = 0.13 m
r_D = 0.42 m
D
r_C = 0.26 m
r_D = 0.83 m
E
r_C = 0.34 m
r_D = 1.08 m
Downing near-field correction applied
No near-field correction applied
F
r_C = 0.21 m
r_D = 0.67 m
G
r_C = 0.34 m
r_D = 1.08 m
H
r_C = 0.26 m
r_D = 0.83 m
I
r_C = 0.34 m
r_D = 1.08 m
Downing near-field correction applied
No near-field correction applied
J
r_D = 0.83 m
r_C = 0.26 m
B, in decibels
r, in meters

Figure 3-1.

Thus, the reverberating volumes sampled by the ADPs in this study are over an order of magnitude larger than those sampled in the Downing and others (1995) experiments and the amount of averaging in the acoustical measurements made by the ADPs used in this study is more than two orders of magnitude greater than in the Downing and others (1995) experiments. Therefore, because of the large differences between the reverberating volumes and the amount of averaging, it is not known whether the empirical near-field correction of Downing and others (1995) should apply to the acoustical measurements made by ADCPs or ADPs. In addition, because none of the ADPs used in this study make acoustical measurements in cells located at distances of $r<r_C$, use of the more conventional definition of the critical distance would thus indicate that no near-field correction should need to be applied.

Comparison of data processed with and without the Downing and others (1995) near-field correction suggests that the Downing and others correction is generally an overcorrection in the region between r_C and r_D, and that within region between r_C and r_D, the use of no near-field correction ($\psi_{NF}=1$) generally performs better (fig. 3-1). The examples shown in figure 3-1 were selected because they capture the typical behavior of ADP measurements at the various study sites with and without inclusion of the Downing and others (1995) correction. In all but one of the examples shown (that is, fig. 3-1*F*), use of the Downing and others (1995) correction degrades the measurements of relative backscatter, *B*, along the beam by overcorrecting the data in the cells that fall in the region between r_C and r_D. This apparent overcorrection sometimes results in values of *B* in these cells that are much higher than the values of *B* in the cells located at slightly greater distances along the beam (see, for example, figs. 3-1*B*, *D*, *E*, *H*, and *J*), which is not physically realistic. The overcorrection has the greatest effect at higher concentrations of silt and clay, when *B* can be measured in fewer cells (fig. 3-1*J*). In this case, inclusion of the Downing and others (1995) correction, by overcorrecting the data in the first cell, generally results in greater variance in the measurements of *B* along the beam. This occurs because inclusion of the Downing and others (1995) empirical correction in the method results in greater variance about the regressions used to calculate the sediment attenuation coefficient (method described in appendix 7). Because it is not clear that the Downing and others (1995) empirical near-field correction is even appropriate for the types of ADPs used in this study, and because inclusion of this correction either has minimal or apparently detrimental effects on the measurements made by these ADPs, the Downing and others (1995) correction is not used in this study.

Appendix 4. Comparison of the Effects of Water Temperature, Pressure, and Salinity on the Water Absorption Coefficient

At the small depths and low-salinity conditions that generally occur in rivers, water temperature provides the only meaningful control on the value of the water absorption coefficient (α_W). Figure 4-1 illustrates that the dominant control on the water absorption coefficient is change in water temperature, with lesser and relatively unimportant regulation of this coefficient by changes in water depth (pressure) and salinity. At each value of water temperature, the bars plotted include the combined range of the effects of pressure and salinity. Shown in this figure are the values of α_W calculated by the methods of Schulkin and Marsh (1962) and, for comparison, Ainslie and McColm (1998).

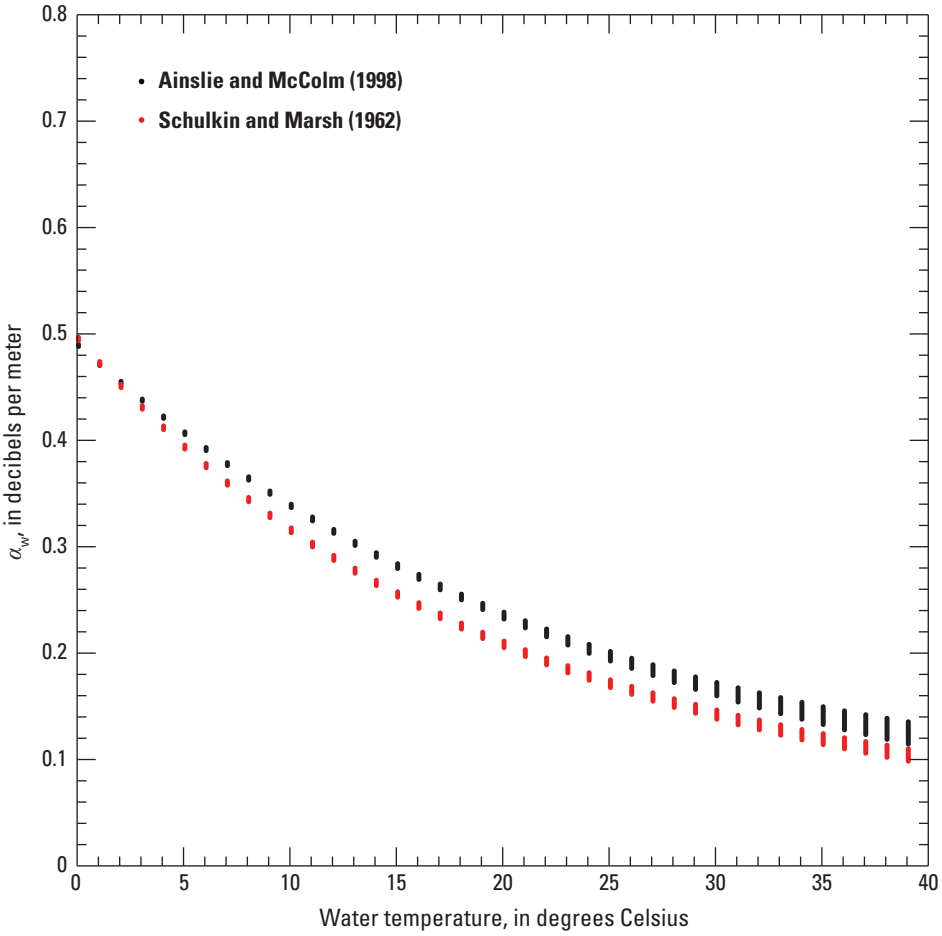

Figure 4-1. The water absorption coefficient, α_W, plotted as a function of water temperature in 1-degree increments over wide ranges of pressure and salinity; the lengths of the vertical lines at each 1-degree increment indicate the total range in α_W at each 1-degree increment resulting from changes in water depth ranging from 0 to 20 m and changes in specific conductance (a measure of salinity) ranging from 100 to 4,000 mS/cm at 25 °C. The ranges in both water depth and specific conductance used in this plot are larger than those found in almost all rivers where an acoustic-Doppler profiler might be deployed.

Appendix 5. Details of Grain-Size Distributions Used to Develop Theoretical *B´* Relations at the CR87 and RG-RGV Study Sites

At the CR87 study site, the grain-size distribution of the suspended sand under typical conditions is characterized by $D_{50\text{-XS-SAND-REF}}$=0.125 mm and σ_G=0.63ϕ (on the basis of 1,770 EDI measurements made between August 21, 1999, and November 17, 2013). Because the sand is mostly composed of quartz, the density of the suspended sand is assumed to be equal to the density of quartz (2,650 kg/m^3) at all study sites. Solution for the theoretical values of α_{UNIT} at the 600-kHz, 1-MHz, and 2-MHz acoustic frequencies that agree with the measured values of α_{UNIT} within a few percent (fig. 6 in the main part of the report) indicates that the suspended silt and clay at the CR87 study site is best characterized as having a D_{50}~0.0008 mm, σ_G~3ϕ, and ρ_S~2,500 kg/m^3. This lower-than-quartz density value for ρ_S is also justified on the basis of the documented presence of lower-density clays in the Colorado River (see "Physical Basis for the Sediment Attenuation Coefficient" and "Estimation of the Grain-Size Distribution and Wet Density of the Silt and Clay: Attenuation Constraint" sections in the main part of report). Use of these parameters to characterize the typical grain-size distributions and densities of the suspended sand and the suspended silt and clay at this study site also results in the theoretical predictions of *B´* at the 600-kHz, 1-MHz, and 2-MHz frequencies plotted in figures 14*A–C* (in the main part of the report) that are in excellent agreement with the empirical values of *B´* calculated relative to the BBC relations plotted in figure 11 (in the main part of the report).

At the RG-RGV study site, the grain-size distribution of the suspended sand under typical conditions is characterized by $D_{50\text{-XS-SAND-REF}}$= 0.105 mm and σ_G= 0.65ϕ (on the basis of 35 EWI measurements made between December 11, 2010, and January 30, 2014). Solution for the theoretical values of α_{UNIT} at the 1-MHz and 2-MHz acoustic frequencies that agree with the measured values of α_{UNIT} within a few percent indicates that the suspended silt and clay at the RG-RGV study site is best characterized as having a D_{50}~0.002 mm, σ_G~2.7ϕ, and ρ_S~3,200 kg/m^3. This higher-than-quartz density value for ρ_S suggests the dominance of higher-density chlorite-group clays in suspension in the Rio Grande. This prediction of chlorite clay in suspension is reasonable given that chlorite has been described in the volcanic and intrusive igneous rocks that supply sediment to the Rio Grande in the study area (Udden, 1907; Stevens, 1969; West Texas Geological Society, 1972; Henry and others, 1989). Use of these parameters to characterize the typical grain-size distributions and densities of the suspended sand and the suspended silt and clay at this study site result in the theoretical predictions of *B´* at 2-MHz frequency that are in excellent agreement with the empirical values of *B´* plotted in figure 14*D* (in the main part of the report).

Appendix 6. A Method for the Detection and Correction of Discharge-Correlated Shifts in the BBC Relation at High Values of *S*

A key requirement for accurate acoustical measurements of $C_{XS\text{-}SAND}$ is that the BBC relation does not shift over time as a result of changes in the relation between C_{SAND} in the ensonified part of the cross section and $C_{XS\text{-}SAND}$. Unfortunately, there are multiple processes in sand-bedded rivers that could cause the BBC relation to shift through changes in either the vertical or lateral distribution of suspended sand in the cross section. Examples of these processes are (1) bed scour and fill (Colby, 1964; Topping and others, 2000a, b), (2) changes in the spatial distribution of the bed sand (Anima and others, 1998; Schmidt and others, 2007; Buscombe and others, 2014), (3) changes in the grain-size distribution of the bed sand (Rubin and others, 1998, 2010; Topping and others, 1999, 2000a, b), and (4) density stratification (Gelfenbaum and Smith, 1986; McLean, 1991, 1992; Wright and Parker, 2004). Although these processes may typically be correlated with water discharge, they may also lag discharge. For example, sand introduced to a river during a tributary flood will travel downstream as a sediment wave, with a component in suspension, in the bedload, and in the bed (Topping and others, 2000b). As the front of this sediment wave reaches a given cross section far downstream from the tributary that supplied the sand, the changes in the sediment conditions at this cross section will greatly lag the changes in water discharge associated with the tributary flood. These changes in sediment conditions can include changes in bed elevation, the lateral distribution of bed sand, the grain-size distribution of bed sand, and perhaps also in density stratification (as a result of the changes in the bed-sand conditions). All of these changes may greatly influence the relation between C_{SAND} in the ensonified part of the cross section and $C_{XS\text{-}SAND}$, thus causing shifts in the BBC relations for the two ADPs. If at all possible, care should therefore be taken to not deploy ADPs at locations where these processes could have a large effect on the acoustical data, especially in cases where these processes could greatly lag changes in water discharge. However, in some cases, like in the Rio Grande at the RG-CAS and RG-RGV study sites, several of these processes likely occur over long reaches of the channel and are thus unavoidable.

In this appendix, we provide examples of how to recognize and correct discharge-correlated shifts in BBC relations under conditions of relatively high $C_{XS\text{-}SILT\text{-}CLAY}$—conditions where it may be difficult to directly detect shifts in BBC relations. In cases where large shifts in BBC relations greatly lag discharge (as in the example above), there may be no method to correct for these shifts. In these unfortunate situations, there may be no recourse but to either accept larger-than-normal errors in the acoustical measurements of $C_{XS\text{-}SAND}$ or to move the ADPs to locations not affected by these shifts.

The Rio Grande at both the RG-CAS and RG-RGV study sites is a sand-bedded channel subject to large amounts of bed scour (up to several m) and large ranges in stage (up to 7 m) during floods. The ADPs at these study sites are deployed such that the horizontal beams project through the flow ~1 m above the bed at low discharge. As discharge increases, the bed scours at the ADP locations at both study sites. For example, as discharge increases from <30 m^3/s to ~250 m^3/s, channel cross sections measured during EWI measurements indicate that the flow depth above the ADP horizontal beams at the RG-RGV study site increases by ~1.5 m while the bed below these beams scours by ~1 m. Thus, as discharge increases, the vertical distance between the horizontal beams and the bed increases almost as much as the vertical distance between these beams and the water surface. If one assumes a simple Rouse-profile shape for a suspended-sand concentration profile (for example, McLean, 1992), then, because of the substantial increase in distance between the horizontal beams and the bed, an identical suspended-sand concentration "sampled" by the fixed horizontal beams is likely to be related to a larger value of $C_{XS\text{-}SAND}$ at higher discharge than at lower discharge. Therefore, large amounts of bed scour under an ADP deployed close to the bed may result in large discharge-associated changes in the relation between C_{SAND} sampled by the acoustic beams and $C_{XS\text{-}SAND}$. As a result of the bed scour in this example, identical values of $\overline{B}$ and α_S will therefore be associated with a lower value of $C_{XS\text{-}SAND}$ at lower discharges than at higher discharges.

Another process that is likely to occur in a sand-bedded river and can result in similar behavior in the relation between C_{SAND} in the ensonified part of the cross section and $C_{XS\text{-}SAND}$ is density stratification. As discharge increases and the amount of coarser sand in suspension increases, the increased vertical gradient in a suspended-sand concentration profile results in the development of density stratification that will gradually damp the turbulence (Gelfenbaum and Smith, 1986; McLean, 1991, 1992; Wright and Parker, 2004). The key result of this density-stratification process pertinent to this study is that, as discharge increases, the vertical gradient in the suspended-sand concentration profile will increase such that, without any bed scour required, an identical C_{SAND} sampled by the fixed horizontal beams will be related to a larger value of $C_{XS\text{-}SAND}$ at higher discharge than at lower discharge. As in the case of bed scour, this process could therefore also result in large discharge-correlated changes in the relation between C_{SAND} in the ensonified part of the cross section and $C_{XS\text{-}SAND}$. As the effects of density stratification increase with increasing discharge, identical values of $\overline{B}$ and α_S will likely be associated with progressively higher values of $C_{XS\text{-}SAND}$.

At least one of these processes (or one of the other processes listed at the beginning of this appendix) is likely to be present at an ADP-deployment site, but in many cases the effects of these processes will be minor and can be neglected. In essence, both bed-scouring and density-stratification processes result in a downward shift in the BBC relation (that is, the y-intercept of the BBC relation becomes more negative) as water discharge decreases. Depending on how large the effects of these processes are at any given ADP-deployment site, this downward shift may be inconsequential, and therefore unimportant, or relatively large and important. Large amounts of bias will be introduced into acoustical measurements of $C_{XS\text{-}SAND}$ if a large discharge-correlated downward shift in the BBC relation is not recognized and corrected.

In rivers where $C_{XS\text{-}SILT\text{-}CLAY}$ is always relatively low compared to $C_{XS\text{-}SAND}$, discharge-correlated shifts in BBC relations can be detected directly by simply regressing BBC relations for different ranges in discharge. Unfortunately, in rivers with naturally high values of $C_{XS\text{-}SILT\text{-}CLAY}$, this direct approach is usually impossible, owing to the fact that S>>2 at higher discharges, and accurate BBC relations cannot be regressed under such conditions. Because of this complexity, we have developed the following indirect approach for detecting discharge-correlated BBC shifts that does not require relatively low $C_{XS\text{-}SILT\text{-}CLAY}$. This approach utilizes F-tests to detect relations between water discharge and $\log_{10}(S)$ under conditions of constant $\overline{B}$ and α_S. If no such significant relations exist, no unique relation between $\overline{B}$ and $C_{XS\text{-}SAND}$ exists under conditions of constant α_S, and the grain-size distribution of the suspended sand is relatively constant, then the lack of relation between $\overline{B}$ and $C_{XS\text{-}SAND}$ is likely the result of the backscatter masking process depicted in figure 16 in the main part of the report. However, if these F-tests indicate that there are significant relations between water discharge and $\log_{10}(S)$ under conditions of constant $\overline{B}$ and α_S and at values of $\log_{10}(S)$ less than those where backscatter masking is expected to occur (see, for example, fig.16 in the main part of the report), discharge-correlated BBC shifts are likely present (fig. 6-1). If further analysis indicates that these significant relations arise because of positive correlations between water discharge and $C_{XS\text{-}SAND}$ at constant $\overline{B}$ and α_S (fig. 6-2), and it is impossible to choose a different ADP-deployment location, corrections must be made to achieve acceptable accuracies in acoustical measurements of $C_{XS\text{-}SAND}$. The presence of uncorrected discharge-correlated BBC shifts will result in increased upward scatter in measurements of $\log_{10}(S)$ relative to theoretical relations between α_S and $\log_{10}(S)$, at values of α_S less than those where backscatter masking (depicted in figures 16–17 in the main part of the report) becomes important. Thus, lack of recognition of these shifts will result in underpredictions of $\log_{10}(S)$ over lower and moderate ranges in α_S and therefore result in severe underpredictions of B' at all but the highest values of α_S.

Correction for the negative effect of discharge-correlated BBC shifts on acoustical measurements of $C_{XS\text{-}SAND}$ is usually possible through application of discharge-weighting factors to $\log_{10}(S)$. In some cases, application of discharge-weighting factors may also allow reasonable estimation of $C_{XS\text{-}SAND}$ under conditions of backscatter masking at high values of S. In the cases of the 1-MHz-ADP and 2-MHz-ADP at study site RG-RGV, shown in figures 6-1*A–B* and 6-2*A–B*, discharge-weighting the measured values of $\log_{10}(S)$ reduces both the mean value and variance in $\log_{10}(S)$ at constant $\overline{B}$ and α_S to be in better agreement with theoretical predictions of $\log_{10}(S)$ in figure 6-3. In the 1-MHz-ADP example, the discharge-weighting factor that results in the best agreement between measurements and theory across all values of $\overline{B}$ is (Q/80), where Q is the water discharge (in m^3/s) associated with each measurement of $\log_{10}(S)$. In the 2-MHz-ADP example, the discharge-weighting factor that results in the best agreement is (Q/71). These discharge-weighting factors are only applied when Q is less than the value in the denominator. Once discharge-weighting factors are determined, corrected values of $\log_{10}(S)$ at any given value of $\overline{B}$ and α_S can therefore be estimated by dividing the theoretically predicted values of $\log_{10}(S)$ by these discharge-weighting factors.

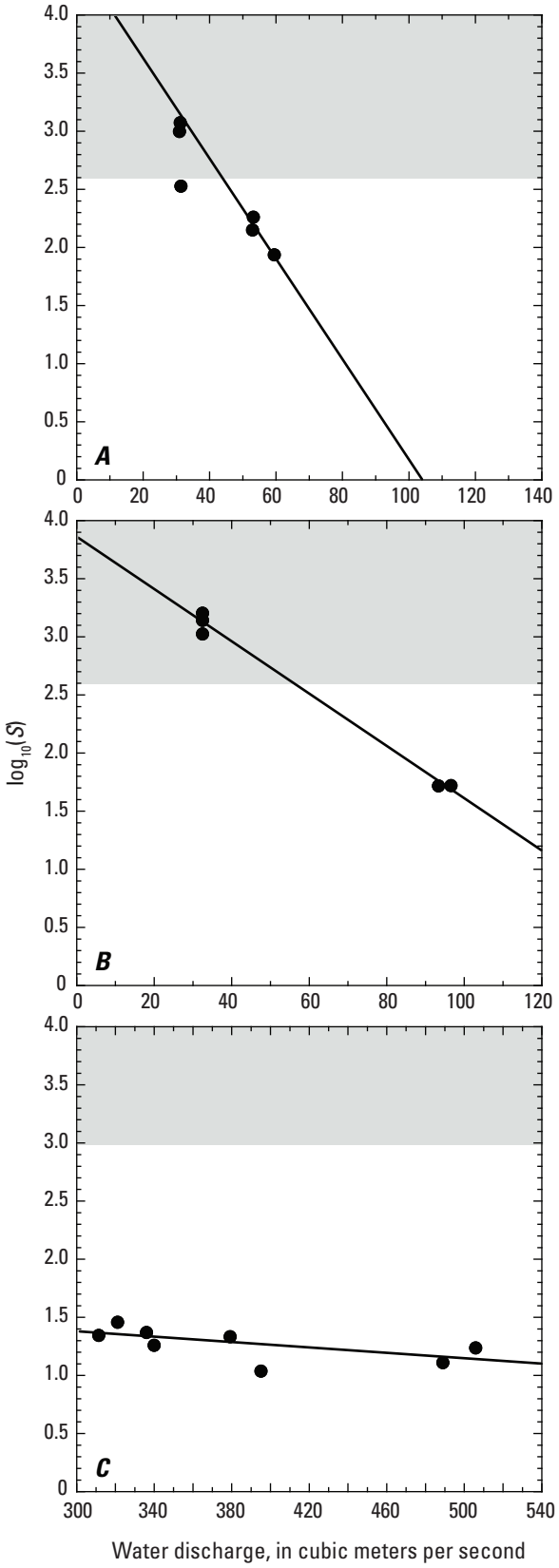

Figure 6-1. Examples of the presence and absence of significant relations between water discharge and $\log_{10}(S)$ at constant $\bar{B}$ and α_S. Regressions used in F-tests are depicted as solid black lines. ***A***, Significant relation (p_{SIG}=0.031) between water discharge and $\log_{10}(S)$ for the 92–94 dB range in $\bar{B}$ and the 4.0–4.5 dB/m range in α_S for the 1-MHz ADP at the RG-RGV study site. ***B***, Significant relation (p_{SIG}=0.0018) between water discharge and $\log_{10}(S)$ for the 81–83 dB range in $\bar{B}$ and the 33–34 dB/m range in α_S for the 2-MHz ADP at the RG-RGV study site. ***C***, Lack of a significant relation (p_{SIG}=0.10) between water discharge and $\log_{10}(S)$ for the 86–88 dB range in $\bar{B}$ and the 1.6–1.8 dB/m range in α_S for the 1-MHz ADP at the CR87 study site. Gray shaded regions denote approximate ranges of $\log_{10}(S)$ where backscatter masking is expected. Measurements of $\log_{10}(S)$ are from the periods used to develop the base-backscatter-calibration relations. Further F-test analyses (fig. 6-2) indicate that the significant relations in ***A*** and ***B*** arise purely from significant relations between water discharge and $C_{XS\text{-}SAND}$, and not from relations between water discharge and $C_{XS\text{-}SILT\text{-}CLAY}$.

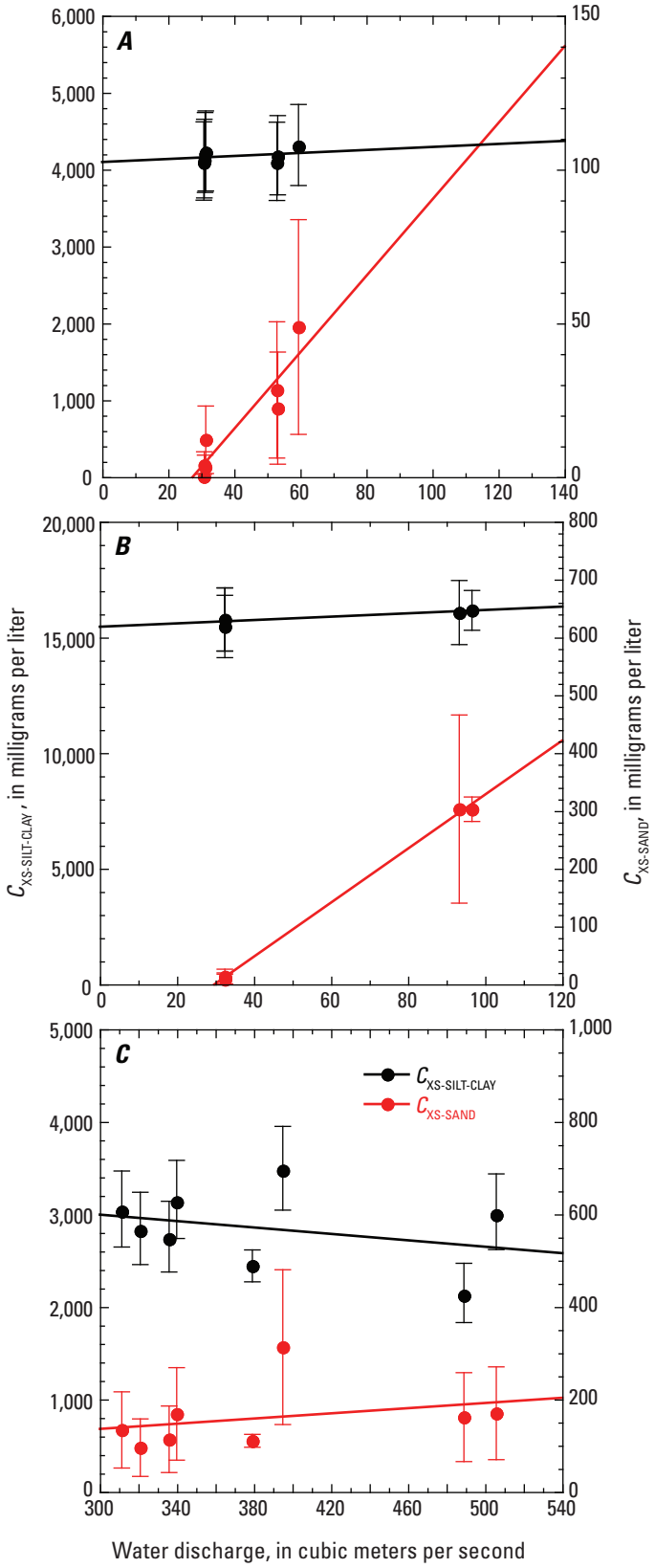

Figure 6-2. Examples of the presence and absence of significant correlations between water discharge and $C_{XS\text{-}SAND}$ at constant $\bar{B}$ and α_S for the measurements depicted in figure 6-1. There is no significant correlation between water discharge and $C_{XS\text{-}SILT\text{-}CLAY}$ in any of these examples. ***A***, Significant relation (p_{SIG}=0.0027) between water discharge and $C_{XS\text{-}SAND}$ for the 92–94 dB range in $\bar{B}$ and the 4.0–4.5 dB/m range in α_S for the 1-MHz ADP at the RG-RGV study site. ***B***, Significant relation (p_{SIG}=9.7×10^{-9}) between water discharge and $C_{XS\text{-}SAND}$ for the 81–83 dB range in $\bar{B}$ and the 33–34 dB/m range in α_S for the 2-MHz ADP at the RG-RGV study site. ***C***, Lack of a significant relation (p_{SIG}=0.46) between water discharge and $C_{XS\text{-}SAND}$ for the 86–88 dB range in $\bar{B}$ and the 1.6–1.8 dB/m range in α_S for the 1-MHz ADP at the CR87 study site.

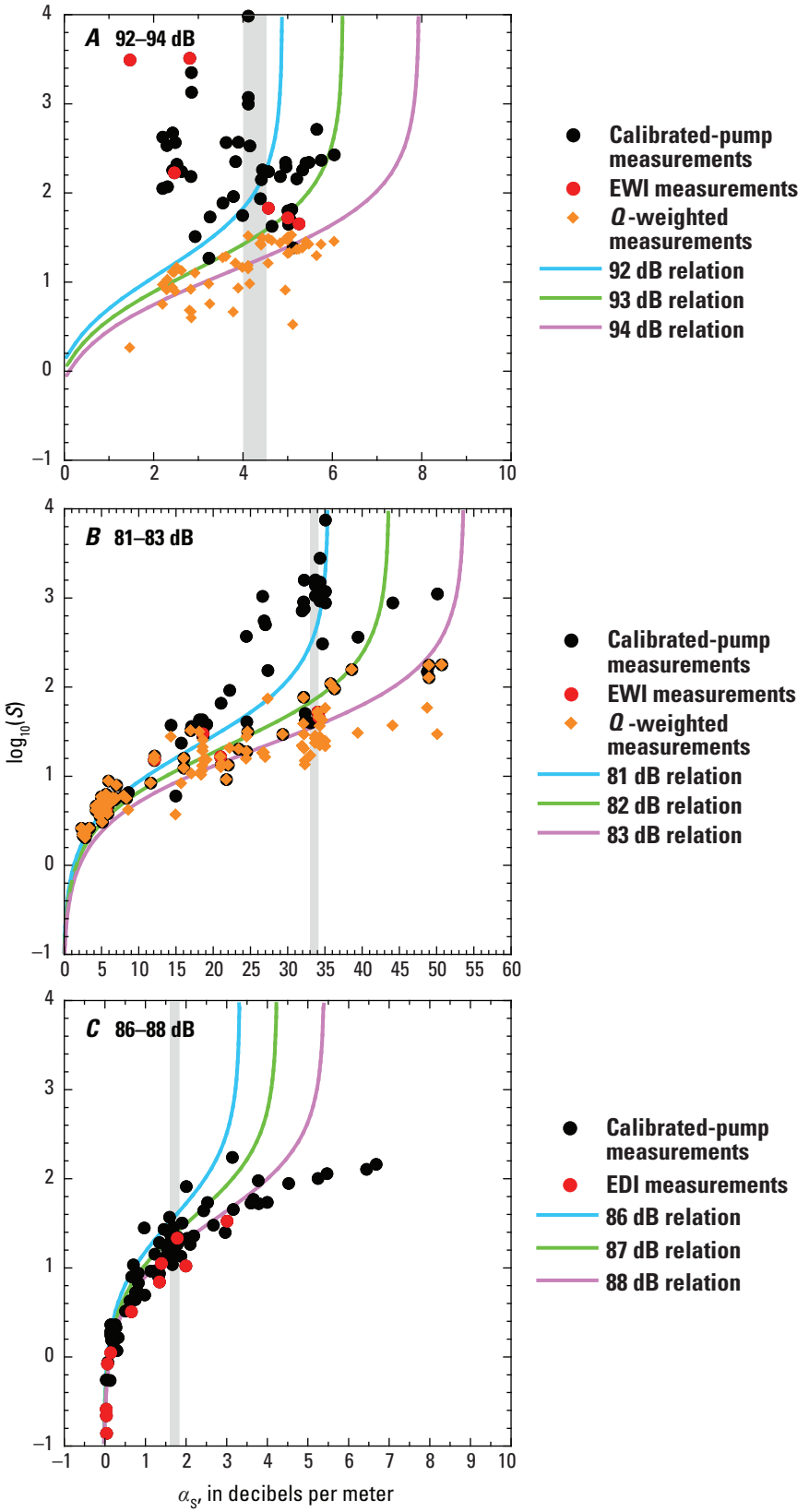

Figure 6-3. Examples of the increased upward scatter in measured $\log_{10}(S)$ relative to theoretical $\log_{10}(S)$ that arises from discharge-correlated base-backscatter-calibration (BBC) relation shifts affecting the examples in figures 6-1 and 6-2. Gray shaded regions denote the ranges in α_s used in the examples in figures 6-1-and 6-2. Theoretical and measured relations between α_s and $\log_{10}(S)$ for the (***A***) 92–94 dB range in $\bar{B}$ for the 1-MHz acoustic-Doppler profiler (ADP) at the RG-RGV study site; (***B***) 81–83 dB range in $\bar{B}$ for the 2-MHz ADP at the RG-RGV study site, and (***C***) 86–88 dB range in $\bar{B}$ for the 1-MHz ADP at the CR87 study site (data in this plot are the same as in figure 17*A* in the main part of the report). Equal-width increment (EWI), equal-depth increment (EDI), and calibrated-pump measurements of $\log_{10}(S)$ are indicated. Multiplying the measurements of $\log_{10}(S)$ by the discharge-weighting factors in the text for the two RG-RGV examples in ***A*** and ***B*** that exhibit discharge-correlated BBC shifts in figures 6-1*A*–*B* and 6-2*A*–*B* greatly improves the agreement between theoretical and measured relations between α_s and $\log_{10}(S)$. No discharge weighting is required in the CR87 example in ***C*** because discharge-correlated BBC shifts were not detected in figures 6-1*C* and 6-2*C*.

Appendix 7. Single-Frequency ADP Calibration Procedure

In order, the 13 steps in the single-frequency calibration procedure are as follows:

(1) Determine which horizontal beams to use and the maximum number of cells to use. Factors that will limit the maximum cell number are: beams hitting the opposite bank, beams hitting or grazing an underwater bar, or beams grazing the water surface at low stage. Because suspended-sediment conditions are rarely uniform along the acoustic beams, cell number is directly related to error. Decreases in cell number result in increases in the variances in both α_S and $\overline{B}$, with the effect on $\overline{B}$ being greater than the effect on α_S (figs. 7-1–7-2) Because α_S is the basis for acoustical measurements of $C_{XS\text{-}SILT\text{-}CLAY}$ and α_S and $\overline{B}$ are used in combination for acoustical measurements of $C_{XS\text{-}SAND}$, these increases in variance in α_S and $\overline{B}$ will directly result in greater error in acoustical measurements of $C_{XS\text{-}SILT\text{-}CLAY}$ and $C_{XS\text{-}SAND}$ (fig. 7-3). In addition, once the maximum cell number is determined, this value cannot be reduced without changing the ADP calibration. Otherwise, substantial biases in α_S and $\overline{B}$, and therefore also in $C_{XS\text{-}SILT\text{-}CLAY}$ and $C_{XS\text{-}SAND}$, may be introduced.

(2) If more than one beam is used, average the raw measurements of A between the corresponding cells in each beam (for example, see fig. 3*A* in main part of report). These average values of A among the beams are then converted to B_F in each cell where A exceeds the effective noise floor (for example, fig. 3*B* in main part of report). Calculation of the effective noise floor is an iterative process described in steps 3–5, below.

(3) An initial effective noise floor is calculated as the sum of the instrument noise floor and the noise-floor offset. The instrument noise floor is the noise floor recorded at each time step by the ADP. The noise-floor offset is iteratively determined as the value added to the instrument noise floor to result in an effective noise floor that exceeds the values of A in the distal part of the beam where A tends to asymptotically approach the instrument noise floor in a curved manner (fig. 7-4). Because of this asymptotic behavior, selection of a noise-floor offset that is too low will yield linear regressions in step 4 with slopes that are too low as a result of fitting a concave-up curve with a line. As stated in step 5, selection of noise-floor offsets that are too low will result in an incorrect dependence of α_S and $\overline{B}$ on the number of cells where A exceeds the effective noise floor.

(4) A least-squares linear regression is used to regress the values of B_F on r to solve for α_S using the working effective noise floor determined in the previous step. α_S is equal to the slope of this regression divided by –2.

(5) Calculate B in each cell using the values of B_F and α_S. Average the values of B first among equivalent cells in each beam used and then among all cells along the beams where A exceeds the effective noise floor to calculate the beam-averaged backscatter, $\overline{B}$ (for example, fig. 3*C* in the main part of report).

(6) Time series of α_S and $\overline{B}$ during conditions of varying, but high, $C_{XS\text{-}SILT\text{-}CLAY}$ are evaluated to ensure that large step changes in α_S and $\overline{B}$ do not coincide with changes in the number of cells where A exceeds the effective noise floor. If such step changes are observed (fig. 7-5), the value of the noise-floor offset is increased and steps 4–5 are repeated. In our study, noise-floor offsets have been found to range from 5 to 30 counts, depending on ADP and deployment location.

(7) Determine whether non-physical correlations exist between α_S and non-sediment-related parameters, such as stage (figs. 7-6–7-7). If such correlations exist, the ADP deployment location must be moved to a region of more spatially uniform flow. Flow patterns in regions of nonuniform flow, such as in lateral recirculation eddies (Schmidt, 1990), may change substantially with changes in stage (Schmidt and Graf, 1990). These stage-dependent changes in flow pattern may greatly alter the lateral distribution of suspended sediment along the acoustic beams, thus changing spatial patterns in A along the acoustic beams, ultimately affecting the calculated values of α_S and $\overline{B}$. Because accurate acoustical suspended-sediment measurements depend on α_S varying mainly as a function of the characteristics of the suspended sediment, α_S must either remain constant or increase slowly as stage increases. Inverse correlations between stage and α_S are indicators of poor ADP deployment locations affected by stage-dependent changes in spatial flow patterns. A slight positive correlation between stage and α_S is acceptable, because suspended-sediment concentration is generally positively correlated with stage, although this correlation may be poor depending on the magnitude of temporal changes in the upstream sediment supply.

(8) Time average α_S and $\overline{B}$ and merge the time-averaged values of α_S and $\overline{B}$ with the laboratory-processed EDI, EWI, and calibrated-pump measurements. Depending on the hydrologic flashiness of the river, time-averaging windows ranging from 30 minutes to 1 hour centered on the temporal midpoint of each EDI, EWI, or calibrated-pump measurement give the best results.

(9) Regress relations between time-averaged α_S and $C_{XS\text{-}SILT\text{-}CLAY}$. Because calibrated-pump measurements of $C_{XS\text{-}SILT\text{-}CLAY}$ are reasonably accurate, especially at higher concentrations, and these measurements typically include higher-concentration values of $C_{XS\text{-}SILT\text{-}CLAY}$ than are typically captured during EDI or EWI measurements, all EDI, EWI, and calibrated-pump measurements are included in these regressions. Depending on ADP and site characteristics, one or two relations may need to be regressed to provide the most accurate calculation of $C_{XS\text{-}SILT\text{-}CLAY}$ over the entire range of the domain in α_S. In many cases, where the suspended-silt-and-clay concentration is likely constant along the length of the acoustic beams, the theoretically expected linear relation between α_S and $C_{XS\text{-}SILT\text{-}CLAY}$ (on the basis of equation 27) provides the best fit between α_S and $C_{XS\text{-}SILT\text{-}CLAY}$ (for example, fig. 6 in main part of report) Although these empirically determined, best-fit linear relations between α_S and $C_{XS\text{-}SILT\text{-}CLAY}$ typically require a small positive or negative y-intercept, sometimes the best relation does pass through the origin, as expected on the basis of theory. In other cases, where either (a) the lateral distribution of suspended-silt-and-clay concentration may systematically change along the acoustic beams as a function of concentration, or (b) the clay-mineral content or grain-size characteristics of the suspended silt and clay may vary as a function of concentration, better fits between α_S and $C_{XS\text{-}SILT\text{-}CLAY}$ can be obtained by dividing the domain in α_S into two parts, where a two-part relation between α_S and $C_{XS\text{-}SILT\text{-}CLAY}$ is then regressed. In these cases, the relation between α_S and $C_{XS\text{-}SILT\text{-}CLAY}$ in the lower part of the domain is best described by either a line or second order (typically concave-down) polynomial, and the relation between α_S and $C_{XS\text{-}SILT\text{-}CLAY}$ in the upper part of the domain being best described by a line.

(10) Develop the BBC relation by using least-squares linear regression to solve for coefficients K_1 and K_2 in equation 60 (for example, see fig. 11 in main part of report). The values used for $\overline{B}_{BASE}$ in this regression are the time-averaged values of $\overline{B}$ associated with $C_{XS\text{-}SAND}$ that meet the following two criteria: (a) $D_{50\text{-}XS\text{-}SAND}$ is within 1/4ϕ of $D_{50\text{-}XS\text{-}SAND\text{-}REF}$, and (b) suspended-sand measurements are associated with relatively small S values, preferably only those with values of $S \leq 2$ where silt and clay contributes negligible amounts of backscatter (for example, see fig. 14 in main part of report). $D_{50\text{-}XS\text{-}SAND\text{-}REF}$ is usually set equal to the values of the nearest 1/4-ϕ increment. Although K_1 largely depends on the SL associated with each ADP, both K_1 and K_2 will depend on the local site geometry and flow characteristics (if the average C_{SAND} and $D_{50\text{-}SAND}$ along the acoustic beams were directly proportional to $C_{XS\text{-}SAND}$ and $D_{50\text{-}XS\text{-}SAND}$, then K_2 would equal the theoretical value of 0.1). Empirical values of K_2 may have a large range, but they typically fall within the range from 0.07 to 0.15. Because EDI and EWI measurements provide a much more accurate measurement of $C_{XS\text{-}SAND}$ than do calibrated-pump measurements, only EDI or EWI measurements should be used in the development of the BBC relation if sufficient EDI or EWI measurements exist at low S values.

(11) Use equation 66 to calculate B'. The grain-size distribution of the sand used in this calculation is that used to develop the BBC relation in step 10. D_{50} and σ_G of the suspended silt and clay are solved for iteratively to find the values of D_{50} and σ_G that, at all frequencies present at a study site, results in the best agreement between theoretical and empirical values of B' (for example, fig. 14 in main part of report) and in the best agreement between theoretical and empirical values of α_{UNIT} (for example, fig. 6 in main part of report).

(12) Conduct comparisons between theoretically predicted and measured values of $\log_{10}(S)$ over the entire range of α_S and $\overline{B}$ associated with EDI, EWI, and calibrated-pump measurements to evaluate the quality of the ADP calibration. If the calibration is good, the agreement between the theoretically predicted and measured values of $\log_{10}(S)$ will be good, and should look like those in figure 17. In cases where there is only slight systematic disagreement between the theoretically predicted and measured values of $\log_{10}(S)$, some improvement in the agreement is possible through minor adjustment of the relation between α_S and $C_{XS\text{-}SILT\text{-}CLAY}$.

If physical processes are present in the river at the ADP deployment site that result in substantial shifts in the BBC relation (see appendix 6), then the agreement between the theoretically predicted and measured values of $\log_{10}(S)$ will be poor, exhibiting increased upward scatter of the measured values of $\log_{10}(S)$ relative to the theoretical values of $\log_{10}(S)$ (see, for example, figs. 6-3*A–B* in appendix 6). In such cases, F-tests should be conducted to determine whether significant relations exist between Q and $\log_{10}(S)$ or between Q and $C_{XS\text{-}SAND}$ at constant $\overline{B}$ and α_S (for example, fig. 6-1 in appendix 6). In some cases, where significant relations are detected, discharge-weighting factors may be developed and applied to the theoretical predictions of $\log_{10}(S)$ to mitigate the impact of discharge-correlated BBC shifts, and therefore result in an ADP calibration with acceptably low levels of error in the acoustical measurements of C_{SAND}. As described in appendix 6, the discharge-weighting factor takes the following form:

$$\left(Q / Q_{THRESH}\right) \quad (7\text{-}1)$$

where

Q_{THRESH} is the threshold discharge below which substantial systematic shifts in the BBC relation are detected on the basis of the methods described in appendix 6.

When discharge-weighting factors are required, the theoretical predictions of $\log_{10}(S)$ are adjusted by dividing by the discharge-weighting factor. The need for discharge-weighting factors at a study site depends on the suspended-sediment conditions in the river and not on the properties of the ADPs. Therefore, when discharge-weighting factors are required, they will be required for both ADPs at a study site. The value of Q_{THRESH} may vary between different-frequency ADPs at the same study site, however, because different-frequency ADPs typically ensonify different volumes of water. In this study, discharge-weighting factors were required only at the Rio Grande study sites and not at any of the Colorado River study sites.

(13) Although acoustical measurements outside the linear range between the logarithm of the gain setting and A should be avoided, sometimes this is impossible. To check for this potential problem, conduct comparisons between theoretically predicted and measured values of $\log_{10}(S)$ at values of $\overline{B}$>~90 dB. If measured values of $\log_{10}(S)$ greatly exceed the theoretically predicted values of $\log_{10}(S)$ in these comparisons, then application of a high-dB correction to the predicted values $\log_{10}(S)$ may improve the single-frequency estimate of $C_{XS\text{-}SAND}$. This correction is only applied under the extremely high values of $\overline{B}$ where the systematic disagreement between theoretically predicted and measured values of $\log_{10}(S)$ is positively correlated with $\overline{B}$. The high-dB correction is added to the theoretically predicted values of $\log_{10}(S)$ after application of any required discharge-weighting factor and takes the following form:

$$\left(-K_3\overline{B}_{THRESH} + K_2\overline{B}\right) \quad (7\text{-}2)$$

where

K_3 is the constant that results in the best agreement between the theoretically predicted and measured values of $\log_{10}(S)$ at values of $\overline{B} > \overline{B}_{THRESH}$.

$\overline{B}_{THRESH}$ is typically slightly greater than ~90 dB, but varies somewhat among the ADPs that require a high-dB correction. The need for a high-dB correction at a study site depends on the properties of an individual ADP and not on the suspended-sediment conditions in the river. Because of the floating-scale bias in the *RL* among different ADPs, identical suspended-sediment conditions may be associated with a measured $\overline{B}$ much less than 90 dB on one ADP, but associated with a measured $\overline{B}$ much greater than 90 dB on a different ADP. Thus, on the first ADP in this example, the value of $\overline{B}$ falls within the linear range between the logarithm of the gain setting and A, whereas on the second ADP, the value of $\overline{B}$ falls within the nonlinear range between the logarithm of the gain setting. In this study, high-dB corrections were only required for the 2008 redesigned version of the OTT SLD ADPs that were deployed at the Rio Grande study sites. For the same suspended-sediment conditions, the values of $\overline{B}$ measured by the post-2008 OTT SLDs were up to 30 dB larger than those measured by identical-frequency Nortek EasyQ ADPs deployed at the same locations.

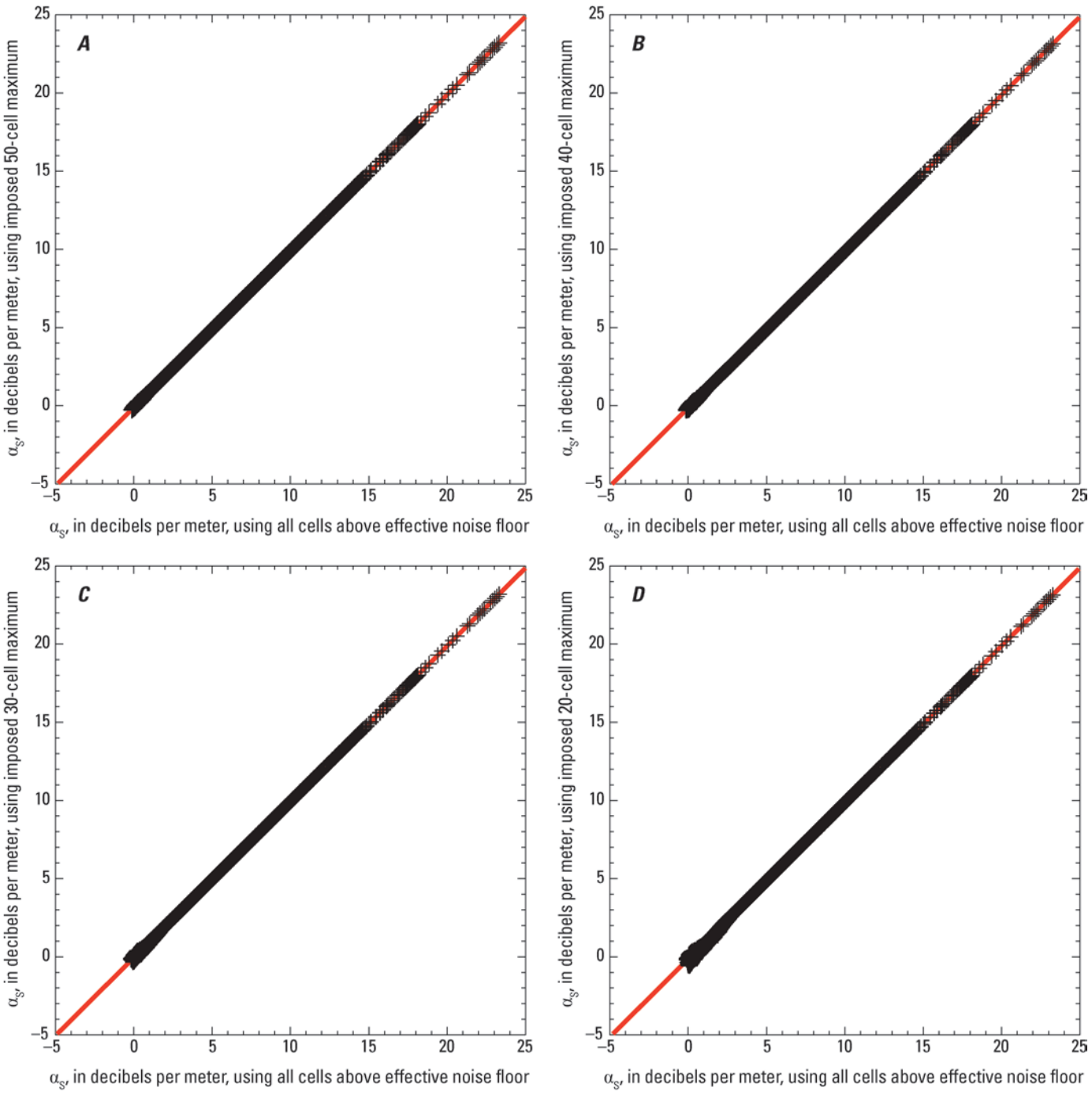

Figure 7-1. Examples of how limiting the number of cells in the acoustic beam affects α_S, the sediment attenuation coefficient. Cell size is not changed between examples; a lower maximum number of cells corresponds to measurements along a shorter length of the acoustic beam. The red solid line is the line of perfect agreement between α_S calculated using different numbers of cells. As the number of cells decreases, α_S becomes negatively biased, and variance in α_S increases, especially at lower values of α_S. The increase in variance with decreasing cell number is a general response; although the increase in bias with decreasing cell number is also a general response, the sign of this bias will vary between different ADPs and deployment locations because the curvature in the measurements along the beam will vary between different ADPs and locations. Data used in these examples are from 277,327 15-minute measurements made using the 1-MHz ADP at the CR87 study site between August 22, 2005, and August 1, 2013. All examples are plotted relative to α_S calculated using the maximum number of cells above the effective noise floor (as many as 64 cells when suspended-silt-and-clay concentrations are relatively low). ***A***, α_S calculated using 50 cells; ***B***, α_S calculated using 40 cells; ***C***, α_S calculated using 30 cells; ***D***, α_S calculated using 20 cells; ***E***, α_S calculated using 10 cells; ***F***, α_S calculated using 5 cells; and ***G***, α_S calculated using 3 cells.

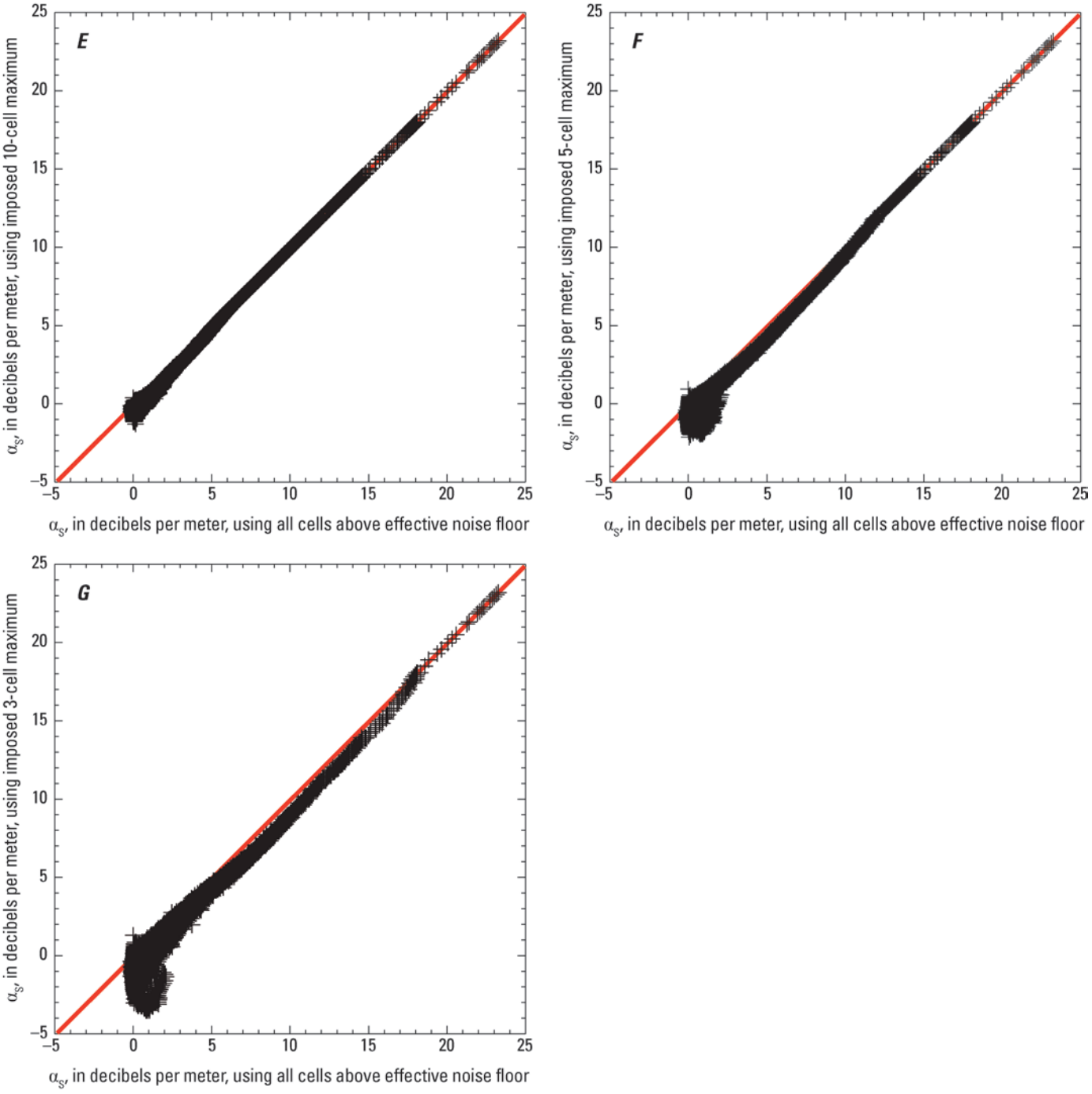

Figure 7-1.—Continued

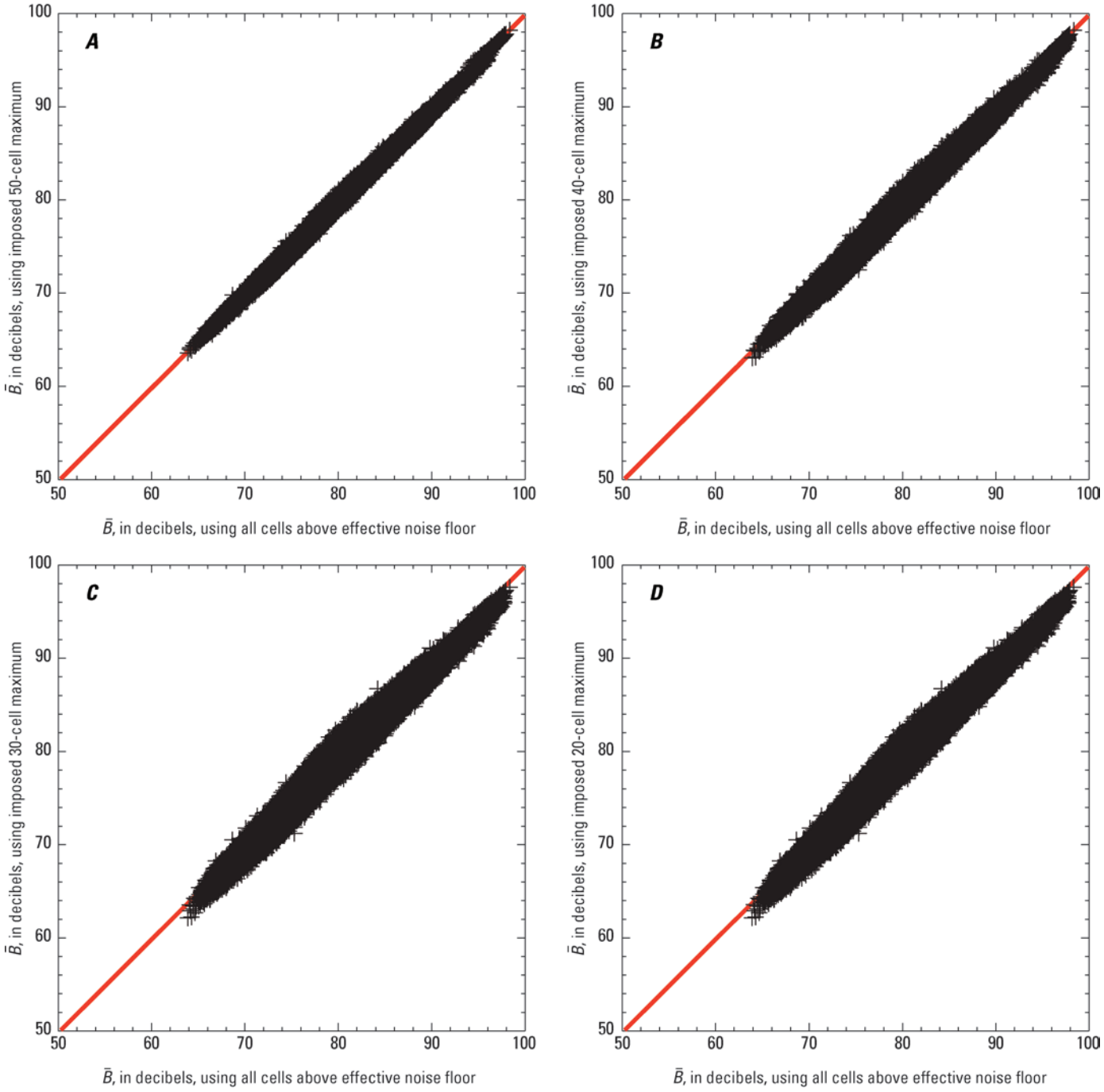

Figure 7-2. Examples of the effect on how limiting the number cells in the acoustic beam affects $\bar{B}$, the beam-averaged backscatter. Cell size is not changed between examples; a lower maximum number of cells corresponds to measurements along a shorter length of the acoustic beam. The red solid line is the line of perfect agreement between $\bar{B}$ calculated using different numbers of cells. As the number of cells decreases, $\bar{B}$ becomes negatively biased and variance in $\bar{B}$ increases; comparison of this figure with figure 7-1 indicates that imposing cell limits affects $\bar{B}$ much more than α_s, the sediment attenuation coefficient. As in the examples in figure 7-1, the increase in variance with decreasing cell number is a general response; although the increase in bias with decreasing cell number is also a general response, the sign of this bias will vary between different ADPs and deployment locations because the curvature in the measurements along the beam will vary between different ADPs and locations. Data used in these examples are from the same acoustical measurements used in figure 7-1. All examples are plotted relative to $\bar{B}$ calculated using the maximum number of cells above the effective noise floor (as many as 64 cells when suspended-silt-and-clay concentrations are relatively low). ***A***, $\bar{B}$ calculated using 50 cells; ***B***, $\bar{B}$ calculated using 40 cells; ***C***, $\bar{B}$ calculated using 30 cells; ***D***, $\bar{B}$ calculated using 20 cells; ***E***, $\bar{B}$ calculated using 10 cells; ***F***, $\bar{B}$ calculated using 5 cells; and ***G***, $\bar{B}$ calculated using 3 cells.

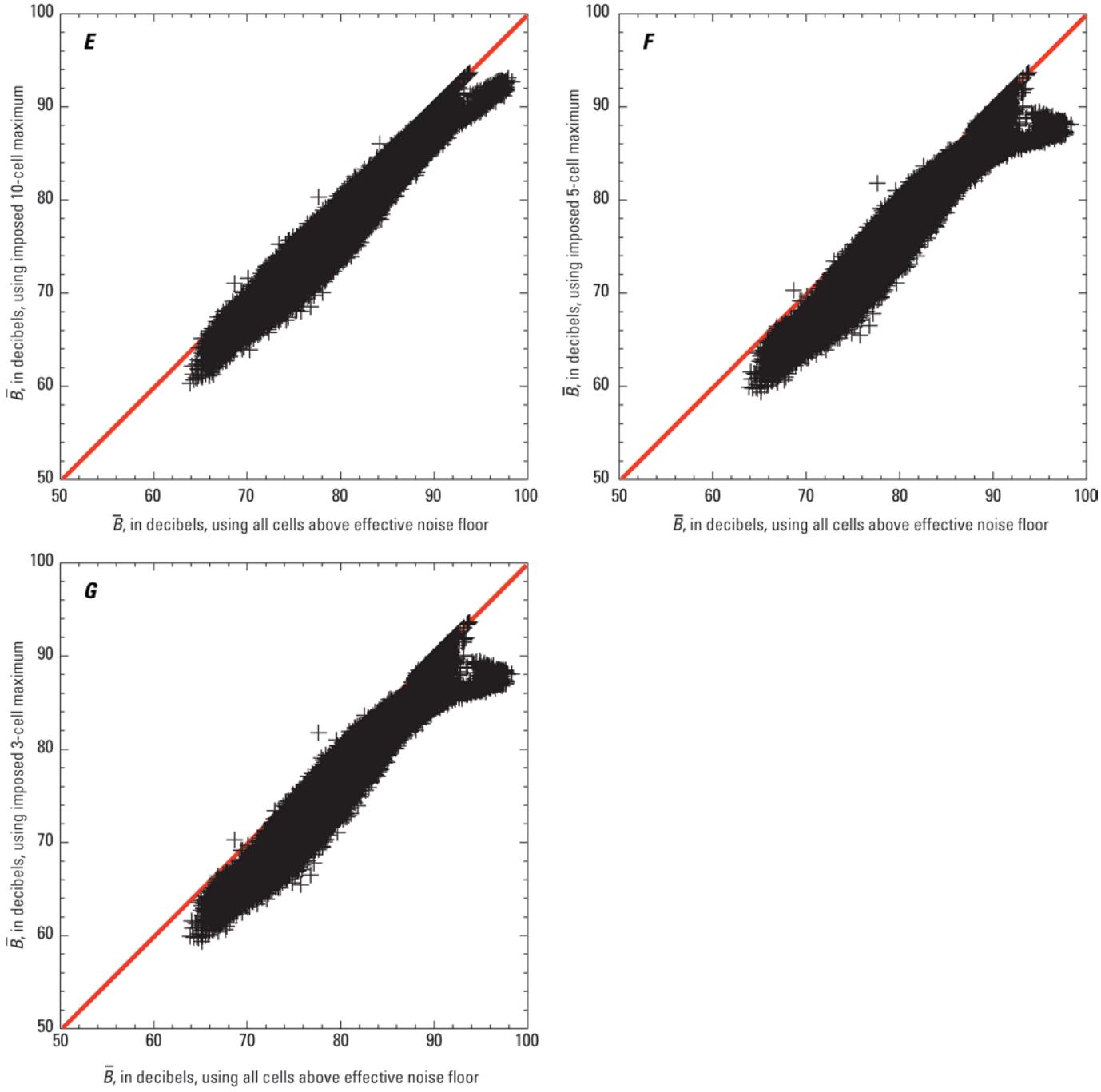

Figure 7-2.—Continued

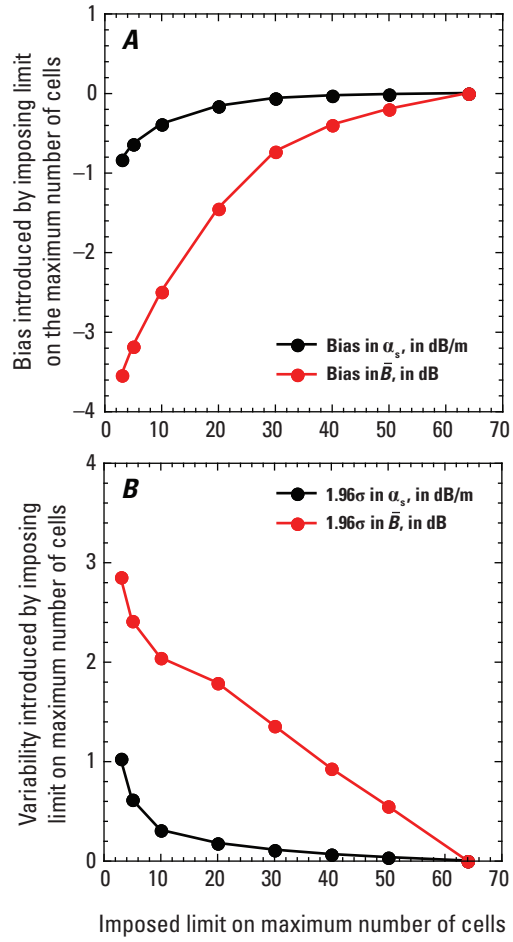

Figure 7-3. Summary of the effects of imposing lower maximum limits on the number of cells on the mean bias and variability in α_S and $\bar{B}$ limits on the number of cells on the (***A***) bias and (***B***) variability in α_S (the sediment attenuation coefficient) and $\bar{B}$ (the beam-averaged backscatter), depicted in figures 7-1 and 7-2. The biases depicted in ***A*** are the averages of the absolute errors in the values of α_S and $\bar{B}$ calculated using the imposed lower limits on the numbers of cells specified for each panel in figures 7-1 and 7-2. The variability shown in ***B*** is set equal to 1.96 times the standard deviation among these absolute errors so that it brackets roughly 95 percent of all observations in a Gaussian-normal distribution. The effect of limiting the maximum number of cells has a much greater effect on $\bar{B}$ than on α_S. Because $\bar{B}$ is linearly related to $\log_{10}(C_{XS\text{-}SAND})$, the rapid increase in the negative bias in $\bar{B}$ and in the variation in $\bar{B}$ indicates that imposing lower limits on the maximum number of cells will greatly increase both the negative bias and random error in acoustical measurements of $C_{XS\text{-}SAND}$. Although the increase in the magnitude of the bias with decreasing cell number is a general response, the sign of the bias will vary between different ADPs and deployment locations because the curvature in the measurements along the beam will vary between different ADPs and locations. The increase in the variability of the absolute error with decreasing cell number is a general response and does not depend on the curvature in the measurements along the beam. This increase in the variability of the absolute error in α_S and $\bar{B}$ will result in an increase in the 68-percent- and 95-percent-confidence level errors in acoustical suspended-sediment measurements made with fewer numbers of cells.

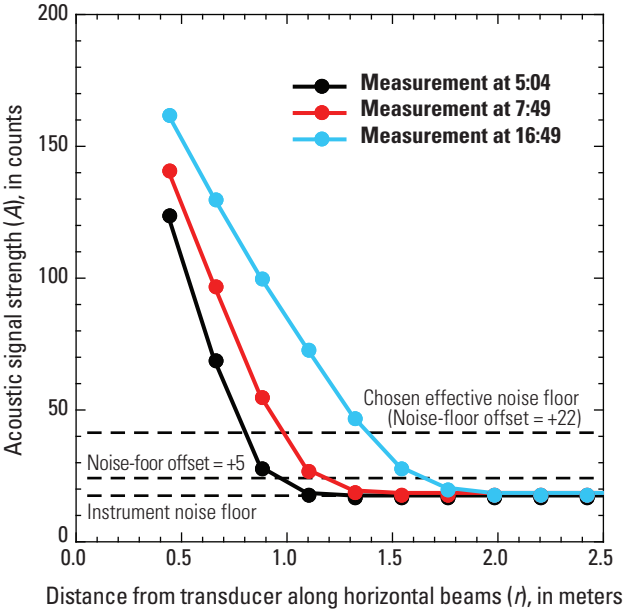

Figure 7-4. Example showing noise-floor offsets required to exclude acoustical measurements in the "curved part" of the acoustic profile immediately above the instrument noise floor. The +5 count noise-floor offset is too small to fully exclude the measurements in the curved part of the profile, whereas the +22 count noise-floor offset (chosen graphically) is large enough to exclude the measurements in this region. These measurements were made using the 2-MHz acoustic-Doppler profiler at the RG-RGV study site on July 28, 2012; times are in Central Standard Time.

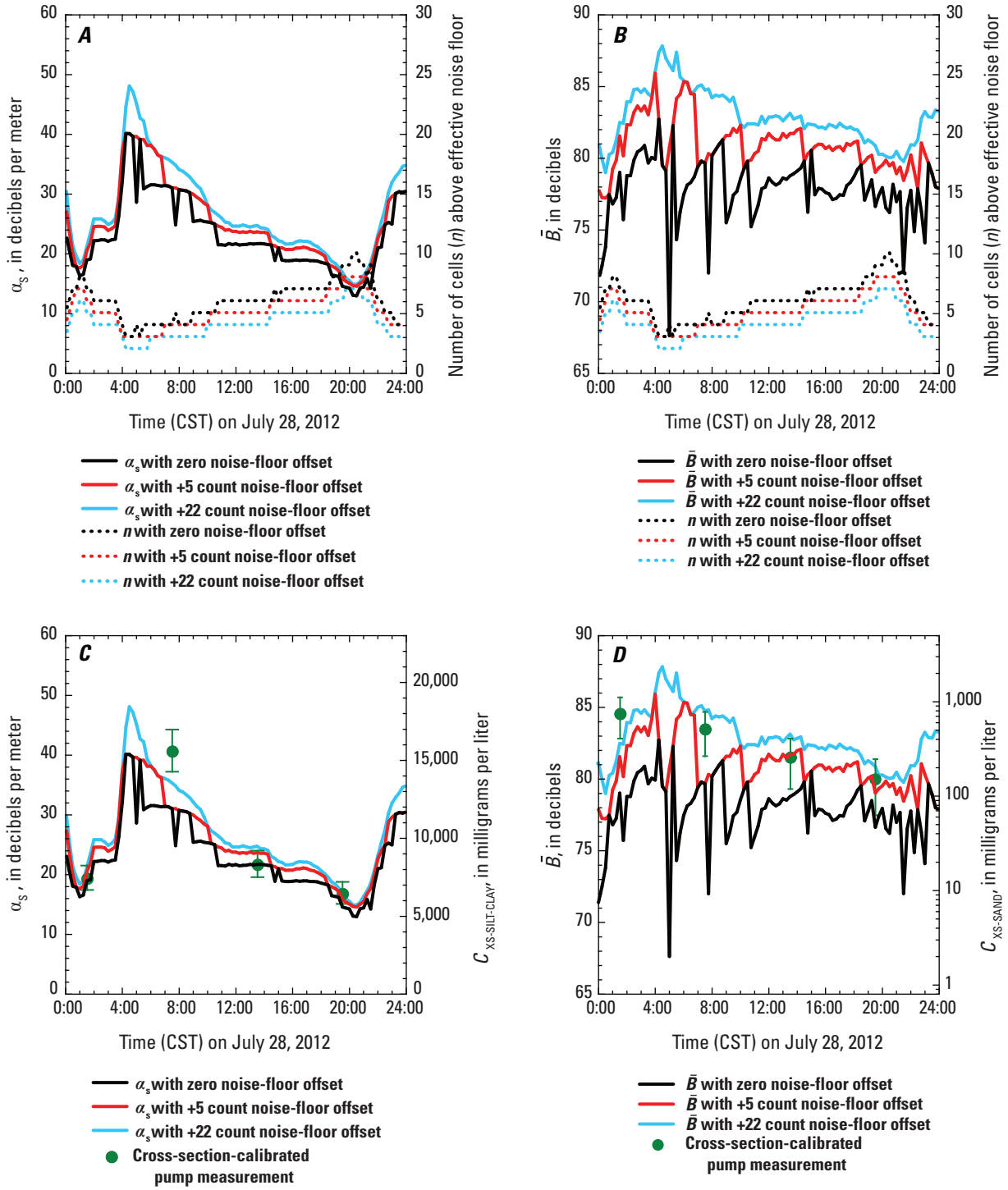

Figure 7-5. Effect of the different noise-floor offsets (depicted in figure 7-4) on calculations of α_s (the sediment attenuation coefficient) and $\bar{B}$ (the beam-averaged backscatter) for the 2-MHz acoustic-Doppler profiler at the RG-RGV study site on July 28, 2012. A noise-floor offset of +22 counts above the recorded instrument noise floor is required to remove the step changes in α_s and greatly reduce the step changes in $\bar{B}$ associated with the changing numbers of cells above the effective noise floor. ***A***, Calculated α_s using 0, +5, and +22 count noise-floor offsets, shown with the number of cells in the acoustic beam that are above the effective noise floor. ***B***, Calculated $\bar{B}$ using 0, +5, and +22 count noise-floor offsets, shown with the number of cells in the acoustic beam that are above the effective noise floor. ***C***, Cross-section-calibrated pump measurements of suspended-silt-and-clay concentration (with 95-percent confidence-level error bars) superimposed on the values of α_s in ***A***. ***D***, Cross-section calibrated-pump measurements of suspended-sand concentration (with 95-percent confidence-level error bars) superimposed on the values of $\bar{B}$ in ***B***. The superimposed suspended-sediment measurements in ***C*** and ***D*** agree most favorably with the smoother variation in α_s and $\bar{B}$ produced by using the higher noise-floor offset of +22 counts. Use of lower noise-floor offsets not only results in large cell-number-dependent step changes in α_s and $\bar{B}$, it also results in periods during which changes in α_s and $\bar{B}$ have the incorrect sign.

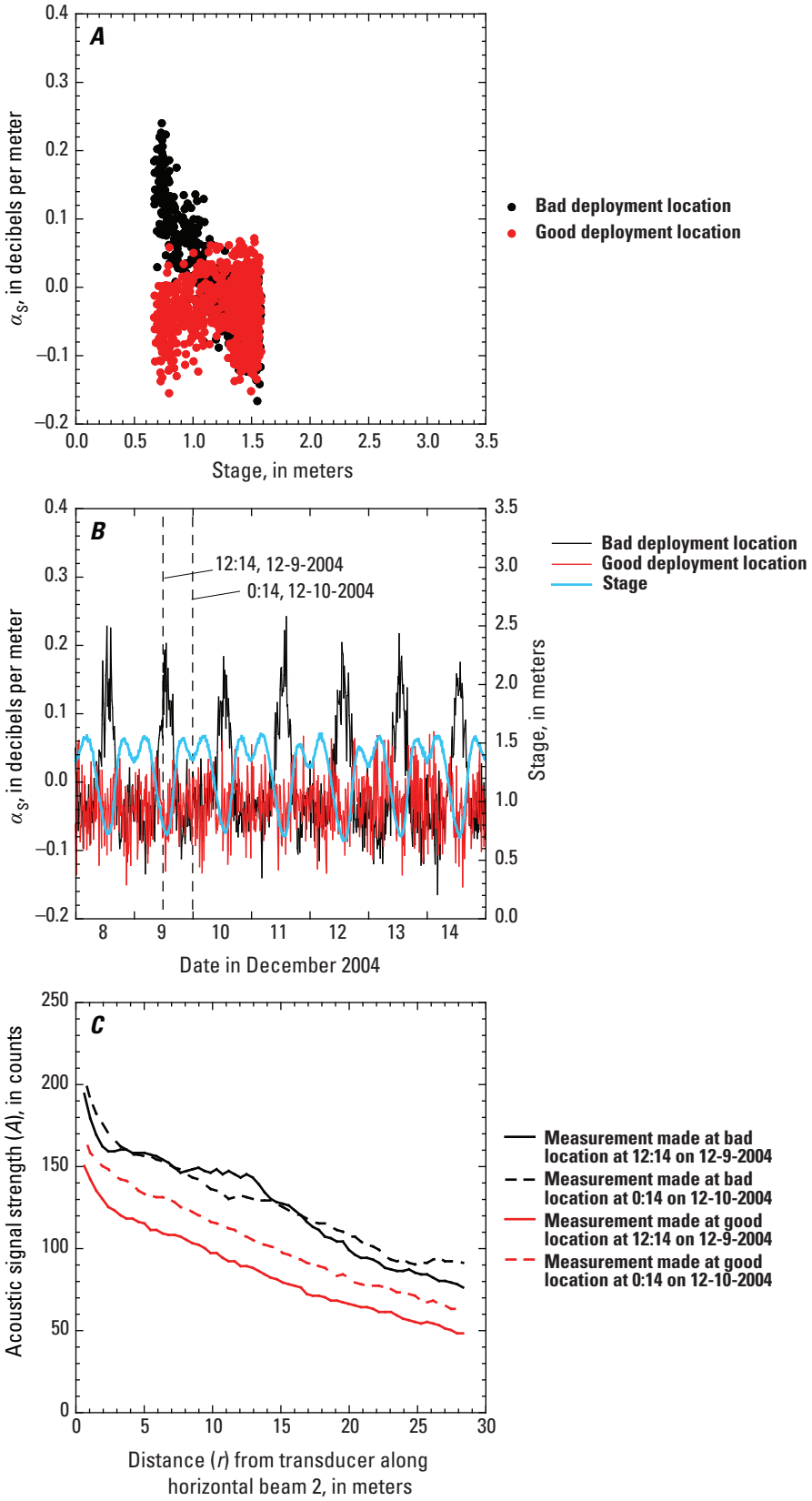

Figure 7-6. 1-MHz acoustic-Doppler profilers (ADP) measurements made at a bad deployment location in a large lateral-recirculation eddy compared to 1-MHz ADP measurements made at a good deployment location in uniform flow above a rapid at the CR30 study site. The bad deployment location corresponds to the location of the "primary site" in Griffiths and others (2012; shown in their fig. 3*A*); the good deployment location corresponds to the location of the "1-MHz ADP" in Griffiths and others (2012; their fig. 3*A*). Stage correlated changes in the calculated values of α_S that arise from likely stage-associated changes in the lateral distribution of suspended-sediment along the acoustic beam dominate the data at the bad deployment location. ***A***, α_S plotted as a function of stage at the bad and good ADP deployment locations. α_S calculated using all 15-minute acoustical measurements made using beam 2 on each ADP from December 8 through 14, 2004. ***B***, Time series of stage superimposed on the calculated values of α_S from both ADPs. Timestamps in Mountain Standard Time of the example raw measurements in ***C*** are indicated. ***C***, Raw acoustical measurements from beam 2 on the two ADPs at the indicated timestamps in ***B*** showing the source of the negative correlation between stage and α_S at the bad ADP deployment location in the lateral recirculation eddy.

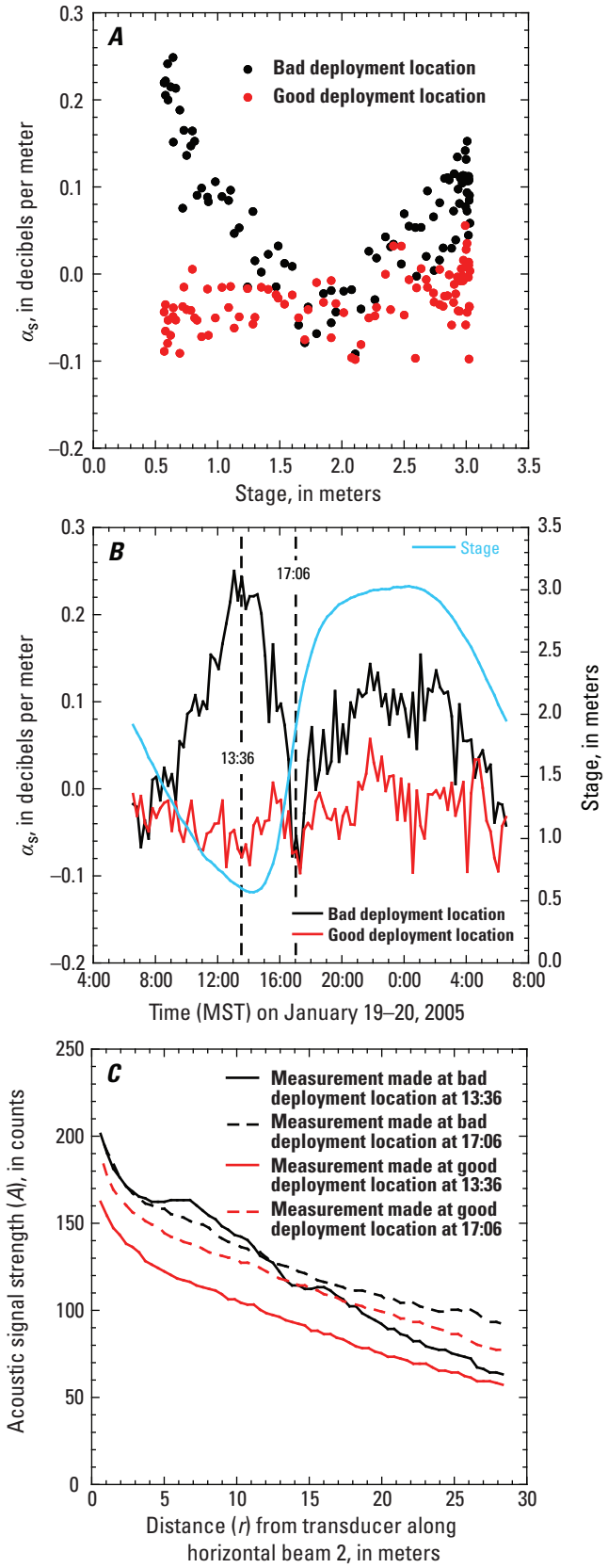

Figure 7-7. Second comparison between 1-MHz acoustic-Doppler profiler (ADP) measurements made at the bad and good deployment locations at the CR30 study site. ***A***, α_s plotted as a function of stage at the bad and good deployment locations. α_s calculated using all 15-minute acoustical measurements made using beam 2 on each ADP from 6:00 MST (Mountain Standard Time) on January 19, 2005, through 6:00 MST on January 20, 2005. ***B***, Time series of stage superimposed on the calculated values of α_s from both ADPs. Timestamps of the example raw measurements in ***C*** are indicated. ***C***, Raw acoustical measurements from beam 2 on the two ADPs at the indicated timestamps in ***B*** showing the source of the negative correlation between stage and α_s at the bad deployment location in the lateral recirculation eddy.

Appendix 8. Multi-Frequency *RUTS*-Based Calculation of $C_{\text{XS-SAND}}$ and $D_{\text{50-XS-SAND}}$

The *RUTS*-based calculation of $C_{\text{XS-SAND}}$ and $D_{\text{50-XS-SAND}}$ proceeds as follows for two paired acoustic frequencies within the 600-kHz to 2-MHz range:

(1) The theoretical *RUTS* for each frequency is calculated using the $D_{\text{50-XS-SAND-REF}}$ and σ_G of the suspended sand typical at the study site.

(2) Because backscatter at higher frequencies is less affected by changes in $D_{\text{50-XS-SAND}}$, the estimate of $C_{\text{XS-SAND}}$ at the higher frequency is chosen as the initial estimate of $C_{\text{XS-SAND}}$ in this calculation.

(3) In cases where the lower-frequency estimate of $C_{\text{XS-SAND}}$ is greater than the higher-frequency estimate, the initial estimate of $C_{\text{XS-SAND}}$ in step 2 is reduced using the theoretical *RUTS* relations and empirical BBC relations for the two frequencies. In these cases, $D_{\text{50-XS-SAND}}$ is coarser than $D_{\text{50-XS-SAND-REF}}$, and the *RUTS* relations for the two frequencies are used to calculate this larger D_{50}. Conversely, in cases where the lower-frequency estimate of $C_{\text{XS-SAND}}$ is less than the higher-frequency estimate, the initial estimate of $C_{\text{XS-SAND}}$ in step 2 is increased using the *RUTS* and BBC relations for the two frequencies. In these cases, $D_{\text{50-XS-SAND}}$ is less than $D_{\text{50-XS-SAND-REF}}$, and the *RUTS* relations for the two frequencies are used to calculate this smaller D_{50}. If the estimates of $C_{\text{XS-SAND}}$ are identical at both frequencies, the initial estimate of $C_{\text{XS-SAND}}$ in step 2 is not modified, and $D_{\text{50-XS-SAND}}$ equals $D_{\text{50-XS-SAND-REF}}$.

Step 3 proceeds mathematically as follows. First, using data from the lower-frequency ADP, calculate the effective $\overline{B}$ for $C_{\text{XS-SAND}}$ estimated by the lower-frequency ADP, and correct for effects of B' and for any discharge-correlated BBC shifts. This first effective lower-frequency beam-averaged backscatter, $B_{\text{1-LOWf}}$, is found by:

$$B_{\text{1-LOWf}} = \left(\log_{10}\left(C_{\text{XS-SAND-LOWf}}\right) - K_{\text{1-LOWf}}\right) / K_{\text{2-LOWf}} \quad (8\text{-}1)$$

where

$C_{\text{XS-SAND-LOWf}}$ is the initial $C_{\text{XS-SAND}}$ estimated by the procedure described in appendix 7 for the lower-frequency ADP,
$K_{\text{1-LOWf}}$ is K_1 from the BBC relation for the lower-frequency ADP, and
$K_{\text{2-LOWf}}$ is K_2 from the BBC relation for the lower-frequency ADP.

Second, calculate the effective $\overline{B}$ on the lower-frequency ADP that would exist for the value of $C_{\text{XS-SAND}}$ estimated by the higher-frequency ADP, and correct for effects of B' and any discharge-correlated BBC shifts (see appendix 7). This second effective lower-frequency beam averaged backscatter, $B_{\text{2-LOWf}}$, is found by:

$$B_{\text{2-LOWf}} = \left(\log_{10}\left(C_{\text{XS-SAND-HIGHf}}\right) - K_{\text{1-LOWf}}\right) / K_{\text{2-LOWf}} \quad (8\text{-}2)$$

where

$C_{\text{XS-SAND-HIGHf}}$ is the suspended-sand concentration estimated by the procedure described in appendix 7 for the higher-frequency ADP, and the values of
$K_{\text{1-LOWf}}$ and
$K_{\text{2-LOWf}}$ are the same as used in equation 8-1.

Step 3 proceeds mathematically as follows. The difference between these two effective values of $\overline{B}$ is then referred to as the lower-frequency backscatter defect, where

$$B_{\text{LOW-DEFECT}} = B_{\text{1–LOWf}} - B_{\text{2-LOWf}} \,. \quad (8\text{-}3)$$

Once $B_{\text{LOW-DEFECT}}$ has been determined, $D_{\text{50-XS-SAND}}$ is set equal to the value of D_{50} along the lower-frequency theoretical *RUTS* relation at $RUTS = B_{\text{LOW-DEFECT}}$. The higher-frequency backscatter defect, $B_{\text{HIGH-DEFECT}}$, is then set equal to the value of *RUTS* along the higher-frequency theoretical *RUTS* relation at $D_{\text{50-XS-SAND}}$. The logarithm of $C_{\text{XS-SAND}}$, using both acoustic frequencies, is then calculated as:

$$\log_{10}\left(C_{\text{XS-SAND}}\right) = K_{\text{1-HIGHf}} + K_{\text{2-HIGHf}}\left(B_{\text{HIGHf}} - B_{\text{HIGH-DEFECT}}\right) \quad (8\text{-}4)$$

where

$K_{\text{1-HIGHf}}$ is K_1 from the BBC relation for the higher-frequency ADP, and
$K_{\text{2-HIGHf}}$ is K_2 from the BBC relation for the higher-frequency ADP.

B_{HIGHf} in equation 8-4 is the effective $\overline{B}$ using the higher-frequency ADP that would exist for $C_{\text{XS-SAND}}$ estimated by the higher-frequency ADP, corrected for effects of B' and for any discharge-correlated BBC shifts, and is calculated by:

$$B_{\text{HIGHf}} = \left(\log_{10}\left(C_{\text{XS-SAND-HIGHf}}\right) - K_{\text{1-HIGHf}}\right) / K_{\text{2-HIGHf}} \,. \quad (8\text{-}5)$$

To prevent calculating overly high values of $C_{XS\text{-}SAND}$ by, in effect, counting silt-and-clay-sized sediment as sand, $B_{LOW\text{-}DEFECT}$ is limited such that the predicted value of $D_{50\text{-}XS\text{-}SAND}$ along the lower-frequency *RUTS* relation can never be less than 0.074 mm (that is, the size class of sand 1/4φ greater than the 0.0625-mm silt-sand break). Not limiting $D_{50\text{-}XS\text{-}SAND}$ at 0.074 mm would result in double counting sediment near the silt-sand break on the basis of both acoustic attenuation and acoustic backscatter.

In cases where more than two frequencies of ADPs are deployed at a study site (for example, the CR87 study site where 600-kHz, 1-MHz, and 2-MHz ADPs are all present), the above method is modified slightly. At the CR87 study site, steps 1–3 are solved twice, once using the 2-MHz ADP for the higher-frequency measurements and the 1-MHz ADP for the lower-frequency measurements, and once using the 2-MHz ADP for the higher-frequency measurements and the 600-kHz ADP for the lower-frequency measurements. Three-frequency values of $C_{XS\text{-}SAND}$ and $D_{50\text{-}XS\text{-}SAND}$ are then calculated as the weighted average of the values of $C_{XS\text{-}SAND}$ and $D_{50\text{-}XS\text{-}SAND}$ calculated using each of the two paired frequencies.

Appendix 9. Plots of Predicted Versus Observed Values of $C_{XS\text{-}SILT\text{-}CLAY}$, $C_{XS\text{-}SAND}$, and $D_{50\text{-}XS\text{-}SAND}$, with Data Segregated by Study Site

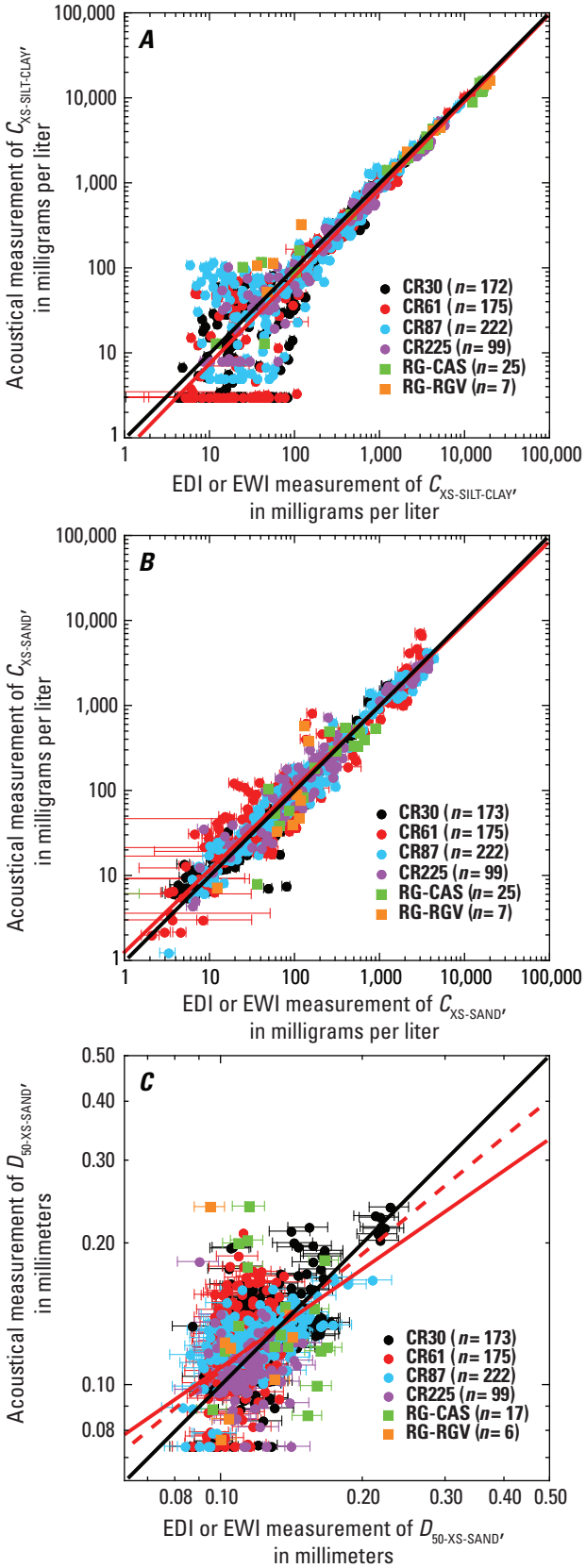

Figure 9-1. Predicted versus observed plots for the equal-discharge increment (EDI) or equal-width increment (EWI) and acoustical measurements of $C_{XS\text{-}SILT\text{-}CLAY}$, $C_{XS\text{-}SAND}$, and $D_{50\text{-}XS\text{-}SAND}$, with data segregated by study site. In each figure panel, the solid black line is the line of perfect agreement; *n* is the number of observations; horizontal error bars indicate the 95-percent-confidence-level combined field and laboratory-processing error in the EDI or EWI measurement. ***A***, Plot of predicted versus observed values of $C_{XS\text{-}SILT\text{-}CLAY}$. Solid red line is the best-fit log-linear regression fit to the data from all study sites in ***A–C***. ***B***, plot of predicted versus observed values of $C_{XS\text{-}SAND}$. ***C***, plot of predicted versus observed values of $D_{50\text{-}XS\text{-}SAND}$. Dashed red line is the best-fit log-linear regression fit to the data from only the CR30 study site (the study site with the largest range in EDI- or EWI-measured $D_{50\text{-}XS\text{-}SAND}$).

Publishing support provided by the U.S. Geological Survey Science Publishing Network, Menlo Park, California and Tacoma, Washington Publishing Service Centers

Manuscript approved for publication March 10, 2016

Edited by Claire M. Landowski

Design and layout by Sharon L. Wahlstrom

USGS

Topping and Wright—**Long-Term Continuous Acoustical Suspended-Sediment Measurements in Rivers**—Professional Paper 1823

ISSN 1044-9612 (print)
ISSN 2330-7102 (online)
http://dx.doi.org/10.3133/pp1823

ISBN 978-1-4113-4033-6